

BOEING

CR-15166-8
D180-22876-4

NAS9-15196
DRL T-1346
DRD MA-664T
LINE ITEM 3

**Volume IV
Microwave Power
Transmission Systems**



(NASA-CR-151668) SOLAR POWER SATELLITE
SYSTEM DEFINITION STUDY. PART 2, VOLUME 4:
MICROWAVE POWER TRANSMISSION SYSTEMS Final
Report (Boeing Aerospace Co., Seattle,
Wash.) 283 p HC 313/BF A01

N78-20158

Unclass
C9495

CSCI 101 G3/15



Solar Power Satellite

SYSTEM DEFINITION STUDY
PART II

D180-22876-4

CONTRACT NAS9 15196
DRL T-134-6
ORD MA-664T
LINE ITEM 3

Solar Power Satellite

SYSTEM DEFINITION STUDY PART II

VOLUME IV
MICROWAVE POWER TRANSMISSION SYSTEMS
D180-22876-4
DECEMBER 1977

Submitted To
The National Aeronautics and Space Administration
Lyndon B. Johnson Space Center
in Fulfillment of the Requirements
of Contract NAS9-15196

Supervised By

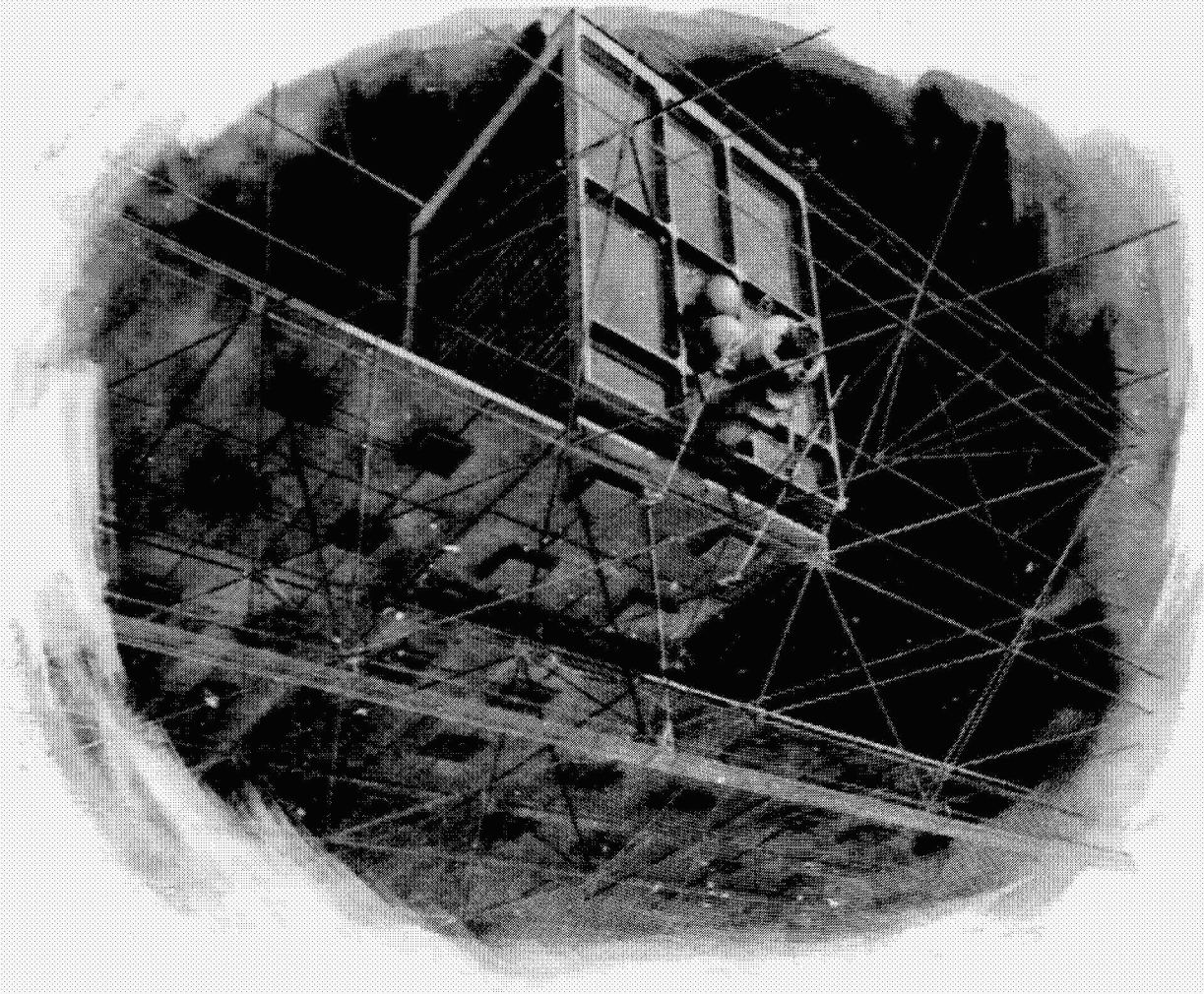
E. J. Nalos
E. J. Nalos

Approved:

G. R. Woodcock
G. R. Woodcock
Study Manager

BOEING AEROSPACE COMPANY
MISSILES AND SPACE GROUP—SPACE DIVISION
P.O. BOX 3999
SEATTLE, WASHINGTON

SPS Microwave Antenna Deployment



The subarray deployment machine is shown attaching the basic microwave building blocks to the spaceborne antenna structure. The control cab houses two operators in a shirt-sleeve environment, one of whom is connecting the microwave transmitters to the power bus bar using manipulators.

FOREWORD

The SPS system definition study was initiated in December 1976. Part I was completed on May 1, 1977. Part II technical work was completed October 31, 1977.

The study was managed by the Lyndon B. Johnson Space Center (JSC) of the National Aeronautics and Space Administration (NASA). The Contracting Officer's Representative (COR) was Clarke Covington of JSC. JSC study management team members included:

Dickey Arndt	Microwave System Analysis	Andrei Konradi	Space Radiation Environment
Harold Benson	Cost Analysis	Jim Kelley	Microwave Antenna
Bob Bond	Man-Machine Interface	Don Kessler	Collision Probability
Jim Cioni	Photovoltaic Systems	Lou Leopold	Microwave Generators
Hu Davis	Transportation Systems	Lou Livingston	System Engineering and
R. H. Dietz	Microwave Transmitter and Rectenna	Jim Meany	MPTS Computer Program
Bill Dusenbury	Energy Conversion	Stu Nachtwey	Microwave Biological Effects
Bob Gundersen	Man-Machine Interface	Sam Nassiff	Construction Base
Alva Hardy	Radiation Shielding	Bob Ried	Structure and Thermal Analysis
Buddy Heineman	Mass Properties	Jack Seyl	Phase Control
Lyle Jenkins	Space Construction	Bill Simon	Thermal Cycle Systems
Jim Jones	Design	Fred Stebbins	Structural Analysis
Dick Kennedy	Power Distribution		

The study was performed by the Boeing Aerospace Company. The Boeing study manager was Gordon Woodcock. Boeing Commercial Airplane Company assisted in the analysis of launch vehicle noise and overpressures. Boeing technical leaders were:

Ottis Bullock	Structural Design	Don Grim	Electrical Propulsion
Vince Caluori	Photovoltaic SPS's	Henry Hillbrath	Propulsion
Bob Conrad	Mass Properties	Dr. Ted Kramer	Thermal Analysis and Optics
Eldon Davis	Construction and Orbit-to-Orbit Transportation	Frank Kilburg	Alternate Antenna Concepts
Rod Darrow	Operations	Walt Lund	Microwave Antenna
Owen Denman	Microwave Design Integration	Keith Miller	Human Factors and Construction Operations
Hal DiRamio	Earth-to-Orbit Transportation	Dr. Ervin Nalos	Microwave Subsystem
Bill Emsley	Flight Control	Jack Olson	Configuration Design
Dr. Joe Gauger	Cost	Dr. Henry Oman	Photovoltaics
Jack Gewin	Power Distribution	John Perry	Structures
Dan Gregory	Thermal Engine SPS's	Scott Rathjen	MPTS Computer Program Development

The General Electric Company Space Division was the major subcontractor for the study. Their contributions included Rankine cycle power generation, power processing and switchgear, microwave transmitter phase control and alternative transmitter configurations, remote manipulators, and thin-film silicon photovoltaics.

Other subcontractors were Hughes Research Center—gallium arsenide photovoltaics; Varian—klystrons and klystron production; SPIRE—silicon solar cell directed energy annealing.

D180-22876-4

This report was prepared in 8 volumes as follows:

- | | | | |
|------------|---|-------------|---|
| I | - Executive Summary | V | Space Operations |
| II | - Technical Summary | VI | Evaluation Data Book |
| III | - SPS Satellite Systems | VII | Study Part II Final Briefing Book |
| IV | - Microwave Power Transmission
Systems | VIII | SPS Launch Vehicle Ascent and Entry
Sonic Overpressure and Noise Effects |

CONTENTS

	Page
1. INTRODUCTION	1
2. ANTENNA ARRAY ANALYSIS	3
2.1 Baseline Antenna Array Design	3
2.1.1 Waveguide Radiating Stick Layout	5
2.1.2 Radiating Slot Spacing Considerations	5
2.1.3 Power Density Taper Quantization Studies	7
2.1.4 Alternate Taper Designs	7
2.2 Spacetenna Dimensional Error Analysis	7
2.2.1 Introduction	7
2.2.2 Analysis Model	11
2.2.3 Subarray Tolerances	11
2.2.4 Radiating Stick Tolerances	14
2.2.5 Minor Loss Sources	18
2.2.6 Results and Discussions	19
2.2.7 Subarray Offset Effects	19
2.2.8 Derivation of Mismatch Loss Equation	23
2.3 Circularly Symmetric Array Radiation Pattern Studies	25
2.3.1 Distributions for Constant Main-Beamwidth	25
2.3.2 Reverse Phase Distributions Pattern	29
2.3.3 Pattern Roll-Off Studies	33
2.4 Phased Array Computer Program Development	33
2.4.1 Spacetenna, Ground Grid, Error and Failure Modeling	33
2.4.2 Organization of Minicomputer Time-Share and Mainstream Computer Systems	41
2.4.3 Future Efforts	43
2.5 Inter-Module Phase Control Concepts	44
2.5.1 Phasing Concepts and Pilot Frequency Offset Consideration	46
2.5.2 Remote Phase Synchronization	50
2.5.3 Phase Multiplication Technique to Eliminate Squint	50
2.5.4 Diplexer Design Consideration	50
2.5.5 Klystron Phase Control Circuit	53
2.6 Rectenna Design Considerations and Alternatives	55
2.6.1 Dipole Spacing Requirements	55
2.6.2 Flat Ground Plane Possibilities	55
2.6.3 Hogline High Gain Configuration	58

	Page
3. ALTERNATE CONCEPTS FOR LARGE PHASED ARRAY CONCEPTS	59
3.1 Introduction	59
3.1.1 General Requirements	59
3.1.2 Reference System	59
3.1.3 Alternate Candidate Selection	59
3.2 Alternate Candidates	60
3.2.1 Unfurlable Core-Type Parabolic Array	60
3.2.2 Deployable Parabolic Array	61
3.2.3 Traveling Wave End Fire Array	63
3.2.4 Cylindrical Lens Horn Array	66
3.2.5 Enhanced Element Planar Waveguide Array	74
3.2.6 Horn Array	75
3.3 Discussion of Results	77
4. HIGH POWER TRANSMITTER	79
4.1 Introduction	79
4.2 Alternate RF Sources	79
4.2.1 Amplitron	79
4.2.2 Solid State RF Generation	81
4.3 High Efficiency Klystron Design Configuration	81
4.3.1 Introduction	81
4.3.2 Depressed Collector Design	83
4.3.3 Voltage Regulation	86
4.3.4 Electron Beam Focusing Design	87
4.4 Life and Reliability Assessment	89
4.4.1 Design Approach to Long Life	89
4.4.2 Current and Projected Tube Life Experience	91
4.4.3 Cathode Design Criteria	93
4.4.4 Tube MTBF Configurations	97
4.5 High Power Klystron Trade Studies	98
4.5.1 Specific Weight Comparison	98
4.5.2 Specific Cost Comparison	102
4.5.3 Thermal Dissipation Capabilities	102
4.5.4 Power Level Trade Study	105
4.5.5 Cost Effectiveness Analysis	107
4.6 Interface Assessment	111
4.6.1 Tube to Subarray Module Interface	111
4.6.2 Operation Under Reduced Voltages	112
4.6.3 X-Ray Radiation Level Assessment	114

	Page
5. POWER DISTRIBUTION	121
5.1 Power Distribution System Requirements	121
5.2 Power Distribution and Control System Concept	124
5.2.1 System Concept	124
5.2.2 MPTS Conductor Selection	128
5.2.3 DC/DC Converters	140
5.2.4 Switchgear	140
5.2.5 Energy Storage	159
5.2.6 Weight and Efficiency	159
5.3 Areas for Further Investigation	159
6. ANTENNA INTEGRATION	163
6.1 Introduction	163
6.2 Integration Concept	163
6.2.1 System Requirements	163
6.2.2 Design Constraints	163
6.2.3 System Compatibility	164
6.3 Structural Considerations	164
6.3.1 Design Drivers	164
6.3.2 Structure Selection	166
6.4 Thermal Analysis	166
6.4.1 Thermal Analysis Approach	166
6.4.2 Heat Sources	167
6.4.3 Thermal Control Devices	167
6.5 Reference Design Configuration	167
6.5.1 Component Installation and Integration	171
6.5.2 Power Density Quantization	182
6.5.3 Overall MPTS Characteristics	186
6.5.4 MPTS Mass Estimate	186
6.6 Discussion	191
6.7 MPTS Efficiency Budget	193
6.7.1 Space Power Distribution Losses	193
6.7.2 RF Conversion and Distribution Losses	193
6.7.3 Antenna Array Losses	195
6.7.4 Ground Based Reception and Distribution Losses	195
6.7.5 Effect of Component Failures	196
7. RECOMMENDATIONS	197
7.1 Baseline Design Requirements	197
7.2 Elaboration of Ground Base MPTS Elements	198
7.3 Alternate Design Factors	198

APPENDICES:		Page
A	The Klystron as a Microwave Power Source in the SPS Application	A- 1
A.1	Klystron Failure Modes and Open Construction	A- 2
A.2	Service and Maintenance	A- 7
A.3	Bake-out and Processing	A-12
A.4	Klystron Design for SPS	A-14
A.5	Space Tube Factory and Facility	A-26
A.6	Vari-Krome Metallizing System	A-32
B	Solar Power Satellite Power Control and Distribution Subsystem	B-1
C	Operation of General Electric DC Breaker (Mechanical)	C-1
D	Estimate of RF Field at SPS Array Surface	D-1
E	High Power Capability of Composite Waveguides for SPS	E-1
F	Interaction of Microwaves with the Ionosphere	F-1

LIST OF FIGURES

Figure		Page
2-1	Module Configuration	4
2-2	Waveguide Stick and Slot Array Geometry	6
2-3	Dipole Element Gain vs. Spacing	6
2-4	MPTS Reference Power Taper	8
2-5	MPTS Reference Power Taper Implementation	8
2-6	Comparison of Actual and Quantized 10 dB Gaussian Distribution Functions	9
2-7	Power Density Taper Implementation for 210 KW Klystron Design	9
2-8	Power Density Taper Implementation for 210 KW Klystron Design	10
2-9	Subarray Face Surface Tolerance	12
2-10	Effect of Subarray Tilt	13
2-11	Input Impedance of Standing Wave Stick with 5 Resonant Series Slots	13
2-12	Resonant Slot Conductance vs. Offset	16
2-13	Phase Difference Due to Subarray Offset	22
2-14	Phase Error Due to Subarray Offset	22
2-15	Array Pattern Roll-Off Characteristics	24
2-16	Total Radiation Power vs. Angle	24
2-17	Beam Efficiency	26
2-18	Sidelobe Distributions for Fixed Rectenna Constraints	28
2-19	Spacetenna Size and Power Density	28
2-20	Rectenna Power Density and Rectification Efficiency	30
2-21	Two Beam Bessel Function Synthesis	30
2-22	Pattern Shape vs. Distribution Constant K	31
2-23	Aperture Field Distribution	31
2-24	Spacetenna Pattern	32
2-25	Array Pattern Roll Off Characteristics	34
2-26	Graphical Integration Technique	35
2-27	Total Radiated Power vs. Angle	35
2-28	Beam Efficiency vs. Gap Spacing Between Subarrays	38
2-29	Spacetenna Quarter Section	40
2-30	Effect of DC-DC Converter Failure on Spacetenna Performance	40
2-31	Enhanced Spacetenna	42
2-32	Remote Job Entry Job Processing	42
2-33	Pattern of Rectangular Aperture	45
2-34	Transmitter Phasing Concept	47
2-35	Transmission Line Compensation	51
2-36	Receiver Concept	51
2-37	The Diplexer Problem	52
2-38	Klystron Phase Control Circuit	54

Figure		Page
2-39	Element Orientation	56
2-40	Element Gain	56
2-41	Horizontal Rectenna Configuration	57
2-42	Hogline Rectenna	58
3-1	Unfurlable Gore-Type Parabolic Array	60
3-2	Deployable Parabolic Array	62
3-3	Traveling Wave End Fire Array	64
3-4	End Fire Element Pattern	64
3-5	End Fire Array Pattern for 3λ Spacing	65
3-6	End Fire Element Design Curve	67
3-7	Candidate Lens Subarray	67
3-8	Structural Foam Panel Construction	69
3-9	Lens Configuration	69
3-10	Zoning Alternatives	73
3-11	Enhanced Element Planar Waveguide Array	76
3-12	Slot-Dipole Element	76
3-13	Horn Array	76
3-14	Space Fed Stepped Cylindrical Lens	78
4-1	Reference Klystron Configuration	82
4-2	Estimated Effect of Collector Depression	84
4-3	Klystron Design Parameters	85
4-4	Reference Klystron Depressed Collector Design	85
4-5	Methods of Focusing Klystron Beam	88
4-6	Solenoid Design for High Power Klystron	88
4-7	Microwave Tube Life Trends	94
4-8	Cathode Design Criteria	95
4-9	Klystron Failure Symptom Tree	99
4-10	Possible Failure Mode Distributions	99
4-11	Weight Comparison of HighPower CW Transmitters	101
4-12	Cost Trends in High Power CW Transmitters	103
4-13	Output Gap Geometry	106
4-14	High Power CW Limitations of High Efficiency Klystron	106
4-15	Variation of Klystron Efficiency and Specific Weight with Power Level	108
4-16	RF Transmitter Acquisition Cost for 6 Gigawatt System	110
4-17	Klystron Protective Devices Including Phase Compensation	113
4-18	Klystron Performance When Optimally Matched to Solar Cell Output	113
4-19	X-Ray Radiation Level Assessment	115

Figure		Page
4-20	Geometry for X-Ray Configuration of Klystrons	120
5-1	Effective Temperature of Back of Antenna	122
5-2	MPTS Power Distribution System Block Diagram	125
5-3	DC/DC Converter for Three Segment Depressed Collector Klystron Design MPTS	125
5-4	DC/DC Converter for Five Segment Depressed Collector Designed MPTS	126
5-5	Power Distribution Control Sectors	129
5-6	MPTS Reference Power Conditioning Placement	130
5-7	Distribution Conductors MPTS Antenna (Flat Conductors)	130
5-8	Distribution Conductors MPTS Antenna (Flat Conductors)	131
5-9	Distribution Conductors MPTS Antenna (Flat Conductors)	131
5-10	Distribution Conductors MPTS Antenna (Flat Conductors)	132
5-11	Distribution Conductors MPTS Antenna (Flat Conductors)	132
5-12	Distribution Conductors MPTS Antenna (Flat Conductors)	133
5-13	Circular Downrun Conductors at Radius 140 m MPTS Antenna Structure	136
5-14	Circular Downrun Conductors at Radius 140 m MPTS Antenna Structure	136
5-15	Four Klystron Subarray Conductor Summary	151
5-16	Six and Eight Klystron Subarray Conductor Summary	152
5-17	Nine and Twelve Klystron Subarray Conductor Summary	153
5-18	Sixteen and Twenty Klystron Subarray Conductor Summary	154
5-19	Twenty-four and Thirty Klystron Subarray Conductor Summary	155
5-20	Thirty-six Klystron Subarray Conductor Summary	156
5-21	DC/DC Converter Optimization	156
6-1	Dimensional Tolerances	165
6-2	Klystron Cavity and Solenoid Heat Pipe/Radiator	169
6-3	Klystron Collector Heat Pipe/Radiator	169
6-4	Active Thermal Control for Antenna Systems	170
6-5	Active Thermal Control for DC/DC Converter	170
6-6	70 Kw Klystron	172
6-7	Waveguide Configuration Comparison	175
6-8	Typical Module Thermal Radiator	177
6-9	Integrated Klystron Module	180
6-10	Integrated Subarray	180
6-11	Secondary Truss-Module	181
6-12	Primary Structure	183
6-13	DC-DC Converter Placement Concept	183
6-14	MPTS Alternate Configuration	184
6-15	Power Taper Integration	187

D180-22876-4

Figure		Page
6-16	Antenna Temperature Profile--Sun on Front	188
6-17	Antenna Temperature Profile Sun on Back	188
6-18	Reference Structural Characteristics	189
6-19	Klystron Module LRU	192
7-1	SPS System Integration Flow Chart	200

D180-22876-4

LIST OF TABLES

Table		Page
2-1	SPS Subarray Losses Due to Dimensional Tolerances	20
2-2	Spacetenna Size and Beam Efficiency	36
2-3	Quantized Distribution Modeling	36
3-1	Unfurlable Gore-Type Parabolic Array	60
3-2	Antenna Efficiency Breakdown	60
3-3	Deployable Parabolic Array	61
3-4	Total Efficiency for Parabolic Array	63
3-5	Lens Losses and Efficiencies	71
3-6	Important Lens Tolerances	71
3-7	Configuration Trade Chart	78
4-1	Reference Klystron Design Criteria	80
4-2	Some Features of Amplitron and Klystron Design for SPS	80
4-3	Status of High Efficiency Transistors	82
4-4	Energy Balance in Reference Klystron Design	84
4-5	Features Affecting Transmitter Life	90
4-6	Potential Space Contaminants	92
4-7	Life Data on Current Ground Based Radar Transmitters	94
4-8	Cathode Life Test Data (1977)	96
4-9	Transmitter Weight Trade Study Results	100
4-10	Parametric Energy Distribution in High Efficiency Klystron	104
4-11	Alternate High Power Klystron Designs	108
4-12	50 KW Permanent Magnet Klystron Design	109
4-13	RF Transmitter Acquisition & 10 Year Replacement Cost	109
4-14	X-Ray Scaling Relations	117
4	Minimum Approachable Distance for X-Rays	120
5-1	High Power Klystron Depressed Collector Designs	123
5-2	Klystron Power Regulation Requirements	123
5-3	Five-Segment Depressed Collector Klystron is More Efficient	126
5-4	MPTS Conductors Power Sector Control to Subarrays Circular Conductors 140 Meter Length	137
5-5	Power Sector Control Substation to Antenna Power Sector Conductor Summary	138
5-6	Antenna Power Sector Summary	141
5-7	Antenna Power Distribution Fault Protection	157
5-8	Antenna Power Distribution System	160

D180-22876-4

Table		Page
6-1	Structural Design Factors	165
6-2	Thermal Limitation Assumptions	168
6-3	Waste Heat Sources	168
6-4	Klystron Mass Estimate	172
6-5	Klystron Module Interfaces	173
6-6	Waveguide Conductive Coating Comparison	177
6-7	Klystron Thermal Control	178
6-8	Thermal Insulation	178
6-9	Reference Antenna Mass Estimate	189
6-10	MPTS Mass Comparison	190
6-11	MPTS Mass and Cost Estimate	190
6-12	MPTS Efficiency Chain	194
6-13	Spacetenna Power Distribution and Processing Loss	194

D180-22876-4

REFERENCES

- 1.1 Discussions with Louis Leopold and associates at NASA Johnson Space Center, Houston, Texas.
- 1.2 Technical interchange with R. M. Dickinson, JPL; discussions with S. Fondycc and S. V. Manson and D. Calahan at NASA Headquarters.
- 2.1 Reception Conversion Subsystem (RXCV), For Microwave Power Transmission System, Final Report for JPL Contract No. 95-3968 by Raytheon Co.
- 2.2 Diamond, B. L. (1965a) Phased Array Radar Studies, 1 Jan 63 to 1 Jul 64, MIT Lincoln Labs, Tech. Report TR-381 by Group 44
- 2.3 Hansen, R. C., Microwave Scanning Antennas, Vol. II, Array Theory and Practice, Academic Press, 1966, p. 303.
- 2.4 Ruze, John, Antenna Tolerance Theory - A Review, Proceedings of the IRE Vol. 54, No. 4, April 1966
- 2.5 Reference Data for Radio Engineers 4th Edition, International Telephone and Telegraph Corp., New York
- 2.6 Silver, Samuel, Microwave Antenna Theory & Design, MIT Radiation Laboratory Series, Vol. 12, Boston Technical Publishers, 1964, Chapter 9, Section 9-20
- 2.7 Jasik, Henry, Editor-Antenna Engineering Handbook, 1st Edition, McGraw-Hill, New York, 1961, Chapter 9, Section 9-4.
- 2.8 Allen, John L., Array Antennas - New Applications for an Old Technique, IRE Spectrum, November 1964
- 2.9 Circular Aperture Synthesis, John Ruze, IRE Transactions Antennas & Propagation, November 1964
- 2.10 The Effect of DC-DC Converter Failure on Spaceterram Performance, Boeing Internal Memo 2-3641-2MR-035, October 2, 1977.
- 3.1 Antenna Engineering Handbook, Henry Jasik, Editor, McGraw-Hill Book Co., Inc., 1961.

D180-22876-4

- 3.2 **George C. Southworth: "Principles and Applications of Waveguide Transmission;" D. Van Nostrand Co., Inc., 1950.**
- 3.3 **Reception–Conversion Subsystem for Microwave Power Transmission System: Final Report, JPL Contract No. 953968; Raytheon Co.; Waltham, Mass.**
- 3.4 **Microwave Power Transmission System Studies; NASA Lewis Research Center; Contract NAS3-17835; Raytheon Co.; Waltham, Mass.**
- 3.5 **Clavin, Hubner & Kilburg: "An Improved Element for Use in Array Antennas;" IEEF Transactions on Antennas and Propagation; Vol. AP22 No. 4; July 1974.**
- 3.6 **R. C. Hansen: "Microwave Scanning Antennas;" Vol. I, II, and III; Academic Press, 1966.**
- 3.7 **The Microwave Engineer's Handbook and Buyer's Guide; Horizon House Inc.; 1964.**
- 3.8 **Space-Based Solar Power Conversion and Delivery Systems Study Phase Three Study Contract; NASS-31308; December 16, 1976.**
- 3.9 **William F. Crosswell and Melvin C. Gilreath: "Erectable Yagi Disk Antenna for Space-Vehicle Applications;" NAS TN D-1401; Langley Research Center; Langley Station; Hampton, Va.; October 1962.**
- 3.10 **Ehrenspeck, H. W. and Boehler, H., "A Method for Obtaining Maximum Gain from Yagi Antennas;" IRE Trans. on Antennas and Propagation, Vol. AP-7 No. 4; Oct. 1959, PP 379-386.**
- 3.11 **W. B. Koller and R. B. Higgins: "Broadband Disc-on-Rod Antenna Design;" Goodyear Aerospace Corp.; GER-13461; 8 September 1967; Abstract of Seventeenth Annual Symposium, USAF Antenna Research and Development Program.**
- 4.1 **Informal Data from Power Hybrid Corp., Torrance, California.**
- 4.2 **L. Cantafio, et al. "Photovoltaic Gravitationally Stabilized Solid State Satellite Solar Power Station". AIAA Future of Aerospace Power Systems Meeting, St. Louis, March 1977.**
- 4.3 **P. W. Staecher, D. F. Peterson, "A Survey of Solid State Microwave Power Devices," MIT Report ESD-TR-77-84, July 1977.**
- 4.4 **Annual report of Advisory Group on Electron Devices, 1976, Unclassified Portion.**

D180-22876-4

- 4.5 T. G. Mihran, et al, "Design and Demonstration of a Klystron with 62% Efficiency," IEEE Trans. Electron Devices, Vol. ED-18, No. 2, Feb. 1971.
- 4.6 Klystrons for Microwave Power Transmission System, Shared Applications, Inc., Jan., 1975.
- 4.7 High Efficiency Klystron CW Amplifier for Space Applications, Varian Associates Briefing, Feb. 1976, and IEEE Electron Device Conf., Dec. 1976.
- 4.8 Discussions with J. Griffin, Manager, Klystron Design, Second Electric Microwave Tube Operation, Schenectady, N.Y.
- 4.9 Correspondence with P. Guenard, Thomason-GSF, Bousgre, France, May 1977.
- 4.10 Discussions with Dr. H. G. Kosmahl, Head, Power Amplifier Section, NASA Lewis Res. Center, Cleveland, Ohio.
- 4.11
 - a. E. L. Lien, "High Efficiency Klystron Amplifiers," IEEE Conf. on Electron Devices, Oct. 1969.
 - b. A. D. LaRue, "High Efficiency Klystron in Amplifier for Spacepower IEEE Conf. on Electrical Devices, Dec. 1976.
- 4.12
 - a. Neugebauer and Mihran, IEEE Trans. ED-19, Jan. 1972.
 - b. Discussions with A. D. LaRue, (High Power Tubes, X-ray), E. Lien, (Klystron Design).
 - c. Discussions and Correspondence with W. C. Brown, John Skowon, Geo. McMaster, Raytheon (Weyland) and briefings by W. C. Brown to JSC, August 1977.
- 4.13 G. D. Arndt, L. Leopold, "High Power Microwave Transmission from Solar Space Stations," Instrument Society of America Conference, Oct. 1976, Houston, Texas.
- 4.14 DOD/IEEE Power Tube Conference, Monterey, California, April 1977.
- 4.15 E. J. Nalos, "Impedance of Klystron Cavities," IRE Transaction MIT-e No. 5, Oct. 1955.
- 4.16 Varian Associates Report, "The Klystron as a Microwave Power Source in the Solar Power Satellite Application," prepared for The Boeing Company, Nov. 1977.
- 4.17 E. G. Chaffee JRM Vaughan, "Shuttle Sortie Communication Experiment Definition Study," NASA Lewis Res. Cr., Report CR-135058, Nov. 1975.

D180-22876-4

- 4.18 NASA Contract NAS3-20375, in progress.
- 4.19 NASA Contract NAS3-14385 with Watkins Johnson. Palo Alto. "Design Construction and Long Life Endurance Testing of Cathode Assemblies for Use in Microwave High-Power Transmitting Tubes." NASA CR-135043.
- 4.20 R. Zimmer, et al. "High Power Microwave Tube Reliability Study." Georgia Inst. of Technology Report FAA-RD-76-172, August 1976.
- 4.21 Thomson-CSF Bulletin NTH 6073A. "Life and Reliability of Thomson-CSF X-band Satellite Transponder TWT's, July 1976.
- 4.22 R. E. Thomas, "Electron Emitters, State of Art and Future Prospects," NRL Washington, D.C., presented at Microwave Power Tube Conference, Monterey, California, April 28, 1977.
- 4.23 Discussions with Ralph Foreman, NASA Lewis Research Center.
- 4.24 D. W. Maurer, C. M. Pleass, "The CPC. A Medium Current Density, High Reliability Cathode," BSTJ, Dec. 1967.
- 4.25 Luebke & Caryotakis, "Development of One Megawatt CW Klystron." Microwave Journal, August 1966.
- 4.26 Kosmahl and Albers, "Three Dimensional Evaluation of Energy Extraction in Output Cavities of Klystron Amplifiers." IEEE Trans. ED-20, No. 10, October 1973.
- 5.1 Lyndon B. Johnson Space Center, "Initial Technical, Environmental, and Economic Evaluation of Space Solar Power Concept." JSC-11568, Vol. II.
- 5.2 D. G. Fink and J. M. Carroll, "Standard Handbook for Electrical Engineers," New York, McGraw-Hill Book Company, Tenth Edition, 1968.
- 5.3 Raytheon, "Microwave Power Transmission Studies." NASA CR-134886, 1975.
- 5.4 W. O. Eckhardt and G. A. Jofman, "A 10-kA, 30 Kv Liquid-Metal Plasma Valve Switch for Inductive Energy Storage." IEEE Proc. Sixth Symposium on Engineering Problems of Fusion Research, 75 CH 1 097-5NPS.

D180-22876-4

- 5.5 NASA/OAST, "Power Technology," OAST Summer Workshop, NASA TM X-73964, 1975.
- 6.1 W. H. Armstrong, D. E. Skoumal and J. W. Strayer, "Large Space Erectable Structures - Building Block Structures Study," NAS9-14914 (NASA/JSC), Boeing Aerospace Co., April 1977.
- 6.2 E. A. Skrabek, "Heat Pipe Design Handbook--Part I," NAS9-11927 (NASA/JSC), Dynatherm Corp., August 1972.
- 6.3 T. J. Kramer, "Fluid Flow and Convective Heat Transfer in Square Capillary Ducts Subjected to Non-Uniform Heat Flux," ASME Paper No. 76-WA/HT-29, presented at winter annual meeting, New York, December 6, 1976.
- 6.4 Johnson Space Center, "Initial Technical, Environmental, and Economic Evaluation of Space Solar Power Concepts," JSC 11568, August 1976.
- 6.5 J. C. Jones, SPS Antenna concept drawing, NASA, JSC, September 6, 1977.
- 7.1 D. Arndt, L. Leopold, "Microwave System Parameters for a Shuttle-Constructed Test Program," November 17, 1976.

1.0 INTRODUCTION

Building on the concept of pollution free power generation first conceived by P. Glaser in 1968, and experimental work in microwave beaming by the Raytheon Company, NASA has pioneered the evaluation of a feasible cost-effective Solar Power Satellite system. The present NASA/JSC system-oriented study is the first to address the key element, the Microwave Power Transmission System, in sufficient depth to define a baseline system to a level allowing an accurate determination of mass and cost. To assure best utilization of past effort, this study builds on previous in-house and NASA sponsored work such as the NASA Lewis study with the Raytheon Company, (NAS3-17835), NASA/JSC Solar Power Satellite Concept Evaluation (JSC-12973), extensive discussions with the NASA microwave team (Ref. 1-1) and contacts with other related NASA sponsored work such as that at JPL (Ref 1-2). Although this phase of the current effort emphasizes a klystron transmitter, it does not mean to imply that this is the recommended choice. The best transmitter choice will have to await results of developmental tests on other candidates such as the crossed field amplifier, and possibly even advanced solid state amplifiers.

The concept of space to earth microwave power transmission involves a series of energy conversions which must achieve high efficiency to provide minimum system cost. Solar power is converted to DC which in turn is converted to microwave energy, beamed to earth, where it is finally converted to usable power. A transmitting antenna in geosynchronous orbit is used to beam the microwave energy to large rectifying antenna arrays located on earth. As previously implied, efficiency is a prime consideration in any transmission system, and it is evident that individual elements in the efficiency chain must average over 90% if an overall efficiency of 60% is to be achieved. These efficiency considerations dictate that the antennas be extremely large scale, e.g., the transmitting antenna is on the order of 1 Km in diameter and the receiving antenna is on the order of 10 Km because of the long transmission distance of 37,000 Km. This scale implies that large units of power, on the order of 5 GW-10 GW, must be transferred and that the power source in turn must be very large.

This study established a baseline design for the transmit/receive antenna and the microwave tube. It analyzed and optimized key aspects of efficient energy conversion at both ends of the power transfer link. In addition to establishing this baseline, this report includes a discussion of alternate approaches in the areas of antenna and tube design. An integrated design concept was developed which meets design requirements, observes structural and thermal constraints and exhibits good performance. It was developed in adequate depth to permit cost estimating at the subsystem/component level.

The baseline design for the spaceborne transmitter antenna is the slotted waveguide planar array because it has very high efficiency while also serving as an efficient means to distribute the microwave power from converters to the radiating elements. The basic element of the planar slot array is a length of short circuited waveguide loaded by a series of slots cut in the broad wall. The slots are

D180-22876-4

positioned such that they allow radiation of energy introduced into the guide with uniform amplitude along the length of the guide.

These waveguide radiators are grouped to form a module. Each module is fed by a single 70 KW klystron. The modules are grouped forming a subarray which can be mechanically pointed. Approximately 7000 subarrays comprise the complete spaceborne transmitting array. The number of waveguides in a module is varied to provide the overall array with a 10 dB quantized Gaussian amplitude taper. This taper gives the aperture optimum beam efficiency. Waveguide construction from graphite composites is being given first consideration due to their thermal stability.

For structural and thermal reasons the subarrays may be expected to move relative to one another. However, in order to maintain maximum efficiency, the beam from each subarray must be accurately pointed at the receiving site. This calls for a reference beam to be launched from the center of the ground antenna. This beam is sensed at each subarray and at a reference subarray in the antenna center.

The latter transmits a phase reference to the individual subarrays at which point it is compared with the incoming beam. A difference in phase between these signals is interpreted as a displacement of the subarrays from the nominal reference plane, due for example, to thermal distortion of the structure, and a correction is applied to the phase of the transmitted beam at the subarray so that the required beam front is launched toward the ground antenna.

This effort examined two generic types of devices for converting DC power to r.f. power at microwave frequencies, the amplitron or cross field amplifier (CFA), and the klystron or linear beam is known for moderately high efficiency, high gain and low noise. With the standing wave array concept chosen as a baseline, the klystron has been selected as the initial candidate for evaluation.

The collector or rectifying antenna (rectenna) located on the earth is an array of dipoles each of which is terminated by a filter and diode rectifier. The diodes produce a half wave rectified dc current from the incident microwave ac field. The diodes are grouped in parallel and the groups are serviced to provide the desired voltage for the 5 GW power output of the rectenna. This integrated reception-collection-rectification antenna concept and its technology has resulted in the achievement of an 82% efficiency at an output power level of 32 Kw in a demonstration at the Goldstone, California facility of the Jet Propulsion Laboratory (Raytheon Company 1975).

The overall rectenna covers an area of approximately 100 Km². The collectors are mounted on panels. The panels are tilted to normality with the incoming phase front, but the accuracy need not be great since the individual antenna elements have broad dipole gain patterns, and for the same reason the phase front can be distorted by the atmosphere or ionosphere without appreciably affecting efficiency.

2.0 ANTENNA ARRAY ANALYSIS

In this section the baseline spaceborne reference array is described in detail. The description includes a discussion of slot spacing, stick (radiating waveguide) layout and power density taper quantization. Section 2.2 is an intra-array dimensional analysis. It converts projected dimensional changes in waveguide size, slot size and position into a power loss summary. The spacenna radiation patterns are examined as a function of the power density taper across the array aperture. This power taper is optimized for the best trade between beam efficiency and side lobe level. Overall system efficiency which includes the link between the spaceborne transmitter and the earth-based rectenna was calculated using the NASA-JSC antenna pattern analysis computer program. These calculations were made for varying spacenna size and power taper with a constant diameter rectenna. An initial concept for klystron phase control is described, done in part by the General Electric Company for The Boeing Company. It proposes solutions for problems encountered in the design of such a subsystem. Finally Section 2.0 addresses some aspects of the rectenna design.

The baseline rectenna is an array of dipole antennas. Section 2.6 proposes optimum dipole spacing to minimize the number of elements required. It treats the concept of a flat ground plane array and introduces an alternate approach in the form of the so-called "Hogline" radiator.

2.1 BASELINE ANTENNA ARRAY DESIGN

The baseline klystron module (Fig. 2-1) consists of a single high power klystron with dual outputs feeding a standing wave configuration of the waveguide slot array. The slot array is composed of an even number of waveguide (stick) radiators. The exact number of sticks in a given module and their length is varied across the face of the array to produce an optimum aperture power distribution. This taper is chosen to optimize antenna beam efficiency, as discussed in Section 2.3.1 and is a function of gain and spatial efficiency. Because of the nature of the standing wave design, the stick length has to be an integral number of guide wavelengths, (λ_g). For the dominant mode, at a fixed frequency, this is a function of the waveguide width only.

The klystron modules are grouped to form subarrays, each containing an integer number of modules. To obtain the desired power aperture taper the number of modules (elements) in each subarray will vary. For structural reasons, each subarray will have the same face dimension. The support structure for the waveguide is periodic in nature and is composed of members joined in trihedral lattice. The supporting members consist of a primary and secondary structure; the primary structure must provide three support points for the secondary module and the secondary structure must provide three support points for each subarray. In order to conform to this backing or support structure, the length-to-width ratio of the subarray must be a function of the cosine of the enclosed angle. The implementation of this design is discussed further in Section 6.3.

D180-22876-4

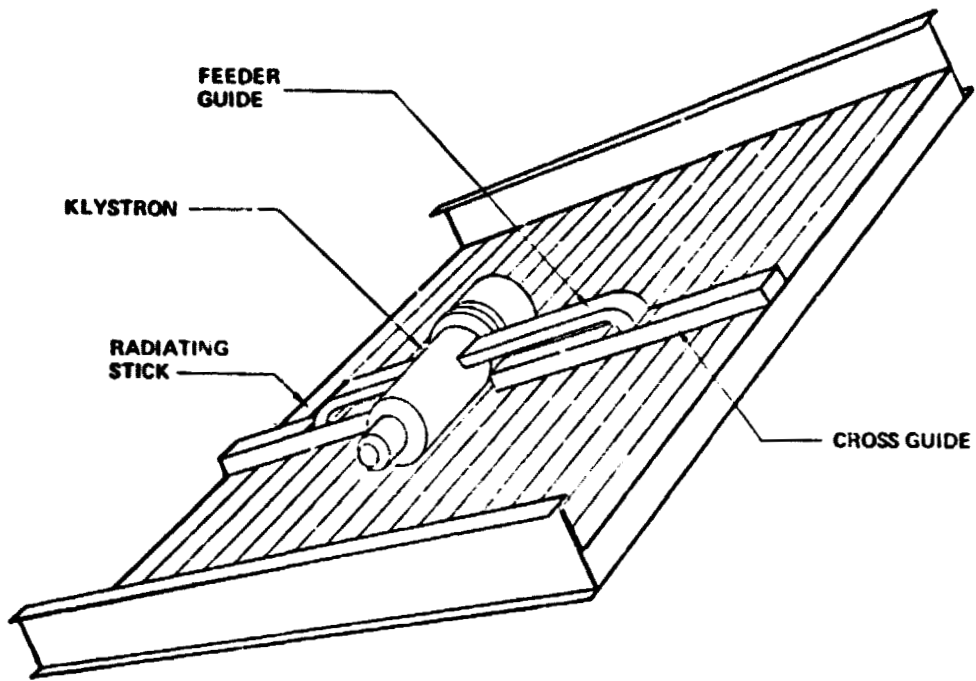


Figure 2-1 Module Configuration

2.1.1 Waveguide Radiating Stick Layout

An element is defined as that portion of the subarray which is fed from a single klystron. The number of elements per subarray is varied to conform with the desired power density across the entire array. In determining the waveguide layouts of the elements it is necessary to consider the interaction between guide wavelength (λ_g) and guide width (W_g), as well as the fact that the stick length is constrained to be a multiple of guide wavelength. Multiples of a half guide wavelength were considered but discarded since the odd multiples would result in an altered mutual coupling environment at the joint of two adjacent sticks. This results in relatively long sticks and a requirement that each stick length have a different slot conductance for proper matching, i.e., each stick length group have a different offset of the slots from the centerline. The longer sticks thus require smaller slot offsets. The layout of the slot geometry for a $1/2$ wavelength stick is shown in Figure 2-2. The trapezoidal cross section of the waveguide has been selected to permit nesting and consequent volume efficiency in transport to orbit.

Wall thickness derives from structural considerations. The height of the waveguide is independent of all the foregoing constraints and is selected to minimize I^2R losses. Using standard waveguide ratios of height equal to one half width, losses are estimated to be .012 dB/meter for copper. These could be cut in half by the use of a square waveguide. The larger guide will not support higher order modes but it can support a cross polarized mode. Methods would have to be devised to suppress such a mode.

2.1.2 Radiating Slot Spacing Considerations

For the SPS design, only on-axis gain is of interest, since in terms of the slot patterns there is for all practical purposes no scanning. To determine whether mutual coupling effects, dependent on slot spacing, will affect on axis gain, the work of Diamond (Ref. 2.2) as reported in Hansen, (Ref. 2.3) was reviewed. In this work, a 7×9 dipole element array was rigorously evaluated and patterns generated for various dipole spacings. In Figure 2-3 the on axis gain values have been plotted from the patterns in Hansen. The underlying solid curve was the computed gain of the area associated with any inter-element spacing. The rigorously calculated points fall about the area gain curve. The pattern ripples are attributed by Hansen to the edge effect in this very small array. An attempt was made to take out this edge effect by averaging the ripples graphically. The smoothed data points (triangular) followed the theoretical area gain curve more closely. It is concluded that for the range of spacings ($.5\lambda$ to $.8\lambda$) considered, the on-axis gain of an array element will automatically adjust itself to the value associated with the area it occupies ($G = 4\pi D_x D_y / \lambda^2$). Within this range, spacing is selected for best impedance matching or other considerations such as fitting the sticks into the various subarray designs as discussed in Section 6.5.

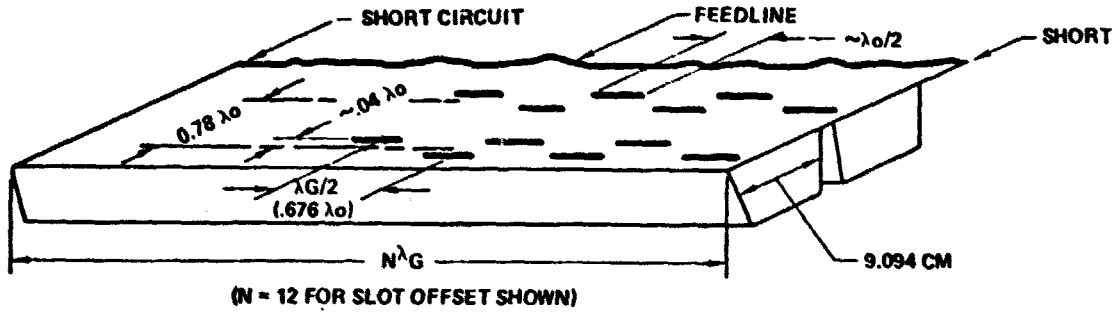


Figure 2-2 Typical Waveguide Stick and Slot Array Geometry

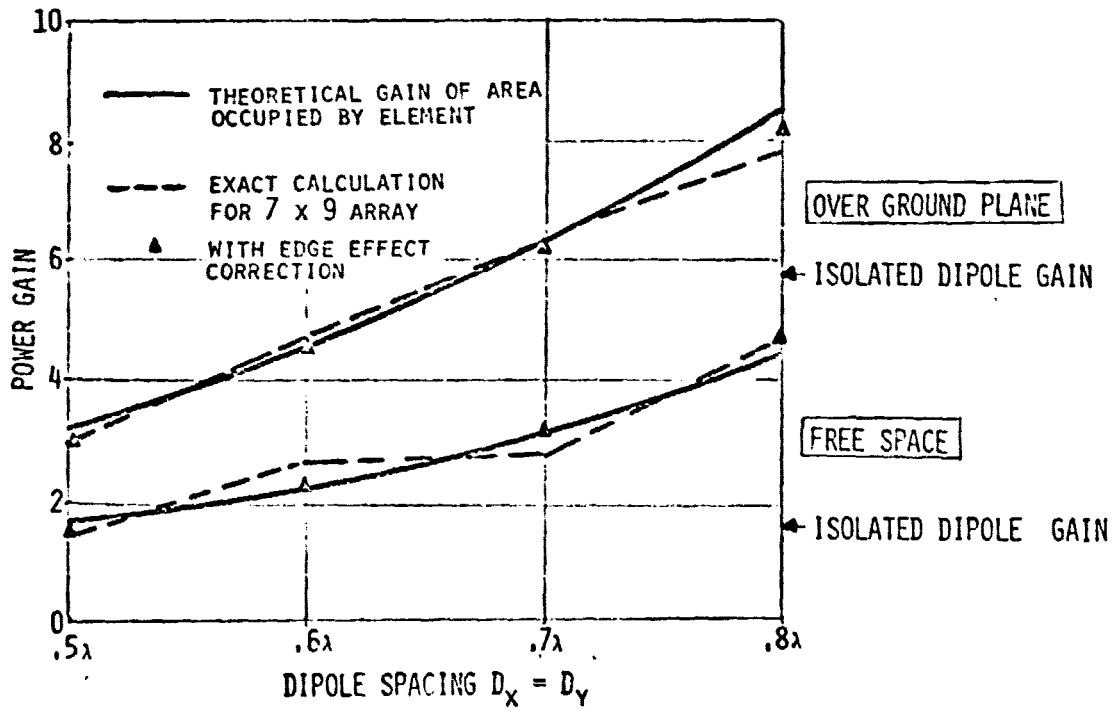


Figure 2-3 Dipole Element Gain vs. Spacing

2.1.3 Power Density Taper Quantization Studies

As previously discussed, in order to obtain maximum beam efficiency the space antenna power aperture distribution must be tapered. In addition to efficiency, all the constraints described in Section 2.1.1 must be satisfied. To meet these requirements, the MPTS reference power taper selected is a ten quantized step approximation of a 10 dB Gaussian taper that will provide a ground output of 5.0 GW for a 1.0 kilometer diameter spaceteenna. This approximation consists of a 9.5 dB taper from the center to the edge element. Figure 2-4 shows both distributions, listing the permissible number of modules per subarray and the power density associated with each. The methods of implementing the subarray quantization are discussed in Section 6.5.1.

To evaluate the effect of stepping the Gaussian spaceteenna distribution, a Fortran program was written using circular symmetry. The steps of quantized distribution #1 shown in Figure 2-5 were obtained as a result of the array design discussed in Section 2.1. Differences between this stepped and the continuous distribution on the close-in sidelobes are shown. A second quantized distribution (#2) was arbitrarily generated to test the sensitivity to step variations. The fourth sidelobe was reduced significantly by this later distribution. The baseline distribution (#1) was also compared to the continuous distribution at larger angles as shown in Figure 2-6. It is noted that the two distributions alternate in producing the higher sidelobes, implying only small differences in efficiency.

2.1.4 Alternate Taper Designs

An optional design employing 210 kw klystrons was also investigated, should such a design be considered at a later time. Power taper data are shown in Figure 2-7 providing a performance essentially equal to the reference design with 1/3 as many tubes.

A sidelobe suppression design was also investigated, using a 14-step 17-dB taper. The sidelobe levels are approximately at 10 microwatts/cm², corresponding to the Soviet public exposure guidelines for microwaves. The taper pattern is shown in Figure 2-8 and corresponds to an antenna 1.2 km in diameter. If 10-kw klystrons were selected, the outer 2 rings of this taper pattern would require a lower power tube, as the power density for these rings is less than one 210-kw tube per subarray.

2.2 SPACETENNA DIMENSIONAL ERROR ANALYSIS

2.2.1 Introduction

This error analysis was undertaken to determine the critical requirements for mechanical control of the space antenna subarrays and to identify all possible sources of efficiency reduction for an accurate assessment of overall microwave power transmission in the Solar Power Satellite System. The errors are grouped in the following categories: subarray tolerances (Section 2.2.3); radiative stick tolerances (Sec. 2.2.4) and minor loss sources (Section 2.2.5).

SPS-1172

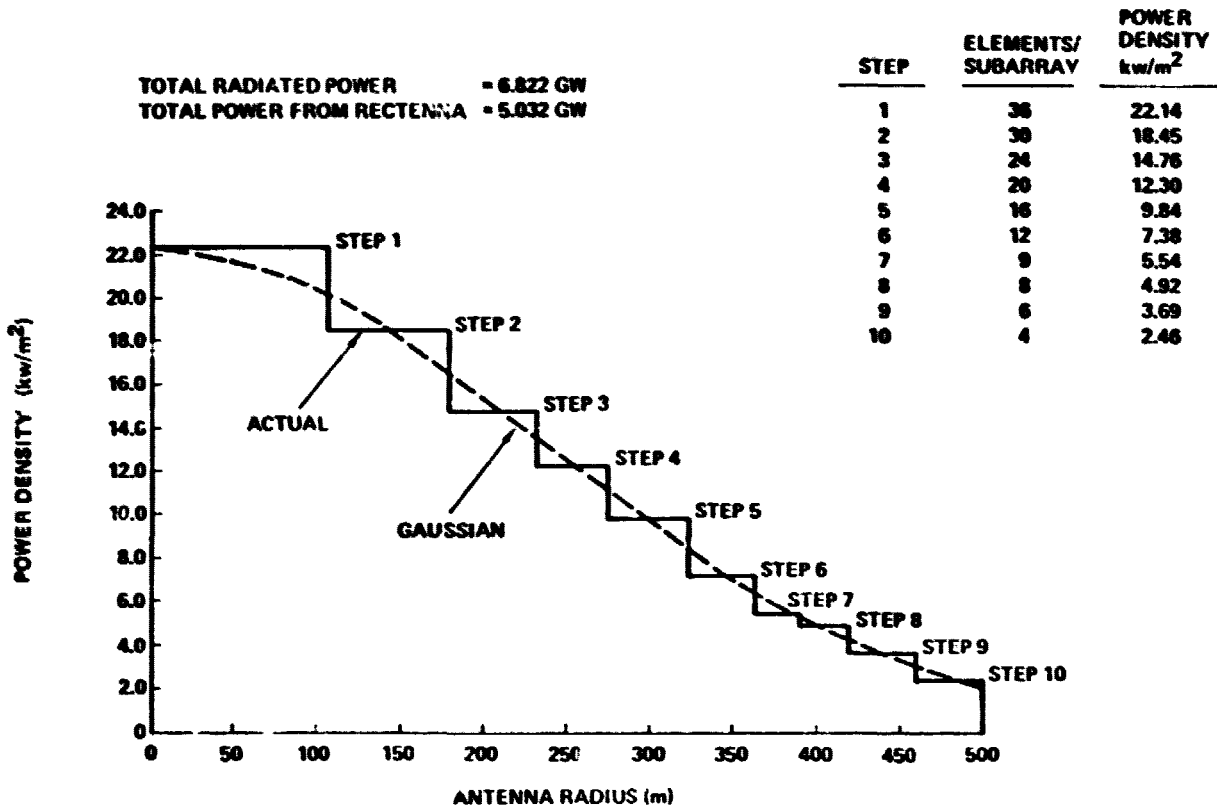


Figure 2-4 MPTS Reference Power Taper

SPS-1188

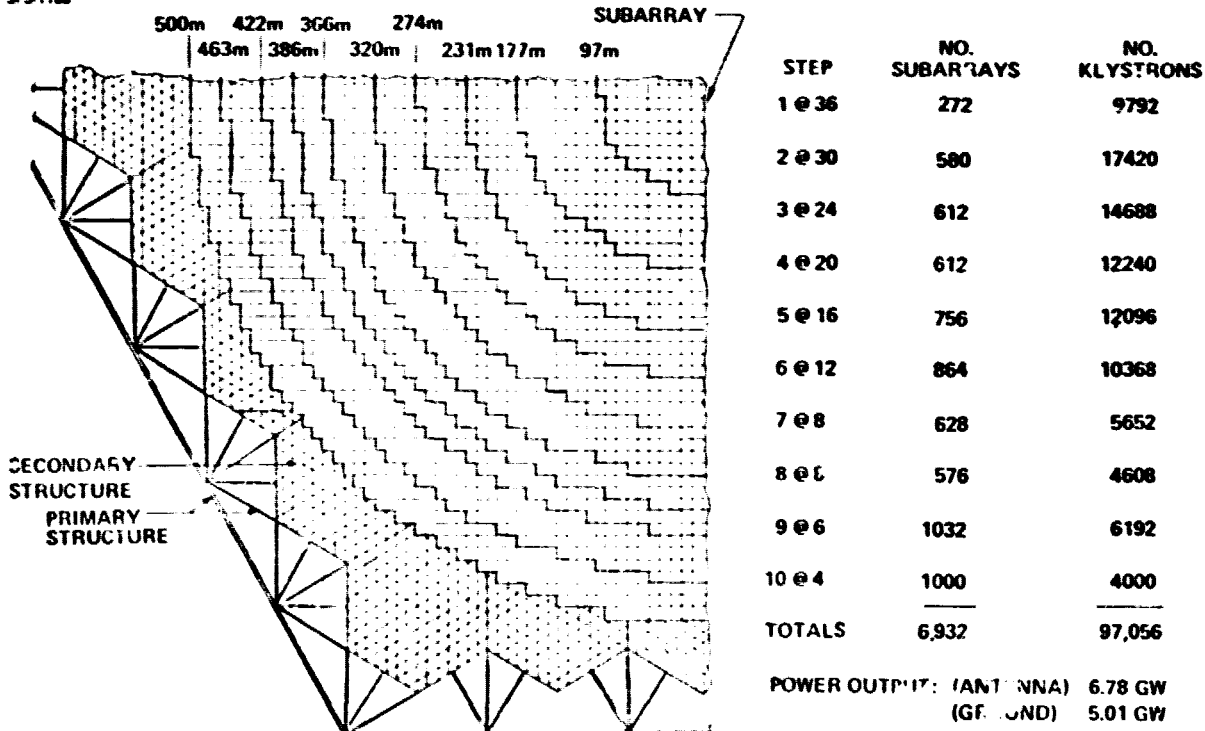
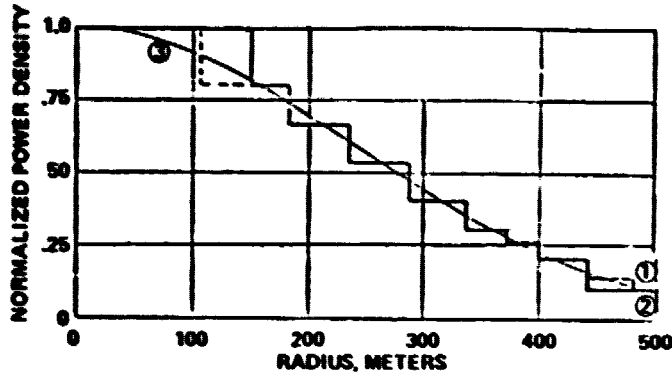
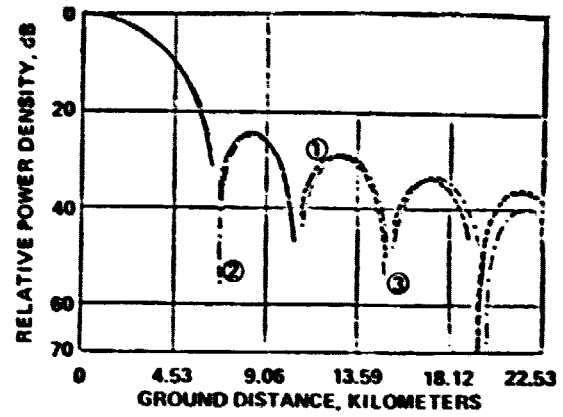


Figure 2-5 MPTS Reference Power Taper Implementation

SP-4311



(A) TRANSMITTER DISTRIBUTION FUNCTIONS



(B) FAR FIELD GROUND DISTRIBUTION

Figure 2-6 Comparison of Actual and Quantized 10 dB Gaussian Distribution Functions

SP-1188

1.0 km ARRAY DIAMETER

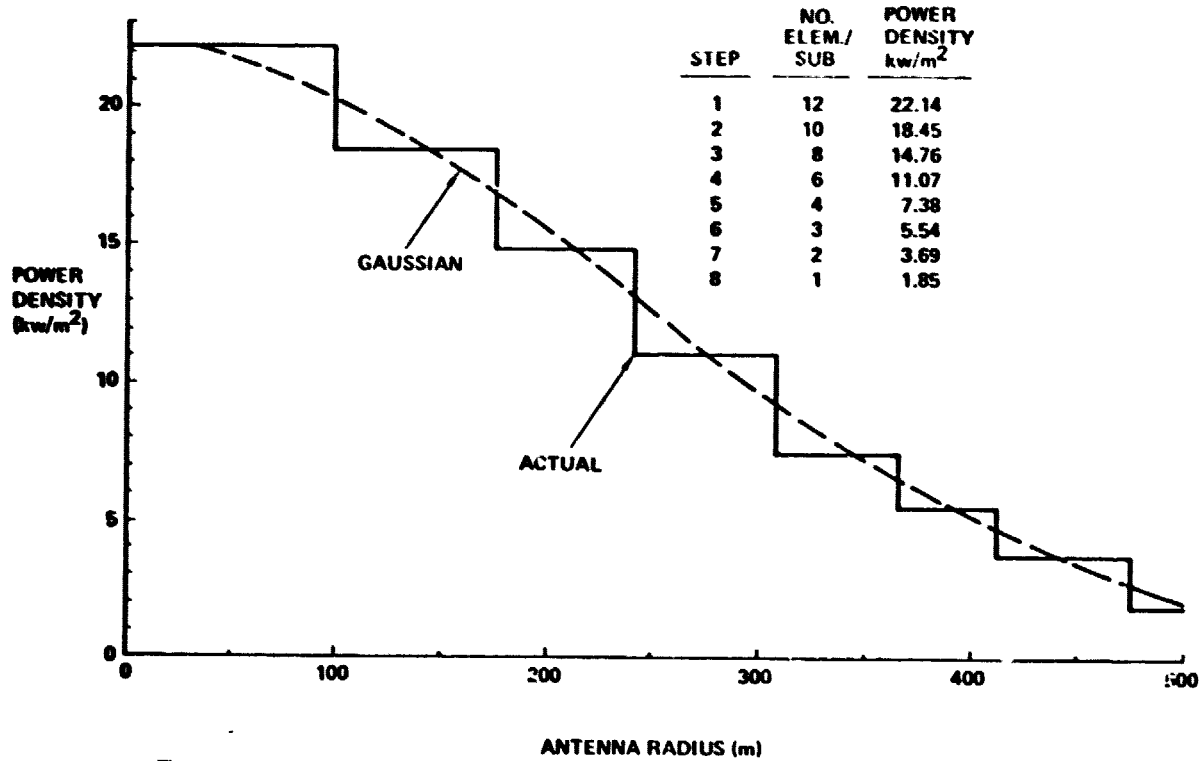
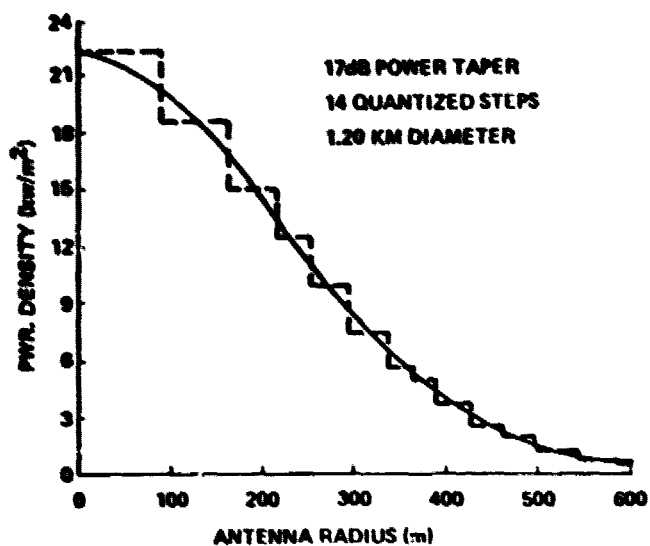
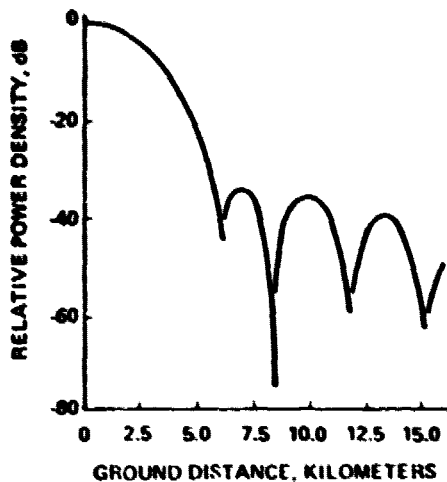


Figure 2-7 Power Density Taper Implementation for 210 kW Klystron Design

SP-1280



(A) ANTENNA POWER TAPER



(B) FAR FIELD GROUND DISTRIBUTION

Figure 2-8 Power Density Taper Implementation for 210 KW Klystron Design

2.2.2 Analysis Model

Each subarray is comprised of a number of modules defined as that portion of the subarray driven by one high power rf generator. The general module configuration is shown in Figure 2-1. Each module is fed in two sections or groups of sticks, each with its own center-fed cross-guide. The selected design calls for a standing wave configuration in both the sticks and the cross guide. Due to the illumination function selected, sticks in the various parts of the spacetenna do not radiate equal power densities, and vary in length from 1.65 meters (10 guide wavelengths) to 4.96 meters (30 guide wavelengths) throughout the array.

For purposes of the error analysis, an average stick length of 2.76 meters (16.7 λ_g) was selected by a weighted average over the array of the number of sticks of different lengths.

2.2.3 Subarray Tolerances

2.2.3.1 Subarray Surface

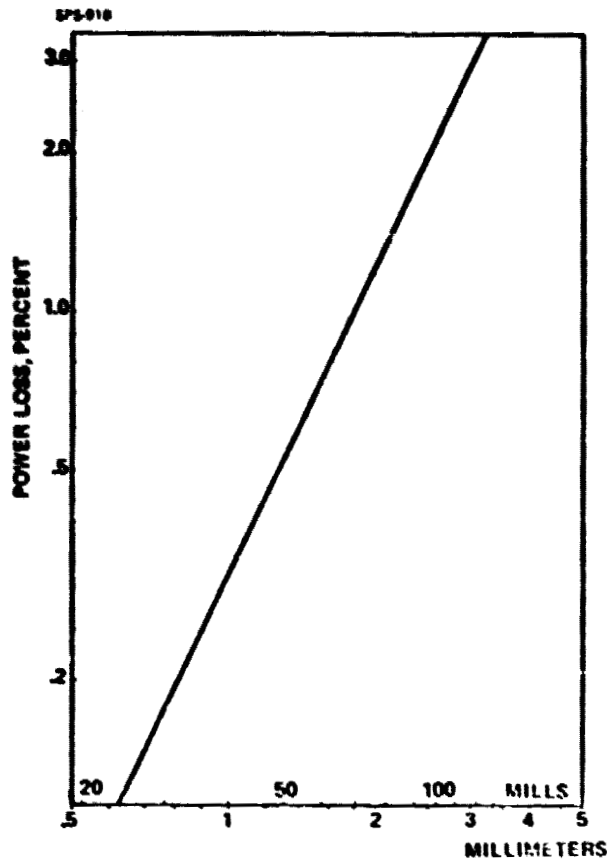
Ruze has investigated the effect of large antenna surface errors. His results are valid for independent random errors where the correlation interval is small with respect to the antenna diameter. In general, these types of errors will reduce main beam gain and create wide angle error sidelobes. From Figure 2-9 it may be seen that a ± 0.5 RMS surface error will produce less than a 1.2% power loss. This value has been selected as a tentative requirement.

2.2.3.2 Tilt of Subarray

The required pointing accuracy for the subarray was arrived at by allowing a 1.2% power loss and solving for the angle on the subarray pattern which gave this loss. This requirement translates to an edge offset of approximately 0.1", independent of subarray size, as indicated in Figure 2-10.

2.2.3.3 Gap Between Subarrays

The requirement on allowable gaps between subarrays was arrived at by computing the reduction in main beam size associated with the increase in the overall array dimension due to subarray gaps. The assumption is that peak power density remains constant as the array opens up but the beam, and the power contained therein shrinks as the inverse square of the array diameter. A 1" gap was found to give a 1.2% power loss for a 10 meter subarray size ($0.11(10g/D)^2 \approx 1.2g$, $g = 2.5$ cm for $2g/D = 0.050$). With the specified subarray gap tolerance of 0.25", this error distribution is 0.13%. See Figure 2-28.



REF. RUZE-PROCEED. IEEE
APR. '68

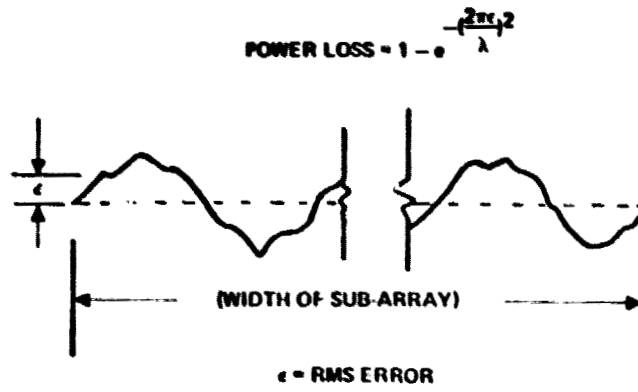
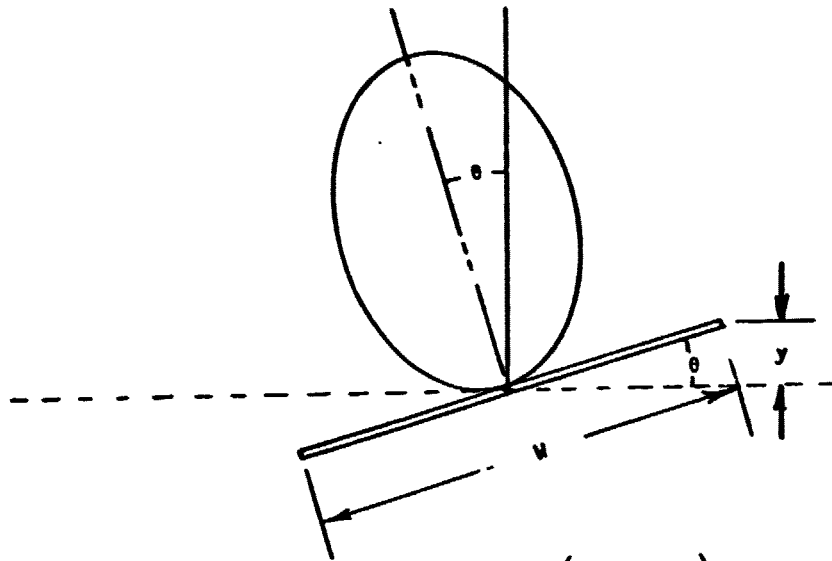


Figure 2-9 Subarray Face Surface Tolerance



Pattern of a uniform rectangular aperture = $\frac{\lambda}{\pi} \frac{\sin(\frac{\pi w}{\lambda} \sin\theta)}{\sin\theta}$

For $\sin\theta = 2y/w$ this reduces to $(\frac{\lambda w}{2\pi y}) \sin(\frac{2\pi y}{\lambda})$

i.e. pattern roll-off is independent of w and depends on y only.

Figure 2-10 Effect of Subarray Tilt

SPS-1600

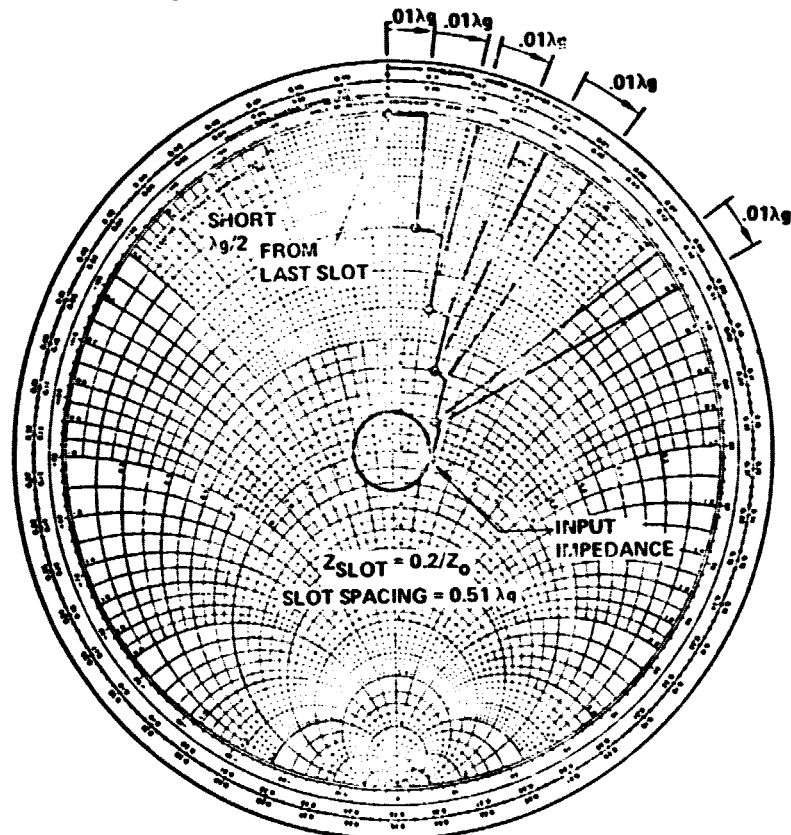


Figure 2-11 Input Impedance of Standing Wave Stick with 5 Resonant Series Slots

2.2.4 Radiating Stick Tolerances

The parameters found to be significant in the resonant stick design are discussed in this section.

2.2.4.1 Stick Length and Slot Spacing

The effect of stick length variation was approached from the standpoint of mismatch as discussed in Silver^{2,6} for the broadside resonant array. It is stated (pg 323) that slot spacing is predominantly an impedance effect; indicating that effects associated with lengthening of the entire stick or change of guide wavelength are primarily to build up the VSWR at the feed or midpoint of the stick. This is illustrated in Figure 2-11 for a string of 5 series slots each deviating by $0.01 \lambda_g$ from the resonant spacing of $\lambda_g/2$. From the Smith chart, it can be seen directly that this deviation is equivalent to the introduction of a normalized susceptance of $b' = .06$. Specifically (at 2.45 GHz, with a $\lambda_g = 6.515$ inches, this translates to $b' = 9.1 \times 10^{-4} \Delta L$ in mils at each slot so that at the center of the stick (i.e., the feed point); these would add up to $N b'$ where N is number of slots per average stick and ΔL is the average deviation of each slot position from $\lambda_g/2$, i.e., 30 mils/33. Thus

$$B' = Nb' = 33(9.1 \times 10^{-4}) \frac{30}{33} = 0.0276$$

The ratio of power delivered to that with the load matched can be written (see Section 2.2.8) as mismatch loss L_M

$$L_M = 1/4(B')^2 = 0.02\%$$

2.2.4.2 Stick Width

The guide wavelength (λ_g) and guide width (a) are related by the equation

$$\lambda_g = \frac{\lambda}{\sqrt{1 - (\lambda/2a)^2}} \quad 2.1$$

To obtain the system sensitivity to width errors we differentiate with respect to a

$$\frac{d \lambda_g}{da} = - \frac{\lambda^3}{4 a^3 [1 - (\lambda/2a)^2]^{3/2}} \quad 2.2$$

Substituting $a = 9.094$ cm gives

$$\Delta \lambda_g = - 1.51 \Delta a \quad 2.3$$

D180-22876-4

Since a change in λ_g is equivalent to a change in slot spacing, $\frac{\Delta \lambda_g}{2}$ may be substituted for Δl in the equation from Section 2.2.4.1

$$\begin{aligned} b' &= 9.2 \cdot 10^{-4} \Delta l \text{mils} \\ &= 9.2 \cdot 10^{-4} \frac{\Delta \lambda_g}{2} = 4.6 \cdot 10^{-4} \Delta \lambda_g \\ B' &= N b' = 4.6 \cdot 10^{-4} N \Delta \lambda_g \end{aligned}$$

which when combined with 2.3 yields

$$B' \cong 0.00069 N \Delta a \quad 2.4$$

For the stated tolerance of $\Delta a = 3$ mils and an $N = 33$ associated with the average stick length, one obtains $B' \cong 0.068$ yielding a mismatch loss of

$$L_M = \frac{1}{4} (B')^2 = 0.12\% \quad 2.5$$

2.2.4.3 Cross Guide Length

For completeness, the cross-guide, which also incorporates a standing wave design, is included, assuming the same composite structure as in the waveguide sticks. If the design turns out to be similar, the losses for the same tolerance of ± 30 mils would be 0.02%.

2.2.4.4 Cross Guide Width

It is expected that on the average, the cross guide length will be approximately equal to one half the stick length. For the same waveguide design, this would produce losses equal to one quarter those due to stick width, i.e., a loss of 0.03%.

2.2.4.5 Slot Offset

A curve of resonant slot normalized conductance (g') vs offset (Figure 2-12) was plotted using scaled data of Jasik Ref. 2.7, Pg. 9-7 for an average stick length of 33 slots. The slope of the curve at this point is

$$\frac{\Delta g'}{\Delta x_{\text{inch}}} \cong \frac{1}{3}, \text{ which for } \Delta x = .002'' \text{ tolerance gives}$$

$$\Delta g \cong 6.6 \times 10^{-4}$$

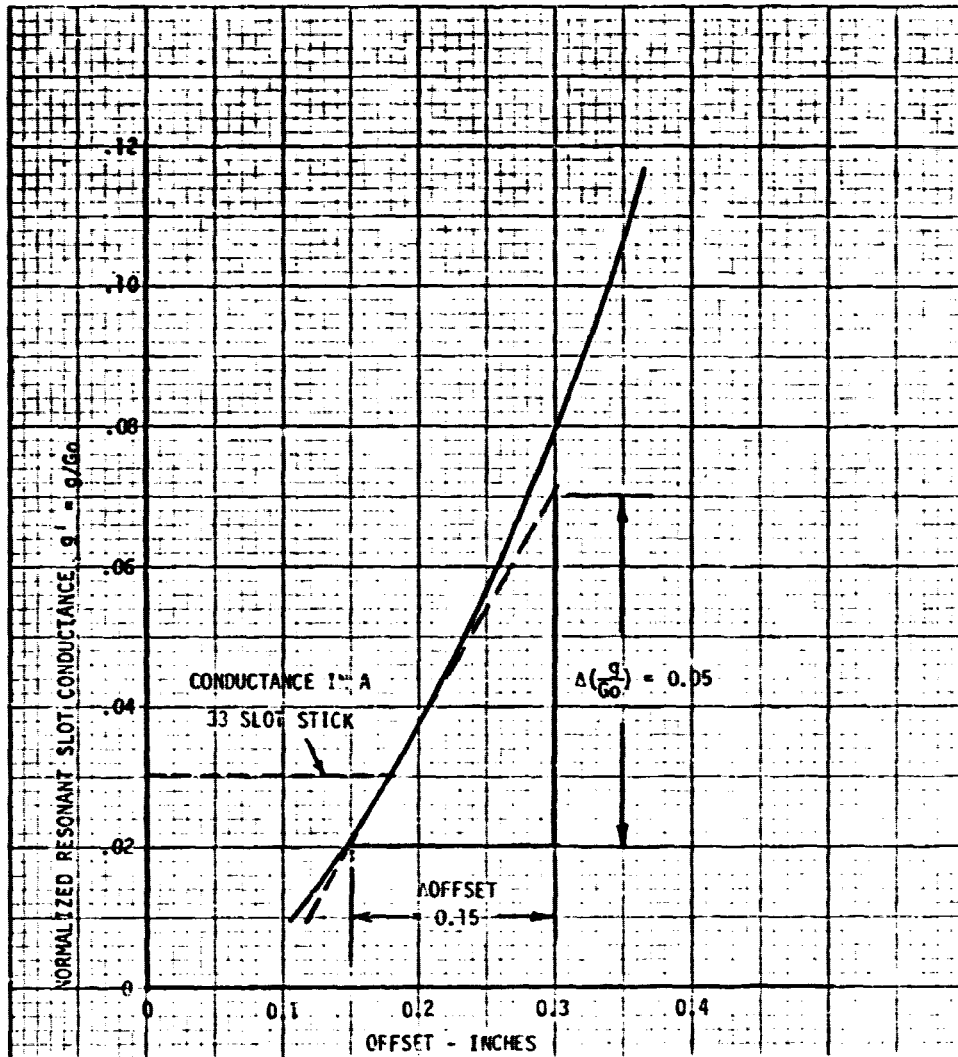


Figure 2-12 Resonant Slot Conductance vs. Offset

D180-22876-4

For a systematic displacement of slots in one direction,

$$G = N\Delta g = 33 \cdot 6.6 \cdot 10^{-4} = .0218$$

and the associated mismatch loss L_M

$$L_M = \frac{1}{4} (.0218)^2 = 0.01\% \quad 2.6$$

The scattering loss produced assuming random slot offset errors may be obtained by relating the conductance error directly to a slot excitation error. As previously calculated, the normalized incremental slot conductance $\Delta g' \cong 6.6 \times 10^{-4}$ for an rms slot tolerance of 2 mils.

In this case, however, since the variation in slot spacing is random, a scattering loss will result.

To obtain the error in an individual slot conductance (Δg) relative to the conductance of the individual slot (g) we note that

$$\begin{aligned} \Delta g' &= \Delta g / G_0 \\ \therefore \frac{\Delta g}{g} &= \frac{\Delta g' \cdot G_0}{g} \end{aligned}$$

but

$$\begin{aligned} \frac{G_0}{g} &= N \\ \therefore \frac{\Delta g}{g} &= \Delta g' \cdot N \end{aligned}$$

Since the power radiated by a lightly coupled shunt slot is proportional to g we may relate the above equation to the effective scattering of power (due to amplitude errors) to the far out side-lobes in an array of radiators as described by Allen (Ref. 2.8, page 125).

$$\begin{aligned} \frac{\text{power scattered}}{\text{power radiated}} &= c^2 = \sigma_A^2 = \frac{\Delta g}{g} = \Delta g' \cdot N \\ &= (6.6 \cdot 10^{-4})(33) = 2.18\% \end{aligned} \quad 2.7$$

In this case there will be no mismatch loss since the average conductance per slot remains constant.

This loss is considered to be intolerably large and the offset tolerance has been tightened to 1/2 mil reducing the above loss in direct proportion to 0.55%.

2.5 Minor Loss Sources

The following effects were studied and found to produce negligible losses (less than 0.01%).

2.5.1 Feeder Guide

The waveguide runs between the klystron and the cross guides are of the traveling wave type, attached to the cross guides directly at the frequency of operation. The potential beam steering associated with the phase errors between the two halves of the array module powered by one klystron was found to be negligible.

2.5.2 Stick Taper & Beam Squint

According to Silver^{2.6} (pg. 323), both amplitude taper and beam squint could result from stick length and width variations; the losses associated with these are stated to be insignificant compared to losses due to impedance mismatch previously calculated.

2.5.3 Slot Longitudinal Spacing

A similar analysis to that in Section 2.2.4.1 may be used to determine the effect of a random longitudinal error in slot spacing. In this case X' , the normalized reactance at each slot would be expected to add not in proportion to N as before, but statistically, as the \sqrt{N} . Thus the expected value of the total reactance is

$$E\{X'\} = \sqrt{N} \quad X' = .674\sqrt{N} \quad (9.2 \cdot 10^{-4}) \Delta l \text{ mils} \quad 2.8$$

where Δl represents the 1 σ value of the position error.

2.5.4 Slot Length

The effect of slot length was evaluated by obtaining the susceptance variation with length from Figure 9-5 of Jasik^{2.7}. From the slope of this curve it was established that

$$B' = \frac{\Delta B}{G_0} = 0.00003 \Delta l \text{ mils}$$

where Δl is the slot length tolerance. This leads to an insignificant power loss (less than 0.01%) using a 2 mil tolerance and the procedures of Section 2.2.4.

2.2.5.5 Thermal Effects

The thermal integrity of the primary and secondary portions of entire array dictates the use of low CTE composite material. The natural choice for the waveguide stick material is also a graphite type composite material. (Typical CTE = 0.54×10^{-6} in/in/°k) Thus, from the microwave point of view, the dimensional changes associated with a selected temperature change (ΔT 55°k) are negligible.

The expansion of an average stick over this ΔT amounts to 3.2 mils which is 9.4 times smaller than the manufacturing tolerance. Since X' is proportional to Δl and mismatch loss $\approx (X')^2$, the loss in this case is

$$0.03\% \div (9.4)^2 \cong 0.0003\%, \text{ i.e., negligible}$$

For a ΔT of 517°K; and $\Delta l = 30$ mils, the loss would be .03% as in Section 2.2.4.1.

2.2.6 Results and Discussions

The significant nondissipative power losses in the delivered main beam on the ground were developed for given subarray dimensional tolerances. The results are summarized in Table 2-1. Since the loss component is considered to be independent, the losses are directly additive. As anticipated, the dominant loss is due to slot offset.

For a given power density, the power radiated by each slot must be constant. Thus, for shorter stick length with less power in the stick, the slots must be coupled more heavily, i.e., further away from the centerline, resulting in a smaller percentage error for a fixed tolerance. With long sticks, the desired offset goes to very small dimensions and a given tolerance results in a relatively large percentage amplitude error. Improvement may come, therefore, from either tighter tolerances or from shorter stick designs. For example, using data in Figure 2-12, with an average stick length of 6.3λ reduces the offset error losses to 1.24% with a 2 mil tolerance or 0.31% with a $\frac{1}{2}$ mil tolerance.

Nondissipative power losses total 1.87% resulting in an effective antenna efficiency of 98.1%. To this value must be added the waveguide I²R losses and the scattering losses associated with the inter-subarray (or intermodule as the case may be) amplitude and phase control errors.

2.2.7 Subarray Offset Effects

The problem addressed is that of the effect of offset of the subarrays from the ideal plane perpendicular to the line of sight. These offsets are along the line of sight and are due to random or systematic variations in the supporting structure or subarray pointing system. It is the purpose of the phase control system to correct the effect of these offsets and produce a properly phased array in

D180-22876-4

Table 2-1 SPS Subarray Losses Due to Dimensional Tolerances

SPS 1043

<u>DIMENSION</u>	<u>TOLERANCE</u>	<u>EFFECT</u>	<u>MAIN BEAM POWER DEGRADATION</u>
SUBARRAY SURFACE	±50 MILS RMS	SCATTERING FROM PHASE VARIANCE	0.50% (1)
TILT OF SUBARRAY	0.1" AVERAGE	SUBARRAY PATTERN GAIN REDUCTION	0.50% (1)
GAP BETWEEN SUBARRAYS	± 0.25" AVERAGE	ARRAY FILLING LOSS (~ AREA LOSS)	0.13%
STICK LENGTH	±30 MILS	MISMATCH LOSS	0.02% (2)
WIDTH	±3 MILS	MISMATCH LOSS	0.12
CROSS GUIDE LENGTH	±30 MILS	MISMATCH LOSS	0.02% (2)
WIDTH	±3 MILS	MISMATCH LOSS	0.03%
SLOT OFFSET	±0.5 MILS	SCATTERING FROM AMPLITUDE VARIANCE	0.55% (4)
TOTAL			1.87%

LEGEND: ALL LOSSES ARE ADDITIVE.
 (1) INDEPENDENT OF SUBARRAY SIZE.
 (2) INDEPENDENT OF STICK LENGTH.
 (3) REFERRED TO AVERAGE STICK LENGTH OF $16.7 \lambda_g = 2.76$ METERS.
 (4) ASSUMES MEAN SLOT OFFSET ERROR IS ZERO.

D180-22876-4

the boresight direction. The question is asked, will these physical offsets cause subarrays to become decorrelated in phase at angles well off boresight preventing the orderly roll off of the sidelobe radiation patterns?

The subarray geometry is shown in Figure 2-13. Normally a planar array will experience a systematic change of phase with the angle of arrival of the wavefront. This relation is expressed as

$$\Phi_n = \frac{2\pi}{\lambda} S_n \sin\theta \quad 2.9$$

which is the phase difference of the n^{th} subarray with respect to the central subarray due to wave path length difference. This systematic behavior produces a sidelobe roll off of 30 dB/decade of angle in a circular planar array.

In practice, the subarrays may be considered to be offset by a distance h_n from the plane of the central subarray as illustrated in Figure 2-13-b.

The phase control system will, in every case, introduce a compensating phase shift Φ_s

$$\Phi_s = \frac{2\pi}{\lambda} h_n$$

At some angle θ off boresight a path length difference

$$S_n \sin\theta - h_n \cos\theta$$

is introduced as seen in Figure 1-(c). The total differential phase shift of each element then is derived from the sum of the above,

$$\phi_n = \frac{2\pi}{\lambda} [S_n \sin\theta - h_n \cos\theta] + \phi_s \quad 2.10$$

which reduces to

$$\phi_n = \frac{2\pi}{\lambda} [h_n (1 - \cos\theta) + S_n \sin\theta] \quad 2.11$$

The $S_n \sin\theta$ term is identifiable as the phase shift associated with the planar error free array. The $h_n (1 - \cos\theta)$ term represents the error introduced by the offset. Behavior of the associated phase shift is plotted in Figure 2-14 for several offsets. Systematic errors in offset are expected to result in some shifting and raising of average far-out sidelobes. Random errors on the other hand will produce a sidelobe error plateau, similar to that produced by the phase control errors between the subarrays. If the subarrays are omnidirectional, the sidelobe level would be given by Allen as:

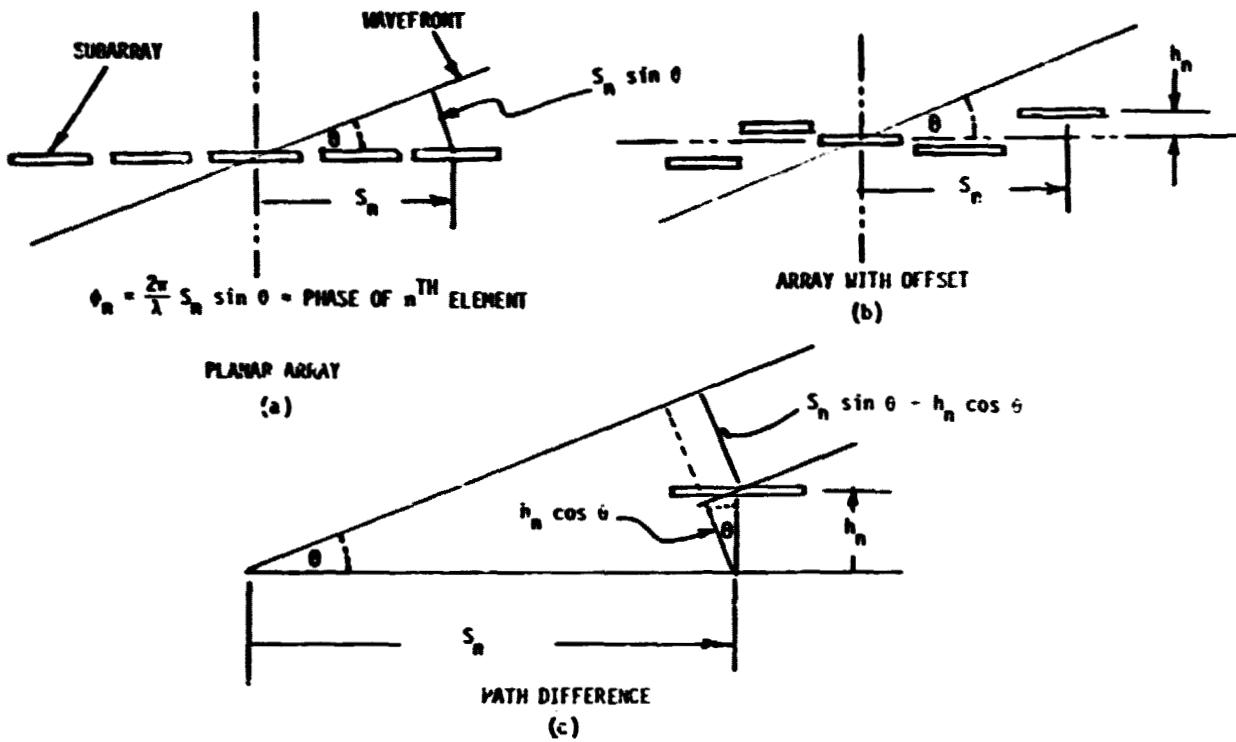


Figure 2-13 Phase Difference Due to Subarray Offset

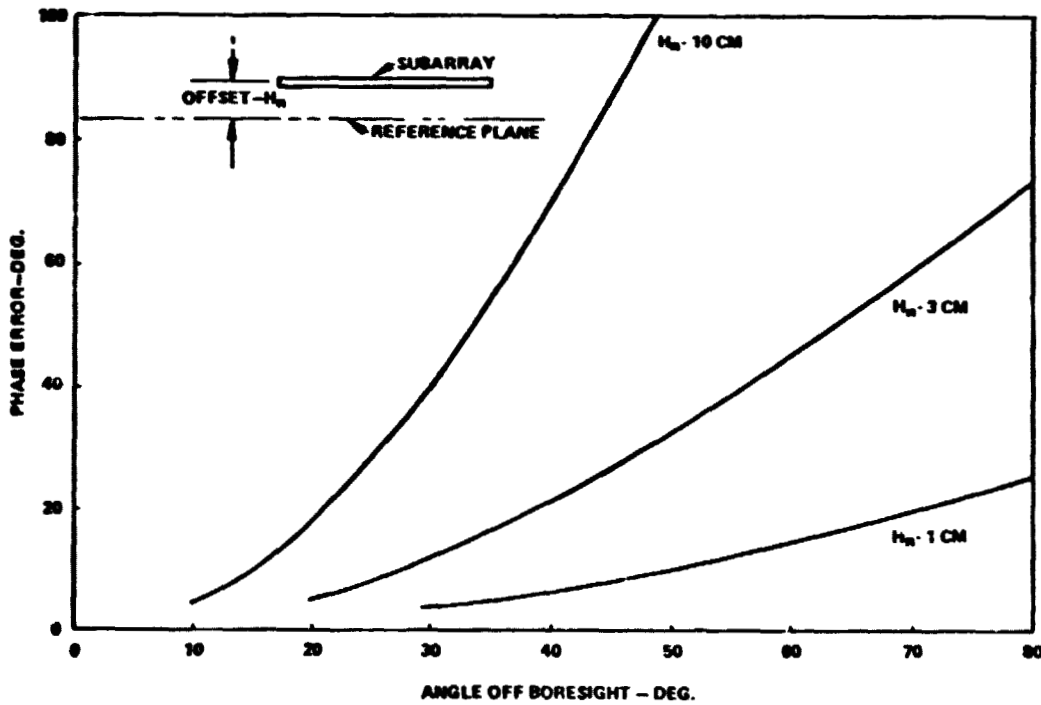


Figure 2-14 Phase Error Due to Subarray Offset

$$\text{ERROR SIDELobe LEVEL} = \frac{\epsilon^2}{N} = \frac{\sigma_\phi^2}{N} \quad 2.12$$

where σ_ϕ = the mean square phase error
 N = the total number of subarrays

For random errors in h_n

$$\sigma_\phi^2 = \left[\frac{2\pi}{\lambda} h_n (1 - \cos\theta) \right]^2 \quad 2.13$$

the factor $(1 - \cos\theta) \cong \theta^2$, i.e., by combining (7), (8) and (6), we obtain

$$\text{ERROR SIDELobe LEVEL} \propto \theta^4$$

However, the average pattern of the subarray is rolling off at 30 dB/decade of angle as seen in Figure 2-15. Therefore, the net error sidelobe level varies as $(\theta^4)(\theta^{-3}) = \theta$ for values of $\theta < 30^\circ$, i.e., 10 dB/decade of angle.

Several estimated plateaus for different offsets are shown in Figure 2-15. Using a graphical integration technique, an 18 cm random offset will scatter significant energy in the region between 30° - 90° off axis. Since the power loss can be seen from Figure 2-16 to be proportional to the offset squared, the power loss will drop rapidly with tighter tolerances on random offset. It is estimated that a random tolerance of 3 cm would result in a power loss of less than 0.1%.

To evaluate the effect of systematic offset errors in an accurate manner will require the incorporation of the expected offset contours into the array computer program. An estimate of the effect might be obtained by setting up a simple linear model incorporating the angularly variable phase error from which could be calculated the approximate efficiency reduction associated with various systematic tolerances.

2.2.8 Derivation of Mismatch Loss Equation

From ITT Handbook, Reference 2.5, page 569, line (3)

$$\begin{aligned} \frac{P_m}{P} &= \frac{(R_g + R_1)^2 + (X_g + X_1)^2}{4 R_g Z_0} = \frac{\text{matched power}}{\text{unmatched power}} \quad 2.14 \\ &= \text{loss @ the input to a line of } Z_0 = R_1 + jX_1 \end{aligned}$$

if we assume the line is matched and of $Z_0 = R_1$ such that $X_1 = 0$ then

SPS-1641

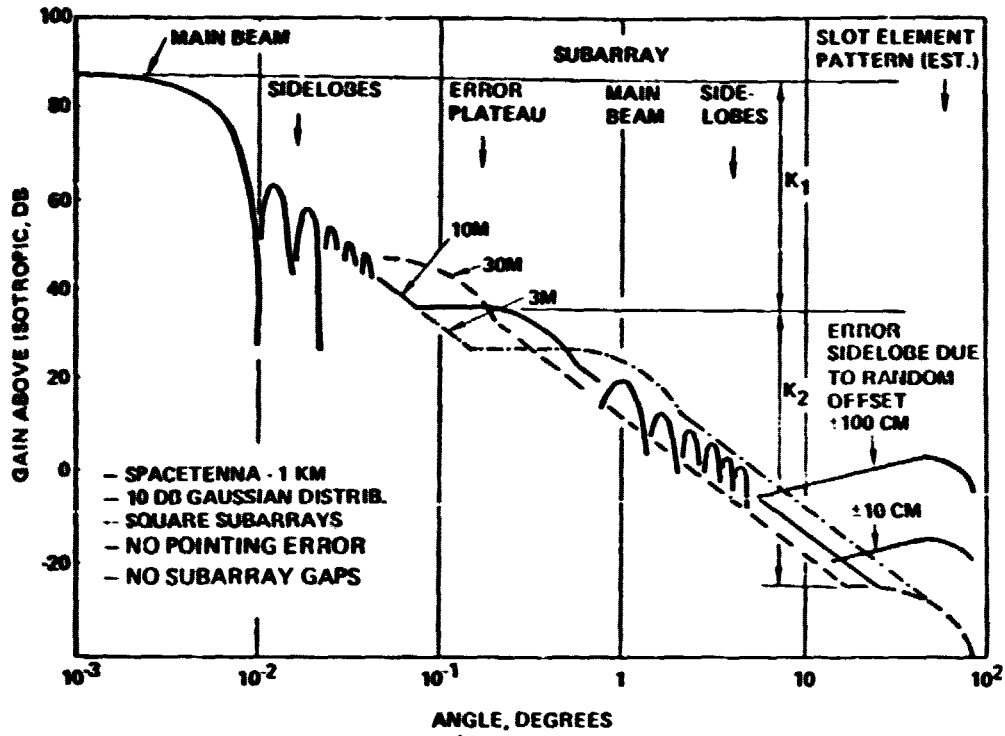


Figure 2-15 Array Pattern Roll-Off Characteristics

SPS-1646

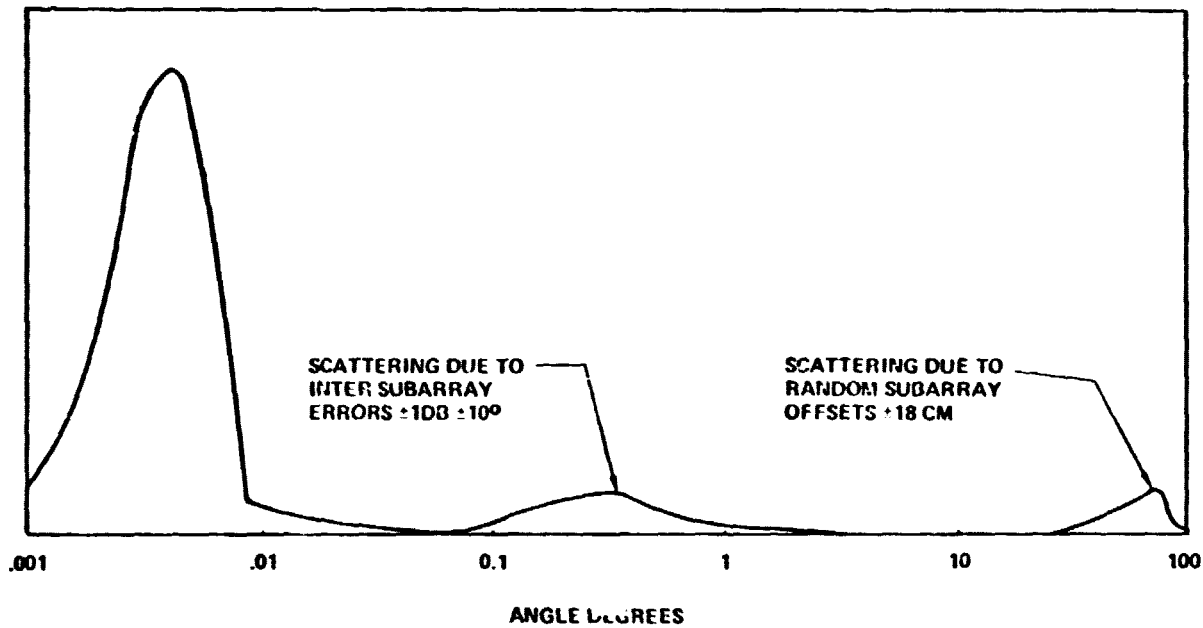


Figure 2-16 Total Radiation Power vs. Angle

D180-22876-4

$$\frac{P_m}{P} = \frac{(R_g + Z_0)^2 + X_g^2}{4 R_g Z_0}$$

if we further let the generator resistance be:

$$R_g = Z_0$$

$$\begin{aligned} P_m &= \frac{(2Z_0)^2 + X_g^2}{4Z_0^2} \\ &= 1 + \frac{1}{4} \left(\frac{X_g}{Z_0} \right)^2 \end{aligned} \quad 2.15$$

but

$$\frac{P_m - P}{P} \approx \text{Mismatch Loss} \approx \frac{P_m}{P} - 1$$

$$\therefore \text{Mismatch Loss} \approx \frac{1}{4} \left(\frac{X_g}{Z_0} \right)^2$$

or

$$\approx \frac{1}{4} \left(\frac{B}{Y_0} \right)^2 \text{ in admittance terms} \quad 2.16$$

2.3 CIRCULARLY SYMMETRIC ARRAY RADIATION PATTERN STUDIES

Beam efficiency is of prime importance in the design of the spacetenna and must be thoroughly investigated and optimized. An optimum design will reflect the tradeoff between beam efficiency and minimize aperture size and consequently weight and cost. This section examines spacetenna pattern characteristics and overall system efficiency for a variety of power density tapers across its aperture.

2.3.1 Distributions for Constant Main Beamwidth

Starting from fundamental relationships, an expression for beam efficiency was derived in terms of a circularly symmetric aperture field distribution $f(\rho)$ where ρ^* is the normalized spacetenna radius and $e(\theta)$ the field pattern of the antenna. (See Figure 2-17.) The spatial efficiency factor is obtained from the integral of the far field power density $[|e^2(\theta)|]$ out to an arbitrary angle of interest from boresight θ_0 . Normalizing to the on-axis value of power density by dividing by

Most authors use ρ as the radial coordinate and r as the normalized radius where $r = \rho/a$ and a is the aperture radius. We have here chosen ρ^ as the normalized radius and r as the radial coordinate (i.e., $\rho = r \cdot a$).

CIRCULARLY SYMMETRIC
APERTURE DISTRIBUTION

$$\eta_B = \underbrace{\left[\frac{1}{2 \epsilon_{MAX}^2(\theta)} \int_0^{\theta_0} \epsilon^2(\theta) \sin \theta \, d\theta \right]}_{\text{SPATIAL EFFICIENCY}} \left[\frac{4\pi}{\lambda^2} \right] \underbrace{\left[a^2 \right]}_{\text{PHYSICAL APERTURE}} \underbrace{\left[\frac{\left[2 \int_0^1 f(\rho) \rho \, d\rho \right]^2}{2 \int_0^1 [f(\rho)]^2 \rho \, d\rho} \right]}_{\text{APERTURE EFFICIENCY}}$$

EFFECTIVE APERTURE
GAIN

Figure 2-17 Beam Efficiency

$\epsilon_{\max}^2(\theta)$ gives a spatial efficiency factor that is unity for an isotropic antenna integrated to $\theta_0 = \pi$, which is equivalent to integrating over the entire sphere, because of circular symmetry. The spatial efficiency of more directive antennas will go down in a manner approximately the inverse of their directivity. The beam efficiency then is simply a measure of how well the spatial efficiency and gain of an antenna balance each other. The aperture efficiency is the loss associated with the taper of the field over the aperture relative to a uniform distribution. This is sometimes referred to as illumination efficiency.

The relative radiation patterns were obtained by numerical integration of the expression

$$\epsilon(\theta) = \int_0^1 f(\rho) J_0\left(\frac{2\rho\pi a}{\lambda} \sin\theta\right) \rho \, d\rho \quad (2.17)$$

All were then normalized to the null width of the 10 dB Gaussian distribution function. These patterns are shown in Figure 2-18 together with the Spacenna size required. The power required to deliver 5 GW output was computed by:

$$P_{IN} = \frac{\text{power delivered}}{(\text{rectification eff.})\eta_B}$$

where η_B is the main beam null-to-null efficiency for each distribution obtained from Figure 2-17.

Power density distributions across the spacenna were then obtained by dividing by the integral of the normalized field distribution over the aperture to give the maximum power density, P_D^{\max}

$$P_D^{\max} = 2\pi a^2 \int_0^1 [f_\eta(\rho)]^2 \rho \, d\rho$$

where $f_\eta(\rho)$ is the normalized aperture field distribution made dimensionless by dividing by its peak or central value $f_\eta(\rho_0)$

$$f_\eta(\rho) = \frac{f(\rho)}{f(\rho_0)}$$

The result of these calculations is shown in Figure 2-19. The various tapered power densities are rather similar, the most significant difference being the addition of the tails, which clearly control the sidelobe levels.

The above calculations assume a constant average rectenna efficiency. For a more exact calculation of the ground power output, the variation of rectenna efficiency with power level should be included. The low sidelobe patterns which tend to have narrower shoulders will probably experience an average rectification efficiency that is somewhat lower than the broader shouldered patterns.

SPS 000

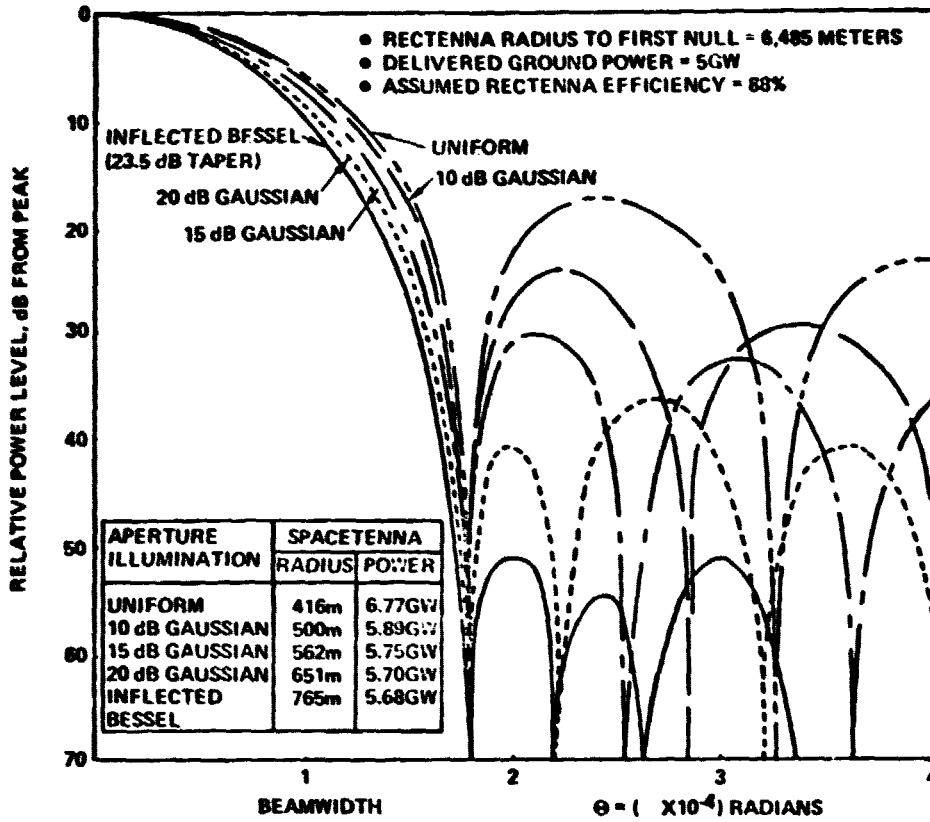


Figure 2-18 Sidelobe Distributions for Fixed Rectenna Constraints

SPS 000

- RECTENNA RADIUS TO FIRST NULL = 6,485 METERS
- DELIVERED GROUND POWER = 5GW
- ASSUMED RECTENNA EFFICIENCY = 88%

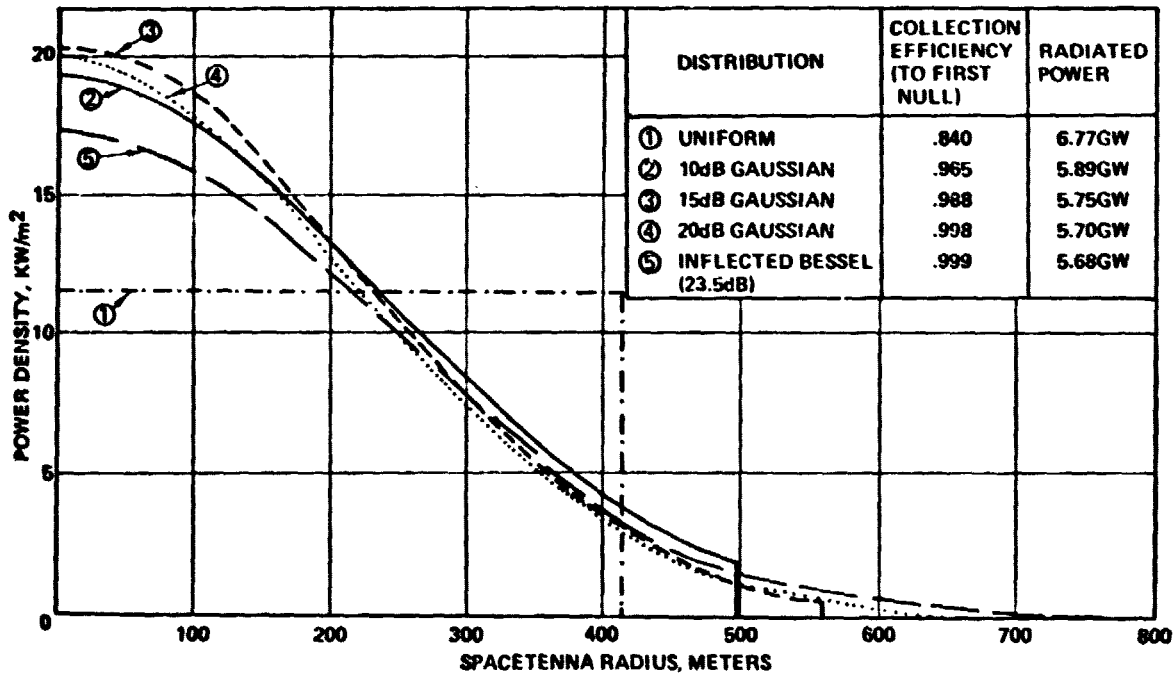


Figure 2-19 Spacenna Size and Power Density

The peak rectenna power density ($P_D^{\text{rect. pk.}}$) may be obtained directly from the peak spacetenna power density

$$P_D^{\text{RECT PK.}} = P_D^{\text{MAX}} \frac{4\pi^2 a^4}{H^2 \lambda^2} \left[\int_0^1 f_\eta(\rho) \rho d\rho \right]^2$$

where H is the altitude (or range) of the spacecraft.

Multiplying by the pattern then gives a rectenna power density curve as shown in Figure 2-20. Coupled with a curve of rectification efficiency vs. power density (obtained from JPL), the rectification efficiency vs. rectenna radius may then be obtained as shown. In the evaluation distributions with significantly broader shoulders, it is important to go through the above process iteratively, i.e., the average rectification efficiency should be obtained for a particular power input and the power output calculated.

2.3.2 Reverse Phase Distribution Patterns

In order to improve the overall collection efficiency by increased beam flatness out to the rectenna edge as well as provide an additional means of sidelobe control, a two beam synthesis with resultant phase reversals at some portions of the spacetenna was considered. These phase reversals are obtained by a fixed phase shifter at the klystron input and represent a first step towards a continuously variable phase distribution across the spacetenna, should this be more desirable. The results indicate that it is possible to synthesize a pattern that is considerably more flat-topped than the 10 dB Gaussian or other patterns that we have investigated. The price paid for this improvement is increased spacetenna size or a larger rectenna.

It is possible to increase the flatness of the beam without limit with arbitrarily large apertures and large numbers of beam components. The results of the two beam synthesis are illustrated in Figure 2-21. The angle of the first null in the central pattern which is the peak of the second pattern occurs at a value of μ_1 which is just the 1st root of the first order Bessel function. The first pattern is produced by a uniform distribution while the second pattern is produced by a J_0 distribution. The height of the shoulder at μ_1 and the sidelobe level may be controlled by adjusting the relative magnitude k of the two distributions. This later process is illustrated in Figure 2-22. If k is greater than 2.48, a phase reversal will occur in the aperture voltage. The inflected Bessel distribution previously investigated exhibits this property (k=2). For the reverse distribution considered (k=4.35) the results are shown in Figures 2-23 and 2-24, with the 10 dB Gaussian distribution for comparison. A small change in k could match the sidelobe levels. The usefulness of this type of distribution should be further investigated including the effect of rectification efficiency.

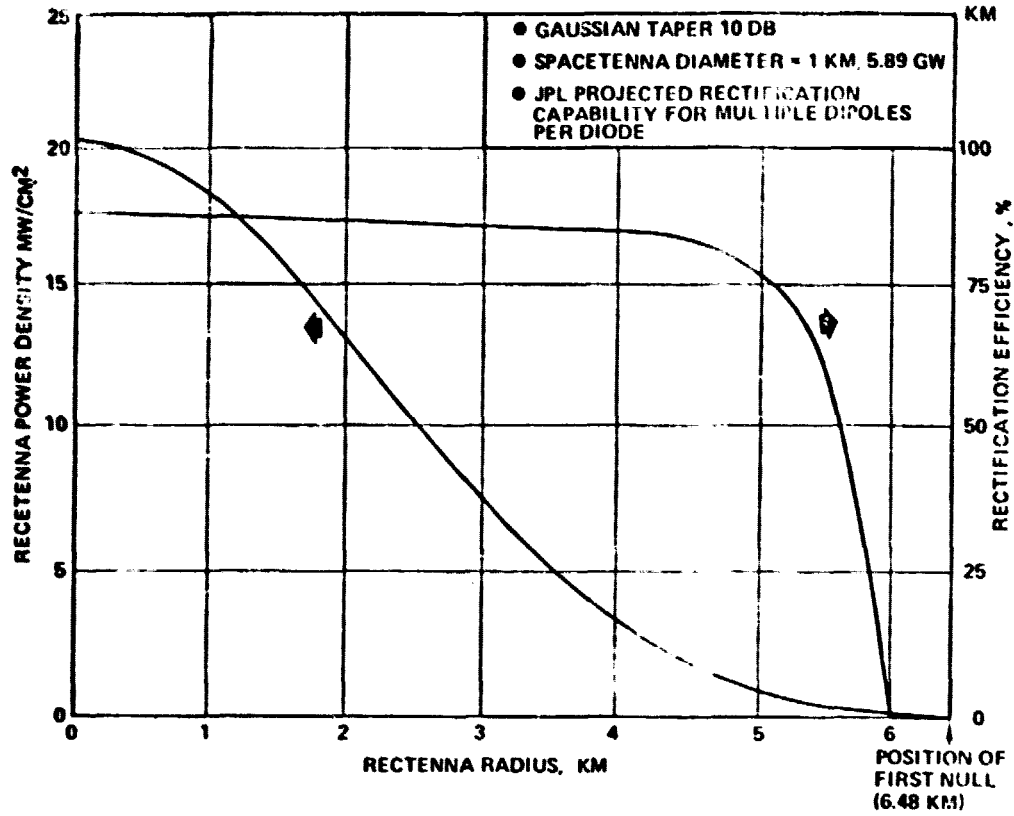
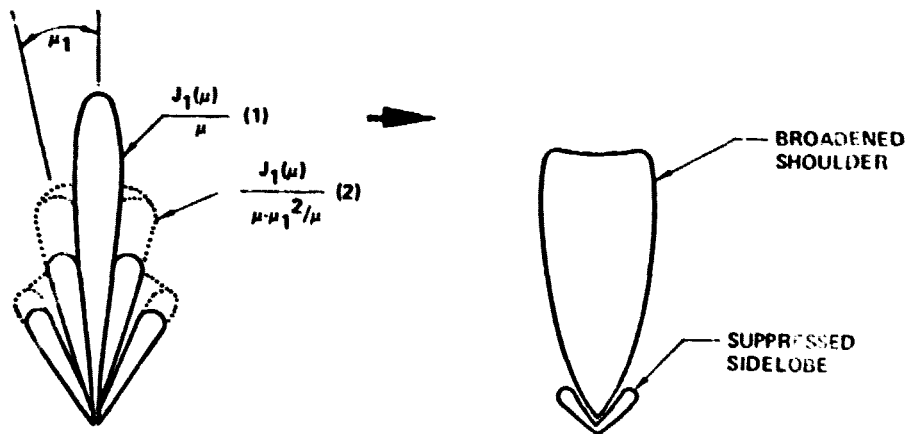


Figure 2-20 Rectenna Power Density and Rectification Efficiency

SPS-1104



$\frac{J_1(\mu)}{\mu}$ PATTERN PRODUCED BY UNIFORM DISTRIBUTION $f(\rho) = 1$

$\frac{J_1(\mu)}{\mu \cdot \mu_1^2/\mu}$ PATTERN PRODUCED BY BESSEL DISTRIBUTION $f(\rho) = J_0(\mu_1 \rho)$

Figure 2-21 Two Beam Bessel Function Synthesis

SPS-1500

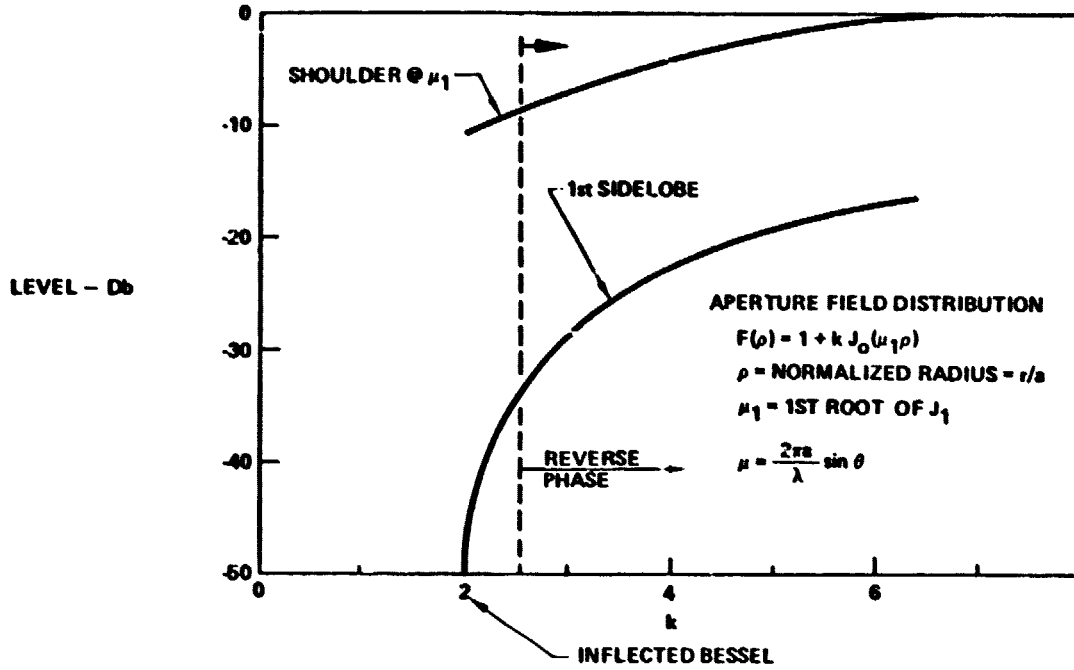


Figure 2-22 Pattern Shape vs. Distribution Constant K

SPS-1500

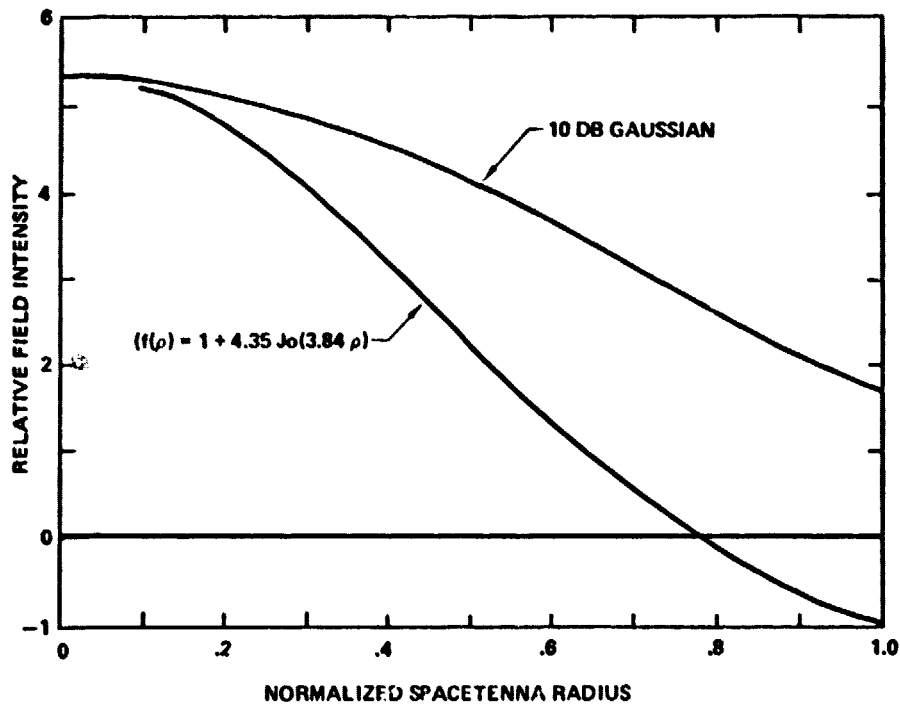


Figure 2-23 Aperture Field Distribution

PS 1800

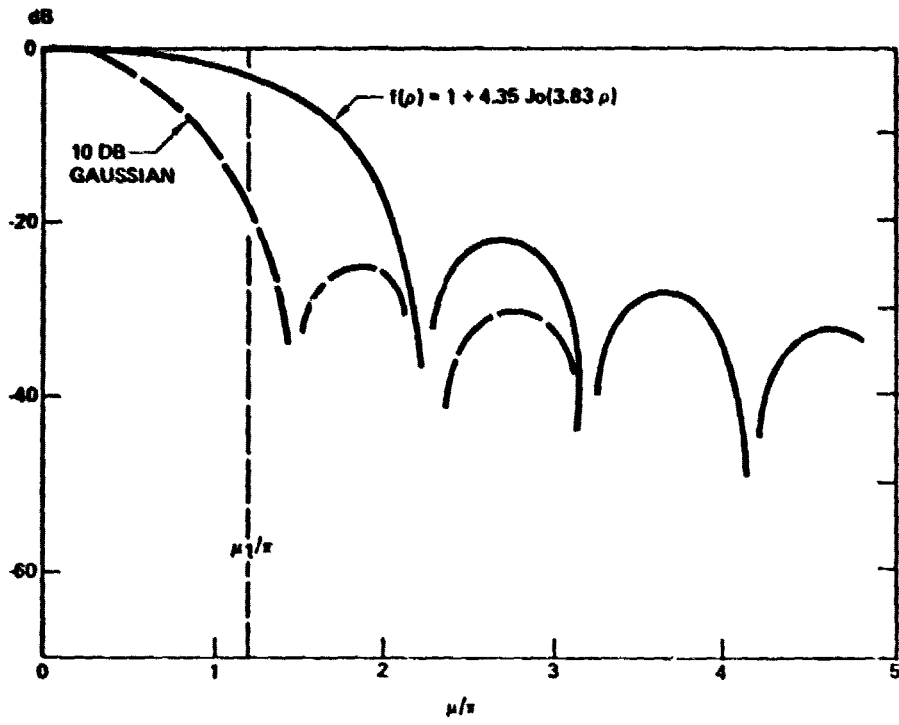


Figure 2-24 Spacetenna Pattern

2.3.3 Pattern Roll-off Studies

In order to verify the energy distribution at distances far away from antenna boresight, it was necessary to determine the roll-off characteristics of the entire antenna. This was done by a numerical integration technique applied to the radiation pattern of the 10 dB Gaussian taper distribution. It was established that the sidelobes rolled off at 30 dB/decade of angle. This coincidentally is the roll-off rate of a uniform circular aperture. Figure 2-25 shows the first five sidelobes of the main beam and the average power line, 3 dB below the peaks. Next, the error plateaus were computed from the assumed error magnitudes and the number of subarrays associated with three different subarray sizes. The aperture efficiency, η , was also obtained by numerical integration. Next the subarray roll-off characteristics were obtained by numerically integrating the square aperture distribution for each of 19 different cuts over a 45° sector of ϕ . These cuts were then averaged at each θ to give the pattern shown. The resultant subarray sidelobes also roll off at 30 dB/decade of angle. There is an additional error plateau associated with the randomly scattered power by each slot in the subarray. This second plateau will in theory roll off in accordance with the radiation pattern of the slot. To obtain a clearer view of how the total energy is distributed, the average pattern level as a function of angle can be integrated graphically by adding a $\sin \theta$ term as shown in Figure 2-26. By weighting this with an additional multiplier proportional to θ , it is possible to take out the area bias produced by the logarithmic plot. Repeating this in terms of power rather than dB, as shown in Figure 2-27, gives a curve, the area under which represents the radiated power.

2.4 PHASE ARRAY COMPUTER PROGRAM DEVELOPMENT

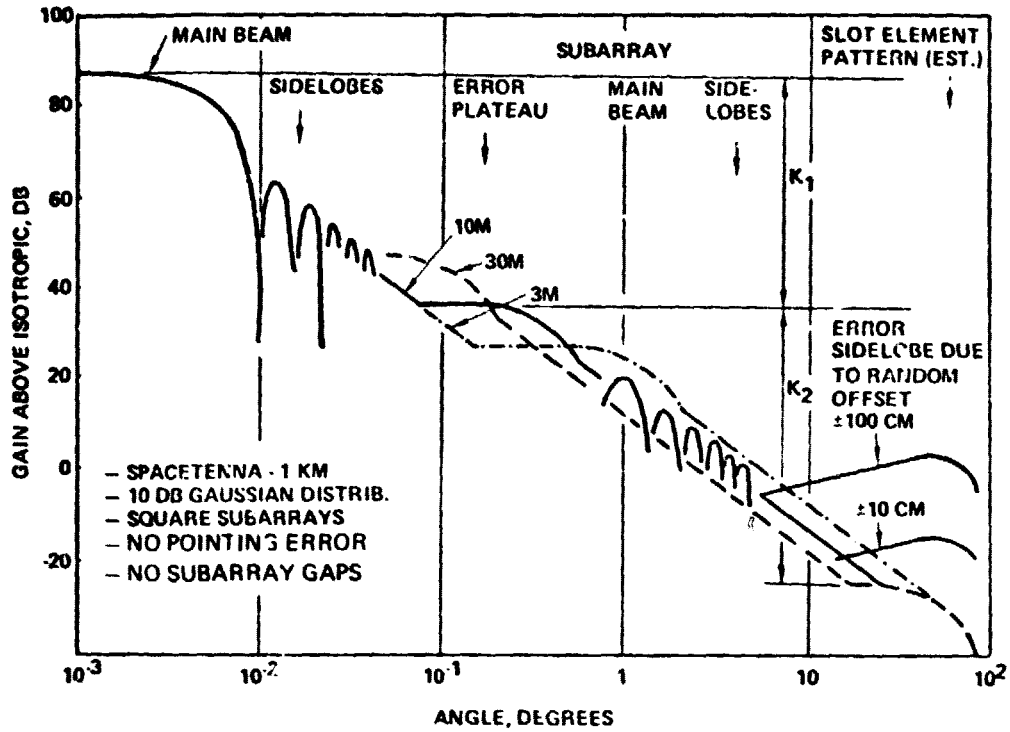
The computer programming efforts, which began concurrently with Part II, have been directed primarily to beam pattern analysis. The following reasons have been specified as the purpose of the computer programs: verification of the reference design; definition of feasible departures such as quantized distributions and gap spacing between subarrays; exploration of new design options like the Inflected Bessel and Reverse Phase distributions; the study of far-out sidelobe roll-off characteristics; calculation of the average rectenna efficiency; and the analysis of errors and failures.

2.4.1 Spacetenna, Ground-Grid, Error and Failure Modeling

Early in the computer program development stage, basic language programs were written to model various power taper distributions and to compare their beam efficiencies. The equation for the normalized electric field pattern is

$$E(\theta) = \int_0^1 \rho f(\rho) J_0 \left(\frac{2\rho\pi a}{\lambda} \sin \theta \right) d\rho$$

where ρ is the normalized radial distance. In Section 2.3.1, the equation for the beam efficiency is shown in Figure 2-17 and the equations used to model the spacetenna distribution functions are in Table 2-2. The five quantized distributions described in Section 2.1.3 are modeled as normalized amplitudes as shown in Table 2-3.



- ARRAY GAIN ABOVE ISOTROPIC FOR 1 KM CIRCULAR SPACETENNA

$$G = \frac{G_0 \cdot n}{1 + \epsilon_1^2 / P} = 37.46 \text{ DB} \quad (n = 90.2\%, P = 98\%)$$

- SPACETENNA DISTRIBUTION IS 10 DB GAUSSIAN - NUMERICAL INTEGRATION GIVES 30 DB/DECADE ROLL-OFF.
- SQUARE SUBARRAY: 19-CUT NUMERICAL INTEGRATION GIVES 30 DB/DECADE ROLL-OFF.
- ERROR PLATEAUS:

SUBARRAY LEVEL: $K_1 = nPN_1/\epsilon_1^2$
 $\epsilon_1^2 = .064$ FOR 10⁰ RMS ERROR; ±1 DB AMPLITUDE ERROR

$N_1 = 7.854$ SUBARRAYS

SLOT LEVEL: $K_2 = N_2/\epsilon_2^2$ WHERE $N_2=12$, 648 SLOTS PER SUBARRAY

$\epsilon_2^2 = .01$, CORRESPONDS TO ROUGHLY .006" SLOT ERROR (EMPIRICAL)

Figure 2-25 Array Pattern Roll-Off Characteristics

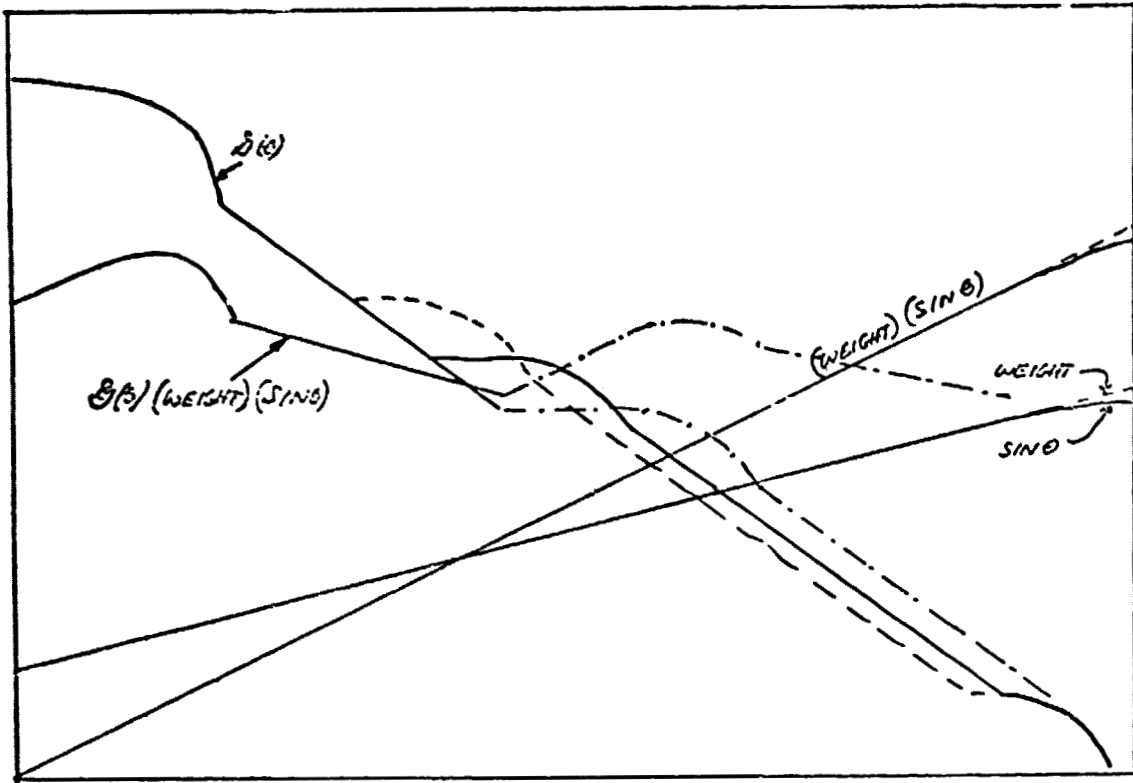


Figure 2-26 Graphical Integration Technique

SPS 1648

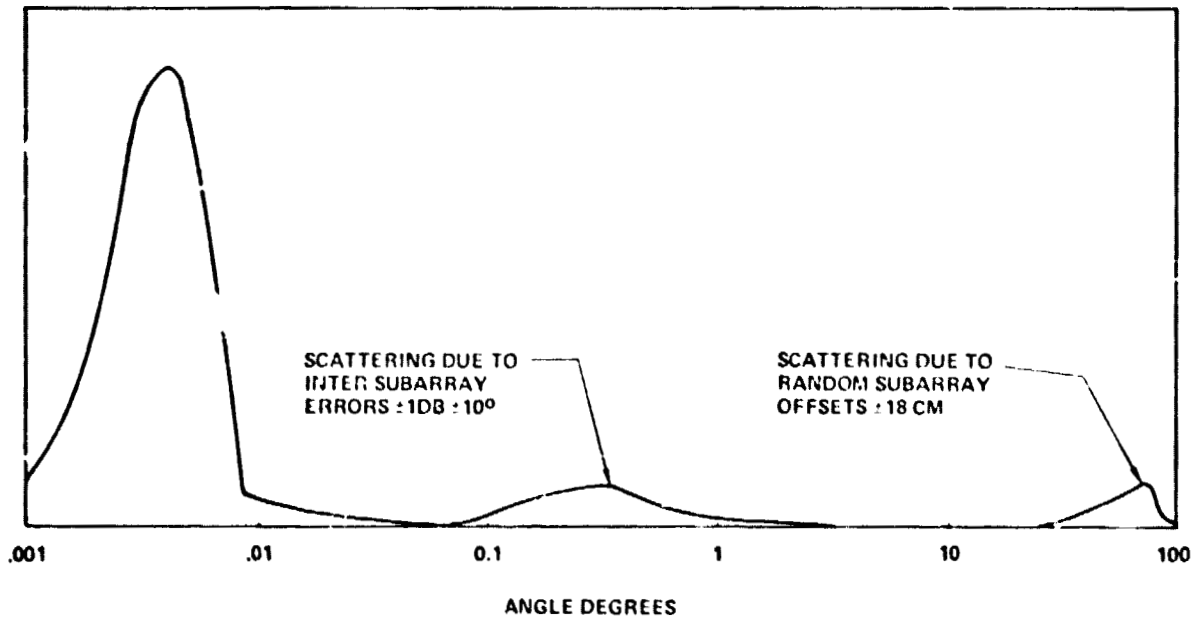


Figure 2-27 Total Radiated Power vs. Angle

Table 2-2 Spacetenna Size and Beam Efficiency

COMPARISON FOR FIXED RECTENNA SIZE
RECTENNA RADIUS TO FIRST NULL = 6.485 METERS

SPACETENNA DISTRIBUTION	SPACETENNA RADIUS (METERS)	BEAM EFFICIENCY (%)
CONTINUOUS UNIFORM	416	84.0
CONTINUOUS 10 dB GAUSSIAN $e^{-1.1513(\rho^2)}$	500	96.5
CONTINUOUS 15 dB GAUSSIAN $e^{-1.72694(\rho^2)}$	562	98.8
CONTINUOUS 20 dB GAUSSIAN $e^{-2.302585(\rho^2)}$	651	99.8
CONTINUOUS 23.5 dB INFLECTED BESSEL $1.0 + 2.0 J_0(3.8317\rho)$	765	99.9
CONTINUOUS 17 dB REVERSE PHASE $1.0 + 4.35 J_0(3.8317\rho)$	762	97.9
CONTINUOUS 13.7 dB REVERSE PHASE $1.0 + 6.16 J_0(3.8317\rho)$	762	96.0
QUANTIZED #1 10 dB GAUSSIAN 10 STEP	500	96.41
QUANTIZED #2 10 dB GAUSSIAN 9 STEP	500	96.9
QUANTIZED #3 9.5 dB GAUSSIAN 10 STEP	500	96.39
QUANTIZED #4 17 dB GAUSSIAN 14 STEP	595	99.1
QUANTIZED #5 16.8 dB GAUSSIAN 8 STEP	502	96.4

Table 2-3 Quantized Distribution Modeling

QUANTIZED DISTRIBUTION NUMBER	1	2	3	4	5
Normalized Amplitude for Step 1	1.0000	1.0000	1.0000	1.0000	1.0000
" " " " 2	.8944	.8944	.9129	.9129	.9129
" " " " 3	.8149	.8149	.8165	.8165	.8165
" " " " 4	.7288	.7288	.7454	.7454	.7071
" " " " 5	.6325	.6325	.6667	.6667	.5774
" " " " 6	.5477	.5477	.5774	.5774	.5002
" " " " 7	.5164	.5164	.5002	.5002	.4082
" " " " 8	.4472	.4472	.4714	.4714	.2891
" " " " 9	.3651	.3162	.4082	.4082	
" " " " 10	.3162	.3162	.3333	.3333	
" " " " 11				.2891	
" " " " 12				.2357	
" " " " 13				.1667	
" " " " 14				.1408	

In July 1977, the spacetenna/rectenna simulation program "Bigmain," running for NASA Johnson Space Center (JSC) on the Univac 1110 in Fortran V, was converted and modified to Fortran IV so as to run on the Boeing Computer Services (BCS) Mainstream system. The purpose of "Bigmain" is to simulate the types of antenna systems which might be used for the SPS transmission of power. Studies were performed using the following subarray sizes: square 18m by 18m, square 10m by 10m, rectangular 9.929m by 11.464m (the reference design), and circular with a diameter of 18m. The circular subarray has a beam efficiency of 76% which corresponds to the loss of radiating area in the spacetenna. Gap spacing between subarrays was also studied with the results shown in Figure 2-28.

Two types of array excitation were used with "Bigmain:" The continuous Gaussian amplitude distribution with uniform phase and chosen power taper, and the quantized stepped array distribution with uniform phase and chosen values of step size, step number, and power taper. Amplitude, phase, and failure errors have been modeled in the spacetenna program. Although originally the random number generator was not implemented on our system, because of its machine dependence to the Univac 1110, BCS system routines have been utilized and the number generator is now running.

In "Bigmain" the ground-grid is specified as a planar circular area where the electric fields are determined. The field at any particular point on the grid is computed using scalar wave equations with approximations that make them accurate in the Fresnel zone. The equations are not valid for the very near field, but give very good results in the Fresnel zone, $D^2/\lambda < R < 2D^2/\lambda$, and the far field $R > 2D^2/\lambda$, where D is the diameter of a circular spacetenna or the diagonal of a rectangular spacetenna, λ is the wavelength of the transmission signal, and R is the range from the spacetenna to the ground-grid.

The electric field at any particular point is determined by calculating the field from each subarray in the spacetenna to the given grid point and then summing all the fields to give the total field at that grid point.

There are several methods of sampling points on the grid. In most runs, the beam from the spacetenna is extremely symmetrical about the boresight of the ground-grid. In these cases, sampling grid points along the X or Y axis out to a given radius can effectively describe the entire circular field on the ground-grid. In some runs, the errors generated in the spacetenna degrade the symmetry to such an extent that samples are taken at points equally spaced over the entire circular grid system to the outermost sampling radius. These runs are usually quite expensive.

The total power collected by the ground-grid is calculated by multiplying the power density at a point by the incremental area associated with that point to give the power over that area, and then summing up the power from each sample. Efficiencies with respect to the total power collected on the ground-grid and with respect to the total input power of the orbiting spacetenna are calculated at incremental grid distances out to the specified diameter.

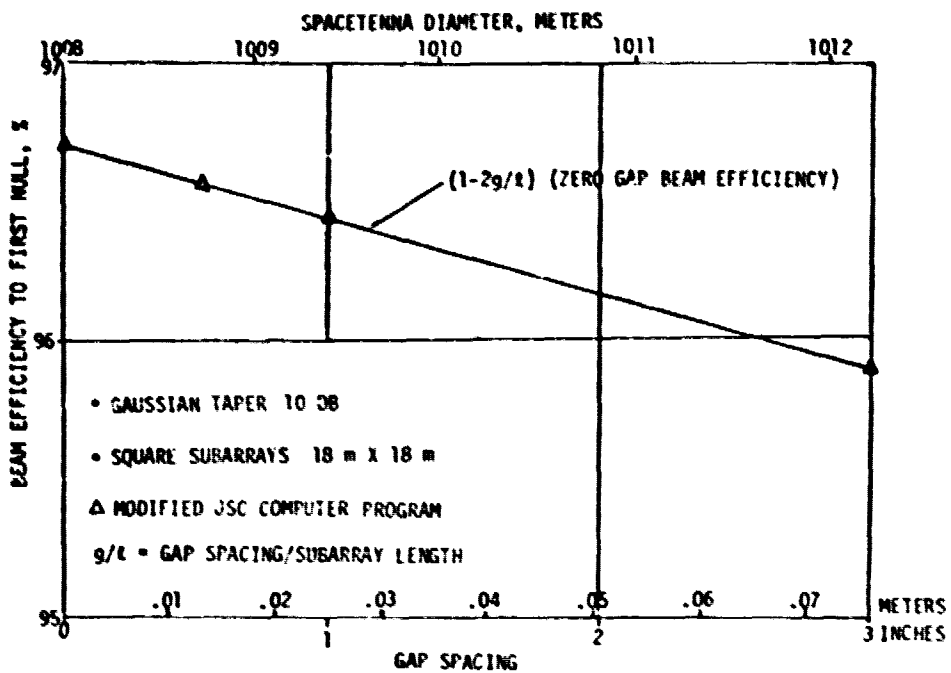


Figure 2-28 Beam Efficiency vs. Gap Spacing Between Subarrays

A study was done to show the effect of grid step size on beam efficiency by changing the step size from 161.5m to 5m. Forty radial grid steps, 161.5m each, gave a beam efficiency of 96.71% at a run cost of \$10. Using a step size of 5m, 1292 steps gave a beam efficiency of 96.69% at a run cost of \$200. Since the cost factor of 20 seemed like a large price to pay for a 0.02% beam efficiency difference, the 161.5m step size was normally chosen.

The "Bigmain" computer program was exercised to provide estimates of performance degradation due to the failure of one DC-DC converter which supplies processed power to 420 klystrons, each 70 kW RF. The results indicate an antenna efficiency degradation of roughly 0.4 to 0.5% and an increase in the first sidelobe level of about 0.1 to 0.3 dB, depending on the location of the failed converter. The total power loss thus approaches 0.9%, since the additional disconnected RF power is added to the reduced array efficiency.

The modeling of the baseline SPS design is shown in Figure 2-29 for the case of a 10 step quantized illumination function having a 9.5 dB taper and a 1 Km spacetenna radiating 6.5 GW with 92,857 klystrons each having a 70 kW RF output. The areas chosen to be representative of a DC-DC converter failure are indicated near the center and at the out periphery. Each DC-DC converter supplies processed power to an average of 420 klystrons. Since only 15% of the klystron supplies required processed power, the DC-DC converter size for 420 klystrons is roughly $(\frac{70}{85} \times .15)(420) \cong 5.1$ MW for a klystron efficiency of 85%.

The computer models a single converter failure at the spacetenna edge as an outage of 72-10 by 10 meter subarrays and therefore a drop of 29.4 megawatts (420 klystrons at 70 kW each).

The method of analysis employs a sampling of 40 points along the positive X or Y axis of the ground-grid with ring power summation. The results are tabulated in Figure 2-30. A square loop method of analysis for power summation with samples along circular loops is too expensive in terms of required computer time.

Since the power summation was done only along two specific axes to conserve computer time and averaged over a ring area representative of a single value, the results are approximations for the cases where the failed area is asymmetrically located in the array. To ascertain whether this asymmetry is serious, similar runs were made for 2 and 4 failed areas in which symmetry is preserved (see Figure 2-30). Since the results did indeed indicate that both the efficiency reduction and sidelobe level increase in dB scaled as expected (i.e., by a factor of 2 and 4), it can be assumed that the errors due to averaging the x and y results (which are quite different for the asymmetric single failure at the periphery) are negligible. Moreover, the interpolated radial position of the first null on the rectenna, on the basis of which the efficiency is calculated, did not deviate by more than 250 meters (the grid step size), with the unperturbed value at 6525 meters. The total loss in the rectenna output must, of course, include the RF power loss as well as the reduced antenna efficiency.

SP-4388

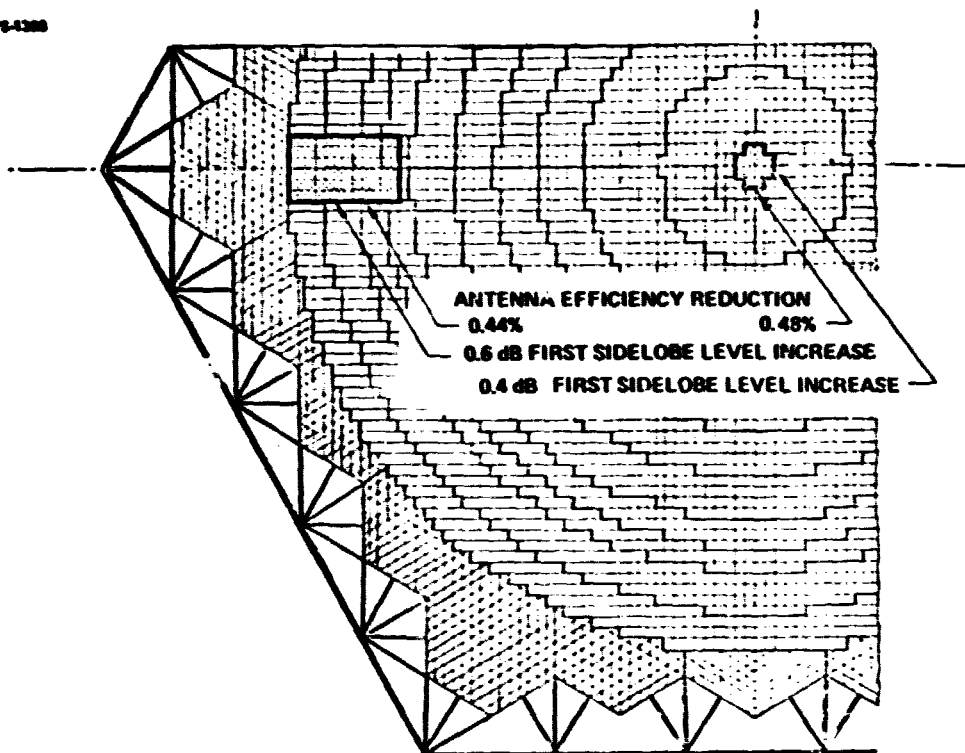







Figure 2-29 Spacetenna Quarter Section

TYPE OF FAILURE ¹	SPACETENNA GEOMETRY	AXIS	BEAM EFFICIENCY		SIDELOBE LEVEL		POWER DENSITY		FIRST NULL RADIAL POSITION ³	RECTENNA ² POWER REDUCTION %
			%	$\Delta\%$	dB	dB	$\frac{\text{mW}}{\text{cm}^2}$	Δ		
NONE		Both	96.59	0	-24.75	0	23.57	0	6525 m	0
SINGLE CONVERTER AT THE CENTER ($\Delta A = .15\%$)		X	96.11		-24.35		23.44		6480 m	.91
		Y	96.11		-24.35		23.44			
		AVR	96.11	.48	-24.35	.40	23.44	.13		
AT THE EDGE ($\Delta A = .92\%$)		X	97.43		-24.45		23.26		6560 m	.86
		Y	94.88		-23.81		23.26		6440 m	
		AVR	96.155	.435	-24.13	.62	23.26	.31		
TWO CONVERTERS ($\Delta A = 1.85\%$)		X	98.30		-24.12		22.96		6610 m	1.71
		Y	93.20		-22.95		22.96		6370 m	
		AVR	95.75	.84	-23.54	1.22	22.96	.61		
FOUR CONVERTERS ($\Delta A = 3.67\%$)		X	94.815		-22.41		22.35		6470 m	3.51
		Y	94.815		-22.41		22.35			
		AVR	94.815	1.78	-22.41	2.34	22.35	1.22		

1. Each converter failure corresponds to 420 klystrons disconnected.
2. To first null.
3. Interpolated with computer step size of 250 m.

Figure 2-30 Effect of DC-DC Converter Failure on Spacetenna Performance

It is of interest to note that the loss of beam efficiency is approximately equal to the power loss in percent. For example, the change in beam efficiency due to the failure of a single converter at the edge is 0.435%. The power loss is $29.4 \text{ MW}/6.5 \text{ GW} = .452\%$. The first sidelobe level increases at approximately 0.5 dB per converter failure. It is of interest to note that the loss in antenna efficiency is roughly equal to 3 times the area loss near the center of the array, and about half the area loss near the periphery.

Program "Tiltmain" is a modified version of "Bigmain." The modifications give "Tiltmain" the ability to simulate errors in the attitude control of both the total antenna system and the individual subarrays. It was learned by talking with NASA JSC that run costs, in the order of \$5000, are prohibitive. Only a half a dozen runs or so of "Tiltmain" have been made by NASA JSC. For the time being it has been decided not to convert "Tiltmain" onto the Boeing computer system.

An enhanced spaceteenna was modeled by adding an additional 576 square 18m by 18m subarrays (8 legs at 72 subarrays per leg (Fig. 2-31)). An improved power taper in the design of the legs is possible and will be a topic of future investigation.

2.4.2 Organization of Minicomputer Timeshare and Mainstream Computing Systems

Boeing's MTS (Minicomputer Timeshare System) is configured around two digital machines: the PDP 11-70 and the PDP 11-45. Both Fortran and Basic Plus languages are employed via 56 ports. The 11-70 has 330,000 (16-bit words) of memory and the 11-45 has 128,000 words of memory. A single user is limited to 16,000 words of working core.

The MTS was used to run early studies of distribution pattern comparisons. MTS is now utilized for pre-processing editing before the "Bigmain" program is sent off to the MAINSTREAM-EKS system.

MAINSTREAM-EKS (Enhanced Kronos System), a BCS (Boeing Computer Services) computing system, is configured around five CDC large-scale mainframes: a 6600, two Cyber 74's, and two Cyber 175's. Each computer has a minimum of 131,072 sixty-bit words of central memory. The operating system is KRONOS 2, substantially enhanced by BCS. A permanent file system and 1 million words of ECS (extended core storage) are shared by the mainframes. ECS is used not only as an extremely rapid swapping medium but also for communication between the computers.

MAINSTREAM-EKS is provided from the BCS 6600 Data Center located in Renton, Washington. At the data center are six high-speed 512-line printers, twenty 844-disk storage devices (for online permanent files), ten 1/2" 7-track tape drives, three 1/2" 9-track tape drives and miscellaneous other equipment. The modified "Bigmain" Program is run via RJE (remote job entry) from the Boeing Space Center in Kent, Washington. Figure 2-32 shows the interaction between the remote job entry terminals and the central site. Remote job entry is via one of 4 cope controllers, each of which has multiple ports containing line printers, card readers and plotters. Choice of service

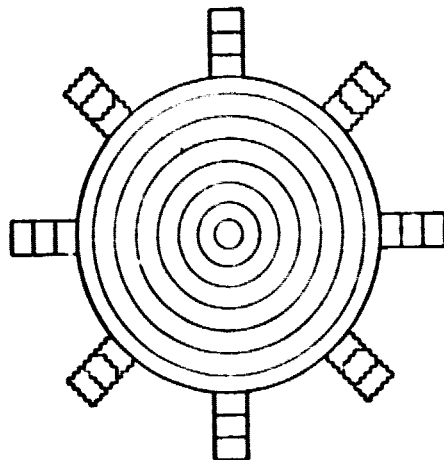


Figure 2-31 Enhanced Spacetenna

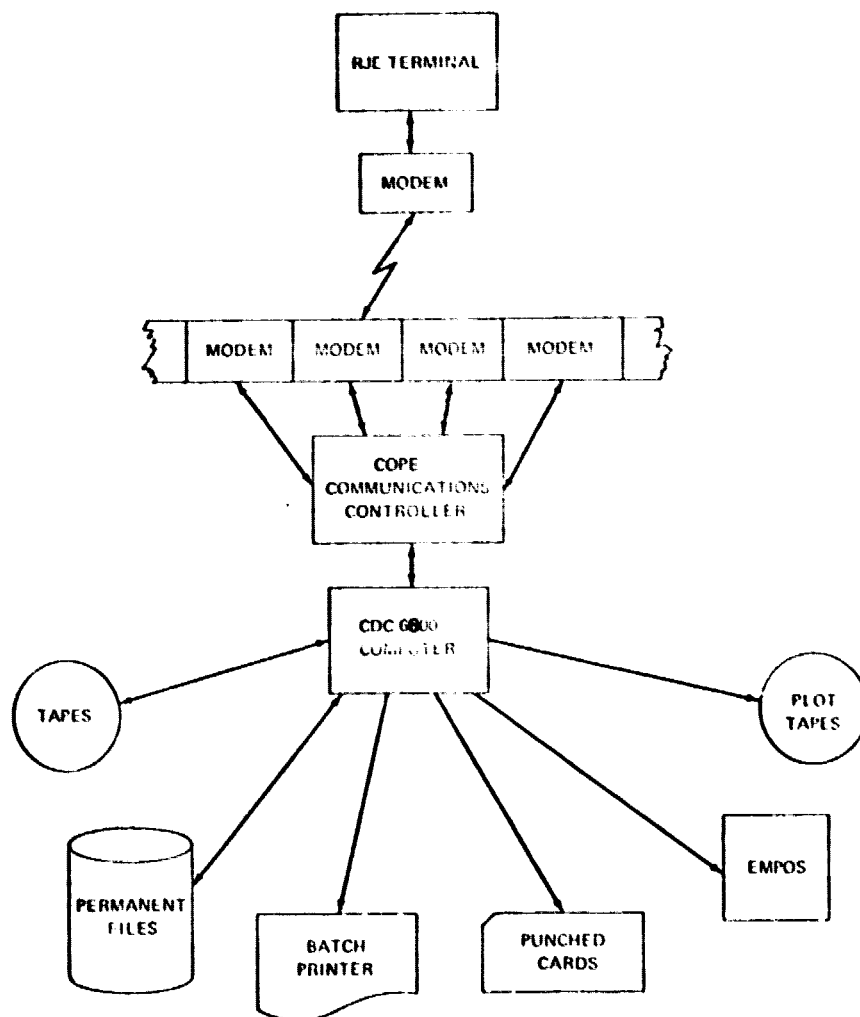


Figure 2-32 Remote Job Entry Job Processing

response times, consistent with the workload requirements, give rise to the most economical service. Five levels of response times are available, ranging from 1 to 16 hours, plus standby (from 16 hours to 7 days). The full range of MAINSTREAM-EKS services, including compilers, application programs, and utilities are put to task through RJE by "Bigmain."

This computing system was chosen because it is ideally suited to scientific and engineering applications due to the precision and high speed of the central processor and the amount of central memory and peripheral storage available to each job. Also a broad variety of *offline* services may be accessed, including plotting, microfilm, microfiche, volume printing, and special form printing.

A very important service which is heavily employed in the continuing modification of "Bigmain" is no-charge consultation. The consultants are system software specialists. Their biggest contribution is in the area of JCL (Job Control Language).

A system subroutine was chosen in order to be able to model errors in "Bigmain." Subroutine "RAND" generates uniformly (or normally) distributed random real numbers. The multiplicative congruential method is used to generate the uniformly distributed numbers, which are uniform over the interval from 0 to 1. The subroutine is called only once by the "Bigmain" program and returns an array of 3500 uniform random numbers. A starting multiplier and a fixed multiplier are specified in the passing of parameters so that the array of numbers is reproducible, enabling analysis to disregard differences in output due to a difference in the set of uniform random numbers.

2.4.3 Future Efforts

In this section eight topics will be presented each of which is directly related to the advancement of the "Bigmain" computer program.

(1) Microwave Beam Sidelobe Analysis

Analyze far sidelobe behavior as a function of phase control precision, transmitter, failures, and illumination taper and taper quantization. Make analyses of potential methods for minimizing sidelobe intensities. Consideration will be given to the addition of sidelobes from multiple spacetennas with rectennas in proximity.

(2) Baseline Configuration Modeling

Input Boeing's baseline spacenna configuration with 6392 rectangular, 9.928m by 11.464m, subarrays. The spacenna would be elliptically modeled and would have elliptically quantized power density steps. Because of the lack of non-circular symmetry, square-loop summation, which is expensive, will have to be employed.

(3) Subarray Offset Studies

Prior efforts show that the random offsets produce low losses for reasonable tolerances such as ± 3 cm. On the other hand, systematic errors are expected to be large. The incorporation of

D180-22876-4

the expected offset contours into the array computer program will quantitatively evaluate the effect of systematic offset errors in an accurate manner.

(4) Three Dimensional Pattern Plots

Modify the ground-grid, X, Y coordinate output along with the power density so as to input data to existing Boeing plot routines creating 3D power density contours.

(5) Specific Array Program Development

Streamline the general "Bigmain" computer program by eliminating unwanted design options such as excitation with spherical phase. By doing away with the undesired programming, not only will the run time and output listing time be reduced but clarity of process flow will be increased.

(6) Enhanced Spacetenna Design

Collapsed array design was done for the four legs on the rectangular X and Y coordinates. The design of the four legs on the 45 degree planes could be greatly improved by going through the proper collapsed design procedure with consideration for the four other legs. Leg width and height changes may also be used as design parameters.

(7) Choice of Pattern Cut

Presently only two pattern cuts of the far-field are able to be studied, the principal cuts along the X and Y axes. Incorporating new and modifying existing programming will enable the user to choose parameters so that the program steps through the ground-grid to approximate any pattern cut desired.

(8) Wide Angle Aperture Equations

It is hoped to extend the capability of this program to include wide angles in the subarray aperture equations using the expression in Figure 2-33. This equation is more accurate than the presently employed equation due to the fact that there is no small angle approximation.

2.5 INTER-MODULE PHASE CONTROL CONCEPTS

As part of a small subcontract with the General Electric Co., Electronic Systems Division, Syracuse, N. Y., an initial approach to module phase control was defined by Mr. C. R. Woods. The tasks addressed include (1) phasing concepts and pilot frequency offset considerations; (2) remote phase synchronization; (3) phase multiplication technique to eliminate squint; and (4) diplexer design considerations. This work is summarized below.

A basic approach to transmitter phasing was synthesized. The effect on beam squint of the separation between transmit and received frequencies is analyzed. This effect was shown to be small so that large (100's of MHz) separation can be used if necessary. Concepts for implementing various portions of the system are shown, but no attempt has been made to consolidate them.

$$E(\phi, \theta, X, Y) = \frac{\sin\left(\frac{\pi X}{\lambda} \frac{\sin \theta \cos \phi}{\sqrt{1 - \sin^2 \theta \sin^2 \phi}}\right) \sin\left(\frac{\pi Y}{\lambda} \frac{\sin \theta \sin \phi}{\sqrt{1 - \sin^2 \theta \cos^2 \phi}}\right)}{\frac{\pi^2 XY}{\lambda^2} \frac{\sin^2 \theta \cos \phi \sin \phi}{\sqrt{1 - \sin^2 \theta \sin^2 \phi} \sqrt{1 - \sin^2 \theta \cos^2 \phi}}}$$

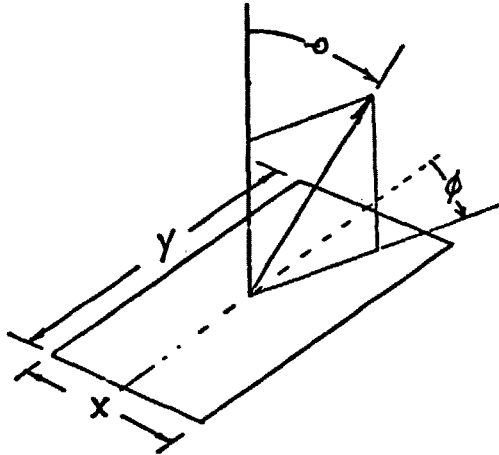


Figure 2-33 Pattern of Rectangular Aperture

The diplexer problem was analyzed, assuming a conventional diplexer. The analysis indicates that the problem can be overcome with relative ease. A Boeing suggested technique of compensating for klystron tube phase variations is also described. Further work is clearly necessary in this area to bring the concepts to a level of detailed subsystem definition.

2.5.1 Phasing Concepts and Pilot Frequency Offset Considerations

It is important that the frequency of the pilot signal transmitted from the ground differ from the frequency transmitted from the satellite by as much as possible. Making this frequency difference largely relaxes the requirements on the diplexer design and also improves the receiver noise figure, thereby requiring less pilot signal power from the ground.

A block diagram of the transmitter phasing concept is shown in Figure 2-34. The phase of the pilot signal transmitted from the ground is $n\omega t$. This is generated from a reference oscillator on the ground. The frequency ω may be chosen to be some convenient value (say around 100 MHz) and the factor n raises the frequency to the S-band region.

The plane of the satellite antenna array is shown, although there is no requirement at all for the array to be planar. A central reference receiver is shown along with two receivers which are used to phase transmitters. These transmitters use the same antennas as are used by the receivers. The phase of reference signals received at the three antennas are $n\omega(t-T_0)$, $n\omega(t-T_1)$ and $n\omega(t-T_2)$, where the path delays are, for example,

$$T_1 = \frac{1}{c} \int_{L_1} k(n\omega) ds$$

and similarly for T_0 and T_2 . The velocity of light is c and $k(n\omega)$ is the refractive index of the ionosphere at the frequency $n\omega$. The integral for the delay T_1 is taken over the path L_1 . Note that, in the absence of the ionosphere, the delay is

$$T_1 = L_1/c$$

The troposphere is neglected since its refractivity is not dependent on frequency.

The receivers all use phase lock techniques so that received phase is maintained. A typical receiver concept is described separately. The central receiver output enters a frequency doubler where the phase is doubled. The output is sent by transmission line to the two subarrays shown. Using round-trip phase compensation techniques, the phase shift in the transmission line can be eliminated, thus the phase at each subarray receiver is $2n\omega(t-T_0)$. A method for compensating transmission line delay is shown in Section 2.5.2.

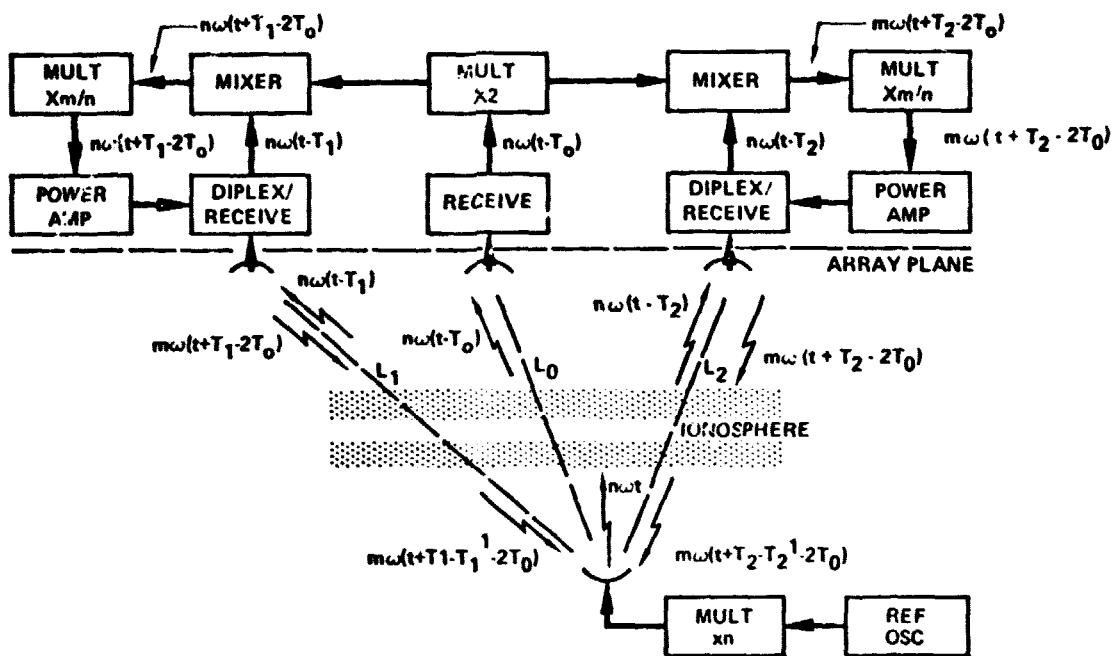


Figure 2-34 Transmitter Phasing Concept

D180-22876-4

Mixers at each subarray produce the outputs with phases $n\omega(t+T_1-2T_0)$ and $n\omega(t+T_2-2T_0)$. These enter a device which multiplies the phase by the factor m/n . This would be done using a phase lock frequency offset method such as the receiver concept described. These methods are well known and maintain phase throughout. The multiplier outputs which are amplified and transmitted are $m\omega(t+T_1-2T_0)$ and $m\omega(t+T_2-2T_0)$.

The phase of signals received at the ground in the vicinity of the pilot transmitter are

$$m\omega(t+T_1-T_1'-2T_0)$$

$$m\omega(t+T_2-T_2'-2T_0)$$

The time delay T_1' is given by

$$T_1' = \frac{1}{c} \int_{L_1} k(m\omega) ds$$

and similarly for T_2' . Note that T_1' is the same as T_1 except that the refractive index in the ionosphere is evaluated at a different frequency ($m\omega$ rather than $n\omega$).

The difference between the phase of the signals on the ground is a measure of the beam squint. This difference is

$$\Delta\phi = m\omega [(T_1-T_1') - (T_2-T_2')] \tag{2.18}$$

Note that in the absence of the ionosphere the delays are equal ($T_1 = T_1'$ and $T_2 = T_2'$) and the phase difference $\Delta\phi = 0$. Thus, in the absence of the ionosphere, there will be no squint regardless of the orientation of the satellite array.

The ionosphere causes $\Delta\phi$ to be different from zero and therefore causes some squint. The squint will depend on the frequency difference ($m\omega - n\omega$) but will be small. This difference will now be computed.

For the frequencies of interest, the refractive index in the ionosphere may be approximated by

$$k(n\omega) \approx 1 - KN'(n\omega)^2$$

where K is a constant, and N is the electron density. Substituting in the expression for the time delay gives, for example

D180-22876-4

$$\begin{aligned} T_1 &= \frac{1}{c} \int_{L_1} [1 - KN/n\omega]^2 ds \\ &= \frac{L_1}{c} - \frac{K}{c(n\omega)^2} \int_{L_1} N ds \end{aligned}$$

Finally, substituting similar values for T_1 , T_2 and T_2' , the phase difference is

$$\Delta\phi = \frac{m\omega k}{c} \left[\frac{1}{(m\omega)^2} - \frac{1}{(n\omega)^2} \right] \left[\int_{L_1} N ds - \int_{L_2} N ds \right] \quad 2.19$$

Note that the error is proportional to both the frequency difference (first term in brackets) and to the difference in the ionosphere on the two paths (second term in brackets).

The displacement of the beam on the ground is approximately

$$d = \frac{h}{b} \frac{c}{m\omega} \Delta\phi$$

where h is the altitude of the satellite and b is the diameter of the satellite array. Substituting $\Delta\phi$ from above

$$d = \frac{hk}{b} \left[\frac{1}{(m\omega)^2} - \frac{1}{(n\omega)^2} \right] \left[\int_{L_1} N ds - \int_{L_2} N ds \right] \quad 2.20$$

Rearranging terms and assuming that $\Delta\omega = (m-n)m\omega = m\omega$ we get

$$\begin{aligned} d &= \frac{2h}{b} \left(\frac{\Delta\omega}{m\omega} \right) \frac{K}{m\omega^2} \left[\int_{L_1} N ds - \int_{L_2} N ds \right] \\ &= \frac{2h}{b} \left(\frac{\Delta\omega}{m\omega} \right) (\Delta L_1 - \Delta L_2) \quad 2.21 \end{aligned}$$

where ΔL_1 and ΔL_2 are the one-way changes in the electrical path lengths on paths L_1 and L_2 caused by the ionosphere at frequency $m\omega$. Using the following values: $h = 3.8 \times 10^7$ m, $b = 1000$ m, and $d = 500$ m (max. allowable), implies

$$\frac{\Delta\omega}{m\omega} (\Delta L_1 - \Delta L_2) < .0066$$

with ΔL_1 and ΔL_2 in meters.

The difference $(\Delta L_1 - \Delta L_2)$ is hard to evaluate. A typical value of ΔL at the frequency of interest is about 2 meters. However, the values on the two paths will tend to be the same, especially since the paths are only separated by about 10 meters in the highest part of the ionosphere and by even less in the lower ionosphere. If the difference is one percent of the value of ΔL_1 or ΔL_2 , the difference will be 0.02 meters. Then the frequency difference can be as large as

$$\begin{aligned}\Delta f &= (2450)(.0066)/.02 \\ &= 809 \text{ MHz}\end{aligned}$$

This result is probably conservative for the normal or even for a disturbed ionosphere. However, if the radiated power perturbs the ionosphere, the result may be different, and no data are available on this aspect of the problem.

2.5.2 Remote Phase Synchronization

A concept for compensation of the delay in the transmission lines between the central receiver and the subarrays or the subarray groups is shown in Figure 2-35 in simplified form. This concept is based on the same principle as that used for transmitter phasing in that it uses signals transmitted in both directions through the transmission line. It is possible to implement the technique using two different frequencies in the transmission line. It is always necessary to bring a control signal from the central point to each subarray. This signal will be at baseband in the approach shown and will be at the difference frequency if two different frequencies are used in the transmission line. In either case, the control action on the voltage controlled oscillator causes the output of the phase detector to null. This causes the condition $T_0 = T_r$ which is equivalent to tracking the central receiver phase with the subarray controlled oscillator.

2.5.3 Phase Multiplication Technique to Eliminate Squint

A concept is shown in simplified form that could be used for the central or subarray group receivers. It could also be used to obtain the frequency offset shown in Figure 2-34. However, accomplishing the frequency offset in the receivers would probably obviate the additional offsets shown.

The concept shown in Figure 2-36 uses two phase locked loops. The first locked oscillator operates at a submultiple of the received frequency, and this loop establishes the receiver bandwidth. The second loop locks an RF oscillator to the first oscillator. The offset is established by the multiplier m and the frequency ω .

2.5.4 Diplexer Design Considerations

The diplexer is shown in Figure 2-37 along with the transmitter and receiver. The problem is that some of the transmitter power, attenuated by a factor L , enters the receiver. Two separate elements of the problem are illustrated in Figure 2-37. One is that the center frequency is coupled through the diplexer at high power. This signal must be further attenuated by a filter preceding the receiver to prevent damage to the receiver input. A bandpass filter is shown, but a low pass or a notch filter would also work.

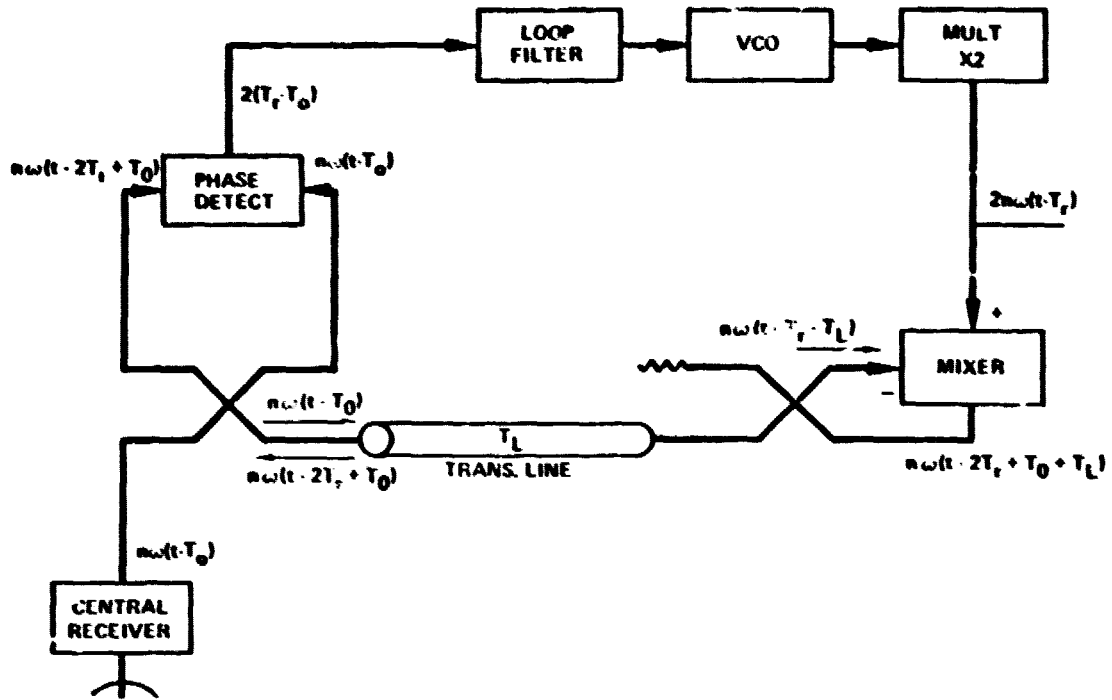


Figure 2-35 Transmission Line Compensation

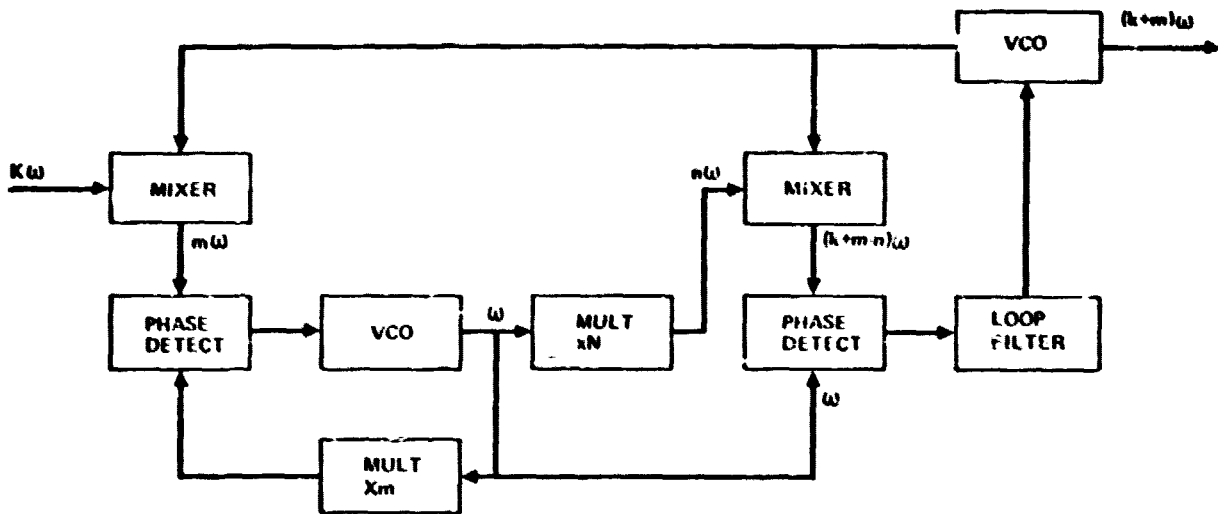


Figure 2-36 Receiver Concept

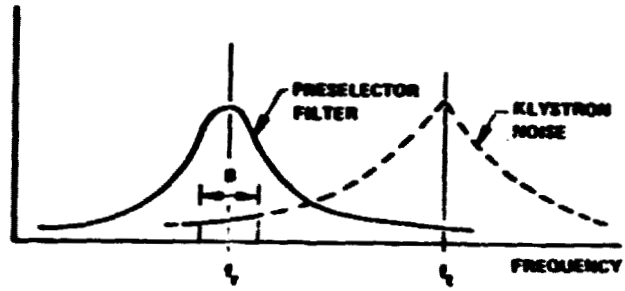
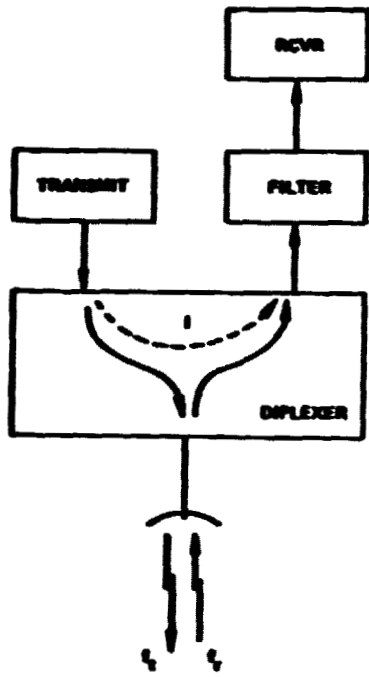


Figure 2-37 The Duplexer Problem

The second element of the problem is that noise sidebands generated in the transmitter also enter the receiver. The sidebands of interest are those which fall in the receiver bandwidth as shown. This noise adds directly to the receiver noise and degrades the sensitivity.

Typical transmit/receive isolation in a diplexer (I) is 30 dB, although better isolation could possibly be achieved in a fixed frequency application such as this one. The power into the receiver first mixer is

$$P_m = P_t / I$$

where P_t is the transmitter power and F is the filter rejection. The transmitter power is 77 dBm and the maximum power allowed in the first mixer is 0 dBm, which is conservative. Therefore, the required filter attenuation is

$$\begin{aligned} F &= 77 - 30 - 0 \\ &= 47 \text{ dB} \end{aligned}$$

It should not be difficult to achieve this rejection, especially if the separation between transmitter and receiver is large. Furthermore, at least 10 dB more power in the receiver could be tolerated without damage.

It should be recognized that the presence of this large signal in the mixer will produce some undesired outputs, and the local oscillator frequency will need to be chosen so that the outputs do not fall in the frequency range of interest.

The AM noise side bands generated by a typical high-power klystron amplifier in a 1 KHz bandwidth and at frequencies far removed from the carriers are about 130 dB below the level of the main carrier. Thus, if the klystron power output is 77 dBm, the noise level will be -53 dBm. This is further reduced by the diplexer isolation (30 dB) to -83 dBm. The equivalent noise in the same 1 KHz bandwidth at the receiver input, assuming a 10 dB receiver noise figure, is -134 dBm. Since the klystron noise is much greater, it is the limiting factor. A received power of -53 dBm is required to assure a 30 dB signal-to-noise ratio which ought to be enough to assure reliable operation. This power can be delivered with, for example, a subarray antenna gain of 20 dB, a transmitter antenna gain of 40 dB and a transmitted power of 79 dBm or about 80 kw.

2.5.5 Klystron Phase Control Circuit

To take care of phase variations in the klystron transmitter tubes, it is proposed to place them in a phase control loop. Such a concept is shown in Figure 2-38 where the conjugated and offset signal is provided by the phase comparator and processor (5) as discussed in the preceding sections. The

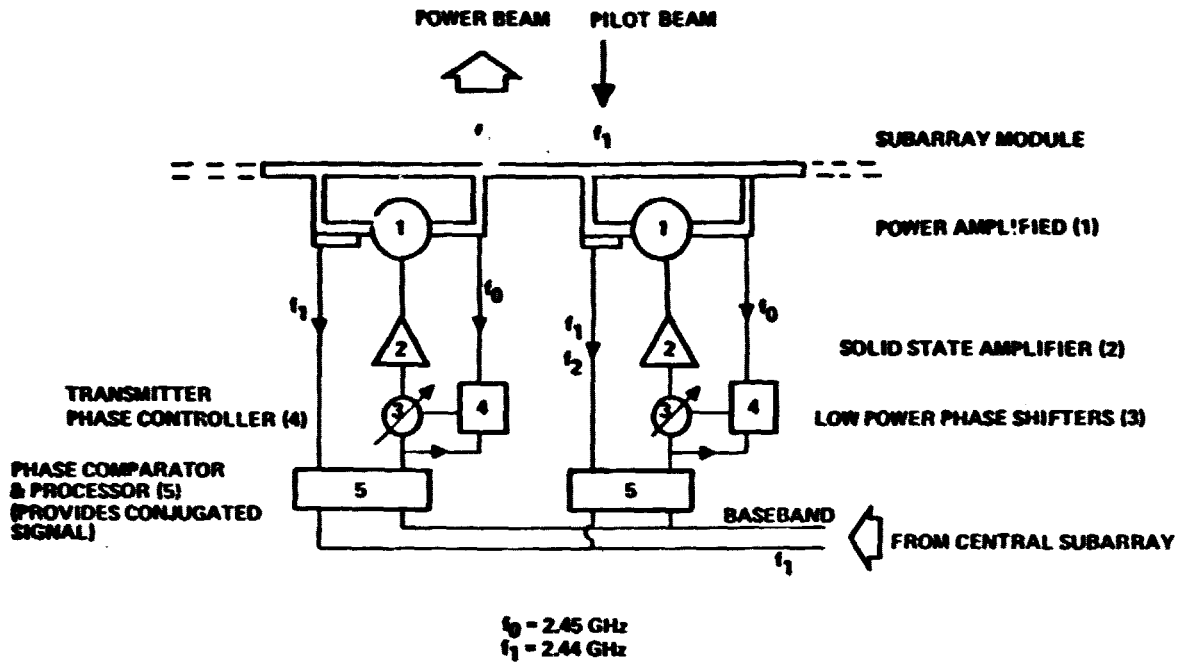


Figure 2-38 Klystron Phase Control Circuit

transmitter signal is sampled and is forced to be in phase with the conjugated signal by the operation of the phase controller (4) on the phase shifter (3).

2.6 RECTENNA DESIGN CONSIDERATIONS AND ALTERNATIVES

2.6.1 Dipole Spacing Requirements

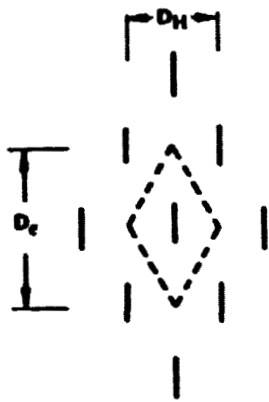
In Section 2.1.2 the effect of the slot spacing that resulted from the quantization of the modules and radiating sticks was investigated. An outcome of this investigation was a tentative conclusion that dipole (square grid) spacings up to 0.8λ could be used, resulting in significant cost savings. In addition, the larger spacings would result in higher diode power levels with associated increased rectification efficiency. The cell area of such a grid would be 96 cm^2 , significantly larger than the Raytheon diamond grid configuration of 50 cm^2 (see Figure 2-39). There is no implication here that square grids are superior, only that larger cell areas may be theoretically possible and practical. It should be noted that dipole spacing and impedance are closely related. Wider spaced elements will result in lower source impedances from which more power may be drawn.

An appropriate approach to answer the question of allowable dipole spacing would be an infinite array analysis. In this approach, edge effects are eliminated and the environment of neighboring dipoles is assumed to extend to infinity in all directions. This is an easier problem to analyze than a finite array. Figure 2-40 is illustrative of the interplay of element spacing (D/λ) and ground plane spacing S/λ on the normalized element gain (the gain per cell area that the element occupies). However, a very small 7×9 element array such as this is highly contaminated with edge effects. The same analysis performed for an infinite array will answer this question.

2.6.2 Flat Groundplane Possibilities

Discussions with NASA personnel have brought out the significance of the cost of the rectenna supporting structure and their interest in the possibility of a flat (horizontal) ground-plane. There appears to be no fundamental reason why such a ground-plane could not be employed. Obviously, a horizontal ground-plane would have to have an element density that was reduced by the cosine of the angle of the arriving ray from the vertical in order to avoid having a larger number of elements than the original array, (see Figure 2-41). The gain, and hence the collecting aperture, of these more widely spaced elements must match, in the θ direction, the peak broadside gain of the reference array elements. Three parameters may be varied to optimize the directional gain of the elements: (1) element spacing, (2) the height above the ground plane and (3) passive reflector.

The element spacing operates on both element impedance and pattern, as does the height above the ground. An example of the latter is a pattern peak at $\theta = 60^\circ$ for $\lambda/2$ ground-plane spacing. The increased spacing available will probably allow the addition of small corner reflectors or fences to

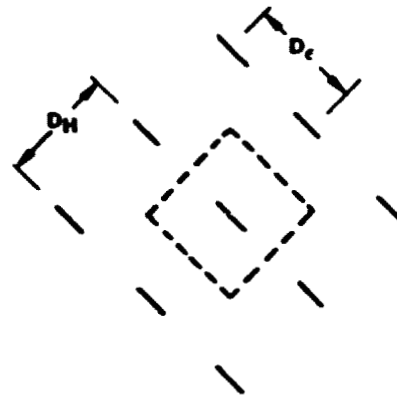


$D_H = .64 \lambda$

$D_c = 1.04 \lambda$

CELL AREA = 50 CM²

OFFSET DIAMOND GRID



$D_H = D_c = .8 \lambda$

CELL AREA = 96 CM²

SQUARE GRID

Figure 2-39 Element Orientation

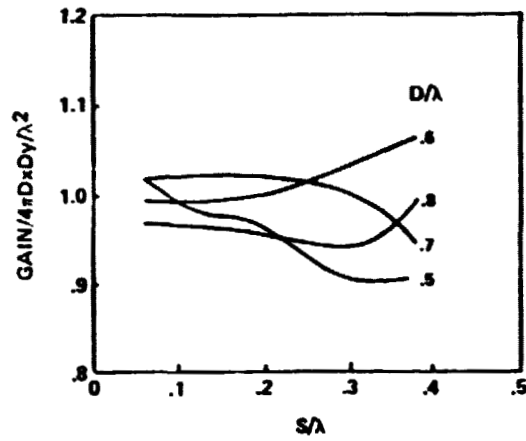


Figure 2-40 Element Gain

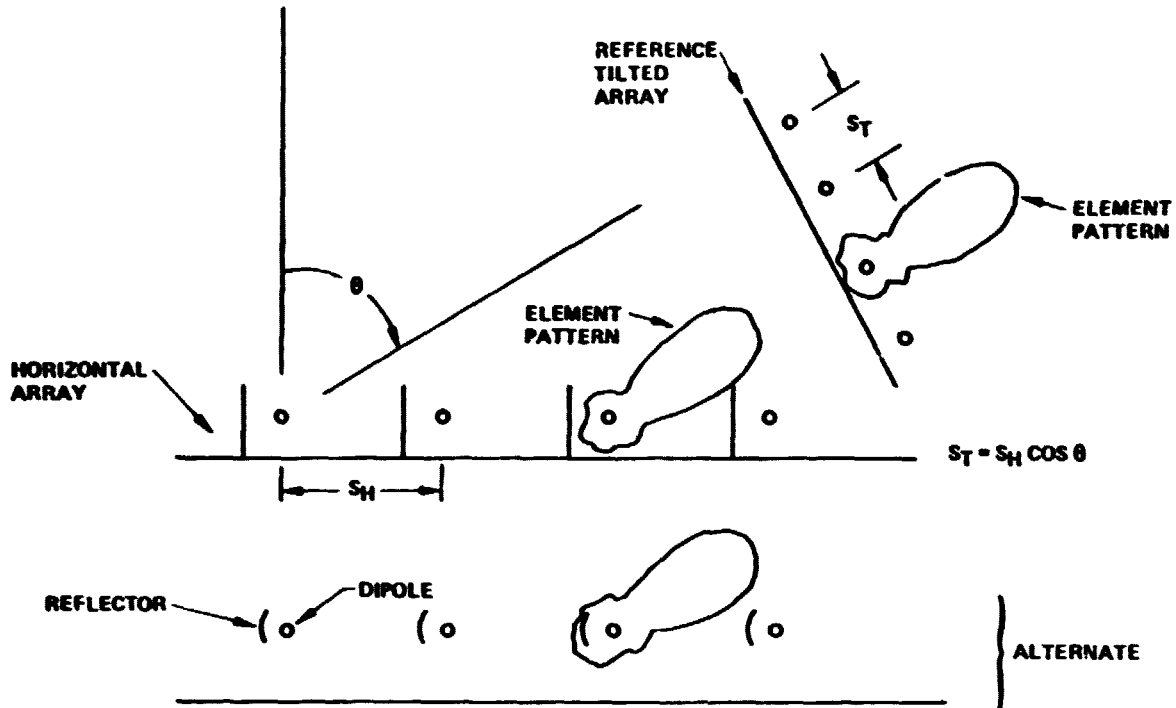


Figure 2-41 Horizontal Rectenna Configuration

suppress the back and enhance the forward lobe. It should thus be possible to build a flat square grid array whose gain in the θ direction is that required for 100% aperture efficiency.

$$G(\theta) = \frac{4\pi S_T^2}{\lambda^2} = \frac{4\pi S_H^2 \cos^2 \theta}{\lambda^2} \quad 2.22$$

This is also the gain provided by a uniform current sheet, even though this sheet is non optimum and has its peak response at broadside, therefore this requirement should be easy to meet since higher gains are achievable with greater complexity. For example, a current sheet with progressive phasing to produce a peak at an arbitrary θ would have a gain:

$$G(\theta) = \frac{4\pi S_H^2 \cos \theta}{\lambda^2}$$

which is greater than the required gain equation 2.22.

2.6.3 "Hogline" High Gain Configuration

A relatively simple high gain antenna, referred to as the "Hogline" antenna, was conceived which has an aperture efficiency of 97%, based on taper loss associated with an $F/D = .25$. It combines the good electromagnetic properties of the combined horn parabola, or hoghorn, with the simplicity and constructional ease of the line fed cylindrical parabola. (See Figure 2-42.) The overlapping characteristics seem well suited to the rectenna application permitting access to the line feeds at ground level, reducing the number of diodes and associated hardware, and allowing operation at high power level and hence high efficiency. The higher power of the diodes and the fact that they are buried deep in a grounded electromagnetic horn would probably make them less vulnerable to damage from the EM fields of the nearby lightning. The horn and reflector could be constructed from the same open wire type of reflecting conductors as previously proposed. The upper size limit would be determined by its directivity and hence the latitude stability of the SPS. The lower size limit would be determined by the diffraction at the edges of the reflector and horn. Further cost and performance trades in this area are recommended.

SPS-1688

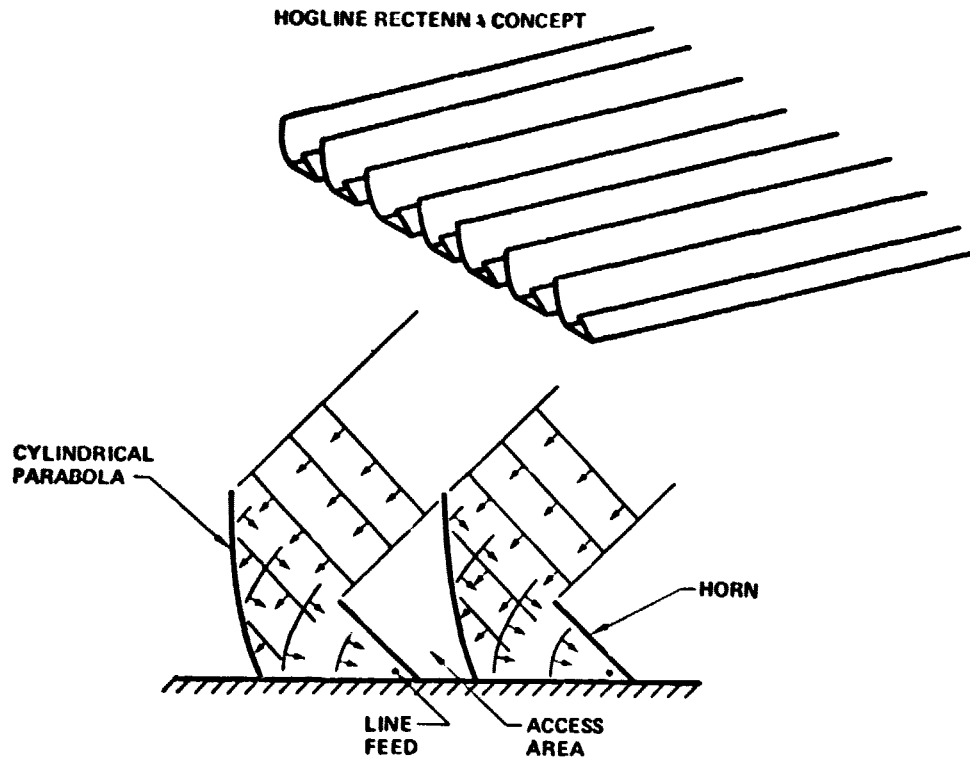


Figure 2-42 Hogline Rectenna

3.0 ALTERNATE CONCEPTS FOR LARGE PHASED ARRAY APPLICATIONS

3.1 INTRODUCTION

The material evolved in this section was conducted on a related Boeing Company IR&D program, except for Section 3.2.4 which was generated under a subcontract with the General Electric Co., Syracuse, New York, and performed by Mr. D. H. Kuhn.

3.1.1 General Requirements

The array aperture is one composed of a family of individual radiators. The pattern characteristics of the array are influenced by the spatial distribution and orientation of the individual radiators and their relative excitation in amplitude and phase. Dynamic control of amplitude and phase gives the array great flexibility in a variety of applications.

Instantaneous beam scanning as well as multiple beam formations are practically attainable with the appropriate excitation network.

Waveguide slot arrays are used in ground and airborne applications for fire control, tracking, weather detection and terminal guidance. Arrays of traveling wave elements, i.e., yagis, helices, log periodics, etc., are used extensively for satellite tracking. Arrays of parabolic structures are employed in the field of radio astronomy. (See Ref. 3.1, 2, 3, 4)

3.1.2 Reference System

A 1 km transmit array together with a 10 dB Gaussian tapered illumination for a 5 GW system was chosen as the model configuration for three reasons: (1) the system operates just below the 23 mw/cm² threshold level expected for nonlinear ionosphere interactions; (2) the power density at the transmit array is at the 21 kw/m² limit due to thermal constraints for the waveguides and transmitters; and (3) a size/cost tradeoff for the rectenna and transmit array has a broad minimum at a 1.0 km array diameter. The specified efficiency of the spaceborne array is 96 percent.

The basic element is a standing wave waveguide slot array as contrasted with the traveling wave array proposed by Raytheon in conjunction with a low-gain high-efficiency amplifier. The klystron has been selected as the baseline microwave tube to provide an alternative design option to the crossed-field amplifier, the amplatron.

3.1.3 Alternate Candidate Selection

The basic requirements of the SPS radiating structure are met in an array of elements which exhibit high-gain and efficient illumination of effective areas. For this reason, omni-directional type radiators were not considered. The candidates considered in this study are:

This work was conducted on a Boeing IR&D program and is included due to its relevance to this contract.

- 3.2.1 Unfurlable Gore-Type Parabolic Array
- 3.2.2 Deployable Parabolic Array
- 3.2.3 Traveling Wave End Fire Array
- 3.2.4 Cylindrical Lens Horn Array
- 3.2.5 Enhanced Element Planar Waveguide Array
- 3.2.6 Horn Array

3.2 ALTERNATE CANDIDATES

3.2.1 Unfurlable Gore-Type Parabolic Array

A candidate element for the paraboloid array is the unfurlable gore prime focus fed parabola (Fig. 3-1). This antenna, when stowed, is lightweight and compact. The qualitative properties are indicated in the table 3.1.

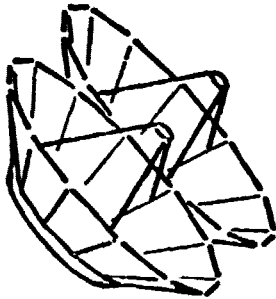


Figure 3-1 Unfurlable Gore Type Parabolic Array

Table 3.1

ADVANTAGES:	<ul style="list-style-type: none"> ● Light weight ● Unfurlable (automatically)
DISADVANTAGES:	<ul style="list-style-type: none"> ● Low aperture illumination efficiency ● Spillover losses ● Blockage losses ● Fabric power limited ● Total aperture not used ● High power density feed

To date models have been constructed for reflectors with diameters in excess of 30 meters. When unfurled, the antenna assumes a pseudo-parabolic shape with metallic ribs covered with metallic mesh. The rib profile is parabolic, but the mesh which is stretched from rib to rib forms a non-parabolic surface. Estimated efficiencies at 3 GHz are given in Table 3.2.

Table 3.2

Factor	Percent
Aperture Illumination Efficiency	75
Spillover Efficiency	85
Polarization Efficiency	98
RMS Surface Error Efficiency	95
Gore Efficiency	79
Blockage Efficiency	97
TOTAL Efficiency of Element	45

This work was conducted on a Boeing IR&D program and is included due to its relevance to this contract.

This value is too low to meet SPS requirements.

Another factor which must be considered in the design of a paraboloid array is packaging. When the circular elements are positioned in close proximity, twenty-one percent of the overall antenna aperture area is unused. This factor is directly proportional to a loss of efficiency for the array. Thus the overall efficiency of such a design would be approximately thirty-six percent. This value is arrived at by multiplying the element efficiency (45 percent) by an 80 percent packing factor.

Because of the low element and packaging efficiency this concept would be difficult to justify in all areas except weight and volume.

The slotted waveguide array for an SPS weighs about 1.66×10^6 kg whereas the mesh reflector array is estimated to weigh 1×10^4 kg, a factor of 100 or more lower. The degree to which the efficiency degradation is offset by weight saving for a specific application must be determined for each case separately.

3.2.2 Deployable Parabolic Array

The description of the deployable parabolic array is much the same as that given for the gored paraboloid, except that the individual radiating surfaces are perfect parabolas. The general qualities are given in the table (see Figure 3-2): (Ref 3.6)

Table 3.3

ADVANTAGES:	<ul style="list-style-type: none">● Light weight● Unfurlable (automatically)● High illumination efficiency● Polarization diversity
DISADVANTAGES:	<ul style="list-style-type: none">● Some blockage loss (~3%)● Low efficiency aperture (22% of available aperture area not used)● High power density feed

The configurations consist of a series of metallic ribs across which a mesh is stretched and tied. Each tie point is adjusted until the mesh formed approaches a parabolic surface. With present state of art, the rms surface error is approximately .030". Analysis of the attainable element efficiencies is tabulated below:

This work was conducted on a Boeing IR&D program and is included due to its relevance to this contract.



Figure 3-2 Deployable Parabolic Array

This work was conducted on a Boeing IR&D program and is included due to its relevance to this contract.

Table 3.4

Factor	Percent
Aperture Illumination Efficiency	98
Spillover Efficiency	99
Polarization Efficiency	97
RMS Surface Error Efficiency	95
Blockage Efficiency	97
TOTAL Efficiency of Element	86.7

This array concept suffers from the same drawbacks as the gored paraboloid array in that the total available aperture area is not used. Thus, the overall efficiency of the array is the product of the element efficiency and the array aperture efficiency. This product is approximately 60 percent.

3.2.3 Traveling Wave End Fire Array

An attractive concept from the thermal and structural point of view is an array of end fire (traveling wave) elements. One promising version of such an array previously analyzed (Ref. 3.1, 9, 10, 11) is the so called "cigar" antenna (Figure 3-3). Because of its symmetry, it can provide polarization diversity, i.e., the element can be adapted to systems using RHCP, LHCP or two orthogonal linear polarizations. Element spacing will be on the order of three wavelengths.

The antenna consists of a metallic rod with metallic disks spaced periodically along its length. The disked rod is excited by a circular or square piece of open-ended waveguide. This arrangement is especially suited to high-power applications.

The cigar antenna has been built and tested by The Boeing Co. and a sample radiation pattern is included (Figure 3-4). This element pattern exhibits a beamwidth of 17 degrees and side lobe levels on the order of -20 db. Using this element pattern, a computer simulation was made of a 6-element subarray. This concept opens the door to the possibility of invoking the Hansen-Woodyard conditions and obtaining additional directivity (gain) for each element (see Figure 3-5).

Figure 3-4 is a measured element pattern of a cigar radiator 10λ long. The beamwidth is 17° and the side lobe level is approximately 30 db down from the peak. Using this measured pattern, a sample array pattern was calculated for a 3λ element separation (Figure 3-5). This is only a sample calculation and more work will be required to optimize the element spacing.

The beam of an endfire array can be scanned beyond endfire causing the "visible" portion of the beam to have a steeper average slope, and giving rise to an increase in directivity (5.6 db higher than the conventional uniformly excited array). The general properties are summarized in the table below:

This work was conducted on a Boeing IR&D program and is included due to its relevance to this contract

D180-22876-4

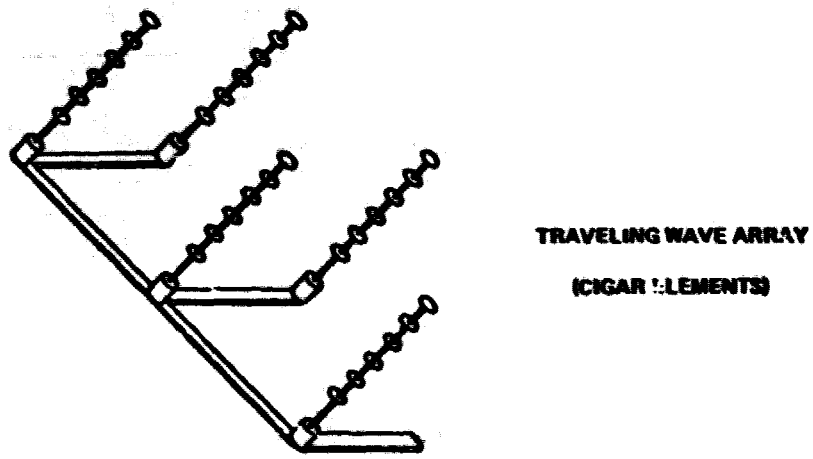


Figure 3-3 Traveling Wave End Fire Array

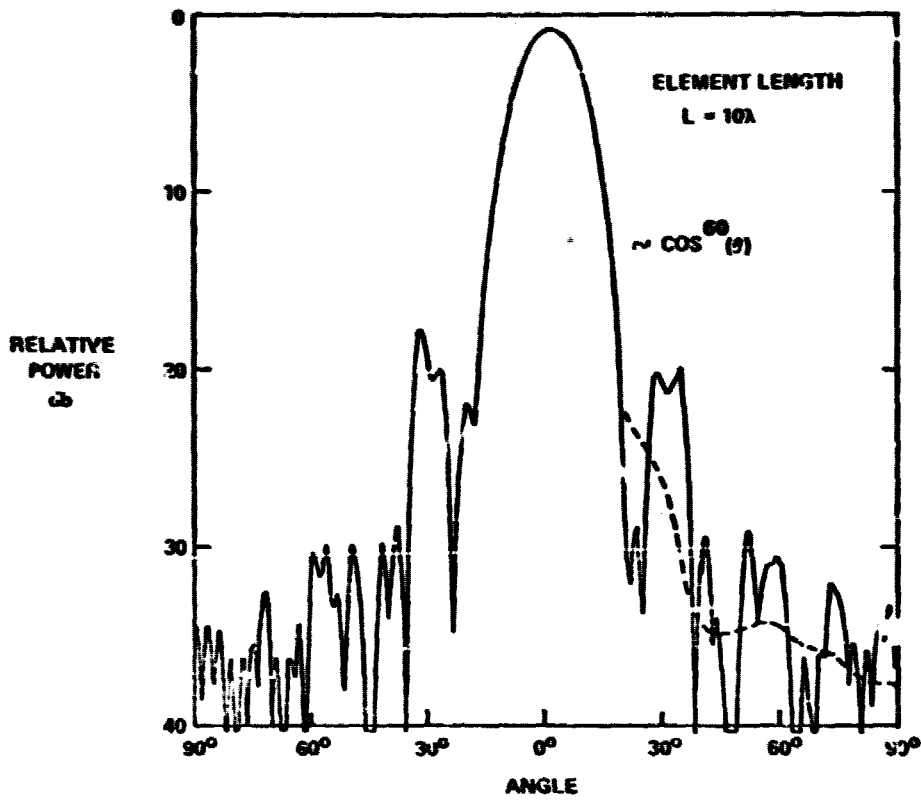


Figure 3-4 End Fire Element Pattern

This work was conducted on a Boeing IR&D program and is included due to its relevance to this contract.

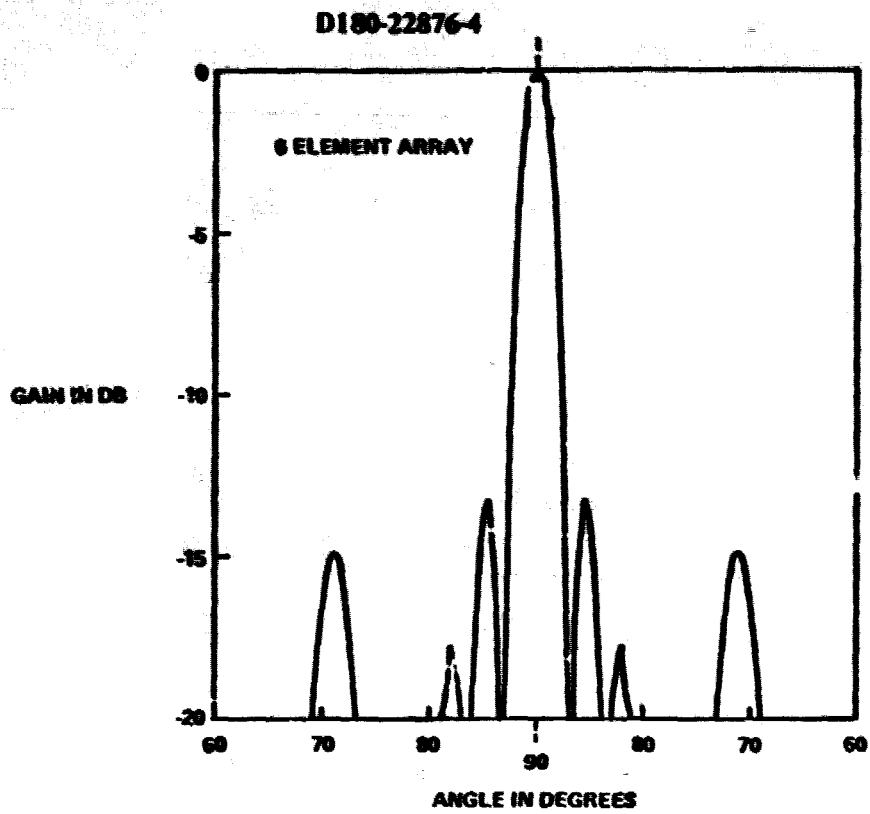


Figure 3-5 End Fire Array Pattern for 3λ Spacing

This work was conducted on a Boeing IR&D program and is included due to its relevance to this contract.

D180-22876-4

ADVANTAGES:

- Open structure (thermal)
- Polarization diversity/control
- High efficiency (super gain)

DISADVANTAGES:

Structural unknowns

Thermally it is also a promising candidate, because it provides an open structure that can radiate excess heat in all directions. (Ref. 3.10)

Figure 3-6 generates curves helpful in the design of endfire arrays. Element gain is plotted as a function of element length for various spacings. Calculations assume an infinite array of endfire elements. For small spacings, it can be seen that the gain of an individual element is limited due to array mutual coupling effects. As the spacing is increased the mutual coupling decreases and the gain rises in a linear fashion.

3.2.4 Cylindrical Lens Horn Array

This section represents material generated by Mr. D. H. Kuhn of the General Electric Co., Syracuse, NY.

3.2.4.1 Subarray Configuration Suitable for the SPS Design

A typical subarray configuration is shown in Figure 3-7 with general characteristics summarized below:

ADVANTAGES:

- High efficiency 97.6%

DISADVANTAGES:

- Occupies increased volume
- Weight
- Increased complexity

The subarray size has been chosen at 10 meters by 10 meters as being small enough to not require active subarray adjustment devices. The subarray consists of 5 cylindrical lenses each 10m by 2m as illustrated. The use of multiple lenses rather than a single lens to cover the entire 10m x 10m subarray has several advantages:

- It allows the RF power sources to be distributed over the subarray for better heat radiation.
- The thickness of the lens region is much less, permitting the lens to be unzoned, thus avoiding the losses associated with zoning.
- Dimensions of material parts is reduced, thereby easing the problems of transportation and construction.

D180-22876-4

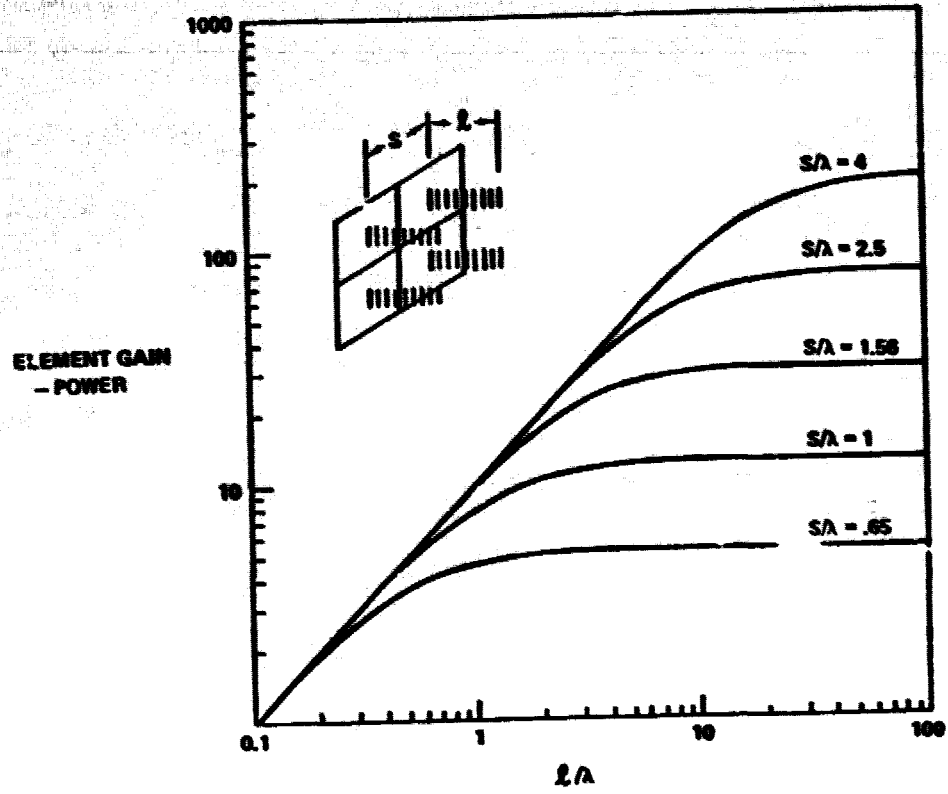


Figure 3-6 End Fire Element Design

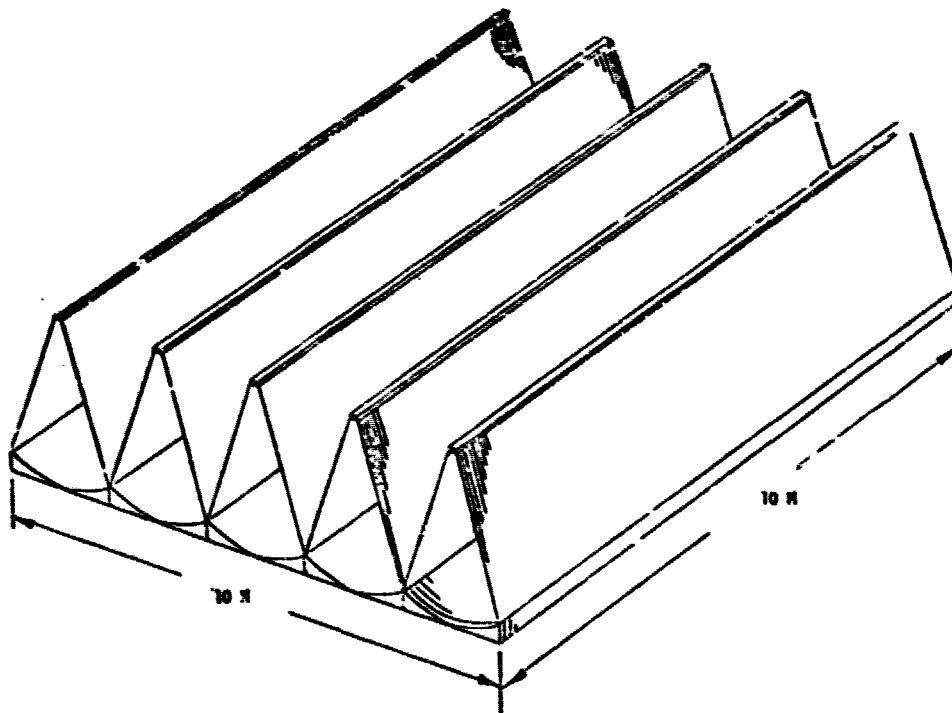


Figure 3-7 Candidate Lens Subarray

RF power may be fed into the subarray in a number of ways. At the center of the SPS array a total subarray power of 2500 kW would be typical. This could be furnished, for example, by 40 klystrons each having a power capability of 62.5 kW or greater. This tube complement can be accommodated by locating 8 klystrons on the waveguide feed of each lens, spacing them at 1.25m intervals and coupling directly into the feed waveguide. As the power level is reduced for the subarrays removed from the center of the array, the number of tubes can be reduced. When it is desired to use less than 5 tubes, a cross guide can be added, coupling to the 5 lens feed guides. The power tubes can then be mounted on the cross guide which distributes their power to the 5 lenses. The lens feed guides and the cross guide would both be resonant arrays, so that the power distribution from the cross guide to the lens guides, and from the lens guides to the radiating slots is equal to all ports, thus providing a uniform excitation of the radiating slots over the entire subarray.

3.2.4.2 Lens Design

A possible lens design is shown in Figure 3-9. The lens consists of a waveguide feed which has longitudinal slots in the broad wall, providing uniform power excitation along the axis of the lens, with polarization perpendicular to the axis. The radiation from the waveguides is guided to the lens by a flared horn. This maintains a cylindrical wave to the lens surface, insuring a uniform power distribution on the lens and avoiding spillover losses. Thus, the structure is really a cylindrical lens corrected horn

A flare angle of 40° is used in the horn section, which results in an F/D ratio of 1.59. This has been chosen to maintain the thickness of the lens section reasonably low, permitting the lens to be unzoned, and thus avoiding the shadowing and diffraction losses which occur in zoned lenses. The lens itself consists of a series of thin plates with a separation of 3 inches, resulting in an index of refraction of 0.6 for the lens. The flared horn sides could be constructed by several alternative methods, such as a wire grid, by panels of structural foam panels, lightly metallized on one side, or by plastic sheets with embedded conductors. If plastic materials are used, they must, of course, be able to survive long periods of time in the space environment.

The recommended solution is a structural foam panel with stiffening ribs and with a thin coat of conductor on the interior surface, as illustrated in Figure 3-8.

One of the important considerations is the reflection of energy at the lens surface. Several design alternatives were considered, such as using a low index of refraction to minimize reflections. It became obvious, however, that the reflection loss could only be reduced to acceptable levels if the lens is matched. It is suggested that the lens be matched by metallic irises at each surface of the lens as illustrated in Figure 3-9. This complicates the construction of the lens plates, but appears to be necessary. Since the lens is desired for a single frequency and is not scanned, it should be able to obtain a good match. For the purposes of estimating losses, it has been assumed that the flat surface is matched to a VSWR of 1.10:1 and that the curved surface is matched to a VSWR of 1.15:1. These are believed to be conservative estimates.

D180-22876-4

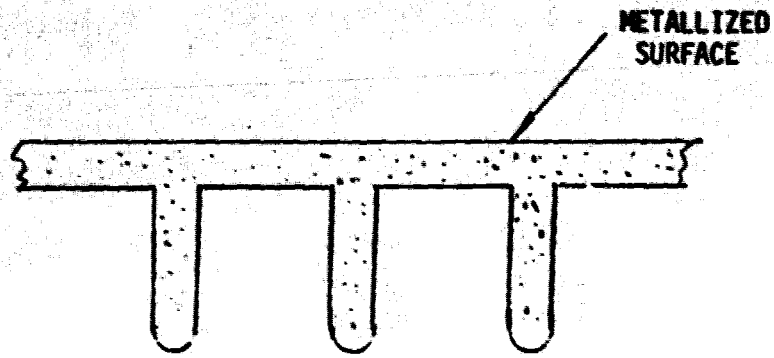


Figure 3-8 Structural Foam Panel Construction

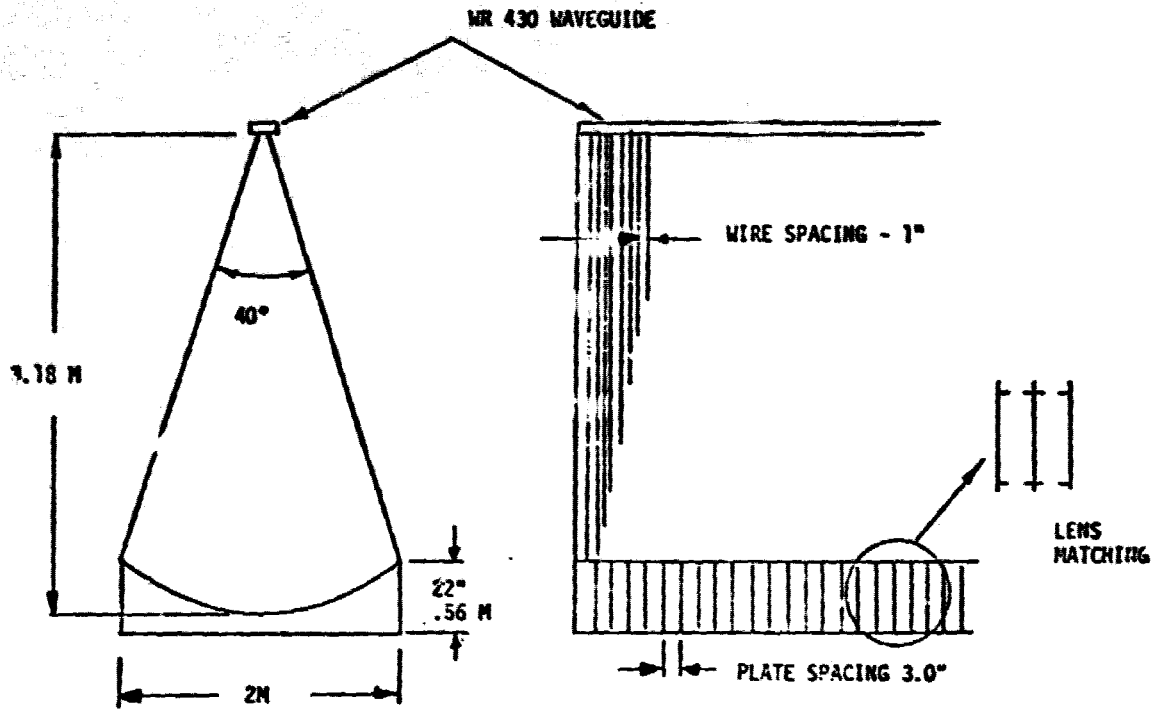


Figure 3-9 Lens Configuration

3.2.4.3 Lens Losses and Efficiency

An estimate of the losses in the lens has been made and tabulated in Table 3.5.

a. Waveguide Attenuation

The losses due to waveguide attenuation varies, depending upon the number of tubes feeding the lens waveguide feed, from a maximum of .0083 for a single feed to a minimum of .0020 for the case of 8 tubes feeding the waveguide. An estimate of .0036 has been made for the total loss averaged over the entire antenna. Aluminum WR-430 waveguide having a loss of .331 dB per 100 ft has been used in this calculation. These computations include the effects of the standing wave in the resonant array.

b. Horn Wall Attenuation

The estimate of the horn wall losses have assumed Al conducting sheets having resistances of .0161 ohms per square, which is a rather poor conditioning surface.

c. Lens Reflections

The lens reflections have been estimated assuming VSWR's of 1.1 and 1.15 can be achieved on the flat and curved surfaces, respectively. Effects of multiple reflections in the lens have been neglected.

d. Lens Attenuation

This loss is due to attenuation of the wave propagating through the lens plate region. Aluminum plates have been assumed.

e. Phase Errors—Lens Plate Spacing

Variations in lens plate spacing causes aperture phase errors and results in energy loss due to imperfect collimation. The loss shown results from an rms phase error of 3.14° , corresponding to errors distributed between $\pm 5.4^\circ$. This results in lens plate tolerances of $\pm .041$ in at the center of the lens of $\pm .009$ in at the edge of the array. Tighter control at the edge of the lens is required due to the greater thickness of the lens at this location. Of course, tradeoffs more favorable on errors may be made once actual error distributions relating to a given construction technique are known.

f. Phase Errors—Waveguide Displacement

Phase errors are also caused if the feed waveguides are not in a perfect plane. The loss given in Table 3.5 for this item corresponds to a tolerance of $\pm .094$ in the displacement of the waveguides. The total lens losses of .0232 or 2.36% are consistent with efficiency goals for the beamforming system of the SPS system. This figure is based upon achieving the tolerances of Table 3.6 and the assumed degree of lens surface matching. These losses do not include that due to misalignment of the overall subarray.

Table 3.5 Lens Losses and Efficiency

FRACTION LOSSES IN LENS

Waveguide Attenuation	.0036
Horn Wall Attenuation	.0057
Lens Reflections (2 Surfaces)	.0071
Lens Attenuation	.0008
Phase Errors - Lens Plate Spacing Tolerances	.0030
Phase Errors - Waveguide Displacement	<u>.0030</u>
TOTAL LENS LOSSES	.0232

Table 3.6 Important Lens Tolerances

Lens Plate Spacing	<u>±</u> .041" at lens center
	<u>±</u> .009" at lens edge
Out of Plane Tolerance on Waveguides	<u>±</u> .094"

3.2.4.4 Construction Tolerances

The critical areas where tolerance must be controlled in the lens antenna is in the feed waveguides, which must be kept aligned in a plane, and in the spacing of the lens plates.

Other physical relationships, such as the tilt of the lens with respect to the feed guides are relatively unimportant.

The tolerance in spacing of the lens plates can be maintained by transverse plates, resulting in an "egg crate" structure. This would have negligible effect on the electromagnetic performance if the transverse plates are thin.

3.2.4.5 Zoning Considerations

Zoning of the lens has been investigated as a possible means of reducing the depth of the lens and, hence, its mass. Figure 3-10 illustrates three methods of zoning. The examples shown in Figure 3-10a and 3-10b illustrate zoning on the refractive surface, resulting in shadowing or energy not properly collimated. This, of course, results either in loss of gain exhibited by higher sidelobe energy or in the scattering of incident energy into uncollimated energy. The type of zoning shown in Figure 3-10 is on a non-refracting surface and does not result in shadowing. S. B. Cohn suggests that, in a cylindrical lens such as is being considered, the edge of the step can be covered with a conducting strip as illustrated in Figure 6c in order to prevent undesirable interaction between waves internal and external to the volume of the lens. This surface is perpendicular to the E-field and, hence, the strip represents an E-plane bifurcation, and presents no impediment to the wave. These steps will also serve to increase the structural rigidity of the lens, and help in manufacturing the required spacing of the lens plates within tolerance.

In the present lens design, zoning is not possible because the increase in the lens depth from center to edge (7.6 inches) is less than one guide wavelength (8.04 inches). Thus, no decrease in mass is possible. For a shorter focal length lens, or a wider aperture, zoning could probably be used to advantage.

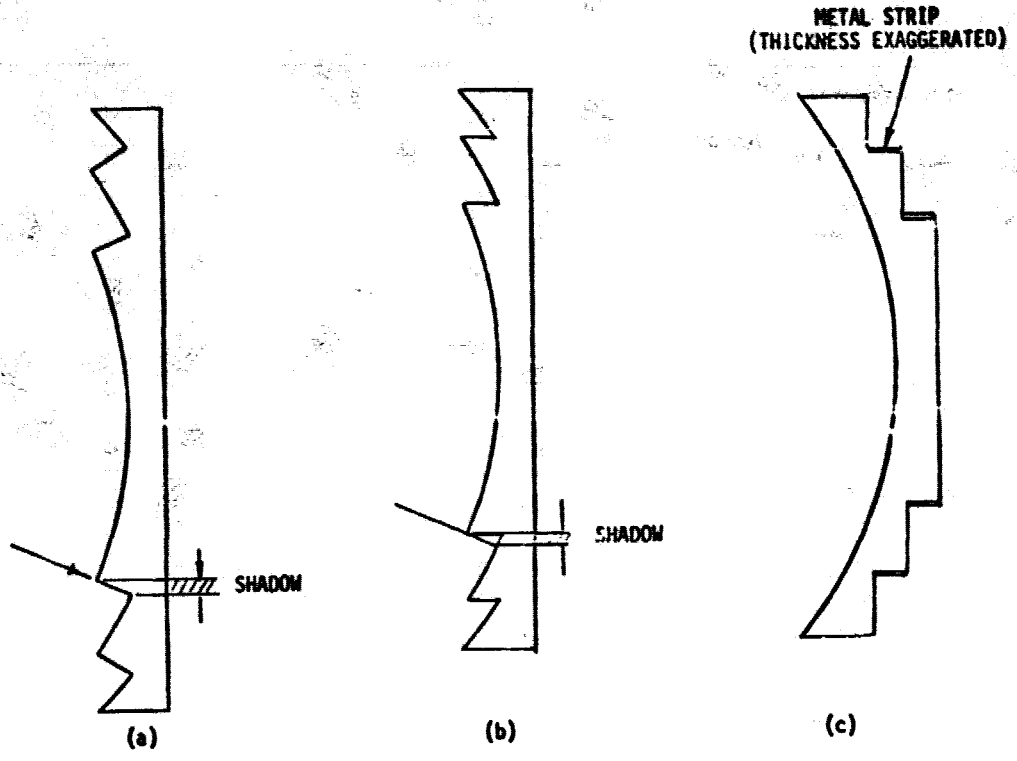


Figure 3-10 Zoning Alternatives

3.2.4.6 Weight Estimation

The weight of the 2m x 10m lens has been estimated with certain assumptions as noted:

Item	Pounds	Kg
1. Waveguide 20 meters long WR430 guide with 0.010 in aluminum walls	4.95	2.25
2. Horn walls Based on Fig 1.5 lbs/ft ³ density Foam - avg. thickness = .5 inch	37.5	17.0
3. Lens plates Avg. height = 7 inches 2 m width Thickness = .01 inches No. of plates = 131	74.5	33.8
4. Matching strips	20	9.1
5. Support structure	<u>42.2</u>	<u>19.1</u>
Total (2m x 10m)	179.1	81.3 Kg
Total wt for 10m x 10m subarray	895#	406 Kg
Wt/square meter	8.95#/m ²	4.06 Kg/m ²

This weight is estimated to exceed that of a slotted waveguide array using by a factor of at least 3:1.

In considering the weight distribution, it is noted that the greatest weight contributors are the lens plates, the support structure and the horn walls, in that order. Although some economics in weight can possibly be made, it does not appear possible to make the reductions needed to match the weight of the slotted waveguide configuration.

3.2.5 Enhanced Element Planar Waveguide Array

The planar waveguide slot array is an excellent candidate for the basic radiating element because of its inherent high radiation efficiency. In the case of the standing wave slot array, uniform aperture illumination is obtained by adjusting the conductance of each slot to be the same value with the total susceptance equal to that of the feeding waveguide. (Ref. 3.5)

This work was conducted on a Boeing IR&D program and is included due to its relevance to this contract.

D180-22876-4

The gain (efficiency) of the array can be further enhanced through the use of the "pseudo" slot dipole radiating element (see Figure 3-11). This element uses parasitic monopole/dipole radiators (see Figure 3-12) in conjunction with the conventional slot. In so doing, the E plane mutual coupling between elements is dramatically reduced. The introduction of these parasites equalizes the E and H plane patterns of the discrete element and eliminates the back lobe in its radiation pattern.

These factors compensate for edge effects and decrease the beamwidth of the composite array, resulting in increased gain. The general properties are summarized in the table below:

ADVANTAGES:	<ul style="list-style-type: none">● High efficiency (~99%)● High pass structure reduces RFI
DISADVANTAGES:	<ul style="list-style-type: none">● Increased weight● Thermal dissipation● Complexity of construction
REMARKS:	Slot Dipole Configuration <ul style="list-style-type: none">● Reduces mutual coupling● Reduces back lobe● Equalizes E & H planes

This design is desirable due to the very high efficiency, the power handling capability of the basic waveguide and the relative ease of fabrication. This concept is well understood and is in wide use for a variety of applications.

Experimental results (Ref. 3.5) for a small slot array, i.e., 60 slots, indicates an improvement in radiating efficiency of approximately 10 percent. In this small array the pattern improvement is a result of the partial elimination of edge effects. This type of element will improve performance of the subarray by eliminating back lobes due to edge effects.

3.2.6 Horn Array

A proposed configuration is an array of conventional pyramidal horns (see Figure 3-13). This concept is attractive from a weight standpoint when the horns are constructed of a mesh. Unlike the cylindrical lens, this concept uses uncompensated pyramidal horns. This idea is less attractive because of the amplitude and phase taper required in the individual horn radiators.

The gain of the ideal aperture is given as $G=4\pi A/\lambda^2$ where A is the aperture area. Southworth (Ref. 3.2) calculates the gain of a $10.5\lambda^2$ pyramidal horn aperture at 18 db. Applying the gain formula for an ideal radiator with this aperture results in a value of 21.2 db. This value is 3.2 db higher than the gain obtainable from a practical pyramidal horn.

This work was conducted on a Boeing IR&D program and is included due to its relevance to this contract.

D180-22876-4

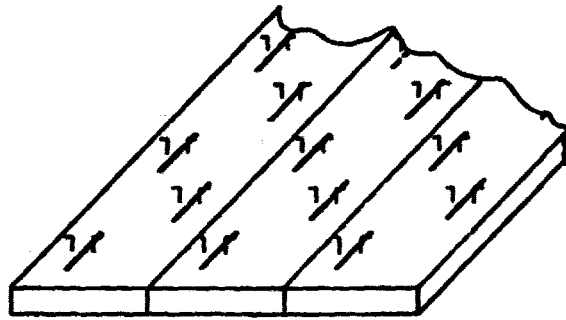


Figure 3-11 Enhanced Element Planar Wave Guide Array

SLOT-DIPOLE

- EQUALIZES E & H PLANE PATTERNS
- REDUCES MUTUAL COUPLING
- REDUCED BACK LOBE

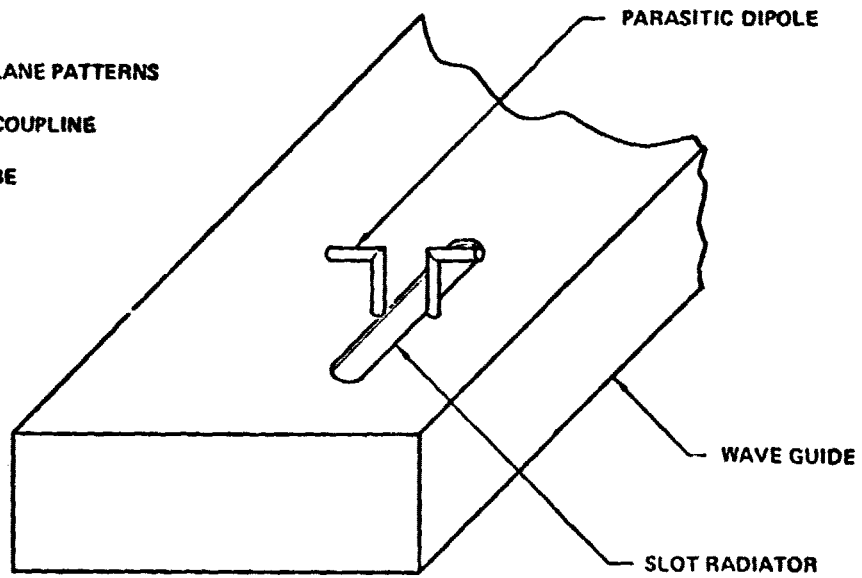


Figure 3-12 Slot-Dipole Element

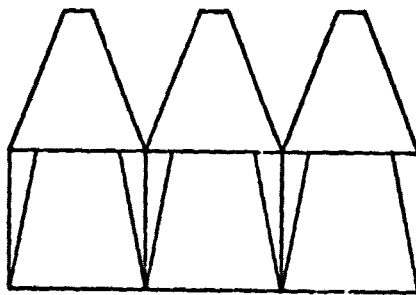


Figure 3-13 Horn Array

This work was conducted on a Boeing IR&D program and is included due to its relevance to this contract.

A horn aperture therefore has an efficiency factor of 44 percent. This low efficiency factor is a multiplier for the overall array aperture efficiency and is unacceptably low for the SPS application. The properties of this array are again summarized below:

- | | |
|-----------------------|---|
| ADVANTAGES: | <ul style="list-style-type: none">● Light weight when constructed of mesh● Good lens efficiency \cong 90% |
| DISADVANTAGES: | <ul style="list-style-type: none">● Low efficiency (44%) with no phase compensation |

The efficiency of the horn aperture can be improved through the use of a lens as shown in Figure 3-14. As indicated, the lens is zoned to conserve space and weight. The efficiency of this arrangement is estimated at about 90 percent.

3.3 DISCUSSION OF RESULTS

Arrays of conventional circular parabolic radiators, although efficient from element to element, suffer a 20 percent overall degradation due to packaging geometry. This fact effectively eliminates the parabolic concept.

The cylindrical lens horn array exhibits high efficiency, however, weight and complex assembly procedures are drawbacks. At present these problems are being addressed and a new design is evolving.

The array of endfire traveling wave elements is a promising concept from a thermal environment point of view. Its elements, spaced approximately two feet apart, provide a transparent open structure for thermal radiation. At present, no comparative weight estimate is available.

Serious consideration must be given to the use of enhanced slot elements in the planar slot array to eliminate efficiency loss due to edge effects.

Table 3.7 is an attempt to summarize and apply a relative weighting factor to the pertinent characteristics of each class of antennas considered. The slotted waveguide array, because of its compatibility in all categories, is considered the first choice in element selection.

This work was conducted on a Boeing IR&D program and is included due to its relevance to this contract.

SPS 003

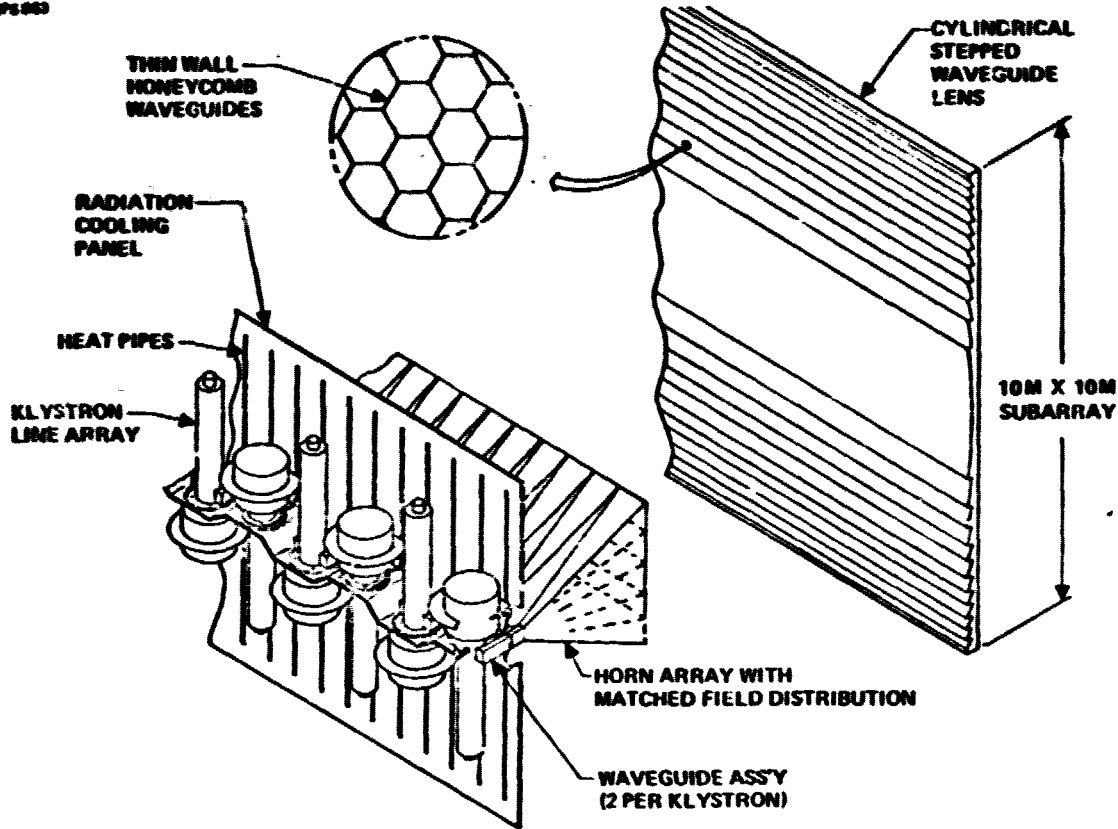


Figure 3-14 Space Fed Stepped Cylindrical Lens

Table 3.7 Configuration Trade Chart

FACTOR	SLOTTED WAVEGUIDE ARRAY	CYLINDRICAL LENS	END-FIRE ARRAY	PARABOLOID ARRAY
ESTIMATED ELEMENT EFFICIENCY*	96-97% CONVENTIONAL 9% ENHANCED	97.6%	98%	60%
WEIGHT	MODERATE	MODERATE (WIRE GRID)	MODERATE	LIGHT (MESH)
MANUFACTURING COMPLEXITY	STRAIGHT FORWARD ASSEMBLY	COMPLEX STRUCTURAL INTEGRATION	MODERATE	MODERATE
THERMAL/POWER COMPATIBILITY	MODERATE (CLOSED STRUCTURE)	MODERATE	GOOD (OPEN STRUCTURE)	GOOD (OPEN STRUCTURE)
R.F./STRUCTURAL COMPATIBILITY	GOOD	GOOD	GOOD	MARGINAL FEED POWER HANDLING CAPABILITY
RISK FACTOR (R&D REQUIRED)	WELL UNDERSTOOD	WELL UNDERSTOOD	COUPLING NEEDS INVESTIGATION	WELL UNDERSTOOD

*DECREASE IN OVERALL EFFICIENCY DUE TO ELEMENT PERFORMANCE.

This work was conducted on a Boeing IR&D program and is included due to its relevance to this contract.

4.0 HIGH POWER TRANSMITTER

4.1 INTRODUCTION

The rf transmitter approach has been to consider high power klystrons to at least the same level of depth as has been done in previous NASA studies for the crossed-field amplifier. This by no means implies that the reference klystron design is the preferred solution; merely that such a transmitter can be integrated into the overall antenna array design and that it does have certain desirable features. The ultimate choice will have to be made on basis of demonstrated performance assessment of both types of devices, particularly in terms of life, efficiency, spurious radiation, ease of integration and replacement, and specific weight.

The reference design approach for the klystron had as its objective high efficiency (>80%) at a reasonable voltage (>40 kV); our discussions with various tube manufacturers have led us to a design with the parameters as given in Table 4.1. These parameters do not result in the lowest specific weight and cost klystron (see trade study, Section 4.5) but provide a baseline on which to establish a reference design.

4.2 ALTERNATE RF SOURCES

Although not within the scope of this study, it is of importance to maintain an awareness of alternate rf sources. Since in the anticipated SPS time scale, state of art advances could occur requiring a review of the current approach. Environmental issues such as noise, X-ray level, and maintainability could preclude the selection of what previously had been reviewed as the most cost effective candidate.

4.2.1 The Amplitron (Ref. 4.12c)

Raytheon, the originator of the amplitron, lists the critical development items as (1) obtaining 85% efficiency with a pure metal cold cathode in a passively cooled system; (2) cold cathode starting with r.f. drive of 1 kW; (3) noise level meeting RFI requirements; and (4) compatibility of passive cooling with r.f. design criteria. Additional factors include (5) overall systems impact of series connection of many amplitrons in the traveling wave array, and (6) systems impact of a low gain amplifier on control circuit complexity. The comparing of specific weights and costs alone are not adequate and should include all aspects of the rf chain including control circuits, phase shifters, required filtering, protective circuits, etc. It is hoped to perform such a trade study in follow-on work. It will also be of interest to see how well the injection-locked magnetron performs in proposed array tests at JPL, and whether it could develop into a potential candidate r.f. source. Some aspects of klystron and amplitron operation are compared in Table 4.2, indicating several factors not covered in previous studies.

Table 4-1 Reference Klystron Design Criteria

POWER LEVEL	70.6 KW	BASED ON A PERVEANCE OF $S = 0.25 \times 10^{-6} = I_p/V_0^{3/2}$ AS DETERMINED TO MAINTAIN HIGH EFFICIENCY @ MAX. VOLTAGE OF 42.1 Kv.
COLLECTOR	5-SEGMENT DEPRESSED COLLECTOR	BASED ON EXPERIMENTAL RESULTS ON COLLECTOR RECOVERY OF $\approx 1\%$, OBTAINED BY UTILIZING AS SMALL REFOCUSING COIL IN THE COLLECTOR SECTION.
RF DESIGN	SINGLE 2ND HARMONIC BUNCHING SIX CAVITY DESIGN	A DESIGN OPTION RESULTING IN HIGH BASIC EFFICIENCY IN A COMPACT DRIFT TUBE CONFIGURATION. TO OBTAIN A GAIN ABOUT 40 db, RESULTING IN A SOLID STATE DRIVER FEASIBILITY AND LOW POWER PHASE SHIFT REQUIREMENTS (< 10 WATTS)
FOCUSING	SOLENOID (REF.) PM/PPM (FUTURE)	TO OBTAIN HIGH EFFICIENCY WITH A LOW RISK APPROACH. IF IN THE PROCESS OF SPS DEVELOPMENT, A HIGH POWER SAMARIUM-COBALT PM/PPM DESIGN CAN BE PROVEN WITH GOOD EFFICIENCY, IT SHOULD BE CONSIDERED.
THERMAL DESIGN	HEAT PIPE WITH PASSIVE RADIATORS	TO OBTAIN THE DESIRED CW LEVEL WITH CONSERVATIVE HEAT DISSIPATION RATINGS.
AUXILIARY PROTECTION	MODULATING ANODE	TO PROVIDE RAPID PROTECTION SHUT OFF CAPABILITY AT THE INDIVIDUAL TUBE LEVEL, HOPEFULLY OBTAINING THE NEED FOR CROW-BAR TYPE OF TURN-OFF.
CATHODE	COATED POWDER OR METAL MATRIX MEDIUM CONVERGENCE	TO OBTAIN A CATHODE EMISSION OF $< 200 \text{ ma/cm}^2$ TO OBTAIN 30 YEAR LIFE TO EMISSION WEAROUT.
POWER EXTRACTION	2-PORT OUTPUT	RESULTING IN RATING 35KW CW PER EACH WAVEGUIDE OUTPUT. CAPABLE OF OPERATING IN VACUUM WITH RADIATIVE COOLING ONLY AT A TEMPERATURE BELOW 200°C.

Table 4-2 Some Features of Amplitron and Klystron Design for SPS

SPS-145

ITEM	AMPLITRON	KLYSTRON
POWER	5 KW WITH 10^6 TUBES	50-250 KW WITH $< 10^5$ TUBES *
EFFICIENCY	85-90% *	80-85%
CATHODE	COLD PURE METAL (AVAIL LIFE DATA - 10,000 HR)	THERMIONIC OXIDE/MATRIX (AVAIL LIFE DATA ~ 50,000 HRS)
GAIN	7 db	40 db
VOLTAGE	20 Kv *	40-65 Kv
SPURIOUS SIGNAL AM (TYP.)	-100 db/KHz 10 MHz FROM CARRIER	-125 db/KHz 5 KHz AWAY FROM CARRIER *
TUBE MTBF	COMPARABLE	COMPARABLE PERHAPS SOMEWHAT LESS
THERMAL DISSIPATION	CONCENTRATED INTERACTION REGION	DISTRIBUTED, COLLECTOR CAN RUN 500-700°C, REQUIRE HEAT PIPES *
PHASE SHIFT TUBE-TUBE TRACKING	HIGH POWER PHASE SHIFTERS 2° PER % CHANGE IN BEAM CURRENT $\pm 15^\circ$ PHASE TRACKING	LOW POWER PHASE SHIFTERS $10^\circ-30^\circ$ PER % VOLTAGE CHANGE $\pm 20^\circ$ PHASE TRACKING *
SPECIFIC COST	~\$20/Kw	\$40 TO \$20/Kw FOR ABOVE POWER RANGE
SPECIFIC WEIGHT	0.4 kg/Kw	0.8 TO 0.4 kg/Kw FOR ABOVE POWER RANGE
ARRAY INTERFACE	SERIES OPERATION NO FEED WAVEGUIDES	POWER ADJUSTS TO VOLTAGE CHANGES CORPORATE FEED
TURN-ON	DIRECT FROM BUS BAR ?	MAY REQUIRE LOGIC SEQUENCE
X-RAY LEVEL (RANGE FOR 5 mR/YEAR)	SAFE @ 1 METER *	SAFE @ 1-1.8 km FOR 70 kw DESIGN

*SIGNIFICANT ADVANTAGE

4.2.2 Solid State RF Generation

The solid state approach to higher power rf generation is also worthy of consideration in view of current developments, but is not a subject of emphasis in this study. Table 4.3 indicates the state of art in bipolar silicon transistors^{4.1} which are the likeliest high efficiency candidate at 2.45 GHz. With projected technology advances, it still appears that power added efficiencies with 10 dB gain will be in the 70-75% region, which is lower than the proposed electron beam devices by about 10%. On the basis of specific weight, they do not look to be very promising. Estimating 0.2 lbs for a 50 watt transistor would result in 1.8 kg/kW, which is several times that of electron beam devices (0.4 to 0.8 kg/kW). Current cost for "large" number of units (10,000) is approximately \$1 per watt, and even if they should decrease by a factor of 10 to \$100/kW, they would be somewhat greater than the projected costs of electron beam devices (\$15-70 per kW). There may, however, be compensating factors such as high reliability, which need to be investigated in an overall cost effectiveness trade study. Also, innovative array integration concepts such as proposed by Aerospace Corporation^{4.2}, deserve further scrutiny in the overall concept.

Other potential solid state candidates^{4.3,4} of interest include Impatts and Field Effect Transistors (FET's). State of art performance in these devices is typically:

- (a) Impatts: Special profile GaAs Schottky barrier diodes have achieved 37% efficiency @ 3 GHz @ 3 watt level. We project 20 watts per device @ 40% efficiency in the 1980 period at junction temperatures compatible with 30 years of life (200°C).
- (b) FET's: Silicon FET's have demonstrated 44% efficiency @ 3 watt level @ 4 GHz and we project performance @ 10 watt level, possibly @ 50-60% efficiency at 2.5 GHz in the 1980 time frame.

Although these devices do not appear to be cost effective (\$1 per milliwatt today) or competitive on an efficiency basis, progress in their rapid development should be monitored for future impact. The Electron Beam Semiconductor (EBS) amplifier also falls in this category.

4.3 HIGH EFFICIENCY KLYSTRON DESIGN CONFIGURATION

4.3.1 Introduction

Considerable data has now been accumulated on the feasibility of an 80-85% high power klystron design from previous studies^{4.5,6,7}, discussions with GE Power Tube Dept.^{4.8}, Schenectady; Thomson-CSF Electron Tubes^{4.9}; and NASA-Lewis^{4.10}. The most likely compact configuration to realize both high efficiency and high gain (~40 dB) is a 6 cavity design with one second harmonic bunching cavity focused by an electromagnet as described by E. Lien^{4.11} of Varian Associates. A refocussing section will probably be required for efficient depressed collector operation. An outline of the klystron configuration is given in Figure 4.1. The preliminary power output is dictated by

D180-22876-4

Table 4-3 Status of High Efficiency Transistors

• **ACHIEVED LABORATORY PERFORMANCE ON CUSTOM UNITS**

300 MHz: 88% COLLECTOR EFFICIENCY ACHIEVED @ 25 WATT CW LEVEL,
11 DB GAIN
(~100 UNITS BUILT)

1 GHz: 75% @ 50 WATT CW, 28 V.D.C.
(~50 UNITS BUILT)

3 GHz: 60-65% @ 10-15 WATT CW, 8.5 DB GAIN
(CORRESPONDS TO 52-57% NET EFFICIENCY)
CAN COMBINE FOUR UNITS INTO A 50W CW PACKAGE @ 5%
DECREASE IN EFFICIENCY.

• **PROJECTED 1979 PERFORMANCE IN HIGH RELIABILITY UNITS**

3 GHz: 80% COLLECTOR EFFICIENCY, 10 DB GAIN WITH MAJOR
DEVELOPMENT EFFORT.
(70-75% NET EFFICIENCY)

100 - 120°C JUNCTION TEMPERATURE REQUIRED FOR LONG LIFE.

SPS-1004

REF. POWER HYBRID CORP.
TORRANCE, CALIFORNIA

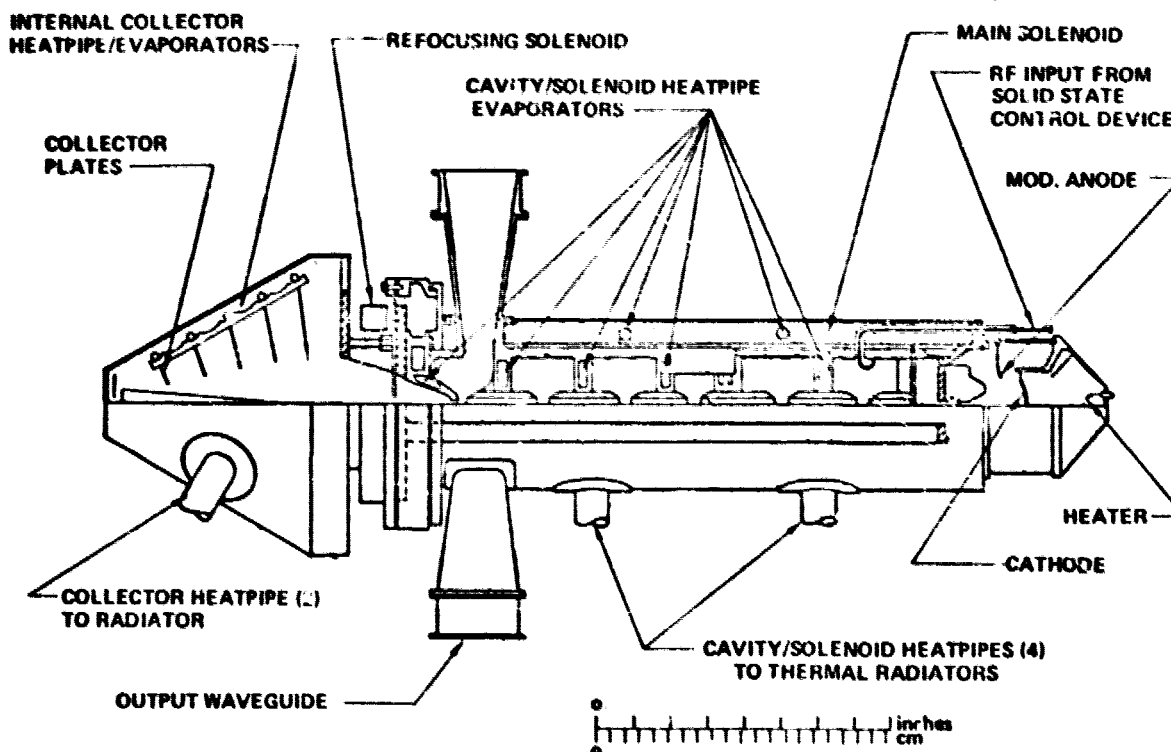


Figure 4-1 Reference Klystron Configuration

the desire to keep the operating voltage low and the 70 kW CW output level resulted from a maximum selected voltage of ~40 kV, obtained from a series connection of two 20 kV supplies. If this requirement can be relaxed, even higher power options become of interest. It is not possible to expect the basic klystron efficiency to exceed 70-75% without collector depression. Although impressive gains have been achieved in raising the basic efficiency from 54% to 70% or so with a 10 stage collector^{4,12}, the estimated efficiency gain due to 5-stage collector depression indicated in Figure 4.2, at the 75% level is only about 8%, resulting in an overall efficiency of about 83%. These are best estimates only, and will have to be verified by experiment, since the velocity distribution of the spent klystron beam entering the collector is not precisely known. An alternate way to arrive at the efficiency estimate is to trace the energy flow through the klystron, as done in Table 4.4, based on best design values obtained from Varian Associates. In this case, slightly different values of collector recovery potentials were used (40% for 3-segment and 60% for 5-segment collector) to evaluate the differential benefit between the designs. It appears that the net benefit of a 5-stage collector over a 3-stage collector is between 1.5 – 3.5 kW per tube. This has the double benefit of less electrical power to be supplied as well as less thermal power in the collector to be dissipated.

It is of interest to note that the range of efficiencies arrived at from Figure 4.2 are 80-86% whereas those derived from the energy balance (Table 4.2) are 82.4% to 86.2%. These values must be reduced by the required solenoid and heater power, estimated @ 1.5 kW, resulting in a net efficiency range of 81.2 to 84.6% based on energy balance. These ranges of efficiencies agree reasonably well and are indicative of what could be expected.

As part of the current study and in support of the klystron implementation Varian Associates undertook a subcontract which is documented separately. A computer run was made (BOEKLY) which largely confirmed the results already indicated, also verifying the perveance selection for high efficiency operation. These results are summarized in Figure 4.3 and will be further discussed in the trade study Section 4.5 and Appendix A.

4.3.2 Depressed Collector Design

One of the greater uncertainties in the design is the velocity distribution of electrons in the output gap, particularly for a high basic efficiency tube. There are few guidelines short of experimental verification which will thus allow the selection of proper depressed voltages at each collecting electrode. Varian has reported that about 10% of the electrons develop twice the d.c. beam voltage in a 50% efficient tube. We estimate that this will be reduced to perhaps 2% for an 80-85% efficient tube. To obtain initial specifications for the collector supply, an estimate was made of the possible voltage ratios required, as indicated in Figure 4.4. The postulated collected currents associated with these are also indicated, the criteria being a reasonable distribution based on extrapolated experience and an energy balance resulting in the expected efficiencies. These were used in setting the supply requirements; the supplies themselves need not be regulated since a 10% fluctuation in them is not expected to affect the operation of the klystron bunching region.

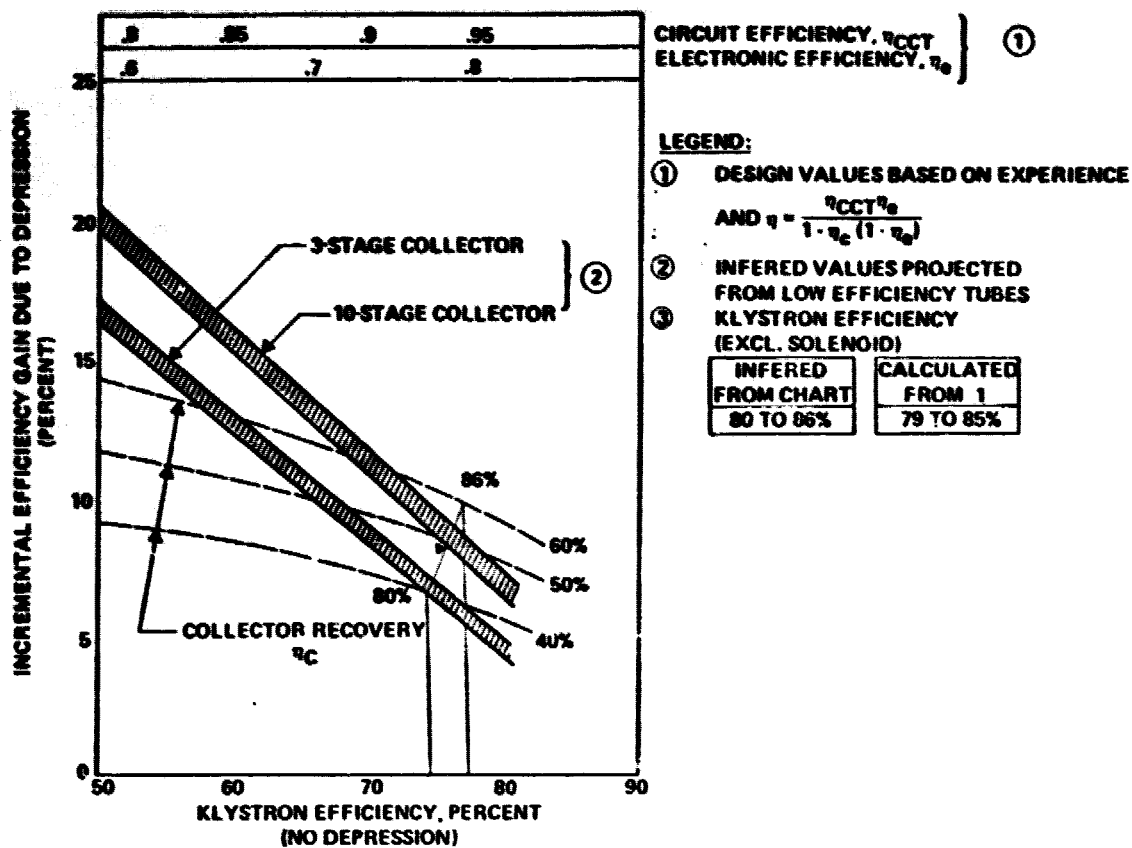
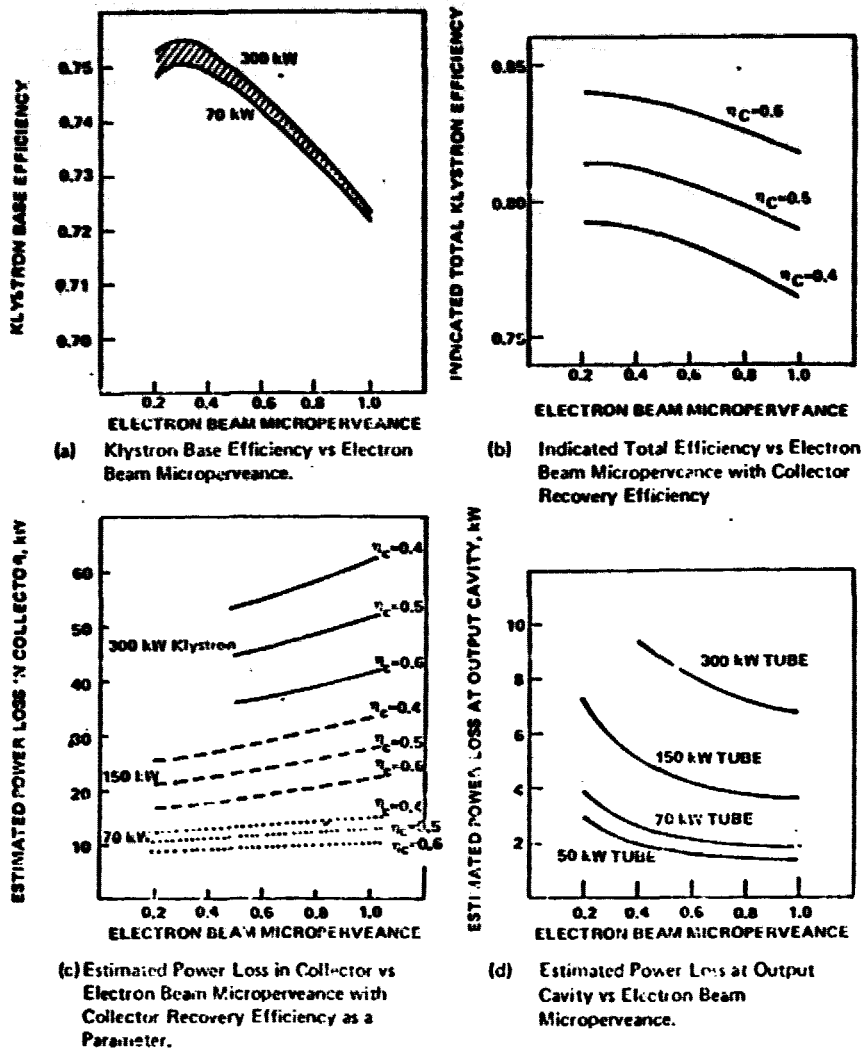


Figure 4-2 Estimated Effect of Collector Depression

Table 4-4 Energy Balance in Reference Klystron Design

	2 SEGMENT COLLECTOR	5 SEGMENT COLLECTOR
BEAM POWER	92.62 Kw	92.62 Kw
RF LOSS IN DRIVER CAVITIES	.40 Kw	.40 Kw
RF POWER PUTPUT ¹	70.66 Kw	70.66 Kw
OUTPUT CAVITY RF LOSS	2.19 Kw	2.19 Kw
OUTPUT INTERCEPTION LOSS ²	1.62 Kw	1.62 Kw
POWER ENTERING COLLECTOR	17.75 Kw	17.75 Kw
COLLECTOR RECOVERY	7.10 @ 40%	10.65 @ 60%
THERMAL LOSS IN COLLECTOR	10.65 Kw	7.1 Kw
NET BEAM POWER	85.52 Kw	81.97 Kw
EFFICIENCY EXC. SOLENOID	82.6%	86.2%
NET EFFICIENCY ³	81.2%	84.6%

1. ELECTRONIC EFFIC. (.79) x OUTPUT CIRCUIT EFFICIENCY (.97) x REMAINING POWER (92.22 Kw)
2. BASED ON 4% INTERCEPTION @ $V_0/3$ (33%) and $2 V_0/3$ (67%) i.e., .0178 $V_0 I_0$
3. INCLUDING 1.5 Kw FOR SOLENOID AND HEATER POWER.



REF. VARIAN ASSOCIATES BOEKLY PROGRAM

Figure 4.3 Klystron Design Parameters

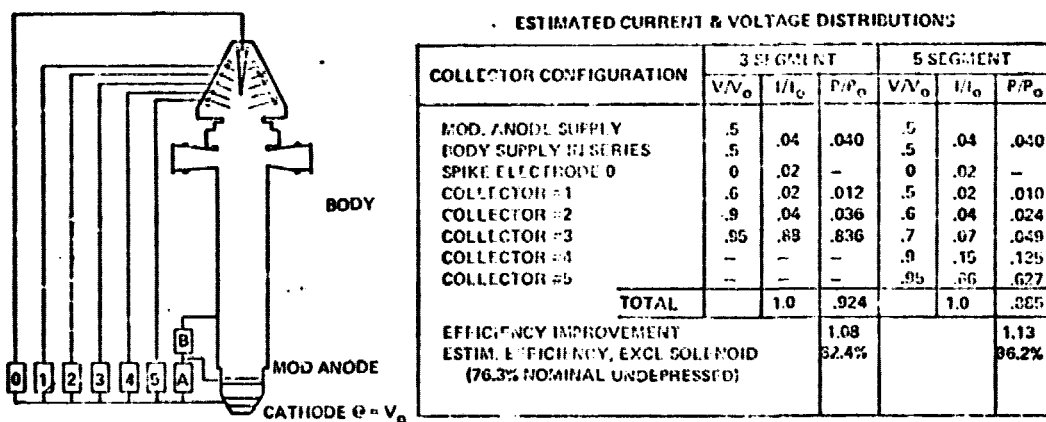


Figure 4-4 Reference Klystron Depressed Collector Design

4.3.3 Voltage Regulation

The klystron drift-tube interaction depends entirely on the electron velocity at the anode which is dependent on the cathode-to-modulation anode voltage and modulation anode-to-body voltage, which are in series with each other. The amount of current intercepted at these electrodes is roughly 4%, which at the full cathode-anode voltage corresponds to 4% of the beam power. The remaining beam current is collected in the collector and does not require regulation. It is adequate if it rises and falls with the beam voltage. The only requirement on the collector voltages is to avoid returning some of the electrons into the interaction regions, which is aided by the presence of the refocusing coil; it is estimated that if these voltages are within $\pm 5\%$ of their nominal values, efficiency will not be degraded.

The requirements on the modulating anode and body voltage are dictated by phase. Consider the klystron design, with an input to output gap transit distance of L , a beam velocity v_0 and frequency f . Then the total phase through the tube will be $360 Lf/v$ degrees. For $v = 1.9 \times 10^7 \sqrt{V_{kv}}$ in meters/sec, $L \cong 16'' = .41$ meters, $f = 2.45 \times 10^9$ cycles/sec, $V = 40$ kv,

$$\phi = \frac{360(.41) 2.45 \times 10^9}{1.9 \sqrt{40} \times 10^7} = 3009^\circ \quad 4.1$$

At 41 kv, this calculation yields 2972° ,

$$\therefore \frac{d\phi}{dV} \cong -37^\circ/\text{kv} \quad 4.2$$

To first order, the effect of subarray-to-subarray phase error is independent of subarray size, determining only the position in space where sidelobe energy is radiated rather than its amount; thus, the phase error at the individual klystron level can be taken as roughly the same as that allotted to each subarray.

Using the criteria of 10° derived by NASA JSC^{4.13}, this translates into a regulation requirement of $\pm 6.7\%$ @ 40 kv, provided there are no other error sources and that klystron-to-klystron phase errors are not correlated. Although it is likely that voltage fluctuations on all klystrons on a given converter will go up and down together, the time delays in distribution, of the order of fractions of microseconds, will make them appear as though they were uncorrelated at a given instant at all klystron terminals. With this in mind, the initial regulation requirement on the modulating anode and body supply were set at 0.5%. However, it is anticipated that this can be relaxed even further, since it is contemplated to include the klystron itself in the phase compensation loop, which will automatically adjust the total phase shift through the klystron via the low power phase shifter at the input, as discussed in section 2.5.5. It is of interest to note that recent tests of equivalent electron beam TWT's have achieved $\pm 7.5^\circ$ tube-to-tube phase^{4.14} on a groundbased phased array application.

4.3.4 Electron Beam Focusing Design

The focusing options for the klystron indicated in Figure 4.5 include (1) straightforward solenoid electromagnetic focusing (EM) based on confined flow experience, (2) multiple-pole electromagnetic focusing with periodic field reversals, introducing the possibility of permanent magnet (PM) implementation, (3) periodic permanent magnet (PPM) focusing used successfully of low and medium power tubes (mostly TWT's) and (4) combined PM/PPM focusing wherein the PM section at the output is used to retain good efficiency as well as best collimation in the high power r.f. region. The low risk approach of (1) was adopted in order to achieve highest efficiency, but R&D efforts in a combined PM/PPM approach should be investigated for possible later incorporation.

The magnetic field required to focus an electron beam is ideally the Brillouin flow value

$$B_0^2 = \frac{69 I_0}{\sqrt{V_0} a^2} \quad \text{in gauss} \quad 4.3$$

where I_0 is in amperes, V_0 in volts and beam radius "a" in meters. This can be written as

$$B_0 = \frac{87 f \sqrt{S}}{\gamma_a} \quad \text{gauss} \quad 4.4$$

where S is the microperveance $S = (I_0/V_0^{3/2}) \times 10^{+6}$, f is frequency in GHz, $\gamma = 2\pi f/v_0$, and $a =$ beam radius.

For good efficiency, the dimensionless parameter γa is designed to be between 0.6 and 0.8, resulting in a value of B_0 for the reference design of

$$B_0 = 87(2.45) \sqrt{.25}/.6 = 178 \text{ gauss}$$

In practice, the actual required magnetic field to achieve high efficiency confined flow is perhaps $3 \times B_0 \cong 530$ gauss. In order to achieve a conservative design, we have initially selected a capability of achieving 1000 gauss in the solenoid when operating at 300°C. Using solenoid design curves obtained from Hughes (Fig. 4.6a) and selecting a minimum ID dimension compatible with directly winding the solenoid on the tube OD (allowing only for a cooling gap) i.e., 3" solenoid ID, one can conduct a trade study of required solenoid power and weight as a function of solenoid OD.

The outer diameter of an S band cavity for optimum klystron design is in the range of $kd = 1-1.5^{4.15}$ where $k = 2\pi/\lambda$. For 2.45 GHz, $\lambda = 4.82$ inches, i.e., $2d = 2.3$ inches max. Allowing for outer wall thickness and a cooling gap, we arrive at a solenoid ID of 3". Figure 4.6b shows the trade of solenoid power and weight with coil OD. Revising the calculations for a solenoid operating temperature of 300°C, according to

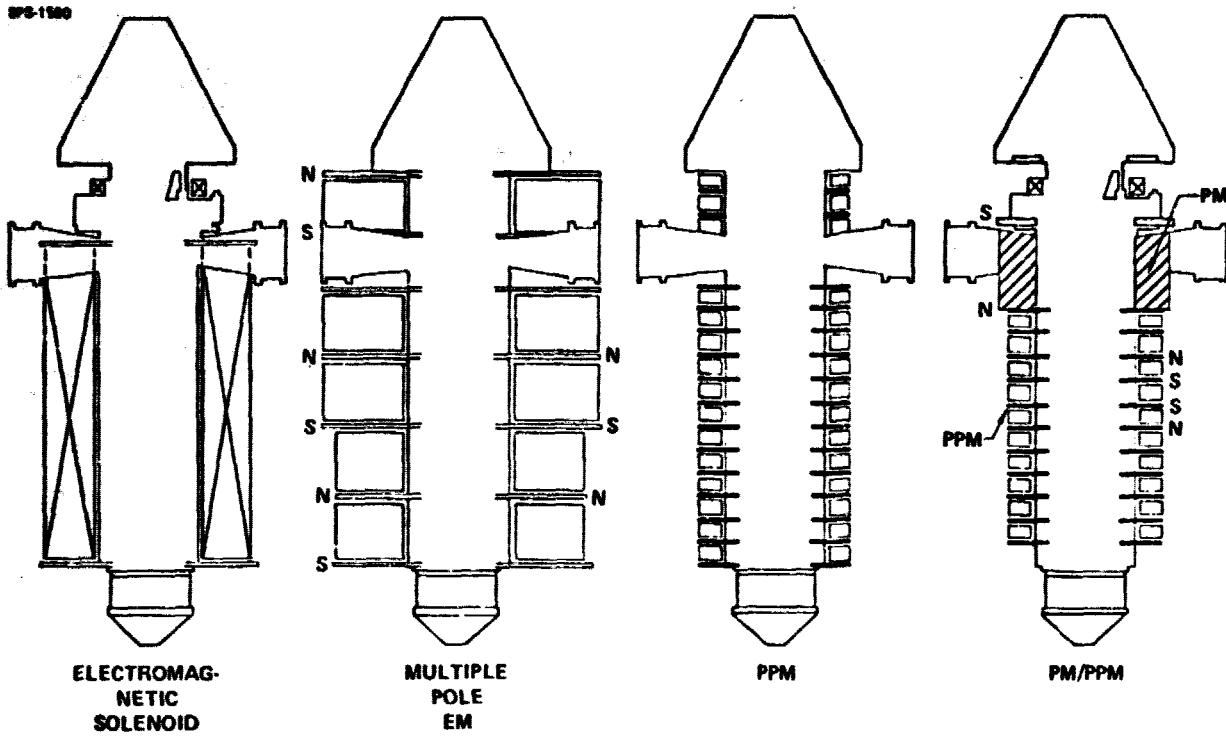


Figure 4-5 Methods of Focusing Klystron Beam

SPS-1677

COPPER SOLENOID 3" ID, 1000 GAUSS, 16.5" LONG

- ① ASSUMES POWER GENERATION @ 3.5 kg/kw AND PASSIVE HEAT REJECTION @ 6.2 kg/kw (125°C).
- ② AS ABOVE, WITH 3.86 kg/kw FOR 300°C HEAT REJECTION.

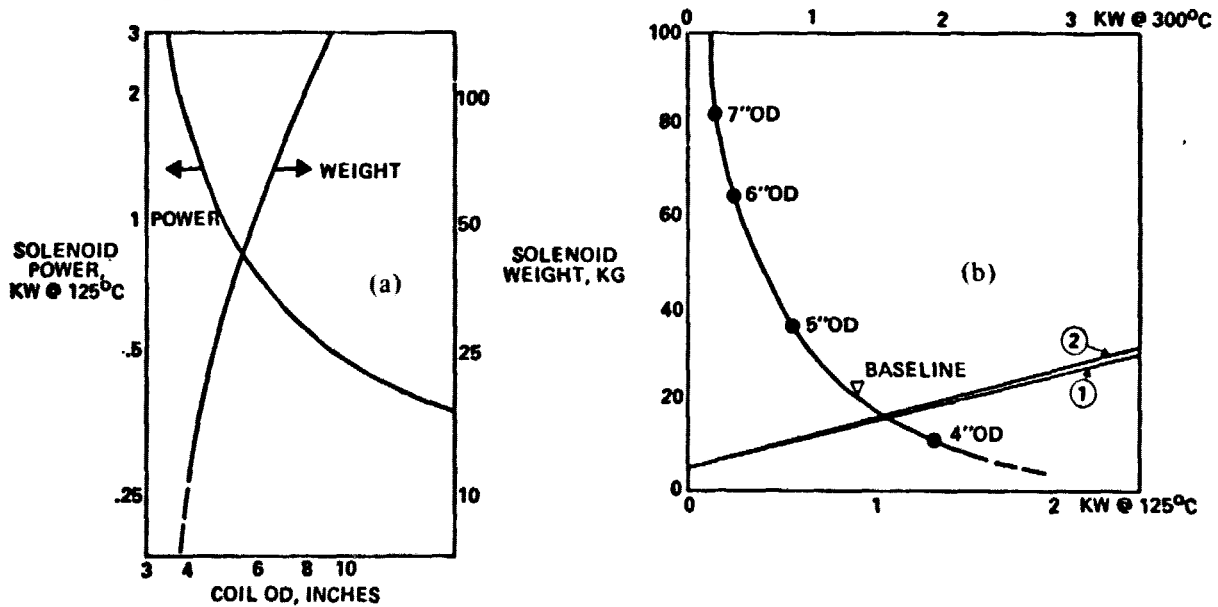


Figure 4-6 Solenoid Design for High Power Klystron

D180-22876-4

$$P = 8.7 B \frac{(R_2 + R_1)}{R_2 - R_1} \left(\frac{1}{\text{space factor}} \right) (1 + .004\Delta T) \quad 4.5$$

where P = solenoid power in watts per inch of axial distance

B = desired field in kilogauss

ΔT = coil temperature above 20°C

Space factor $\cong .8$ to allow for coolant or heat pipe between windings

R_2 and R_1 are outer and inner radius, respectively.

gives the results of Figure 4.6b. Thus, for a 4½" solenoid OD, the required power of 1.4 kw is estimated at 300°C.

If one wishes to optimize the design in such a manner that the weight penalty for additional heat rejection is balanced by the reduced solenoid power of a heavier solenoid, this can be done as indicated in Figure 4.6b. It turns out that this optimization yields the same result at 125°C (assuming 6.2 kg/kw required for passive heat rejection), as at 300°C (assuming 3.86 kg/kw for heat rejection), both indicating solenoid OD of about 4½". The assumption is made that photovoltaic power generation is obtained at 3.5 kg per kw. It is quite possible that with a properly designed tube, the magnetic field requirement may be significantly lower, resulting in possible weight savings in the solenoid.

It is anticipated that the solenoid will consist of copper sheet with glass-like insulation between layers, wound directly on the tube body. With factory adjusted cavity tuning, there will be no protruding tuners. Heat pipe cooling will be provided as indicated in Figure 4.1 and it is possible that the solenoid may be used for baking out the tube in space.

4.4 LIFE AND RELIABILITY ASSESSMENT

4.4.1 Design Approach to Long Life

The stated objective of SPS is the achievement of 30 year life and since the main component of the MPTS system is the r.f. transmitter, its consideration is of paramount importance. The major transmitter elements which contribute to life are: Beam Formation, Beam Focusing, RF circuit design, body and collector design, and external factors such as the power conditioning interface. The associated factors dealing with manufacturing processes, material selection and design approaches are summarized in Table 4.5. The achievement of uniform tube-to-tube performance will require stringent materials control, well defined construction techniques, and special design features such as temperature compensated cavity frequency control. Some of these are further discussed in the Varian Subcontract report^{4.16} and Appendix A.

Table 4-5 Features Affecting Transmitter Life

BEAM FORMATION

CATHODE MANUFACTURING MATERIAL PROCESSING
EMISSION SUPPRESSION FROM SURFACES
CATHODE BASE MATERIAL PURITY--POISONING MECHANISM
EVAPORATION RATES FROM IMPREGNATED CATHODES
HEATER WARMUP
BURN-IN PERIOD--NO INFANT MORTALITY

BEAM FOCUSING

SOLENOID DESIGN/MATERIALS--SPACE BAKEOUT FEASIBILITY AND CONTROL
MAGNETIC CIRCUIT MATERIAL SELECTION SmCo_5 , ALNICO, FLUX CONDUCTORS

RF CIRCUIT

COPPER ALTERNATIVES FOR CAVITIES
PROPERTIES OF LOSSY INTERNAL CERAMICS
OUTPUT WINDOW POWER LIMITS BeO , Al_2O_3

BODY AND COLLECTOR

LEAKAGE OF INSULATORS
SUPPRESSION OF SECONDARY EMISSION

EXTERNAL

LEAD AND CONNECTOR COMPATIBILITY

ORIGINAL PAGE IS
OF POOR QUALITY

D180-22876-4

An initial risk assessment of the unknowns of the space environment have led us to favor a closed envelope approach as a reference design. Further understanding and experience along the line of NASA funded work^{4,17} is needed before a decision to open envelope operation can be recommended. Some of the potential space contaminants are listed in Table 4.6. Some of the concerns with open envelope operation near the Shuttle vehicle deal with outgassing from non-metallic skin of heavy molecules and adsorbed volatile species; cabin leaks (oxygen); fuel cell flash evaporators (water vapor); Vernier control rocket engine exhaust; and main rocket engine outgassing (water vapor).

The degree to which such contaminants can be localized, and the pumping speed of space, etc., have yet to be determined. Space qualified tubes in the 1980-1990 time frame for communication satellite purposes will most likely be of the closed envelope type. NASA Lewis, under a contract with Hughes, Torrance^{4,18} is investigating the feasibility of removing and resealing a TWT collector in a (space) high vacuum environment. Such work, and its continuation, will determine to what degree it is practical to repair, operate, and maintain r.f. power tubes in space.

The NASA objective of 30 year life, in the light of current experience and understanding, thus has to be based on the following phased approach:

- Conservative Design: Emission; RF; Thermal and Stress; Derating
- Determination of Appropriate Manufacturing Procedures
- Adequate Protective Features
 - Modulating Anode
 - System Monitoring Requirements
- Adequate Test Program on Ground
 - Failure Mode Identification
 - Infant Mortality Elimination--Burn-in
- Understanding of Space Environment
 - Processing in Space
 - Open Envelope Operation
- Definition of Maintenance Philosophy
 - Allowable Down Time
 - In-Place Repair Feasibility
- Development of Analytical Model
 - Determine Tube MTBF Required
- Space Test Verification

4.4.2 Current and Projected Tube Life Experience

There have been promising developments in transmitter life in current microwave systems which lend some credibility to the 30 year life objective. There is high DOD interest in improving the

D180-22876-4

Table 4-6 Potential Space Contaminants

SPS-1025

TYPE OF CONTAMINANT	SOURCE	PROBABLE MAGNITUDE	COMMENT
COMBUSTION PRODUCTS: N ₂ , CO ₂ , H ₂ O, CO, H ₂ , ETC.	THRUSTERS OF VISITING SPACECRAFT, FREIGHT, ETC.	INTERMITTENT	MAY DEPEND ON PROXIMITY BAD FOR OPEN TUBES
ATMOSPHERIC GAS: O, N ₂	EARTH'S ATMOSPHERE	STATIC 10 ⁻⁸ TORR, DYNAMIC 10 ⁻⁶ TORR	LOW EARTH ORBIT, 20 ⁰ N.M. BAD FOR OPEN TUBES
LIBERATED GASES	SATELLITE OUTGASSING	UNCERTAIN, DECREASES WITH TIME	MAY BE BAD FOR OPEN TUBES
H ₂ O	WASTE DUMPS, FUEL CELLS	INTERMITTENT	BAD FOR OPEN TUBES
PARTICLES, PAINT CHIPS, INSULATION, ETC.	SATELLITE	MAY CONTINUE FOR LONG PERIODS	POSSIBLY NOT A PROBLEM WITH SHIELDED OPEN TUBES
METEORITES, COSMIC RAYS SOLAR WIND	OUTER SPACE	UNCERTAIN	PROBABLY NEGLIGIBLE PROBLEM FOR TUBES

D180-22876-4

reliability of military systems and modes, funding has been made available by the Air Force to study tube manufacturing technology for higher reliability. As indicated in Figure 4.7, the typical DOD transmitter tube MTBF is several thousand hours. This, however, is based on relatively unskilled field maintenance procedures, generally involving development programs with little emphasis on long life. Only recently, the services have initiated data gathering programs which will shed better light on failure modes with an objective of improving reliability. Sample data from such a program is shown in Table 4.7 indicating that increasing life is being obtained in properly monitored systems. In fact, the best ten high power klystrons running on the BMEWS system have seen 9 years of life and are still running. With proper (costly) burn-in procedures, current space based TWT's are being qualified for 7 years life. Over 100 such tubes currently in space have been running for over 2 years. With this background, it is our opinion that within the SPS development time-frame transmitter tube MTBF's approaching 30 years with the suggested design approach will be feasible. It is important to recognize that significant life test programs on the ground will be required, building on such studies such as NASA Lewis has funded⁴⁻¹⁹ but confined not only to cathodes, but the entire r.f. envelope.

4.4.3 Cathode Design Criteria

The mechanisms limiting thermionic cathode life are primarily evaporation rate of the cathode material, cathode matrix properties, and impurities. The cathode-tube interaction is paramount in realizing long life, regardless of how good the cathode may be in a diode test. The approach to be taken to realize 30 year life must thus be based on minimizing tube-cathode interactions through conservative design, good beam focusing and proper selection of materials to minimize poisoning gases produced by electron bombardment. The current status of cathode emission performance is summarized in Figure 4.8a. The most likely candidates, based on present knowledge,^{4-22, 23} would be either a tungsten matrix cathode operating at a temperature of slightly above 1000°C or a nickel matrix cathode operating at about 800°C. The lower temperature would be preferable from the life point of view but factors such as migration and reactivation feasibility tend to favor the higher temperature cathode. As indicated in Figure 4.8b, conservative current densities associated with emission wearout at 30 year life are typically 0.1 to 0.2 amps/cm². Current life test experience of cathodes of several manufacturers is summarized in Table 4.8. Projected performance with the Philips type B cathode indicates that operation at 1020°C will result in a life of 50,000 hours at 0.5 amps/cm². Our current assessment, based on discussions with the tube industry and experts at NASA Lewis and NRI, suggests that it would probably be unwise to utilize some of the newer cathodes until sufficient life test data of the type sponsored by NASA-Lewis at Watkins-Johnson has been accumulated. Further encouragement with respect to long life in thermionic cathodes can be derived from the work at Bell Telephone Laboratories⁴⁻²⁴ on the so-called Coated Powder Cathode (CPS), which is in use on long life repeaters, capable of 50,000 hours life at current densities approaching 1 amp/cm².

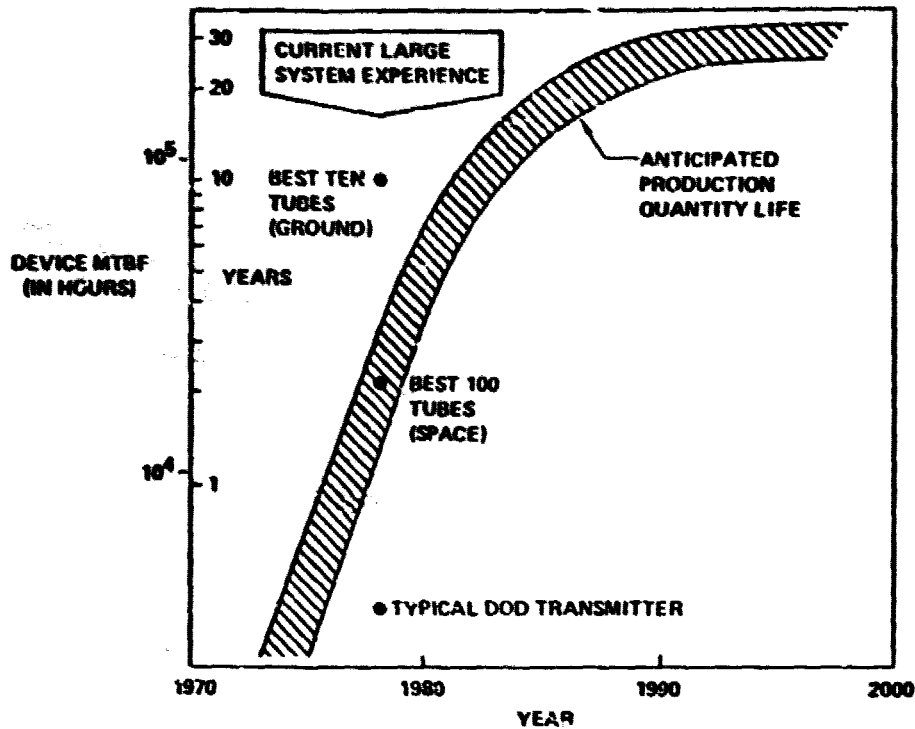


Figure 4-7 Microwave Tube Life Trends

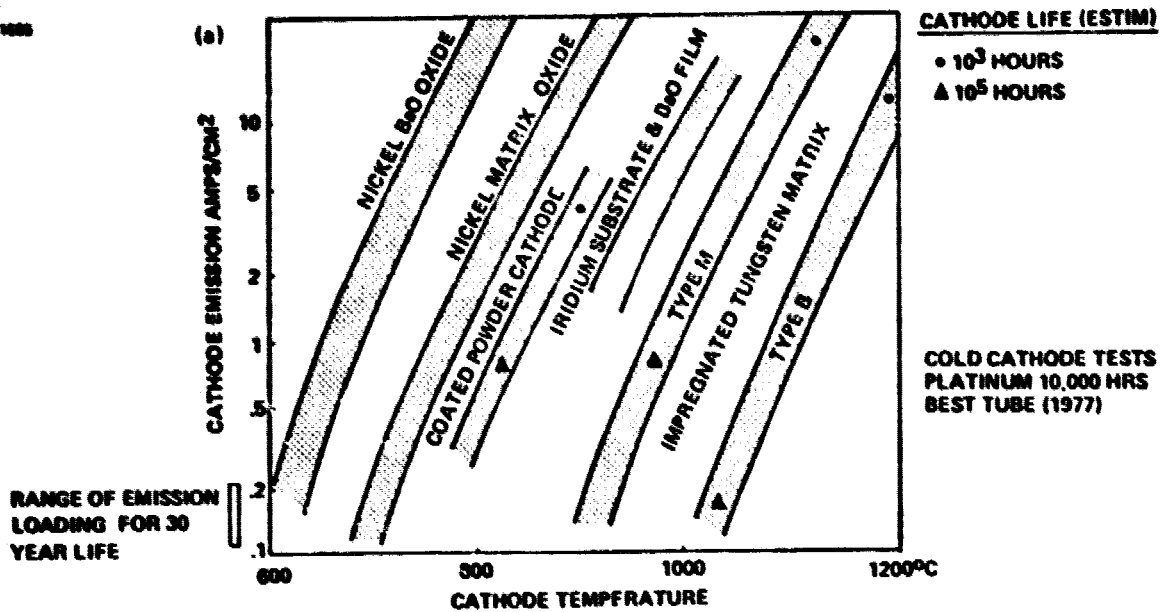
Table 4-7 Life Data on Current Ground Based Radar Transmitters

TUBE TYPE	AVERAGE POWER (KW)	AVERAGE FILAMENT LIFE (HRS)	AVERAGE RADIATE LIFE (HRS)	DATA BASE (NO. FAILED)
KLYSTRON	6.6 KW	30,903	21,271	41
KLYSTRON	15 KW	31,321	27,452	17
KLYSTRON	75 KW	20,223	19,652	36
MAGNETRON	2.8 KW	2,155	1,886	147
MAGNETRON	3.5 KW	2,861	2,125	289
KLYSTRON	5 KW	4,532	4,372	37
KLYSTRON	1 KW	1,615	1,227	102
TWYSTRON	3 KW	3,889	3,287	53
TWT	3 WATTS	6,013	5,104	82
TWT	3 WATTS	14,805	13,002	29
KLYSTRON	75 KW	9,416	9,353	8
KLYSTRON	2 KW	70,570	69,422	6
KLYSTRON	2 KW	57,267	56,880	7
KLYSTRON	10 KW	15,910	15,750	59
KLYSTRON	10 KW	25,390	23,303	29

REF: AF DATA REPORTING SYSTEM GO-92

D180-22876-4

SPS-1000



SPS-1000

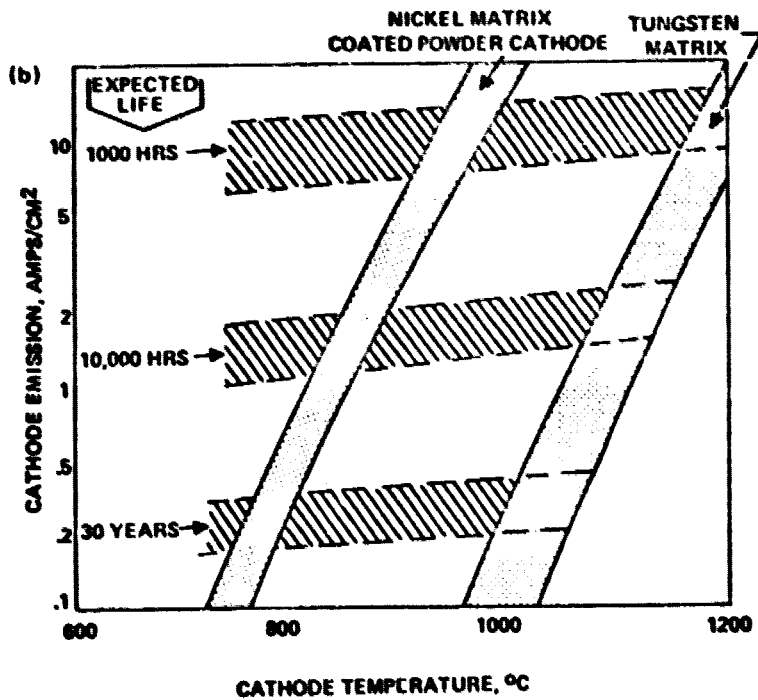


Figure 4-8 Cathode Design Criteria

D180-22876-4

Table 4-8 Cathode Life Test Data (1977)

SPS-1087

MANUFACTURER	OPERATING HOURS	OPERATING TEMPERATURE	FAILED AT
LITTON	5627 8473 6925 8601	1100°C 1100°C 1100°C 1100°C	
PHILLIPS TYPE B	22,847 26,803 27,425 26,932	1100°C 1100°C 1100°C	26,979
PHILLIPS TYPE M OSMIUM COATING	16,047 6,150 1,571	1000°C 1050°C 1000°C	
SEMICON TYPE S	20,858	1100°C 1100°C 1050°C 1100°C	23,073 7,289 20,087
GENERAL ELECTRIC		990°C 1010°C 980°C 1010°C 1015°C	6,807 3,469 2,131 3,288 3,750

REF: NASA LEWIS/W-J
NAS-3-14385

D180-22876-4

With respect to pure metal cold cathode performance, the best available life data indicate 8-10,000 hours life so far in a microwave tube system at 5 GHz using a platinum cathode. The cold Beryllium oxide cathode employed by SFD, (a Varian subsidiary in Union N.J.) in a cross-field phased array application has experienced 18,000 hours life on the best tubes to date. This cathode has a higher secondary emission than platinum but also exhibits a less stable operation due to the oxide layer on the cathode surface. Methods of starting pure metal cathodes are not well defined and may require either a small thermionic cathode, or a radioactive emitter. Clearly, a great deal more of life test data will need to be accumulated for both types of thermionic and cold cathodes to assure 30 year life.

In order to verify whether the reference klystron design can operate with a current density of say 0.15 amps/cm^2 , the following calculation is included: The required cathode area for 2.2 amps is 14.67 cm^2 . For a value of $\gamma a = .6$ and a value of $\gamma = 2\pi f/v_0 = 1.28 \text{ cm}^{-1}$, $a = .6/1.28 = .47 \text{ cm}$ and $\pi a^2 = .69 \text{ cm}^2$. This leads to a cathode to beam convergence of $14.67/.69 = 21.2$ which is considered conservative (values of 100:1 have been implemented).

4.4.4 Tube MTBF Considerations

The achievement of 30 years life at the system or subsystem level does not necessarily translate into a 30 year tube MTBF requirement. Obviously, further refinement in the system model, definition of maintenance procedures, the Lowest Replaceable Unit (LRU) definition, and spares philosophy will have to be made to arrive at specific tube MTBF requirements.

Ideally, of course, a failure model of the transmitter would be desired, in which no failures occurred until wearout mechanisms set in, i.e., avoidance of early mortality. To some degree, this can be achieved by a burn-in procedure to identify and remove infant mortality victims. It is anticipated that with the reference design tube, partial or full bakeout in space will be feasible, avoiding the need to perform costly burn-in on the ground. Also, with mass production, automated manufacture, good quality control, and maintenance, infant mortality can be minimized.

With roughly $N = 100,000$ tubes, if a criteria of 2% of klystrons failed is acceptable, with a scheduled SPS shutdown every 3 months the required tube MTBF would be approximately

$$\frac{(.02N) (\text{Tube MTBF})}{N} = 3 \text{ months} = .25 \text{ years}$$

i.e., $\text{MTBF} = (50)(.25) = 12.5 \text{ years}$. This is compatible with the reference klystron design criteria; however, a more refined reliability model needs to be developed, of which the above exponential model ($\alpha = 0$) is but one case corresponding to a constant failure rate. Such a model is the best possible choice if one has no better a priori knowledge of the failure mechanisms. With proper burn-in procedures, and as better understanding of failure modes is developed, by the elaboration of

the data supplied by Varian in Figure 4.9, other failure models may be developed, with $a \neq 0$ in Figure 4.10 which are likely to result in lesser MTBF requirements than indicated above. As mentioned, with proper burn-in period, infant mortality failures can be avoided and failures shifted toward cathode wearout limitations. The required burn-in period for current space qualified TWT's is of the order of 1500 hours, and burn-in periods as high as 10,000 hours may be required to achieve 30 year life.

4.5 HIGH POWER KLYSTRON TRADE STUDIES

The reference klystron represents an initial point design within the given guidelines of the MPTS study. It is intended primarily as a vehicle to demonstrate its potential in the SPS application. If the operating voltage at GEO can be increased to a value above 40 kv, and if the X-ray level for maintenance and operation is acceptable, other klystron power levels become of interest. The topics which were addressed in this study include specific weight and cost as a function of klystron size; thermal dissipation capability as a function of power level; overall transmitter acquisition and replacement cost as a function of power level; and assessment of comparative X-ray levels as a function of power level. In the process, design parameters were evolved leading to several high efficiency klystron configurations.

4.5.1 Specific Weight Comparison

To arrive at some reliable estimates of specific weights, an investigation of various manufacturer's catalogues was made, augmented by verbal discussions of projected advances, primarily for airborne transmitter applications. The results for amplitrons, klystrons, and TWT's are widely divergent, as indicated in Table 4.9. The projected advances rely primarily on advanced solenoid designs or usage of lightweight permanent magnets, neither of which have been reduced to practice in quantity production. The total tube weights at 2.5 GHz as a function of CW power level are estimated in Figure 4.11a, indicating the advantage of crossed field amplifiers (such as the amplitron) at lower power levels. Replotting these on a normalized basis (Fig. 4.11b) indicates that the specific weights of klystrons and amplitrons become roughly equal at power levels of the order of 200 kw or above. The klystron may have a slight thermal advantage since it will not be limited by the operating temperature of Samarium-Cobalt magnets ($\sim 250^{\circ}\text{C}$) and its collector may operate at much higher temperatures ($500-700^{\circ}\text{C}$). However, the X-ray level will be several orders of magnitude greater, since the penalty of shielding cannot be afforded. In any case, the results were of sufficient interest to consider further a higher power klystron design, particularly from the tube MTBF point of view. There are no compelling reasons to expect a high power tube to have a significantly lower MTBF than a low power tube, except possibly for the cold cathode feature of the amplitron. Thus a significant advantage may accrue in the overall transmitter comparison. The specific weights used in the trade study range from 0.4 to 0.8 kg/kw as based on values given by Raytheon on the 5 kw amplitron and our calculations of the klystron mass.

SPS-1689

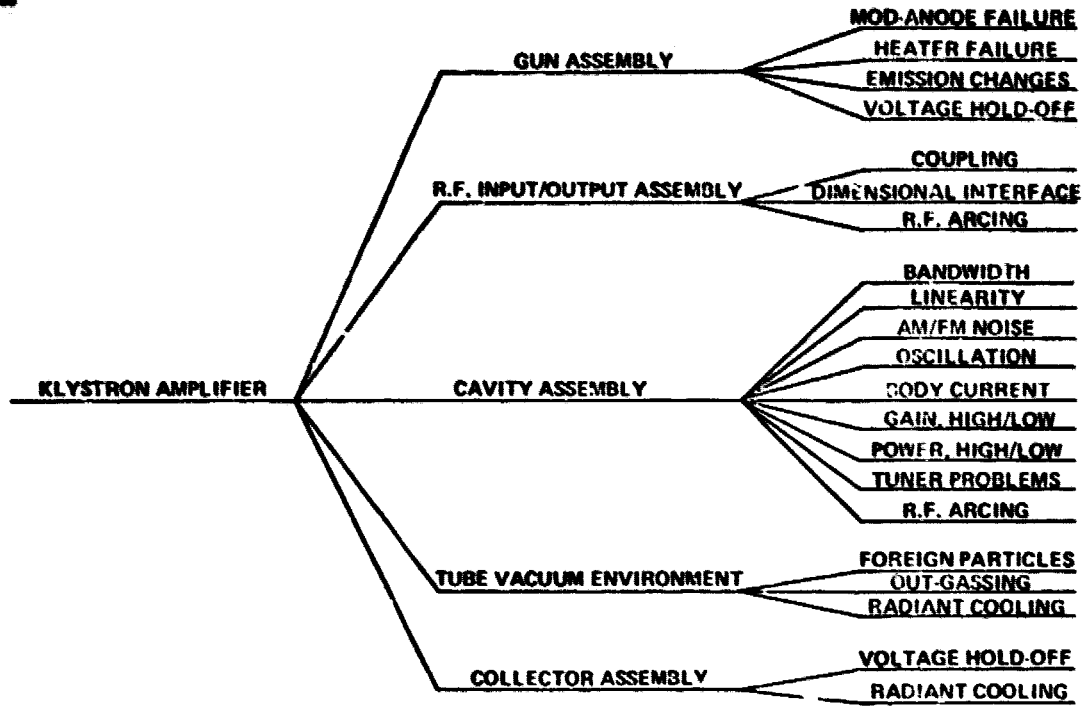


Figure 4-9 Klystron Failure Symptom Tree

SPS-1689

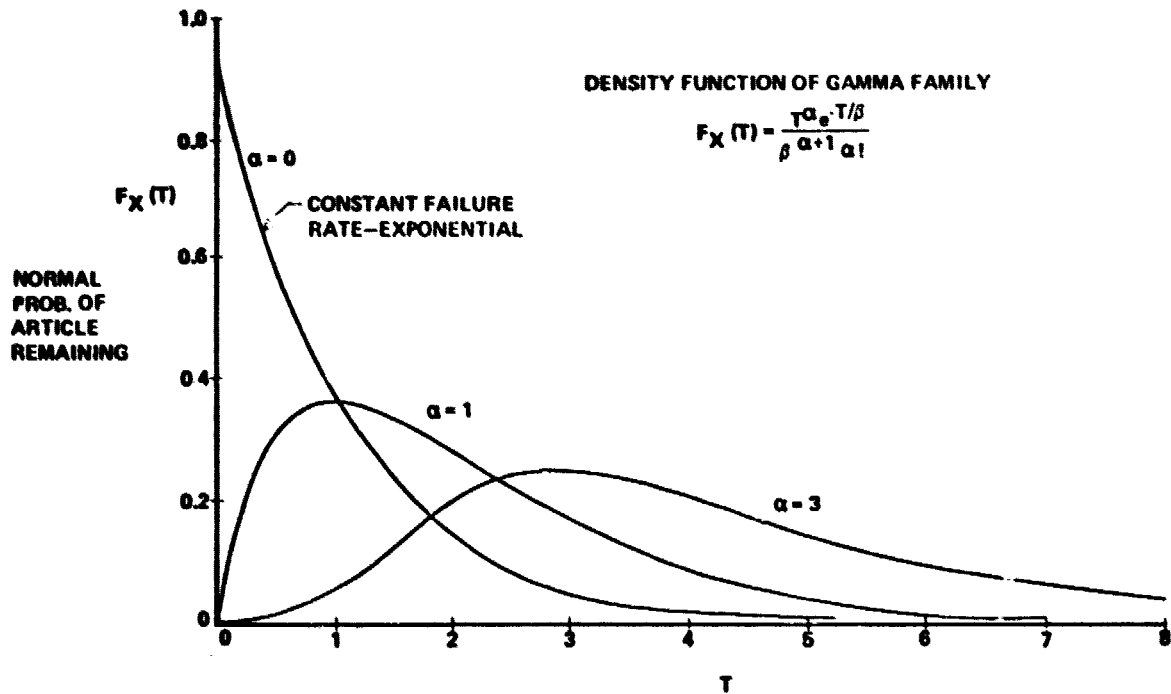


Figure 4-10 Possible Failure Mode Distributions

D180-22876-4

Table 4-9 Transmitter Weight Trade Study Results

- . CW RANGE 5-100 KW PER DEVICE
- . SPECIFIC WEIGHT - LBS PER KW

FREQ. GHZ DEVICE	.5		1		3		10	
	SOA	BEST PROJ	SOA	BEST PROJ	SOA	BEST PROJ	SOA	BEST PROJ
AMPLITRON MED. POWER LOW GAIN SUPERPOWER	18 6	2*	16 5	1.5*	14 4	1.3*	12 3	1.0*
KLYSTRON HIGH GAIN NARROW BAND SOLENOID	12	5**	10	4**	8	3**	6	3**
TWT - COUPLED CAVITY HIGH GAIN 9% BANDWIDTH SOLENOID	22	14	20	10	18	8	16	6
TWT - HELIX, OCTAVE BAND HIGH GAIN MINI-TWT PPM FOCUSED CURRENT DESIGN <500 W CW	100 500	40	40 400	20	35- 350	15	30 300	15

* SAMARIUM COBALT MAGNET TECHNOLOGY

** BASED ON IMPROVEMENTS IN LIGHTWEIGHT SOLENOIDS

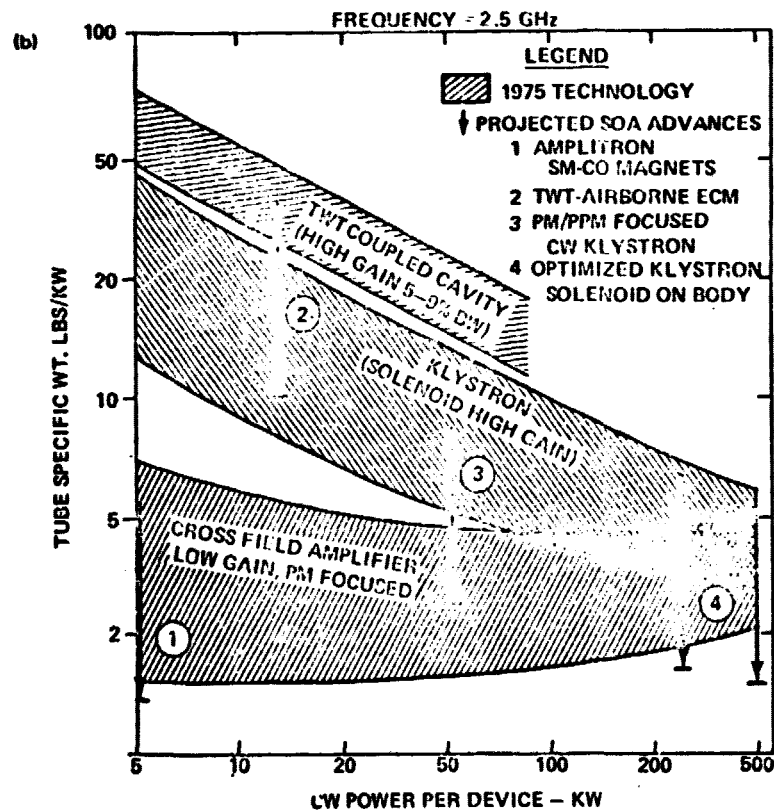
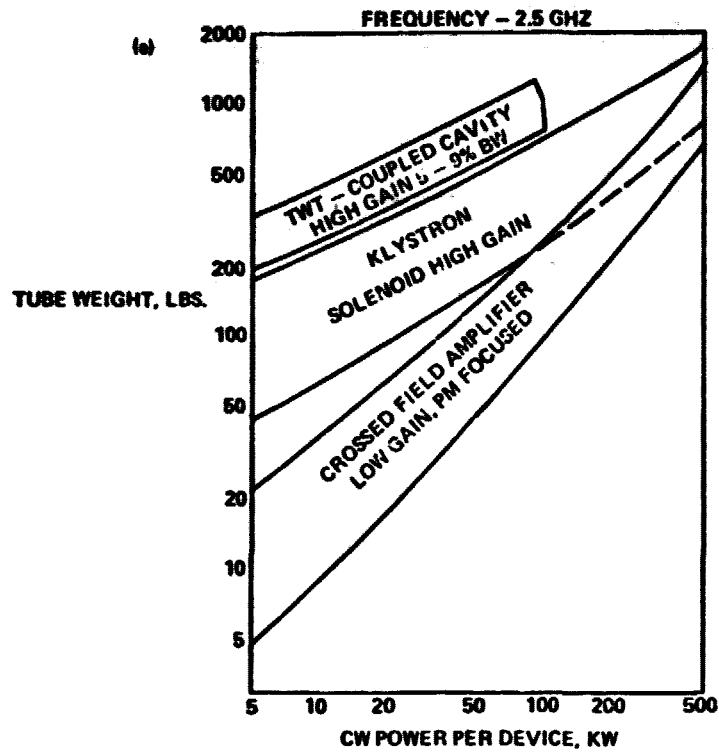


Figure 4-11 Weight Comparison of High Power CW Transmitters

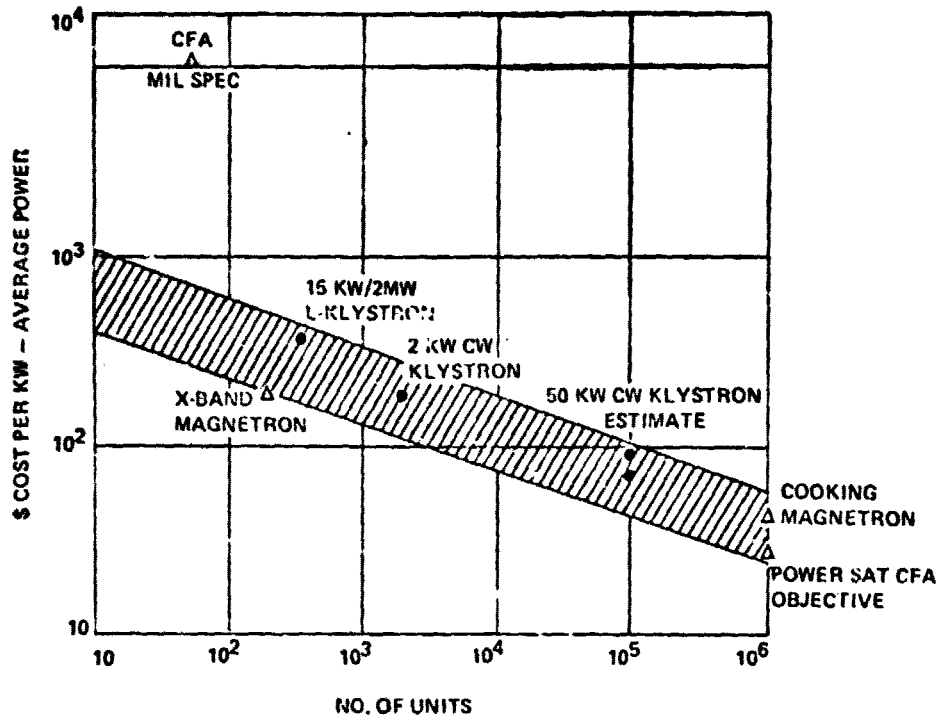
4.5.2 Specific Cost Comparison

The cost studies for high power CW tubes are indicated in Figure 4.12a for certain types of klystrons and magnetrons, as a function of quantity, and in Figure 4.12b as a function of average power. The most reliable benchmark is the mass produced cooking magnetron at about \$30-50 per kw. The amplatron, somewhat more complex, is expected to be mass produced for SPS quantities @ \$20 per kw. The klystron costs used in our parametric study were based on numbers arrived at independently by ourselves and by Varian Associates, and varied from about \$70 per kw at the 50 kw CW level to \$20 per kw at the 250 kw CW level. It is of interest to note the relatively large capital facilities sized by Varian which are roughly amortized within these numbers over the SPS installation period. These are documented in the Varian SPS Subcontract report. (Ref. 4.16)

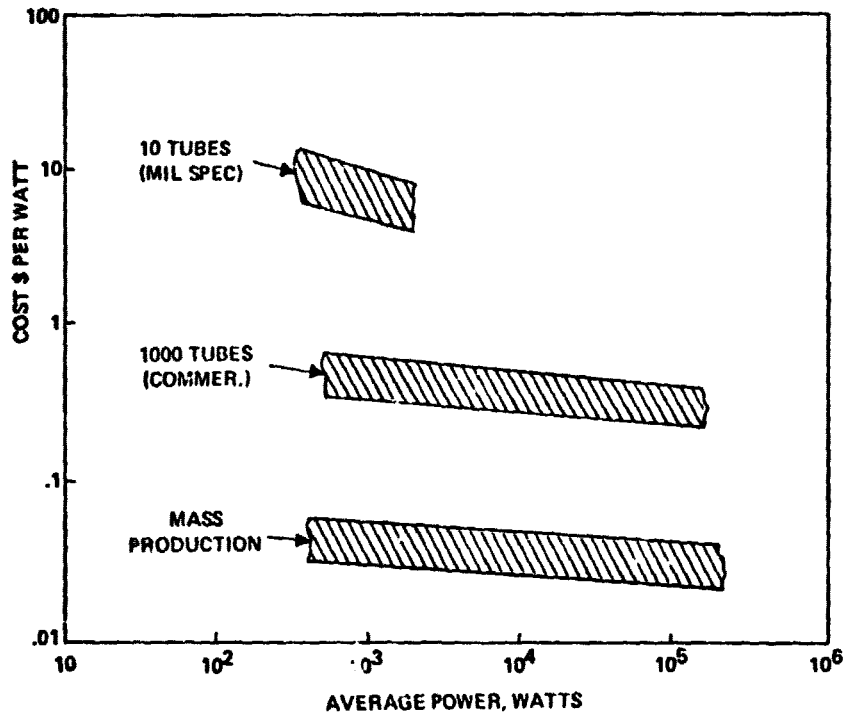
4.5.3 Thermal Dissipation Capability

One of the advantages of the linear beam amplifier such as a klystron is the fact that the different interaction regions, i.e., beam formation, r.f. interaction, and beam collection are physically separate and hence distribute the thermal stresses over a larger area than in a cross-field device. The penalty for this is the fact that to achieve a given efficiency, a more complex design is required, with several power supplies, and even then, the efficiency is likely to be 5% points lower. However, the high resulting gain tends to compensate for this. The thermal distribution in the klystron, in a parametric form, is estimated in Table 4.10. For the reference design, the collector dissipation is 7.1 kw with 60% collector recovery and 9.9 kw with 45% collector recovery. Heat pipe cooling requirements were estimated for the parametric study as follows: For the body and solenoid, operating at 300°C, the following values were used: 2.01 kg per kw with a 1 meter long heat pipe between the tube and the radiator, and 1.32 kg per kw with the radiator directly on the tube. For the collector, operating at 500°C, the values are 0.94 kg per kw for a 1 meter heat pipe and 0.49 kg per kw with the radiator directly on the tube. The liquid metal heat pipe design is detailed in Section 6.3. As a worse case analysis, to dissipate 9.9 kw @ 0.3 kw/cm² requires 33 cm² of heat pipe contact area, which in a collector bucket of over 50 cm in circumference is easily achieved. The heat pipe configuration is indicated in Figure 4.1 for both the collector and the body of the reference klystron design.

Liquid metal heat pipe thermal capability is estimated to be in the range of 0.3 to 0.8 kw per cm² depending on temperature and material, and the values of 0.25 and 0.5 kw per cm² were used in our parametric analysis. In the depressed collector, it was decided to use tungsten as the electrode material because the thermal analysis indicated that with a 500°C wall, the temperature rise could be as high as 1500°C at the inner portion, if 5 kw (out of 9.9 kw) were to impinge on the first electrode closest to the output gap. The collector is designed to accommodate only the above dissipation and provision via external shutoff must be made if the r.f. drive should fail, which would allow the entire beam power to be dumped into the collector. This is accommodated by the use of the modulating anode.



(A) COST VARIATION WITH QUANTITY OF PRODUCTION



(B) COST VARIATION WITH POWER LEVEL AND QUANTITY

Figure 4-12 Cost Trends in High Power CW Transmitters

D180-22876-4

Table 4-10 Parametric Energy Distribution in High Efficiency Klystron

SPS-1683

DRIVER CAVITY LOSSES = 0.4% $V_o I_o$.004 $V_o I_o$	
OUTPUT CAVITY LOSS $(1 - \eta_{cct}) \eta_e \left(\frac{100 - A}{100} \right) V_o I_o = (.97)(.79)(.998) V_o I_o$.023 $V_o I_o$	
OUTPUT INTERCEPTION LOSS FOR n% INTERCEPTION @ OUTPUT GAP 1/4 OF CURRENT INTERCEPTS @ FULL V_o 3/4 OF CURRENT INTERCEPTS @ 1/4 V_o $(.25) + (.75)(.25) \frac{n}{100} V_o I_o = .004375 n V_o I_o$.018 $V_o I_o$ (n-4%)	
USEFUL RF POWER BASED ON UNDEPRESSED EFFICIENCY OF 76.3%	.763 $V_o I_o$	
SUBTOTAL		.808 $V_o I_o$
POWER ENTERING COLLECTOR		.192 $V_o I_o$
COLLECTOR POWER RECOVERED @ 45% RECOVERY (CONSERVATIVE)	.086 $V_o I_o$	
COLLECTOR THERMAL DISSIPATION	.106 $V_o I_o$	
TOTAL	1.00 $V_o I_o$	

D180-22876-4

The most critical portion of the klystron from the thermal point is the output gap. As indicated in Table 4.10, the output gap interception loss is $.004375 n V_o I_o$, where n is the beam interception (%) at the output gap. Although high power klystrons have been built which have in excess of 99% transmission at saturated power output, we have taken the viewpoint that in a high efficiency tube, where the beam should be closely coupled to the output gap, the beam transmission will be reduced to 95 to 98% (3 to 5% beam interception).

The output gap interception for the two above cases is indicated in Figure 4.14, as determined parametrically for 3% and 5% interception. To provide for a somewhat more conservative design, a value of perveance of 0.3 was selected rather than the reference design value of 0.25. This results in:

$$\begin{aligned} \text{Output cavity interception} &= 4.375 \times 10^{-3} (3) V_o^{5/2} (I_o/V_o^{3/2}) \\ &= 4.375 \times 10^{-3} (3) 1000^{5/2} (.3) (10^{-6}) \text{watts} = 1.24 \times 10^{-4} V_{kv}^{5/2} \text{ in kw for 3\% interception} \\ &= 2.06 \times 10^{-4} V_{kv}^{5/2} \text{ for 5\% interception} \end{aligned}$$

The capability of the output gap to handle this interception is estimated from Figure 4.13 from the area available for cooling $= \pi D t = 20 \pi a^2$. For a high efficiency design, the value of the parameter $\gamma a = .6$ must remain constant. Thus the output gap capacity for W watts per cm^2 of heat pipe transfer, $f = 2.45 \times 10^9$, and $v_o = 6 \times 10^7 \sqrt{V}$ is

$$(20 \pi a^2) W = \frac{20 \pi (\gamma a)^2 W}{\gamma^2} = \frac{20 \pi (.6)^2 W}{(2 \pi f / v_o)^2} = .344 V_{kv} W$$

which is plotted in Figure 4.14 for W of 0.25 and .5 kw/cm^2 . It is seen that for a conservative 4% beam interception and $W = 0.25 \text{ kw}/\text{cm}^2$, the beam voltage is about 67 kv.

4.5.4 Power Level Trade Study

Although high CW power klystron capability (i.e., 350 KW ~ 8 GHz) has been reported^{4.25}, such achievement with long life operation remains unproved. The intent of this brief examination is to explore reasonable high power CW limits in case it becomes possible to operate in space at voltages up to say 90 kv. Aside from the thermal loss to the collector which can be dissipated over a relatively large area, the most critical region is the output cavity gap. In the VA 873, a 50 kw klystron at 8 GHz, beam interception in the body is stated to be about 1% (99% transmission). Higher frequency CW tubes must operate even with less interception (99.9% transmission in some cases). In our preliminary analysis we have assumed a range of beam interception from 3 to 5%, with the assumption that the energy content of the intercepted beam is $\frac{1}{4}$ at full voltage and $\frac{3}{4}$ at $\frac{1}{2}$ full voltage (from Varian discussions). The scaling beam voltage is derived from perveance $K = I_o/V_o^{3/2}$; and beam power variation $\sim V_o^{5/2}$.

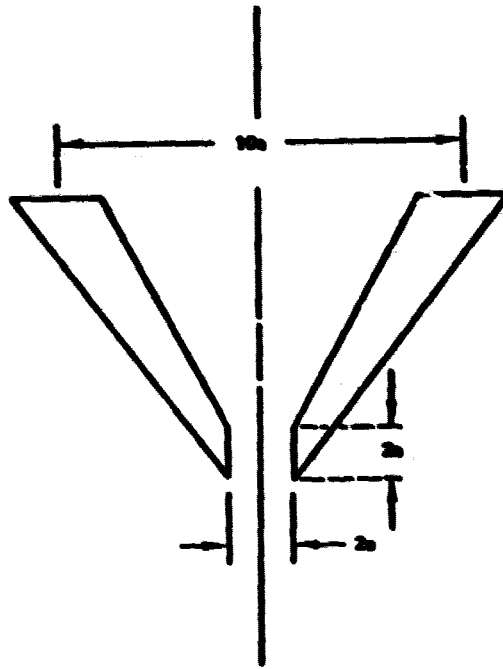


Figure 4.13 Output Gap Geometry

SPS-1820

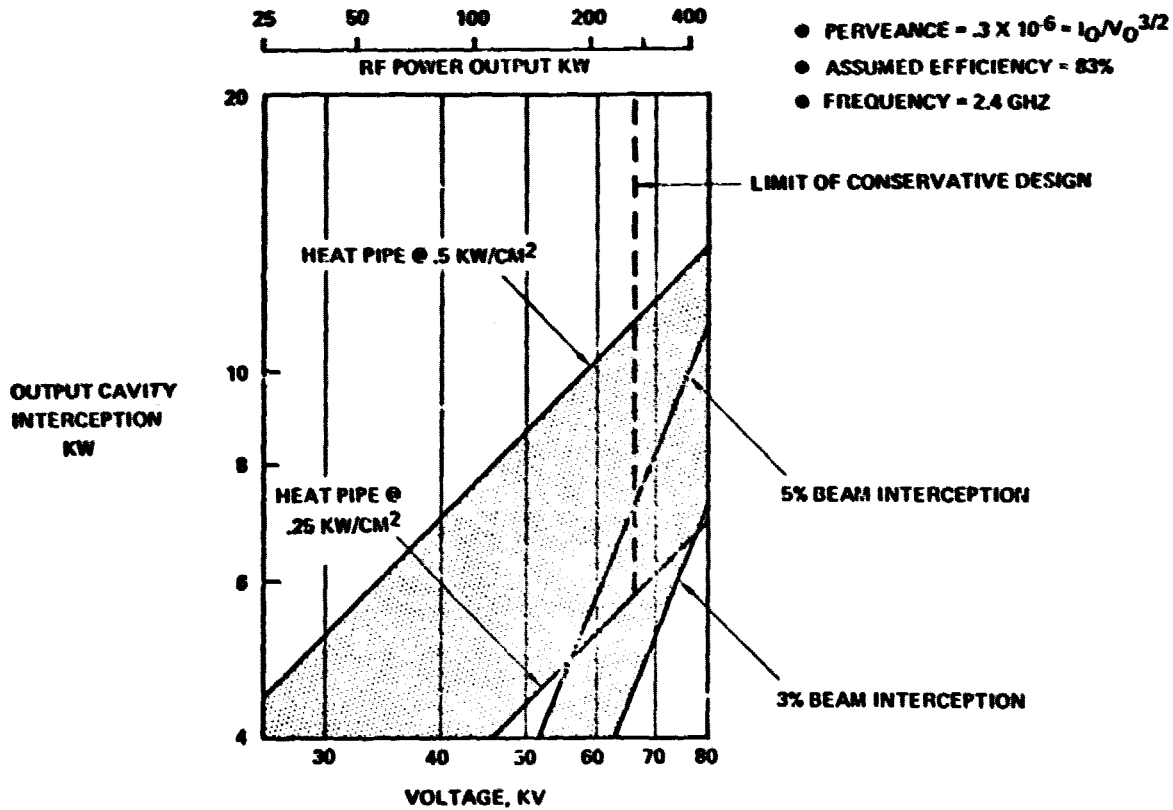


Figure 4-14 High Power CW Limitations of High Efficiency Klystron

The available cooling area in the output gap $\sim a^2$; the design is constrained for good efficiency to $\gamma a < .6(\gamma = \omega/v_0)$, thus resulting in a dissipation capability directly proportional to voltage. Although the work of Kosmahl and Albers^{4,26} suggests that perveance for good efficiency should be less than, say 0.25, the full treatment of output cavity loading suggests that high efficiency can be maintained to values perhaps as high as 0.6. Figure 4.14 indicates the achievable power limits as a function of voltage for the proposed high efficiency design of perveance $S = 0.3 \times 10^{-6}$. Conservative power ratings are close to the 300 kw CW level. For a perveance of $S = .5 \times 10^{-6}$, still within the regime of potentially high efficiency, this power level would correspond to 580 kw. This has encouraged us to investigate in further detail two additional point designs, at 250 kw and at 500 kw respectively. The parameters for these designs are given in Table 4.11. The scaling relations for r.f. section length ($\sim \sqrt{V}$), solenoid power ($\sim B_0^2 L \sim \sqrt{V_0} S$), and tube weight are indicated; a somewhat refined mass estimate for the reference design is carried out in Section 6. The efficiency including solenoid power is somewhat higher than that for the reference design and is indicative of the assumed values in the parametric analysis. It is worth noting (Fig. 4.15) that, even with a longer tube, the efficiency increases by about 2% points due to lower incremental solenoid requirements at higher power. The specific mass decreases dramatically, as predicted in Figure 4.11b, from about 0.8 kg/kw at 70 kw to less than 0.4 kg/kw at 500 kw CW. Thus it appears advantageous to consider a higher power klystron design in the 250 kw region.

As a matter of interest, to establish a comparison between a potential weight saving for a PM/PPM 50 kw design, a similar calculation was made in Table 4.12. Surprisingly, this design did not show any improvement in specific weight and its efficiency turned out to be only 0.2% higher than that of a solenoid focused tube. This advantage may turn out to be more significant if a higher power PM/PPM design turns out to be feasible in the future. In any case the data seems to reinforce the decision to use an efficient wound-on body solenoid in the reference design.

4.5.5 Cost Effectiveness Analysis

With the design data available at this stage, it is possible to provide some initial comparisons of various transmitter designs. For simplicity, the question answered is the acquisition cost of r.f. tubes and 10 year replacement cost of spares, based on a projected transportation cost to space of \$60 per kg. for a system output of 6 GW RF in space. This data is summarized in Table 4.13 and Figure 4.16. The high power klystron has been penalized with a degraded MTBF (30 years for amplatron and 20-28 years for klystron). Also the fact that over 10 times as many sockets are being replaced with the amplatron does not appear in the analysis. The data indicates that on basis of cost of acquisition and replacement of transmitters the klystron becomes competitive with the amplatron at about 500 kw, but is within 25% of the amplatron at the 250 kw with the above assumptions. If the transmitter life is reduced by a factor of 2 from that of Table 4.12, i.e., to 10-15 years MTBF, the increased acquisition costs are indicated in Figure 4.16. It is of interest that the transportation costs still comprise about 47 to 62% of the total cost. If the 250 kw klystron were credited with 30 year life, a specific weight of 0.4 kg/kw and a cost of \$5000 per unit (50 times that of the

D180-22876-4

Table 4-11 Alternate High Power Klystron Designs

POWER VOLTAGE/CURRENT PERVEANCE $K \times 10^{-6}$ RF SECTION LENGTH $\sim \sqrt{V_0}$	70.6kw 42kv/2.2amps .25 16.5in		250kw 85kv/5amps .30 20.5in		500kw 80kv/8.2amps .36 22.8in		
	WEIGHT, kg	POWER, kw	WEIGHT	POWER	WEIGHT	POWER	
TUBE WEIGHT CAVITY, SEALS, BODY ETC. $\sim 1.2 \sqrt{V_0}$ COLLECTOR WEIGHT (EST.) $\sim V_0 I_0$ SOLENOID (EST.) @ 300°C, 1 KGAUSS, $P \sim B^2 \times L \sim V_0^2 K$ HEATER AND REFOCUSING COIL RF LOSSES	10kg 7.0kg 20kg	2kw 1.0kw 4.2kw	15kg 13.2kg 24.8kg	2.9kw 1.5kw 14.7kw	16.6kg 18.7kg 27.9kg	3.9kw 2.0kw 29.8kw	
RADIATOR AND HEAT PIPES	0	1m	0	1m	0	1m	
WEIGHT AND POWER DISSIP'N REQ'D @ 300°C	9.5	14.5	7.2kw	25.3 38.6	19.2kw	47.3 72.0	35.8
WEIGHT AND POWER DISSIP'N REQ'D @ 500°C	4.9	9.3	9.9kw	16.7 32.1	34.1	33.8 64.9	69.0
TOTAL WEIGHT KG	51.4	60.8	95.0	123.7	144	199.8	
SPECIFIC WEIGHT KG PER KW	.727	.260	.300	.495	.288	.400	
EFFICIENCY INC. SOLENOID	80.51%		82.43%		82.67%		

LEGEND:

- SOLENOID FOCUSING, FIVE STAGE COLLECTOR, 45% RECOVERY.
- RF LOSSES AT INPUT, OUTPUT, PLUS 4% INTERCEPTION LOSS TOTAL 4.45% OF $V_0 I_0$
- USEFUL RF OUTPUT = $.7629 V_0 I_0$
- COLLECTOR THERMAL DISSIPATION = $.105 V_0 I_0$
- COLLECTOR POWER RECOVERED = $.0860 V_0 I_0$
- EFFICIENCY = 83.4% EXCLUDING SOLENOID
- HEAT PIPES (1/0 METER) + RADIATOR WEIGHT ESTIMATED @ 2.01/1.32kg/kw @ 300°C (BODY AND SOLENOID)
@ .94/.49kg/kw @ 500°C (COLLECTOR)
- S BAND DESIGN WITH SOLENOID @ 300°C, ID = 3"OD = 4"

SFS 1582

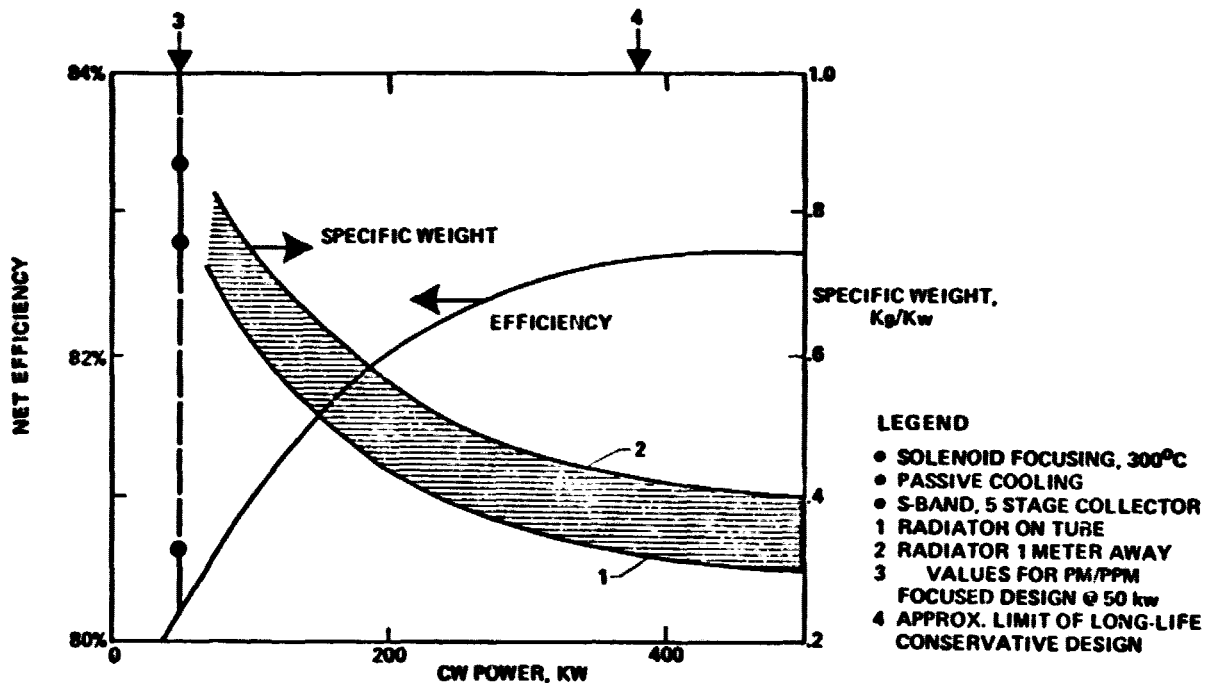


Figure 4-15 Variation of Klystron Efficiency and Specific Weight with Power Level

D180-22876-4

Table 4-12 50 KW Permanent Magnet Klystron Design

VOLTAGE/CURRENT	38KV, 1.81 AMPS
PERVEANCE/BEAMPOWER	S=.244, P ₀ = 69KW
ELECTRONIC EFFICIENCY	0.75
CIRCUIT EFFICIENCY	0.97
RF POWER OUTPUT	50KW
HEATER POWER	.1KW
DRIVER RF LOSSES	.005V ₀ I ₀ = .3KW
OUTPUT INTERCEPTION LOSS	.025V ₀ I ₀ = 1.72KW
RF OUTPUT CAVITY LOSS	.03(50) = 1.50KW
POWER INTO COLLECTOR	15.48KW
COLLECTOR THERMAL INPUT	8.51KW REMOVED @ 500°C
PASSIVE COOLING -	
RADIATOR & HEAT PIPES LIQUID METAL CYCLE @ 2.2/1.5KG/KW FOR 275°C	
@ .94/.49KG/KW FOR 500°C	

WEIGHT ESTIMATE

TUBE & POLEPIECES	12.0KG	o SPECIFIC WEIGHT = .78 TO .83 KG/KW	
COLLECTOR - 5 SEGMENT	6.0		
MAGNETS	7.5		
RADIATOR DISTANCE	0	o EFFICIENCY = 80.7%	
COOLING @ 275°C	5.4		1 METER
COOLING @ 500°C	4.2		8.0KG
			8.0KG
TOTAL WEIGHT	35.1	41.5KG	

Table 4-13 RF Transmitter Acquisition & 10 Year Replacement Cost

SPS-1548

CANDIDATE	POWER PER UNIT, kw	NUMBER PER SYSTEM	ACQUISITION COST		REPLACEMENTS/MONTH	REPLACEMENT COST	SPECIFIC COST \$/KW	SPECIFIC WEIGHT	MASS		INITIAL ACQ'N	10 YR REPLACEMENT	10 YR ACQ'N	10 YR REPL.	TRANS. PORT COST	SYSTEM COST
			PER UNIT \$K	PER SYSTEM \$M					SM	SM						
1	5	7.2x10 ⁶	.1	120	30	3330	40	20	.4	2.4	.8	144	48	352		
2	50	120x10 ³	2.7	324	28	357	116	70	.8	4.8	1.7	288	102	830		
3	70	85,600	2.8	238	26	272	91	40	.8	4.76	1.8	266	108	723		
4	250	24,000	6.0	144	24	84	60	24	.5	3	1.3	180	78	462		
5	500	12,000	7.5	90	20	50	45	15	.4	2.4	1.2	144	72	351		

LEGEND

CANDIDATE		TRANSPORT COST AT \$ 60/kg TO ORBIT
1. AMPLITRON	18kv	EXPONENTIAL FAILURE RATE
2. PM FOCUSED KLYSTRON	38kv	PASSIVE COOLING
3. EM FOCUSED KLYSTRON	42kv	NO BURN-IN COSTS INCLUDED
4. EM FOCUSED KLYSTRON	65kv	
5. EM FOCUSED KLYSTRON	80kv	

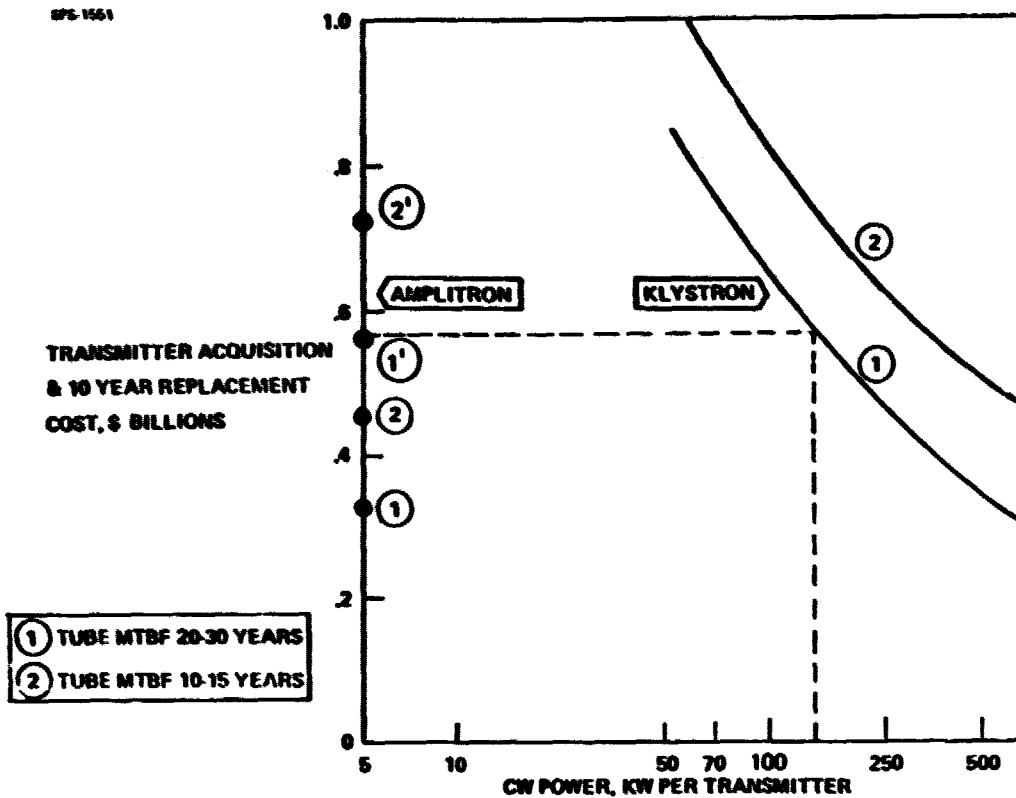


Figure 4-16 RF Transmitter Acquisition Cost for 6 Gigawatt System (Excludes d.c. distribution and maintenance cost differential)

Note: If unprocessed power is used for amplitron DC distribution @ 20 kv 400 kamps (8 GW), this requires an additional 4.4×10^6 kg of conductor weight @ optimum conductor temperature of 50°C as compared to 40 kv 200 kamps distribution for the klystron. This includes the mass of additional solar cells to make up the I^2R loss increase from 7.3% to 12.1%. This translates into a transportation cost differential of \$264 million (@ \$60/kg) as well as an additional solar cell cost @ 50 cents/watt of \$192 mill totaling \$456 million. Thus processed power will likely have to be used for the amplitron, whereas less than 15% processed power is used for the klystron, which makes the above comparison incomplete, favoring the amplitron. With the above considerations, the klystron power level at which the above costs are equivalent will shift to a level below 100 kw. With only 2 times as many dc-dc converters and associated losses, the additional amplitron system cost, using data in Table 5-8, would be \$215.6 million, as indicated in points (1') and (2') above.

amplatron), the acquisition and 10-year replacement cost would be reduced from \$462 million to \$352 million, identical to that of the amplatron. An alternate design of 210 kw, has been proposed for possible follow-on studies. This particular value integrates directly into the MPTS system, with fewer components, and compatibility with quantization requirements of the subarray layout.

4.6 INTERFACE ASSESSMENT

The transmitter interfaces with the various power distribution elements are discussed in Section 5.1 and the thermal and structural interfaces in Section 6. In this section we discuss several questions which came up during the study dealing with protective devices in the tube to subarray module interface to achieve long life; operation under degraded solar cell output or during period of solar flares; and effects of X-rays in the vicinity of the array.

4.6.1 Tube to Subarray Module Interface

The tube interacts with the subarray through the waveguide feed system. The primary requirement is maintenance of a good r.f. match under all conditions. During initial processing or if mismatched, either external or internal arcing may occur. Commercial waveguide components are available to visually detect arcs and use a trigger signal to disconnect the tube rapidly, in this case by connecting the modulating anode to cathode. This can occur in much less than 1 μ sec, adequate to prevent damage.

- *Loss of rf Drive*

With loss of rf drive, the entire electron beam power appears at the collector. The conventional klystron is designed to handle this power. In our case, however, the collector will undoubtedly be designed to handle only the spent electron beam after normal rf interaction. If the loss of rf drive is sensed at the klystron input, modulation-anode power supply may be shut down. This will shut off the electron beam.

- *Electron Gun Arcing*

The most likely region of dc arcing in the circuit arrangement shown is between cathode structure and modulation-anode. In the event of an arc, energy stored in the modulation-anode power supply in the small capacitance C is discharged. The resistance, R, isolates the modulation-anode power supply. Ordinarily the arc extinguishes after a very brief interval, and normal tube performance is restored automatically. Should some unknown fault cause persistent non-clearing arcing, the arc logic could be designed to sense repeated loss of rf output and to shut down the modulation-anode power supply pending replacement of the faulty electron gun.

- *Circuit to Modulation-anode Arcing*

In the event of a dc arc between circuit and modulation-anode, electron beam power would be reduced and normal tube operation would be momentarily interrupted. Energy stored in the circuit to modulation-anode capacitance, similar to the C depicted, is discharged in the arc.

D180-22876-4

Ordinarily the arc extinguishes after a very brief interval and normal tube performance is restored automatically. Should some unknown fault cause persistent non-clearing arcing, the arc logic could be designed to sense repeated loss of rf output and to shut down the modulation-anode power supplies pending replacement of the faulty electron gun.

- *Rf Arcing*

Persistent repeated non-clearing rf arcing in the klystron rf load or output system may result in tube damage. The rf arc logic is designed to sense reflected rf power caused by the arcing and to shut down the modulation-anode power supply pending correction of the problem.

Several other protective features are discussed in Figure 4.17 which provide additional protection. Note the consolidation of all solid state circuits in one enclosure, designed to operate at 100°C for efficient junction temperatures of the enclosed transistors and other solid state devices. This enclosure also contains the phase shift compensation networks for retrodirective subarray module steering using a 2 pilot tone scheme. Further verification of this concept and feasibility of adequate diplexer isolation, frequency offset and power budget must be conducted.

4.6.2 Operation Under Reduced Voltages

The advantages of the klystron configuration is the fact that efficiency and power level do not deteriorate significantly with voltage. To take advantage of this property, we have tried to determine the effect of solar cell degradation on klystron power output. This is indicated in Figure 4.18 for the condition that the klystron characteristics remain on the v-i portion of the solar cells corresponding to maximum d.c. output. This condition can only be achieved if the perveance of the tube is slightly changed. If the modulating anode is mounted on a diaphragm, such an adjustment could be made. It would also be useful for adjustment of tube-to-tube uniformity. It is seen that if the solar cells are not refurbished, the efficiency remains high, but the power output drops significantly. On this basis it was decided to refurbish solar cells and not require the transmitter to adjust perveance for solar cell optimal matching. The variation in perveance is rather nominal, and even if it remained constant, the efficiency would remain high, but there would be some further loss of power due to not being on the maximum VI product point for the solar cell output.

It was also of interest to estimate the effect of major solar flares on the klystron output. It was estimated that the voltage would drop to 97% of its nominal value and the current to 75% of its nominal value. For this condition, the perveance, S, would have to be adjusted from its nominal value of 0.25×10^{-6} to 0.20×10^{-6} via the modulating anode, to accommodate this change. Since the efficiency remains virtually unchanged, the power would drop by $(.97)(.75)$ to $(.727)(70.6) = 51$ kw. If the modulating anode were not adjustable, the above power condition would not prevail, and the voltage would be further reduced to keep the perveance $(I_0/V_0^{3/2})$ constant.

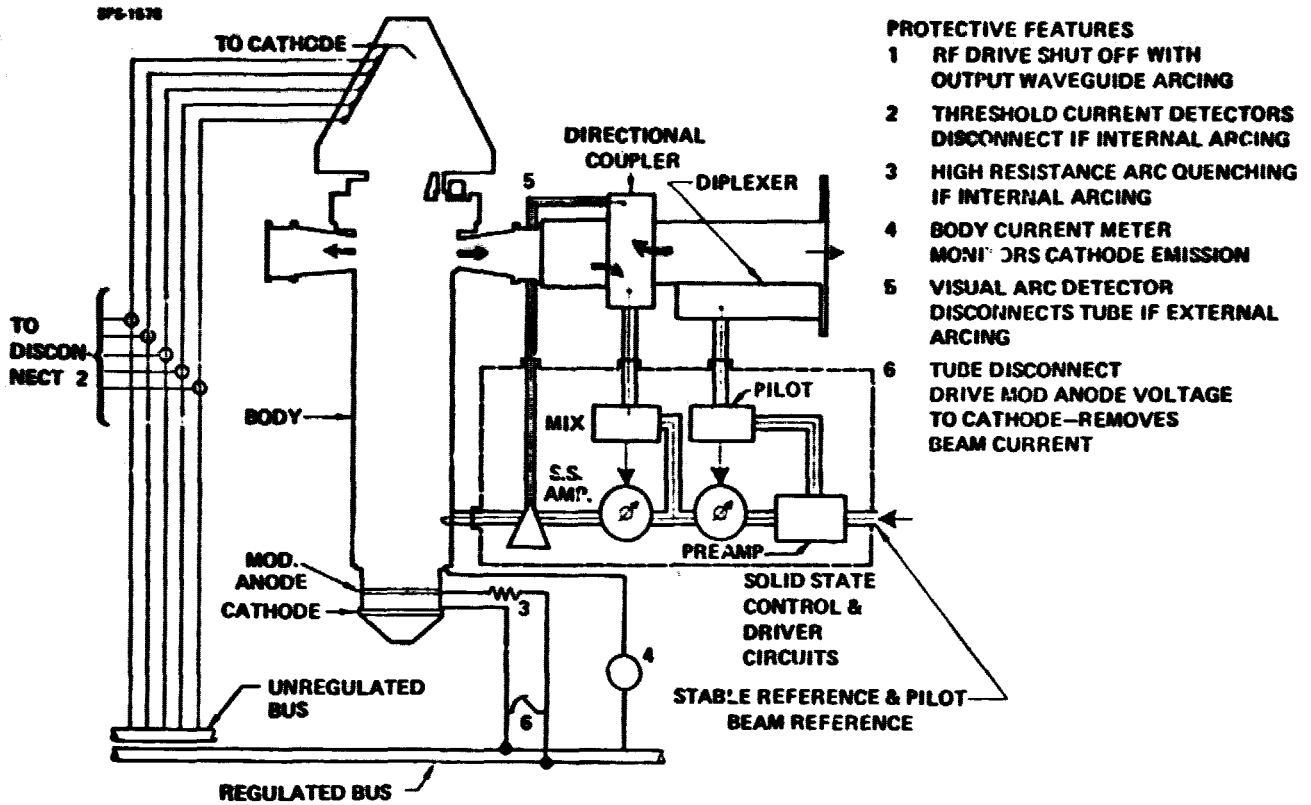


Figure 4-17 Klystron Protective Devices Including Phase Compensation

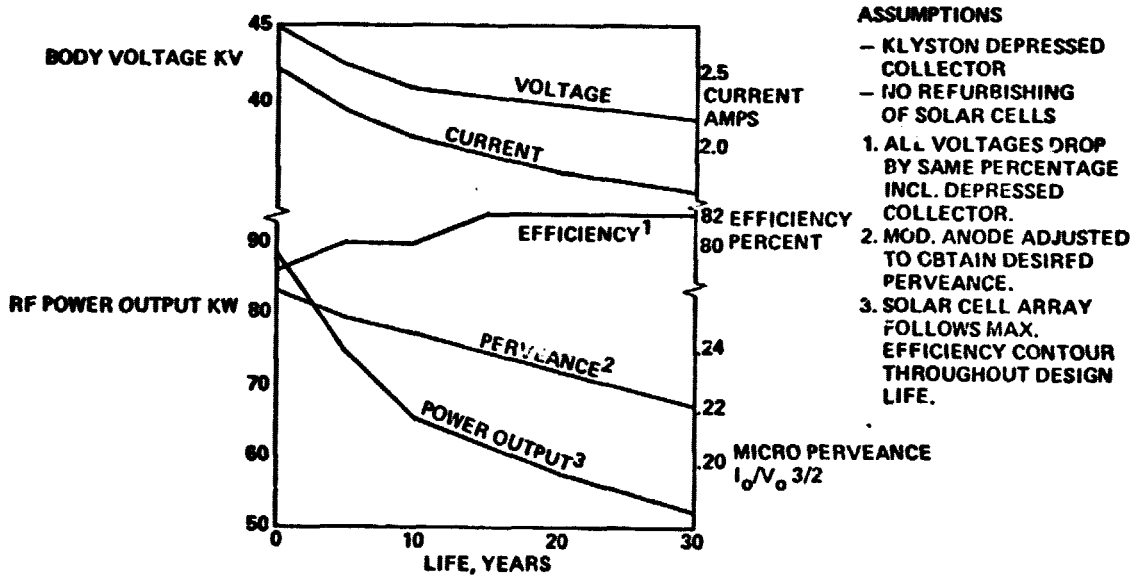


Figure 4-18 Klystron Performance When Optimally Matched to Solar Cell Output

4.6.3 X-ray Radiation Level Assessment

This section summarizes the findings of a short-term task to estimate the x-radiation background level of a six Gigawatt Solar Power Satellite (SPS) involving one of the three following options:

- Option #1 24,000 – 65 kV, 250 kW, 85% efficient klystrons
- Option #2 86,000 – 40 kV, 70 kW, 85% efficient klystrons
- Option #3 1 Million – 20 kV, 6 kW, 90% efficient amplitrans

Assumptions made in these estimates were:

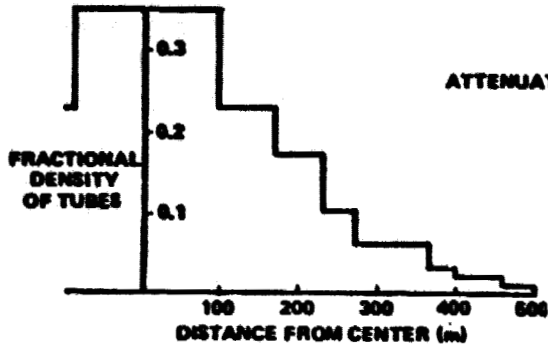
1. Klystrons emit x-rays as point sources at the center of their collectors.
2. The Klystrons are arrayed such that they do not shadow one another.
3. Klystrons are arrayed on a disc platform one kilometer in diameter with a fractional unit density given in Figure 4.19a.
4. Maximum electron energies are $2 V_0$. The reference Varian 500 kw klystron is estimated to have 10% of electrons @ $2 V_0$ and options 1 and 2 above are estimated to have 2% @ $2 V_0$.

4.6.3.1 X-ray Radiation Scaling

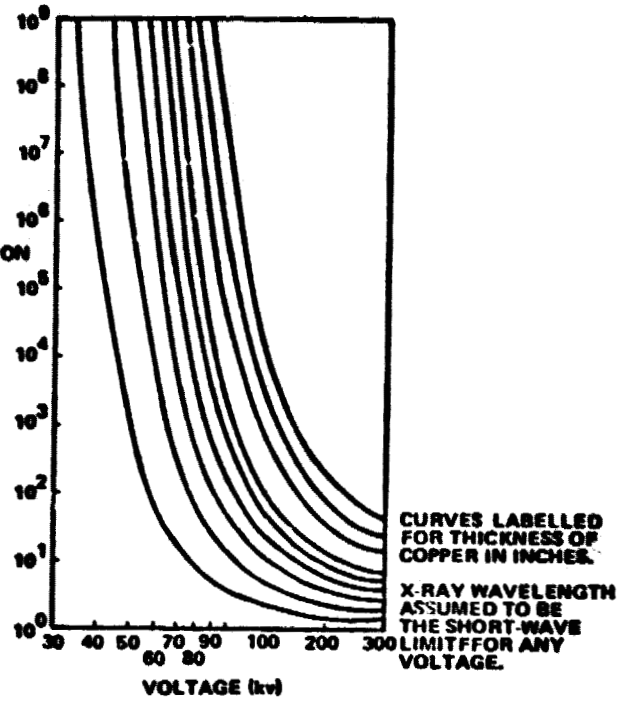
In order to estimate the amount of x-radiation background associated with each of the three options, simple scaling techniques were used based upon an existing known klystron source. This source, a 500 kW, 65 kV, 50% efficient klystron emits 300 mR/hour at 1 meter and has a copper anode configuration with a copper collector of 1/2 inch effective thickness. The equation used to scale the three options is

$$R_x = \frac{(300 \text{ mR/Hr}) \left(\frac{Z_x}{Z_{cu}} \right) (A) (M)}{\left(\frac{10\%}{X\%} \right) \left(\frac{14.8 \text{ amp}}{I_x} \right) (F)}$$

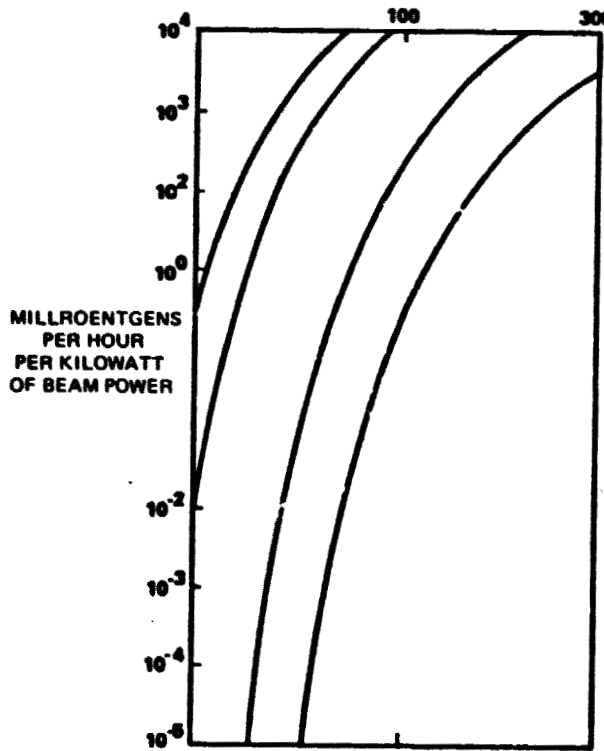
- where
- R_x = X-ray background from option X
 - Z_x = Atomic No. of option X anode (= 74 for Tungsten)
 - Z_{cu} = Atomic No. of Copper = 29
 - A = Attenuation factor due to collector thickness
 - M = Attenuation factor due to collector material
 - X% = Number of electrons @ $2 V_0$
 - I_x = Option X Beam current
 - F = Attenuation factor due to V_0



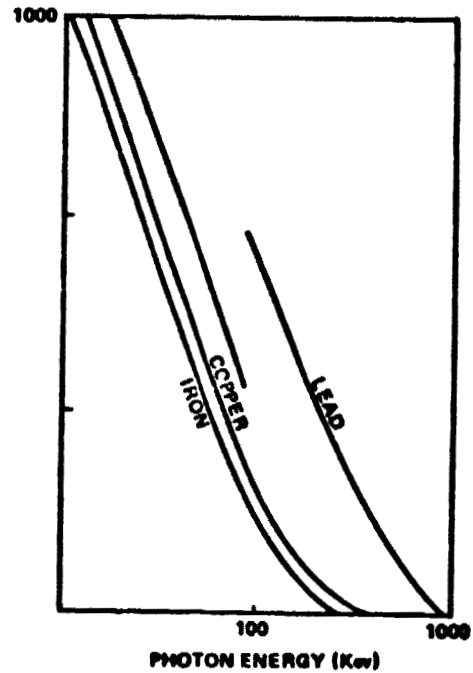
(a) Klystron distribution within space array



(b) X-ray attenuation in copper



(c) X-Ray Intensity from a Klystron through copper shielding



(d) Absorption coefficients of common metals

Figure 4.19 Xray Radiation Level Assessment

D180-22876-4

"A" is simply the ratio of attenuations of option X thickness to the 1/2 inch thickness of the reference collector and is obtained from Figures 4.19b and 4.19c, i.e., for an option X collector thickness of 0.1 inch.

$$A = \frac{\text{Attn}_x}{\text{Attn}_{1/2}} = \frac{3 \times 10^2}{5 \times 10^{-2}} @ 40 \text{ kV} = 6 \times 10^3$$

M, the attenuation factor due to collector material is obtained from Figure 4.19d, e.g., for a collector material of steel (mainly iron)

$$M = \frac{\text{Absorption in Cu}}{\text{Absorption in Fe}} \cong 1.6$$

F, the attenuation factor due to V_o is the ratio of attenuations at V_o for option X to V_o for 65 kV, e.g., for Option #1 $V_o = 40$ kV and

$$F = \frac{10^6}{2 \times 10^1} = 5 \times 10^4 \text{ (see Fig 4.19b)}$$

Table 4.14 summarizes the results of scaling using the above equation.

4.6.3.2 X-ray Radiation From Total Array

A rough estimate of the total radiation from the array of klystrons can be obtained by assuming all the tubes are positioned at the center of the array. This assumption is valid for large distances from the array. Thus the total radiation R_T is given as

$$R_T = \frac{N S}{D^2}$$

where N = Total number of klystrons

S = Radiation level per klystron

D = Distance from the center of the array

However, since the real problem is to find the distance D at which the radiation level is no more than 5 R per year, the maximum allowable radiation level for man, R_T is set to 5 R/Yr and we solve for D

$$D = \sqrt{\frac{NS}{R_T}}$$

Solutions to this equation for options 1a, 1b, 2a and 2b yields the following minimum approachable distances to the total array:

D180-22876-4

Table 4-14 X-Ray Scaling Relations

SPS-1007

	POWER CW	VOLTAGE V_0	CURRENT (AMPS)	TUBE EFF. η	MAX ELECTRON VELOCITY (EST)	NO. OF TUBES	ANODE MAT'L	COLLECTOR CONFIGURATION	X-RAY BCKGND. LEVEL
REFERENCE KLYSTRON	500 Kw	65 Kv	14.8	50%	10% ⊙ $2 V_0$	N.A.	Cu	1/2" COPPER EFFECTIVE THICKNESS	300 MR/MR ⊙ 1 METER (MEASURED)
OPTION #1 KLYSTRON	70 Kw	40 Kv	2.2	85%	2% ⊙ $2 V_0$	86,000	Tungsten	.05" STEEL	21.8 MR/HR
								0.1" STEEL	4.4 MR/HR
OPTION #2 KLYSTRON	250 Kw	65 Kv	5.0	85%	2% ⊙ $2 V_0$	24,000	Tungsten	.05" STEEL	16.6 R/HR
								0.1" STEEL	3.9 R/HR
OPTION #3 AMPLITRON	6 Kw	20 Kv	0.33	90%	1% ⊙ $2 V_0$	1×10^6	Cu	0.25" COPPER	3.3×10^{-4} MR/HR
								0.5" COPPER	3.3×10^{-7} MR/HR

D180-22876-4

1a	-	1.8 Kn.
1b	-	0.8 Km
2a	-	26.4 Km
2b	-	12.8 Km

(a corresponds to the 0.05" steel collector configuration and b corresponds to the 0.1" steel collector configuration.)

In the case of option 3a and 3b, the amplatron source intensity is considerably lower, implying that the minimum approachable distance will be relatively small. Thus the assumption that all the klystrons are equivalently positioned at the center of the array is a poor one and a more realistic distribution will be required.

Referring to Figure 4.19a it is easy to see that for very close distances from the surface of the array (e.g., 1 meter), an observer is basically looking at a plane of uniform x-ray intensity for the innermost step and that the remainder of the steps contribute insignificantly to the total radiation due to their remoteness to the observer (100 meters and beyond). For this assumption then we have the situation depicted in Figure 4.20a where the observer is a distance h from the surface of the array and a distance $h^2 + r^2$ from an element of x-ray intensity I . I is given by

$$I = \frac{0.35 (10^6 \text{ amplitrons}) S}{\pi R^2 (m^2)}$$

where 0.35 is the fraction of the total number of amplitrons from

$$r = 0 \text{ to } r = 100m$$

$$R \cong 100 \text{ meters}$$

$$S = \text{X-ray background level per amplatron}$$

The total radiation S_t seen by the observer is thus given by

$$S_t = 4 \int_0^{\pi/2} \int_0^R \frac{I r dr d\theta}{\sqrt{h^2 + r^2}}$$

or

$$\begin{aligned} S_t &= 2\pi I \int_0^R \frac{r dr}{h^2 + r^2} \\ &= \pi I \left[\ln (h^2 + r^2) \right]_0^R \\ &= \pi I \left[\ln (h^2 + R^2) - \ln h^2 \right] \end{aligned}$$

Substituting for $R \approx 100$ meters, $h = 1$ meter and I given above we have

$$\begin{aligned} S_t &= \pi \frac{0.35 (10^6) S}{\pi (10^4)} \left[\ln(1 + 100^2) - \ln 1^2 \right] \\ &= 35.0 (S) [9.2] \\ &= 322(S) \end{aligned}$$

Thus for option 3a, $S = 3.3 \times 10^{-4}$ MR/Hr and

$$S_{3a} = 0.9 \text{ R/Yr @ 1 meter}$$

and for option 3b, $S = 3.3 \times 10^{-7}$ MR/HR and

$$S_{3b} = 0.9 \times 10^{-3} \text{ R/YR @ 1 meter}$$

The calculations herein indicate that the closest distance at which a man may approach an array of klystrons on a Solar Power Satellite depends a great deal on the design of the klystron. The results for each of the options is given in Table 4.15.

It is probably worthwhile to mention that klystron orientation in the array may make a significant difference in the total x-ray background. This is due to the fact that the base of the klystron is a very effective shield against the x-rays. In other words, the base of the klystrons shade the x-ray source at the collector very effectively. Thus for example if all the klystrons are oriented in the same direction with respect to one another, there is some solid angle θ at both ends of the satellite in the same direction in which the radiation level will be significantly reduced. The angle θ can be estimated from the scale drawing of the klystron design shown in Figure 4.20b. The x-ray background intensity within this cone of angle θ is probably below the level of 5 R/Yr.

Table 4-15 Minimum Approachable Distance for X-Rays

OPTION	POWER CW	COLLECTOR CONFIGURATION	MINIMUM APPROACHABLE DISTANCE
1a KLYSTRON	70 kW	.05" STEEL	1.3 Km
1b KLYSTRON	70 kW	0.1" STEEL	0.8 Km
2a KLYSTRON	250 Kw	.05" STEEL	26.4 Km
2b KLYSTRON	250 Kw	0.1" STEEL	12.8 Km
3a AMPLITRON	6 Kw	1/4" COPPER	SAFE @ 1 METER (0.9 R/YR.)
3b AMPLITRON	6 Kw	1/2" COPPER	VERY SAFE @ 1 METER (0.9 x 10 ³ R/YR.)

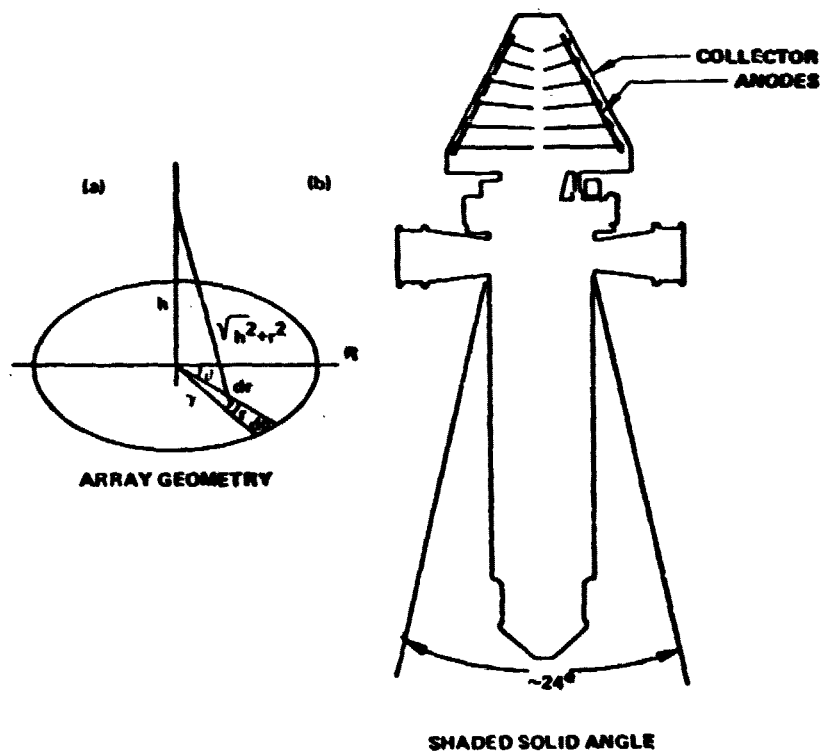


Figure 4.20 Geometry for Xray Configuration of Klystron

5.0 POWER DISTRIBUTION

The power distribution system for the MPTS provides for the distribution of large amounts of power from the rotary joint to DC to RF converters located on the antenna. The DC to RF converters used are klystrons with five depressed collectors and require a wide variety of supply voltages. The klystrons provide 70.66 kW of RF output. During Part I of the study effort, a three stage depressed collector klystron was used as the baseline DC to RF converter to initially define antenna power distribution in order that satellite power generation trades could be accomplished. The following paragraphs discuss the MPTS power distribution system requirements, design concepts and considerations, and unresolved issues.

5.1 POWER DISTRIBUTION SYSTEM REQUIREMENTS

The MPTS power distribution and control system must accomplish the following functions:

- (a) Route raw unconditioned power from the sliprings at the rotary joint to the DC/RF converters contained in the power control sectors on the antenna.
- (b) Provide for conditioning of the power required by the various klystron elements.
- (c) Provide for fault protection, isolation, and control of the various MPTS elements.
- (d) Provide energy storage for periods of times (such as occultation) when the main power busses are not providing power.

The raw power delivered to the antenna must accommodate the antenna power taper. The baseline antenna is a 10-step approximation of a 10 dB gaussian power taper. The effective temperature of the back of the antenna where most of the power distribution equipment is installed is shown in Figure 5-1.

Tables 5-1 and 5-2 show the power and voltage regulation and power requirements of the various klystron elements. These requirements must be satisfied by the voltage regulation capabilities of the power distribution and control system. In general, klystron depressed collector voltages must be regulated within $\pm 5\%$ of their nominal values while all other klystron elements require much more stringent regulation.

In order to optimize the mass of the MPTS, an attempt was made in the tube design to minimize the mass of the components which make up the klystron. This reduction in klystron mass imposes requirements on the power distribution system switchgear to remove power very rapidly in the event of arcing either in the tube or the output waveguide. Minimum mass in the tube implies that the tube elements cannot withstand the heat generated when internal arcs occur for substantial periods of time.

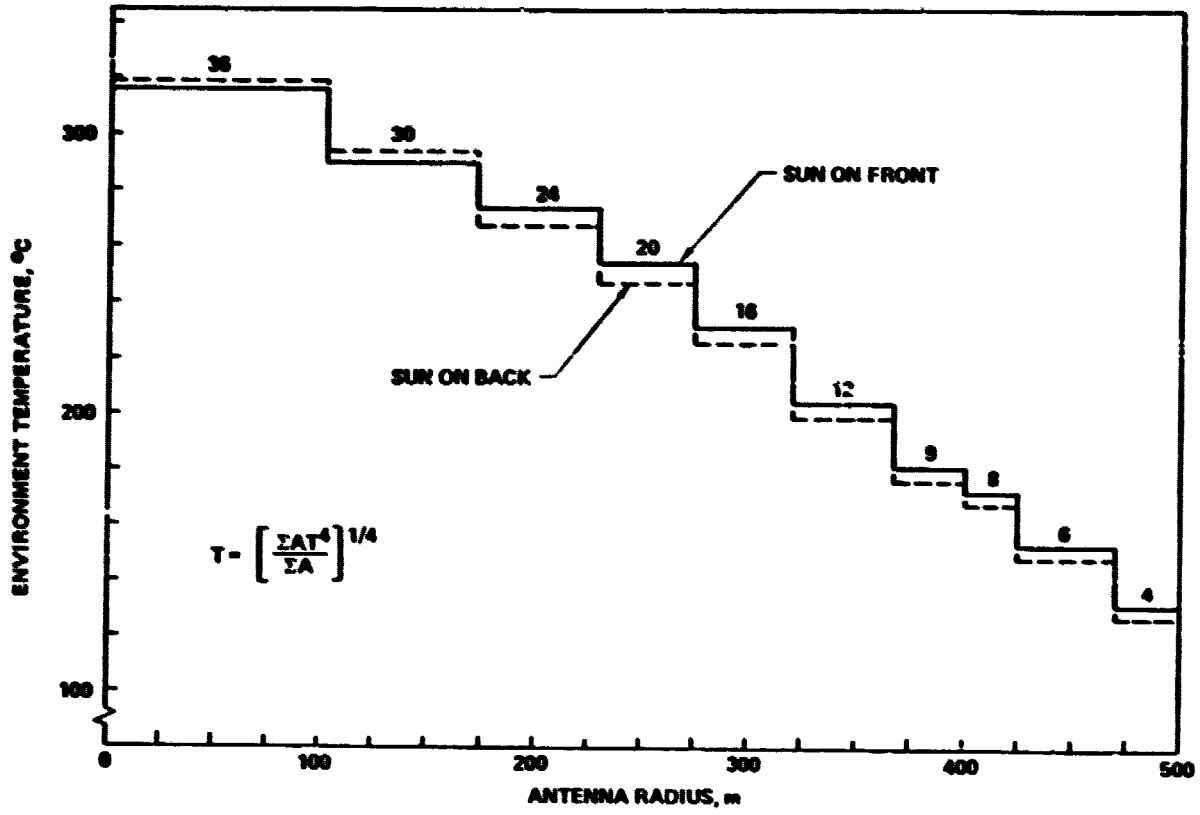


Figure 5-1. Effective Temperature of Back of Antenna

SPS 943

Table 5-1. High Power Klystron Depressed Collector Design

DESIGN PARAMETERS

$V_0 = 42.1$ KV.
 $I_0 = 2.2$ AMPERES
 RF OUTPUT = 70.88 KW

ELECTRONIC EFF. = 79%
 OUTPUT CIRCUIT EFF. = 97%

POWER REQUIREMENTS

KLYSTRON ELEMENT	3 SEGMENT COLLECTOR			5-SEGMENT COLLECTOR		
	VOLTAGE	CURRENT	POWER	VOLTAGE	CURRENT	POWER
MODULATING ANODE	21,050	0.088	1,852.4	21,050	0.088	1,852.4
BODY ANODE (IN SERIES W MOD ANODE)	21,050	0.088	1,852.4	21,050	0.088	1,852.4
SPIKE ELECTRODE 0	0	0.044	---	0	0.044	---
COLLECTOR NO. 1	25,160	0.044	1,107.4	21,050	0.044	926.4
COLLECTOR NO. 2	37,890	0.088	3,334.3	25,160	0.088	2,214.1
COLLECTOR NO. 3	40,000	1.936	77,440.0	29,470	0.154	4,538.4
COLLECTOR NO. 4	---	---	---	37,890	0.330	12,503.7
COLLECTOR NO. 5	---	---	---	40,000	1.452	58,080.0
CATHODE	TBD	TBD	50.0	TBD	TBD	50.0
SOLENOID	TBD	TBD	1,000.6	TBD	TBD	1,000.0
TOTAL POWER			86,636.5			
PROCESSED POWER			5,862.2			
% EFF.			81.56 %			
				83,017.4		
				12,433.7		
				85.11%		

SPS 945

Table 5-2. Klystron Power Regulation Requirements

	% REGULATION
MODULATING ANODE*	± 0.5% V
BODY ANODE*	± 0.5% V
SPIKE ELECTRODE 0	
COLLECTOR NO. 1	± 5% V
COLLECTOR NO. 2	± 5% V
COLLECTOR NO. 3	± 5% V
COLLECTOR NO. 4	± 5% V
COLLECTOR NO. 5	± 5% V
CATHODE	+ 0.5 V, -1.5% V
SOLENOID	± 1% V

*MODULATING ANODE CONNECTED IN SERIES WITH THE BODY ANODE. BODY ANODE CURRENT FLOWS THROUGH THE MODULATING ANODE POWER SUPPLY

Klystron life is impacted by cathode heater power on-off cycles. In order to increase the MTBF of the klystron, it is proposed that heater power be maintained during the period of time when occultation (caused either by the earth or other solar power satellites) occurs. In addition, other MPTS systems (antenna pointing, phase control, avionics, etc.) may require power during occultation or periods when maintenance is being performed on the antenna or satellite and power is not being supplied by the main power busses.

5.2 POWER DISTRIBUTION AND CONTROL SYSTEM CONCEPT

5.2.1 System Concept

Aluminum sheet conductors were selected as the main power busses from the rotary joint slip rings to the switchgear on the antenna since they are the most mass efficient. As was shown in the Part I report, sheet conductors maximize the ratio of surface area (heat rejection area) to cross section area (heat generation area due to I^2R). (Also see Reference 5-1.)

A review of the data shown in Table 5-2 shows that for the klystron with the five depressed collectors, the major amount of power (approximately 85%) is required by the fourth and fifth stages of the depressed collector. For one millimeter thick aluminum sheet conductors operating at 100°C the voltage drop is 0.2327 volts per meter of length regardless of the current, since conductor width is proportional to current. Calculations were made to determine the transmission losses for the other required klystron voltages if they were generated on the satellite and routed to the antenna. The results showed that for a DC/DC conversion efficiency of 96% it was more efficient to use a DC/DC converter to derive all klystron power except for depressed collectors 5 (Collector A power source) and 4 (Collector B power source).

A block diagram of the MPTS power distribution and control system is shown in Figure 5-2. In addition to providing power for DC/RF converters, the system also supplies power for antenna pointing, thermal control systems, energy storage, and antenna control systems.

Each DC/DC converter provides power to approximately 0.5% of the total number of antenna klystrons. The power requirements for the DC/DC converter for the three stage depressed collector klystron used in Part I are shown in Figure 5-3 and for the five stage depressed collector klystron used in Part II in Figure 5-4. An improvement in klystron DC/RF conversion efficiency is realized when the number of depressed collectors is increased from three to five as shown in Table 5-1.

Even though an improvement in DC/RF conversion efficiency is realized in increasing the number of depressed collectors, overall system efficiency may not be increased if power processing losses exceed the additional RF power gained in the DC/RF conversion. Table 5-3 presents the results of an analysis performed to verify that the additional power processing did not significantly impact the overall improvement in systems efficiency realized by using the five stage depressed collector klystron. The system using the klystron with five depressed collectors is more efficient.

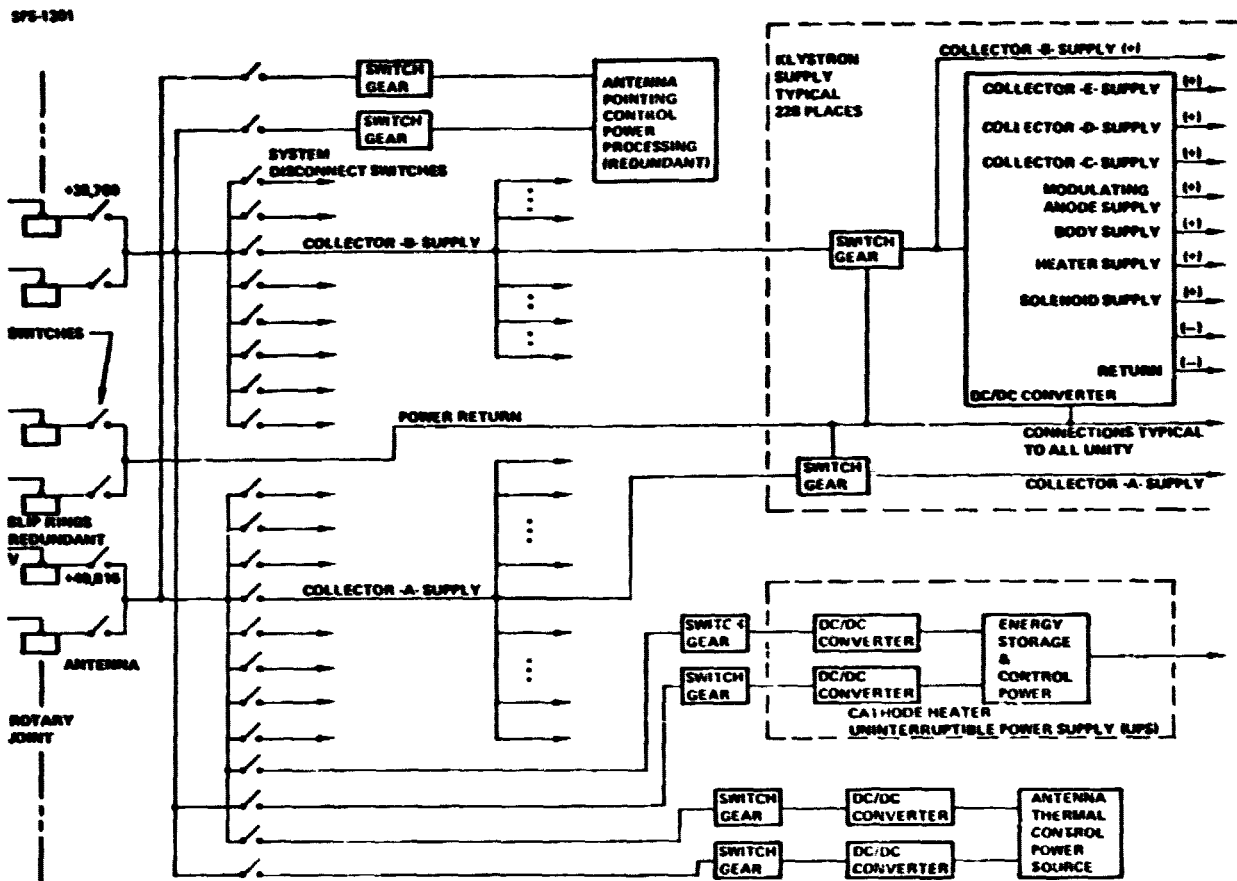
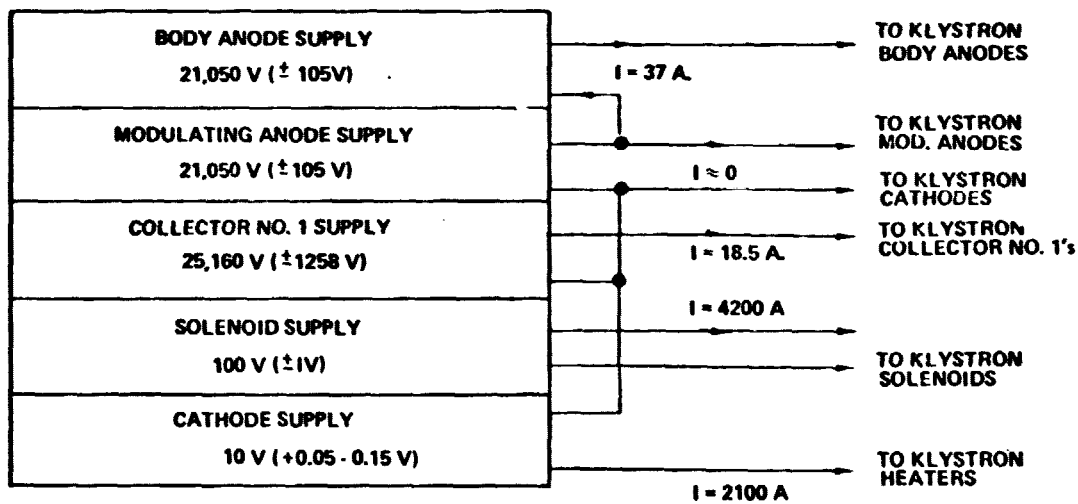


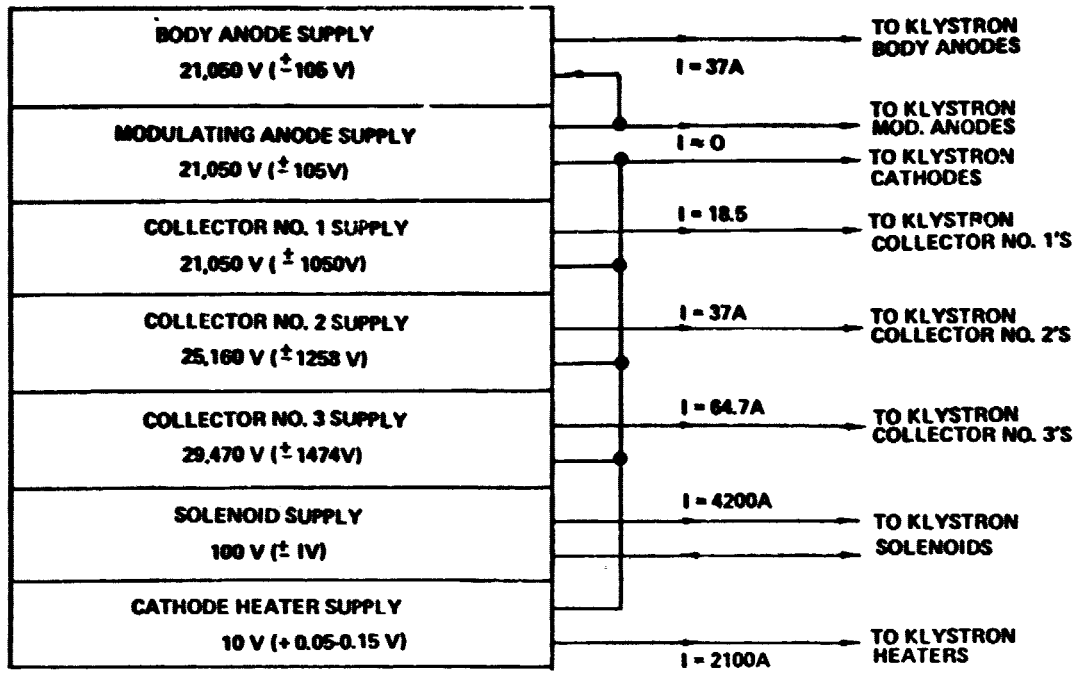
Figure 5-2. MPTS Power Distribution System Block Diagram

SPS 047



$P_{out} = 2,464,160$ W
 $\eta = 0.96$
 $P_{in} = 2,566,833$ W

Figure 5-3. DC/DC Converter For Three Segment Depressed Collector Klystron Designed MPTS



$P_{out} = 5,225,754 \text{ W}$
 $\eta = 0.96$
 $P_{in} = 5,443,494 \text{ W}$

Figure 5-4. DC/DC Converter For Five Segment Depressed Collector Designed MPTS

Table 5-3. Five-Segment Depressed Collector Klystron Is More Efficient

KLYSTRON TYPE	TUBE EFFICIENCY	POWER REQUIRED		TUBE + DC/DC CONVERTER EFFICIENCY
		PROCESSED	UNPROCESSED	
3 - SEGMENT	81.56 %	5,862.2	80,783.3	81.32 %
5 - SEGMENT	85.11 %	12,433.7	70,583.7	84.59 %
	$\Delta = 3.55 \%$			$\Delta = 3.27 \%$

*DOES NOT INCLUDE ANY POWER DISTRIBUTION I^2R LOSSES.

The present antenna structural design concept consists of a relatively sparse primary structure, fairly dense secondary structure and ten different types of antenna subarray elements to achieve a ten step approximation of the desired taper. Within the subarray element, one set of connections provides the interface between the external power distribution system and the subarray distribution system. Power is routed from the power sector substations to the antenna subarray elements. Disconnects are installed at the power sector substations to provide isolation for maintenance and repair.

The power distribution and control system for the antenna is very similar to a conventional earth based system. The choice of locations for the power sector substations presents a problem which is normally encountered with earth-based systems. The optimum location from an efficiency standpoint may not be available because of inaccessibility or because it has been dedicated to other uses. Three locations are possible for the power sector substations: (1) on the back of the secondary structure which is relatively inaccessible, has shorter low voltage conductor runs (and hence lower conductor losses) and is near the high heat source of the klystrons; (2) on the back of the primary structure which is readily accessible and has longer low voltage conductor runs and higher conductor losses; (3) on the antenna face where temperatures are benign but the equipment scatters the RF beam. Option 3 was quickly rejected. The objective of a substation is to give reliable service at minimum cost (Ref. 5-2). This cost is derived from weighing three costs: installation and equipment costs, power losses caused by substation design and location, and revenue losses due to substation outages. Revenue losses due to substation outage is directly related to mean time to repair.

An analysis was performed to ascertain the loss in ground power output due to an outage of one power control sector on the transmitting antenna. One power control sector provides approximately 0.44% of the antenna power. Loss of one power sector results in the loss of approximately 1.0% of the ground output due to loss of the power sector RF output, decreased beam efficiency and increased sidelobes. This results in the loss of 50 megawatts of ground output for each power sector outage. As can be seen, it is important that the substation be located such that it is readily accessible and allows for rapid equipment replacement repair.

The heat which must be rejected by the DC-DC converter thermal control system is from a relatively low source temperature (70°C). (See Section 6.4.2 and 6.4.3.) The view angle to free space for the radiator is increased by moving the radiator back from the klystron installation location. Thus, radiator size is smaller for power sector substations installed at the back of the primary structure than for those installed at the back of the secondary structure.

Based on the above rationale, the power sector substation location was selected to be at the back of the primary structure. Aluminum sheet conductors are routed from the rotary joint to the power sector control substation located at the primary structure truss intersection nodes at the back of the structure.

The MPTS antenna was divided into approximate equal power areas to define power control sectors. The power control sectors are shown in Figure 5-5. The number in circles are the power control sector reference numbers. The other numbers in each sector represent the number of klystrons in each control sector. Figure 5-6 shows the location of the power sector control substation and the associated DC/DC converters. No substations are located on the center structural node, since this node is in the center of the highest waste heat flux region.

Previous studies (Refs. 5-1 and 5-2) have selected a lateral flow distribution system since this concept resulted in a lighter weight system. The electrical feed to the referenced configurations was near the antenna center. With the yoke mount configuration a lateral flow distribution was also selected to provide a lower weight antenna power distribution system.

5.2.2 MPTS Conductor Selection

The conductors for the MPTS power distribution consist of aluminum sheet conductors from the rotary joint to the power sector control substations, circular aluminum conductors from the substations to the subarray interface, and circular conductors on the subarray. The following paragraphs discuss the rationale for conductor selection and the design of the conductor systems for the three areas of conductor service: rotary joint to the substations, substation to the subarrays, and subarray wiring. All conductor analyses shown are for a quarter section of the MPTS antenna.

5.2.2.1 Rotary Joint to Power Sector Control Distribution

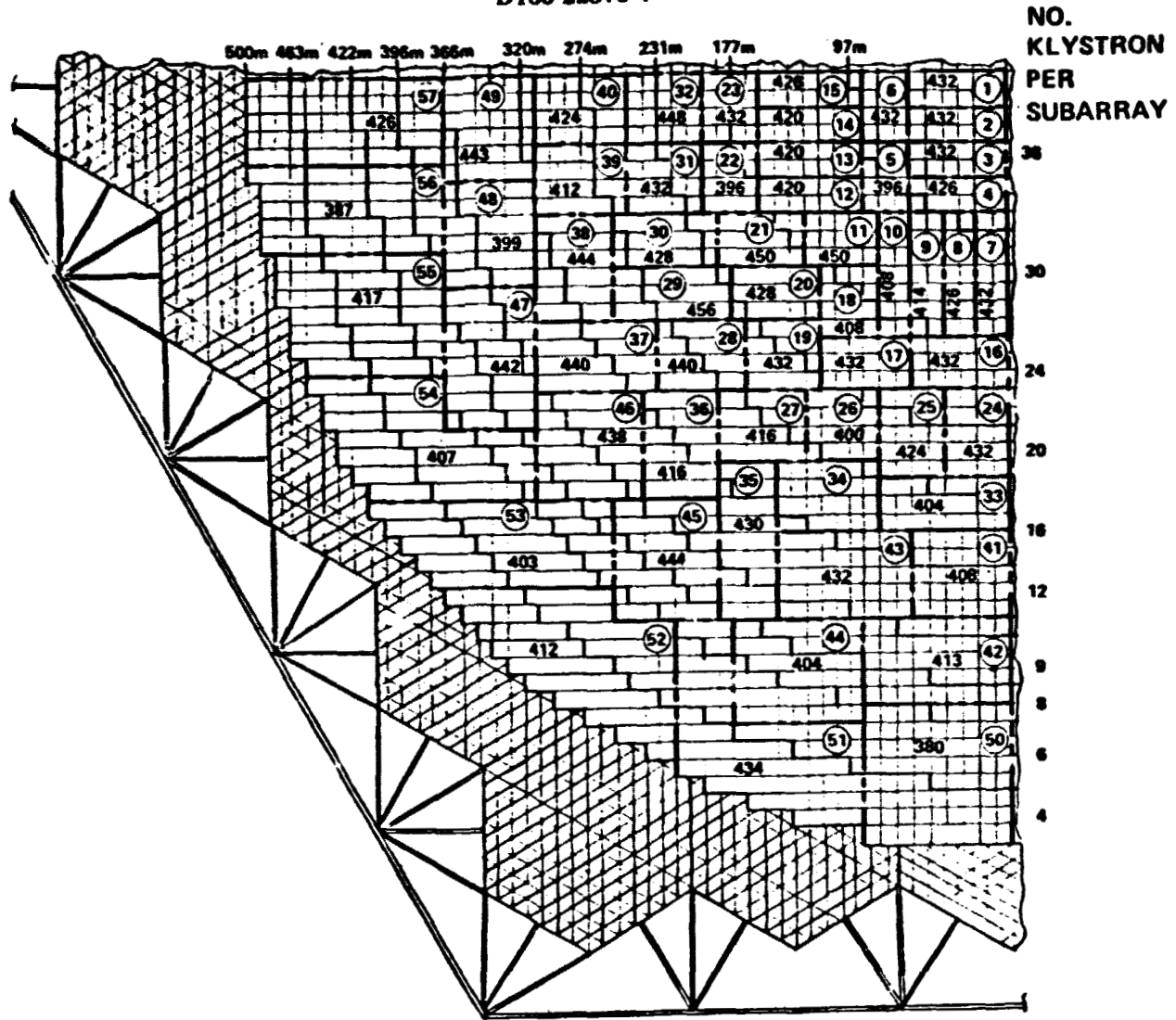
Aluminum sheet conductors were selected for this application since they result in a minimum mass conductor system. Mounting provisions are available for large sheets on the back side of the antenna primary structure. In order to determine the sheet conductor performance as a function of antenna location, the curves shown in Figures 5-7 through 5-12 were developed. Each of the sets of curves are of the form $I/W\sqrt{t} = F(T)$ where

- I = Conductor current in amperes
- W = Conductor width in centimeters
- F(T) = Function of conductor operating temperature (°C)

The curves were developed using a thermal radiative interchange factor computer program. This program includes a ray trace capability to generate views of the conductors to free space and to the antenna to compute, for the conductor location, the conductor thermal performance.

The differences in the curves are primarily due to their location on the antenna and the view factor of the conductor to the antenna background temperature shown in Figure 5-1. For each conductor unit length the mass per unit can be computed (M/L) using the curves of Figure 5-7 through 5-12 for any operating temperature as follows:

D180-22876-4



STEP	NO. SUBARRAYS	NO. KLYSTRONS
1 @ 36	272	9792
2 @ 30	580	17420
3 @ 24	612	14688
4 @ 20	612	12240
5 @ 16	756	12096
6 @ 12	864	10368
7 @ 9	628	5652
8 @ 8	576	4608
9 @ 6	1032	6192
10 @ 4	1000	4000
TOTALS	6932	97,056
POWER OUTPUT: (ANTENNA)		6.79 GW
(GROUND)		5.01 GW

Figure 5-5. MPTS Power Distribution Control Sectors

SPS-1170

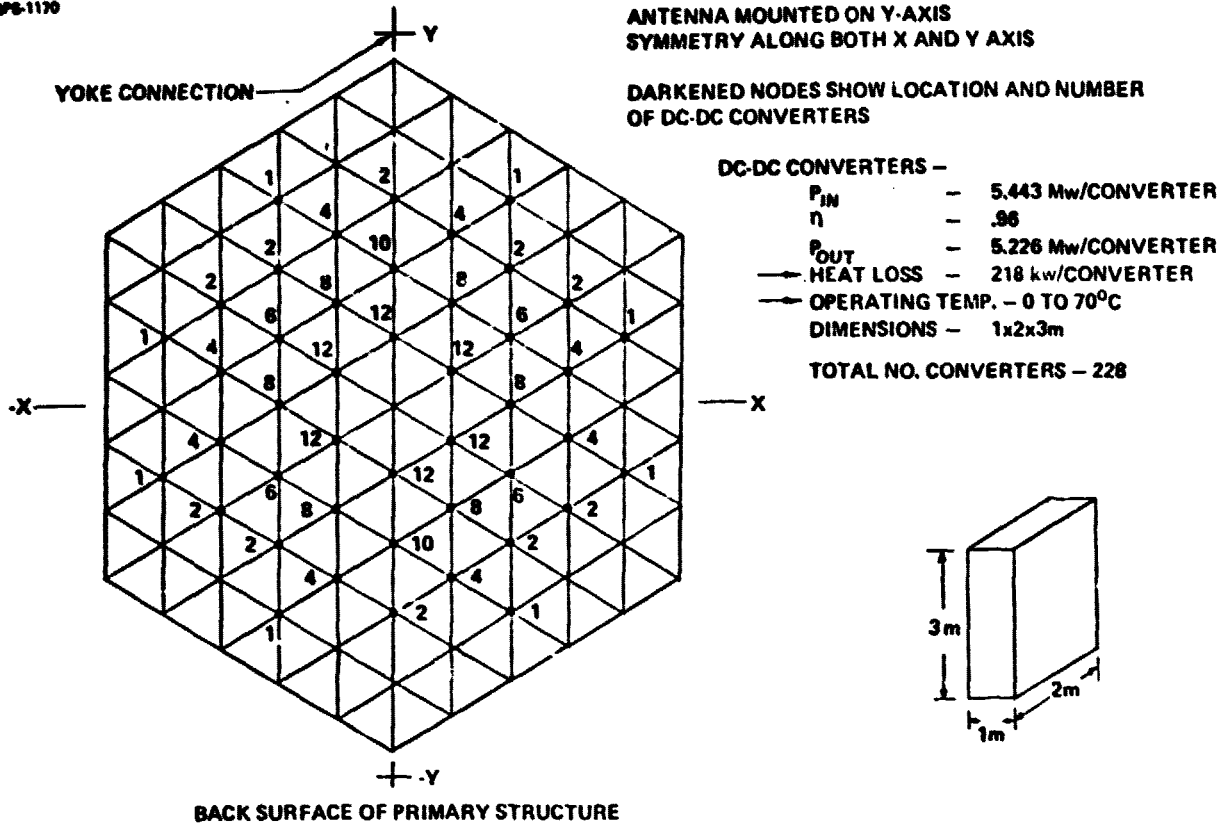


Figure 5-6. MPTS Reference Power Conditioning Placement

SPS-1373

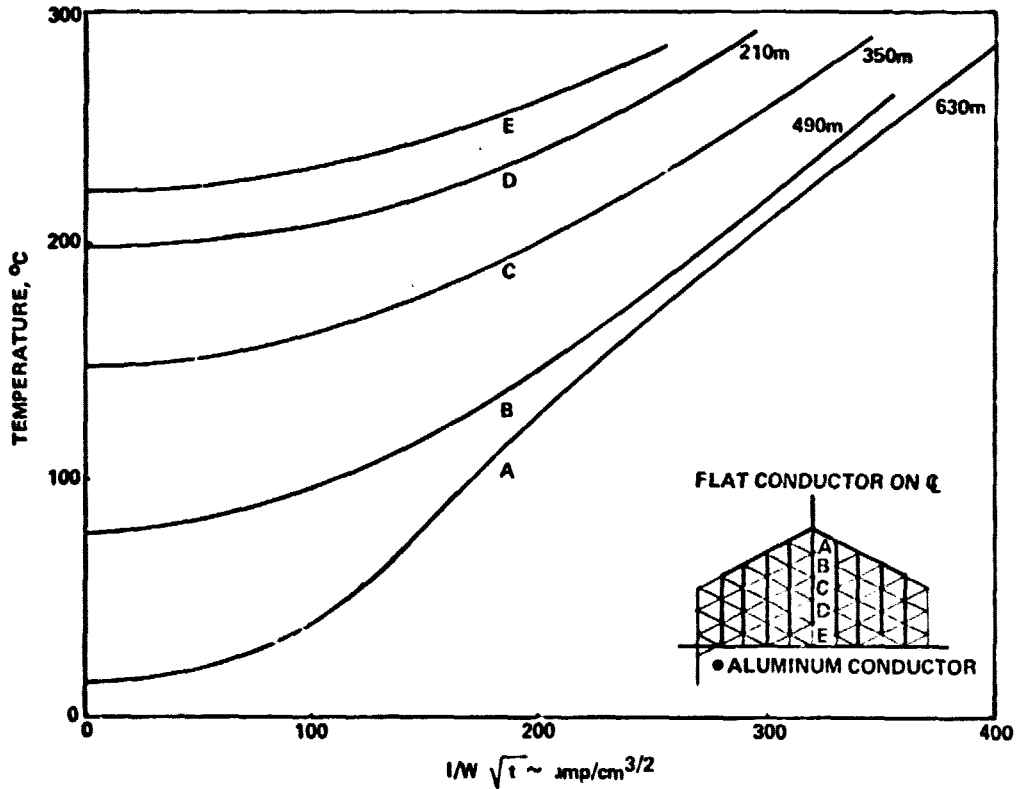


Figure 5-7. Distribution Conductors MPTS Antenna (Flat Conductors)

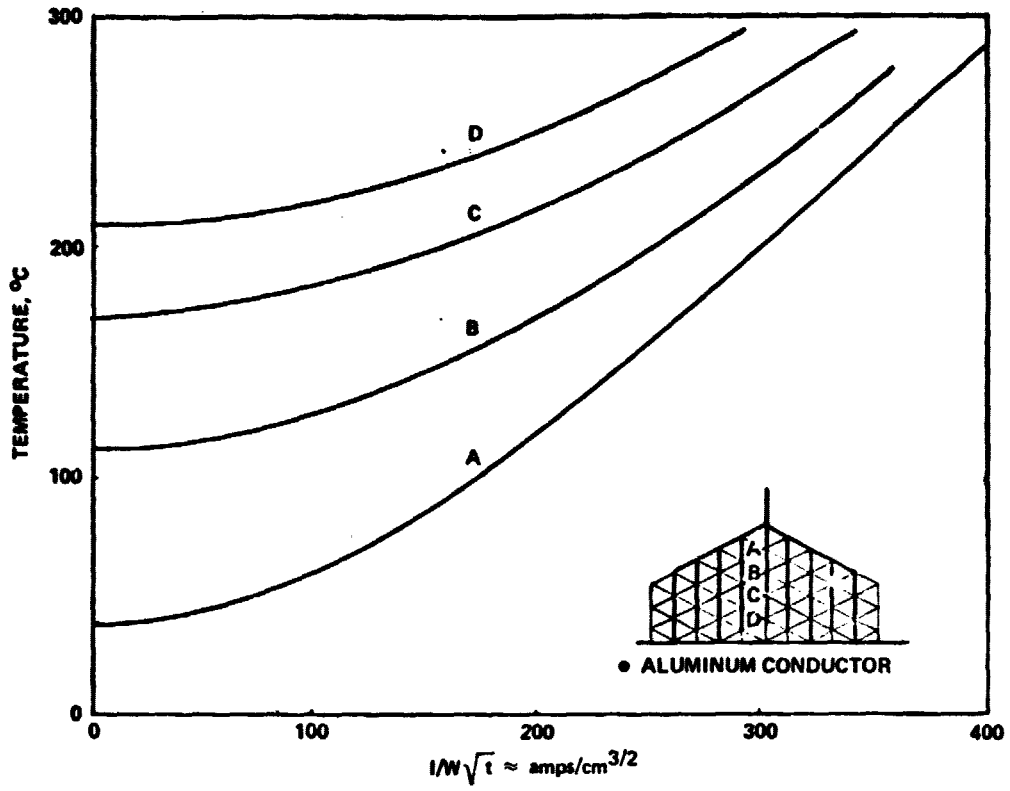


Figure 5-8. Distribution Conductors MPTS Antenna (Flat Conductors)

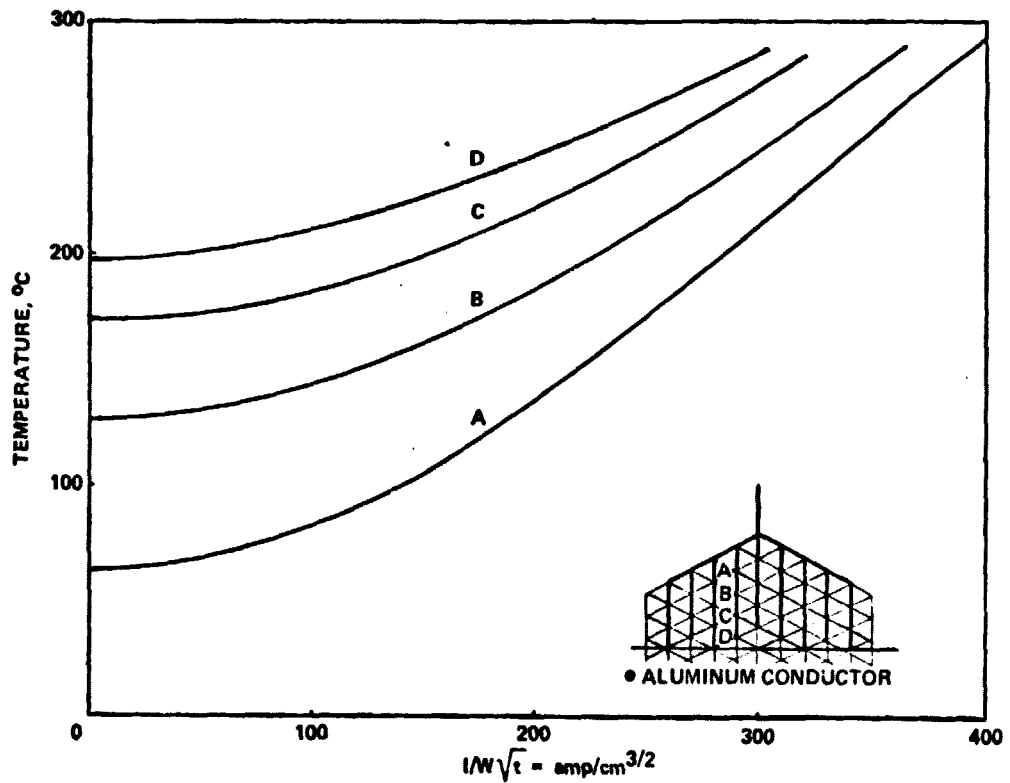


Figure 5-9. Distribution Conductors MPTS Antenna (Flat Conductors)

SPS-1362

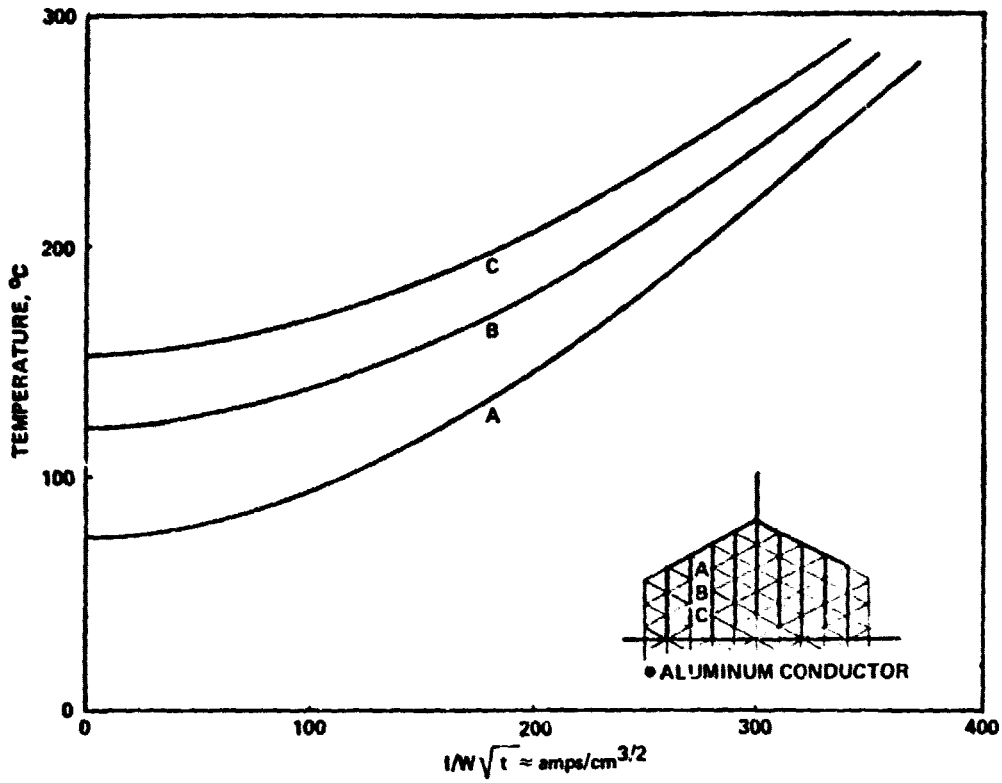


Figure 5-10. Distribution Conductors MPTS Antenna (Flat Conductors)

SPS-1370

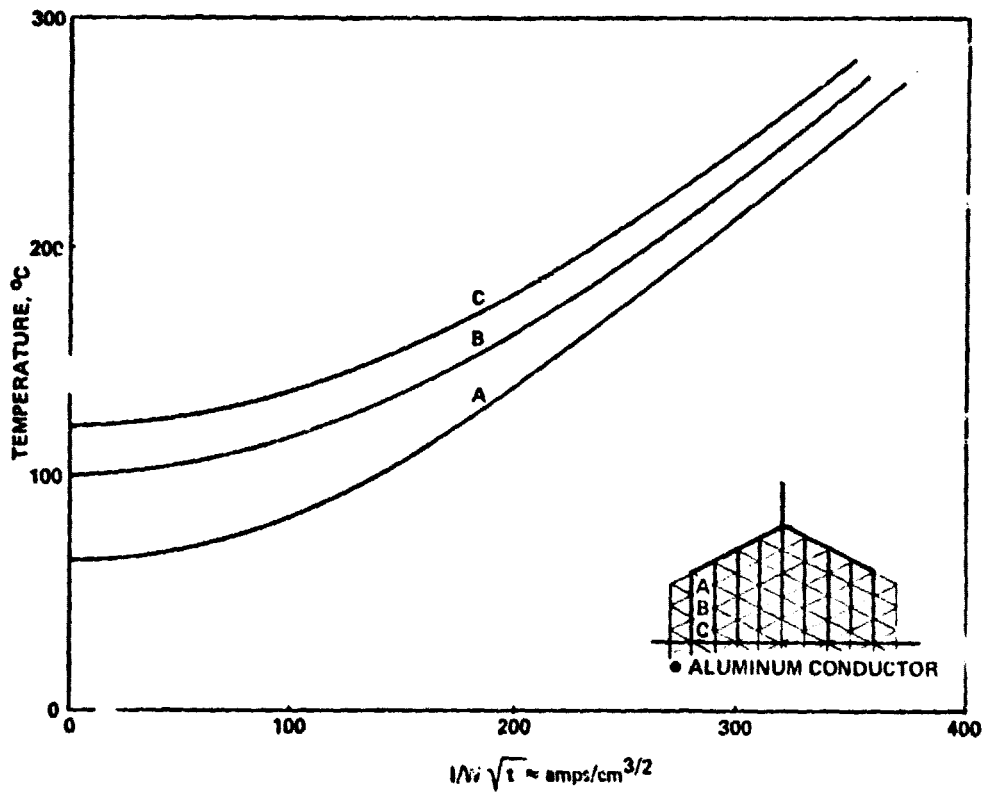
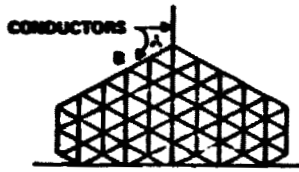
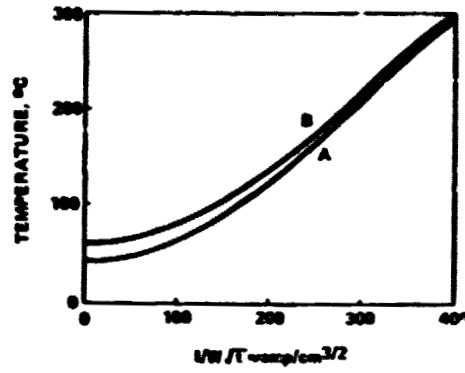


Figure 5-11. Distribution Conductors MPTS Antenna (Flat Conductors)

LOCATION & ROUTING



THERMAL ANALYSIS



FLAT ALUMINUM CONDUCTOR DIMENSIONS T, W

MASS OPTIMIZATION

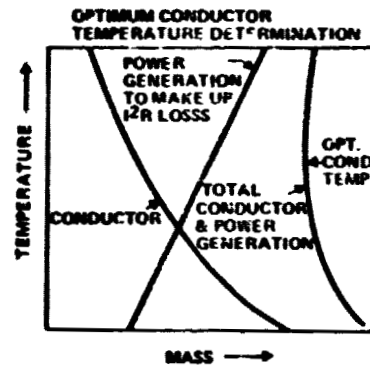


Figure 5-12. Outer Conductors MPTS Antenna (Flat Conductors)

D180-22876-4

M/L = WTσ

where **M/L = mass per unit length (gm/cm)**
W = Conductor width in Cm.
t = Conductor thickness in Cm.
σ = density of aluminum 2.7 gm/cm³

but **I/W √t = F(T)**

then **M/L = $\frac{I \sqrt{t} \sigma}{F(T)}$**

For conductor resistance

R = $\frac{\rho L}{A}$

where: **A = Conductor area cm²**
ρ = Conductor resistivity, Ωcm²
R = Conductor resistance (ohms)

The conductor I²R loss per unit length

$$\frac{I^2 R}{L} = \frac{I^2}{L} \frac{\rho L}{A} = \frac{I^2 \rho}{A} = \frac{I^2 \rho}{Wt}$$

but again

$$\frac{I}{W \sqrt{t}} = F(T)$$

then the per unit loss

$$\frac{I^2 R}{L} = \frac{I^2 \rho}{\frac{I \sqrt{t}}{F(T)}} = \frac{I \rho F(T)}{\sqrt{t}}$$

The photovoltaic power satellite has a mass of 51.71 million metric tons and delivers 16.43 gigawatts to the rotary joint. This yields a specific mass of 3.15 grams per watt for the satellite. The total mass which is attributable to the MPTS conductor system is the mass of the conductors plus the mass of the array required to compensate for the I²R loss of the conductor system.

TOTAL MASS = CONDUCTOR MASS + 3.15 X CONDUCTOR I²R loss.

On a per unit conductor length basis:

$$\frac{M(\text{total})}{L} = M/L + 3.15 \frac{I^2 R}{L}$$

substituting

$$\frac{M(\text{total})}{L} = I\sqrt{T}\left(\frac{\rho}{F(T)} + \frac{3.15 I \rho F(T)}{\sqrt{T}}\right)$$

or

$$\frac{M(\text{total})}{L} = I\sqrt{T} \left(\frac{\rho}{F(T)} + \frac{3.15 I \rho F(T)}{\sqrt{T}} \right)$$

For each conductor segment shown in Figures 5-7 through 5-12, a conductor operating temperature can be selected which will minimize satellite mass. A general case for the selection of the optimum conductor temperature is shown in the inset of Figure 5-12. The conductor mass for the sheet conductors from the rotary joint to the power sector control substations was computed to be 270.577 kilograms with an I²R loss of 145.5 megawatts for the entire antenna.

5.2.2.2 Power Sector Control to Sub-Array Distribution

At the power sector control substation, the sector control switchgear, disconnects and DC-DC converters are located. The klystrons require nine different voltage levels, seven of which are provided by the DC-DC converter. In order to route power to the sub-arrays from the substation, conductors are routed through the primary and secondary structures to the sub-array interface. Circular aluminum conductors were selected in this application in order to simplify the installation. Some sheet conductors for this application would be over a quarter of a meter wide ($t = 1$ mm) and would require extensive support structure to counteract interconductor magnetic forces. Circular conductors, while more massive, require less support and hence less installation hardware.

In order to accomplish conductor sizing, the curves shown in Figures 5-13 and 5-14 were developed. The conductor masses for a 140 meter length and a 420 klystron feed are shown in Table 5-4 for the two locations shown in Figures 5-13 and 5-14. For the calculations shown in Case 1 of Table 5-4 the klystron supply voltages for solenoid and heater were 100 volts and 10 volts, respectively. As can be seen from Table 5-4, the I²R losses for this case are high. Coordination with the DC-DC RF Converter study team members resulted in revising the solenoid and heater voltages to 1000 volts and 30 volts, respectively. Increasing these voltage levels was incorporated in the tabulations shown in Case 2 of Table 5-4. The total of Conductor I²R losses is 55% less and the total of conductor masses are 82% less—a significant improvement. Subsequent conductor mass and loss determination were determined using the Case 2 tabulations.

Power is routed from the power sector control to the antenna power sectors shown in Figure 5-5. Dependent upon the antenna power sector location the conductor data shown in Table 5-4 was used to compute the data shown in Table 5-5. The data shown in Table 5-4 was adjusted to account for the actual conductor length and the actual number of klystrons being fed by a substation. Total conductor mass and losses are shown in Table 5-5 for this portion of the portion of the substation to subarray distribution system.

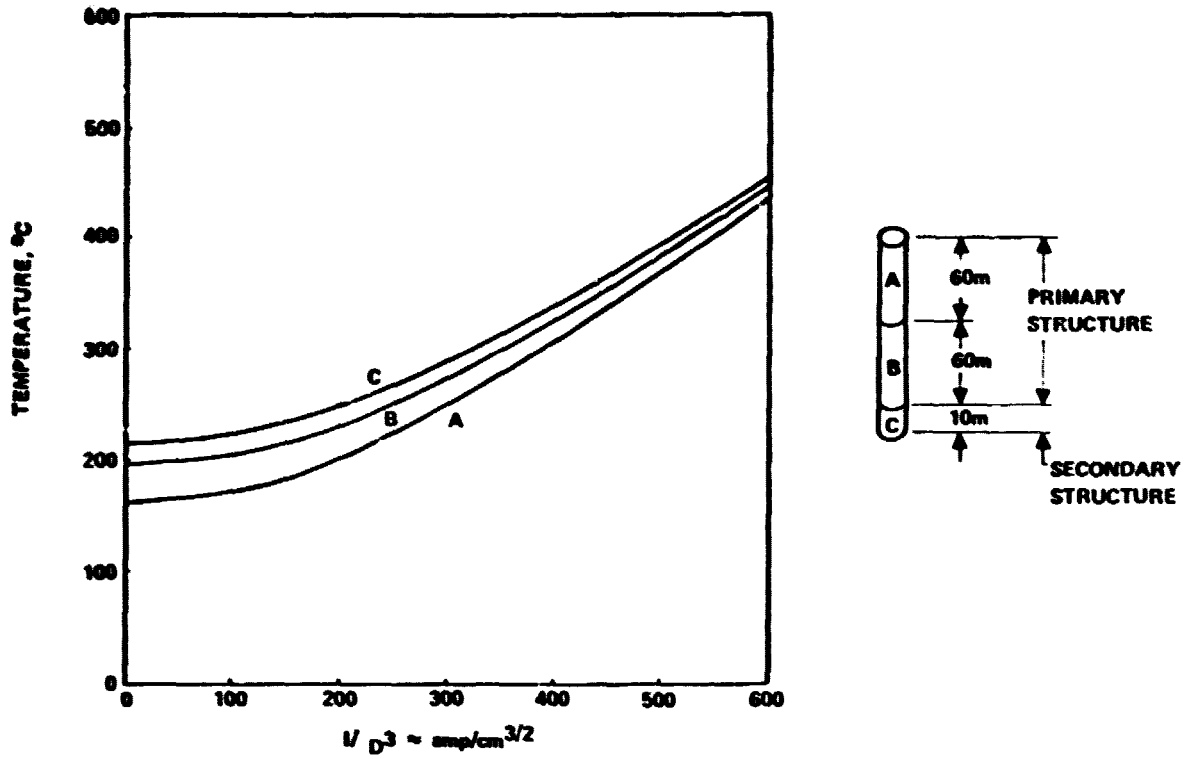


Figure 5-13. Circular Downrun Conductors at Radius 140m MPTS Antenna Structure

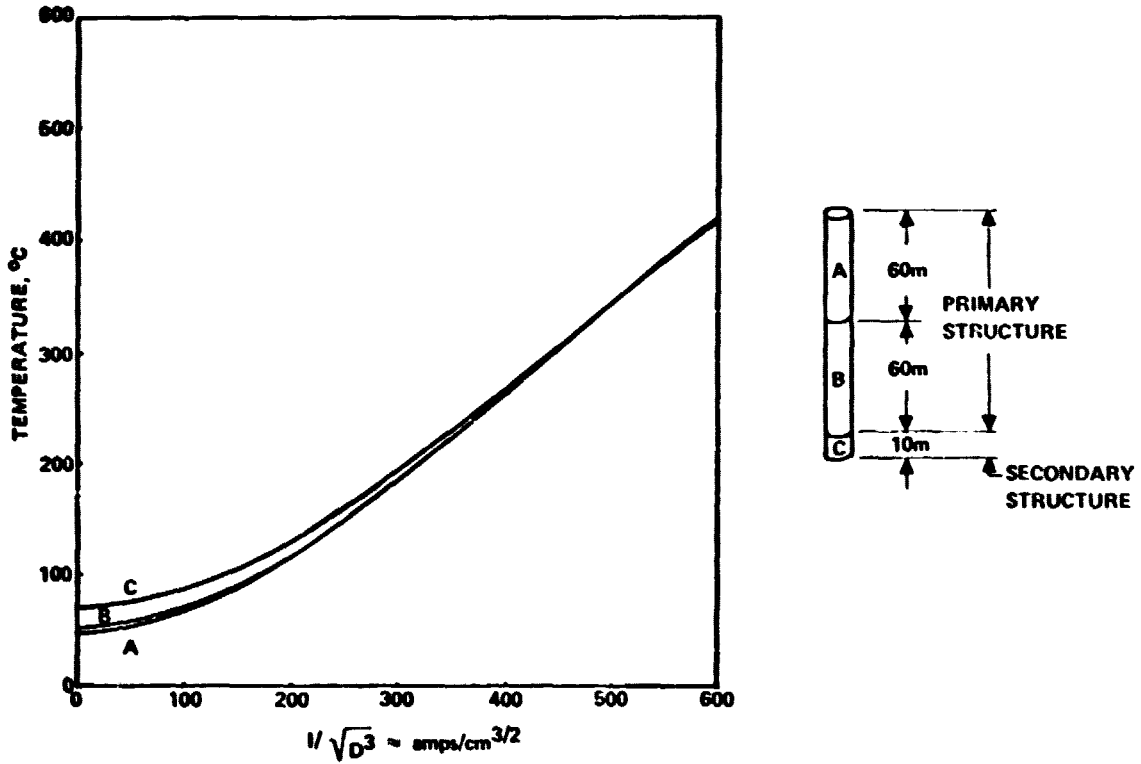


Figure 5-14. Circular Downrun Conductor at Radius 437m MPTS Antenna Structure

D180-22876-4

Table 5-4. MPTS Conductors—Power Sector Control to Subarrays—Circular Conductors—140 Meter Length
SPS-1358

CONDITIONS	CASE 1				CASE 2				NOTES
	CURRENT AMPS	NO. OF WIRES	MASS KG.	I ² R LOSS WATTS	CURRENT AMPS	NO. OF WIRES	MASS KG.	I ² R LOSS WATTS	
$\frac{l}{D^3} = 400$ T = 300°C P = $6.01 \times 10^{-6} \Omega \text{ CM}$ NEAR ANTENNA CENTER	4,200	2	1,365	164,382	420	2	63	35,415	CASE 1: SOLENOID VOLTAGE = 100V HEATER VOLTAGE = 10V CASE 2: SOLENOID VOLTAGE = 1,000V HEATER VOLTAGE = 30V
	2,100	1	271	51,786	700	1	63	24,896	
	64.7	1	3	5,089	64.7	1	3	5,089	
	37.0	2	2	7,012	37.0	2	2	7,012	
	18.0	1	1	2,208	18.5	1	1	2,208	
	-0-	1		-0-	-0-	1		-0-	
	138.6	1	7	8,456	138.6	1	7	8,456	
	609.8	1	52	22,703	609.8	1	52	22,703	
	2,968.6	1	430	65,220	1,568.6	1	184	42,627	
	TOTAL			2,131	326,356			375	
$\frac{l}{D^3} = 450$ T = 300°C P = $6.01 \times 10^{-6} \Omega \text{ CM}$ NEAR ANTENNA EDGE	4,200	2	1,167	192,335	420	2	54	41,437	
	2,100	1	232	60,592	700	1	54	29,125	
	64.7	1	2	5,954	64.7	1	2	5,954	
	37.0	2	1	8,204	37.0	2	1	8,204	
	18.5	1	1	2,583	18.5	1	1	2,583	
	-0-	1		-0-	-0-	1		-0-	
	138.6	1	6	9,894	138.6	1	6	9,894	
	609.8	1	45	26,564	609.8	1	45	26,564	
	2,968.6	1	367	76,310	1,568.6	1	157	49,874	
	TOTAL			1,821	382,437			320	

Table S-5. Power Sector Control Substation to Antenna Power Sector Conductor Summary

DOWNERS					
NODE	SECTOR	LENGTH	KLYSTRONS	MASS	I ² R
*I	*57	125.3	426	1,653	347,171
*II	*31	149.0	432	1,993	418,651
	*32	134.1	448	1,861	390,741
	*39	138.6	412	1,768	371,401
	*40	122.5	424	1,609	337,819
	*49	138.6	443	1,902	399,346
III	1	169.7	432	2,657	407,516
	2	172.8	432	2,705	414,960
	6	140.8	432	2,204	338,116
	14	126.0	420	1,918	294,170
	15	121.8	420	1,854	284,365
	23	126.1	432	1,907	292,489
IV	3	147.2	432	2,307	353,485
	4	138.0	426	2,131	326,856
	5	133.2	396	1,912	293,210
	7	139.0	432	2,176	333,793
	8	130.2	426	2,010	308,319
	9	124.0	414	1,860	285,365
	10	120.8	408	1,786	273,972
	11	124.6	450	2,032	311,680
	12	133.4	420	2,030	311,447
	13	145.6	420	2,216	339,930
*V	17	137.3	432	2,150	329,711
	18	124.1	408	1,835	
	*20	135.4	428	1,795	376,916
	21	131.3	450	1,830	384,921
	23	140.0	440	1,908	400,628
	29	122.0	456	1,723	361,832
	22	139.1	396	1,706	358,265
*VI	30	123.2	428	1,633	342,955
	37	146.0	440	1,989	417,819
	38	144.2	444	1,983	416,419
	47	133.7	442	1,830	384,358
	48	122.5	399	1,514	317,901
	55	143.2	417	1,849	388,384
	56	155.2	387	1,860	390,648
			SUBTOTAL	70,096	12,305,559

Table 5-5. Power Sector Control Substation to Antenna Power Sector Conductor Summary (Continued)

DOWNERS					
NODE	SECTOR	LENGTH	KLYSTRONS	MASS	I ² R
*VII	46	120.6	438	1,636	343,561
	53	140.0	403	1,747	366,957
*VIII	19	138.7	432	1,856	389,711
	26	127.3	406	1,601	336,153
	27	124.1	416	1,599	335,774
	34	128.8	444	1,771	371,947
	35	134.3	430	1,788	375,601
	36	142.0	416	1,829	384,206
*IX	16	139.1	432	1,861	390,835
	24	123.2	432	1,648	346,160
	25	135.4	424	1,778	373,394
	33	129.9	404	1,625	341,329
*X	41	136.8	408	1,729	363,019
	42	124.0	413	1,586	333,084
	43	138.0	432	1,846	387,744
	44	137.0	404	1,714	359,985
*XI	45	131.3	444	1,805	379,167
	52	144.6	412	1,845	387,479
*XII	51	132.2	434	1,777	373,167
*XIII	50	132.9	380	1,564	328,467
*XIV	54	122.0	407	1,538	322,951
				106,239	19,886,250

ORIGINAL PAGE IS
OF POOR QUALITY

The remainder of the substation to subarray conductor system consists of the conductors required at the primary structure/secondary structure interface to distribute power to the subarrays. Individual conductor "drops" are provided through the secondary structure to the subarrays. The tabulations of Table 5-6 present the results of analyses to determine conductor losses and masses for this portion of the conductor systems. Antenna power sector layouts are provided in addition to conductor mass and losses for each power sector layout.

5.2.2.3 Subarray Distribution

The conductors on the individual MPTS antenna subarrays are insulated circular aluminum conductors. The thermal environment for the conductors is relatively benign (Figures 6-16 and 6-17) since the klystron radiator system is designed to radiate away from the waveguide surface. Each subarray conductor is routed from the interface connection at the subarray drop to the klystron. For reliability reasons no conductor taps are made on the subarray to provide for multiple klystron feeds from a single conductor.

Figure 5-15 presents the conductor summary for the four klystron subarray. Also shown in Figure 5-15 are per unit length tabulations of conductor mass and I^2R losses. All subarray conductor calculations for subarray distribution mass and losses were computed using these per unit length values. Figures 5-16 through 5-20 present the results for the other antenna subarray types. Total antenna subarray conductor mass and losses were computed by multiplying these quantities by the number of each subarray types.

5.2.3 DC/DC Converters

The requirements of the DC/DC converters are discussed in Paragraph 5.1. The detailed analysis of DC/DC converters was performed by General Electric and the results are shown in Appendix A. This data was not received in time to incorporate into the baseline MPTS power distribution system design. However, the results of some of the data are summarized in Figure 5-21. The total mass of the figure is composed of the DC/DC converter mass plus the mass of the radiator system to cool the converter plus the mass of the satellite power generation required to generate the converter electrical losses. The minimum total mass occurs at a converter switching frequency of approximately 20 kilohertz which corresponds to a converter specific mass of 1.0 kg/kw and efficiency of 96% which were used for the baseline MPTS power distribution system design.

5.2.4 Switchgear

The antenna power distribution system fault protection scheme is shown in Table 5-7. In addition to the fault protection required in the MPTS Power Distribution System, isolation of the switchgear for maintenance purposes is desirable. The use of isolation disconnects would enable isolation of a single power sector substation without powering down the main power buses. The disconnects are not designed for current interruption and are only operated when no current flow exists (i.e., the downstream breaker is open when the disconnect is operated).

Table 5-6. Antenna Power Sector Conductor Summary

POWER SECTOR TYPE I



SECTOR NO.	KLYSTRONS	DISTANCE
1	432	169.7
2	432	172.8
3	432	147.2
4	426	138.0

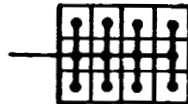
SECTOR BUS = 49.6

$W_T = 7,321$
 $I^2R = 171,060$

SECTOR DROPS = 120

$W_T = 669$
 $I^2R = 79,522$

POWER SECTOR TYPE II



SECTOR NO.	KLYSTRONS	DISTANCE
6	432	140.8
5	396	133.2

SECTOR BUS = 29.8

$W_T = 2,183$
 $I^2R = 51,387$

SECTOR DROPS = 166.0

$W_T = 463$
 $I^2R = 48,708$

POWER SECTOR TYPE III



SECTOR NO.	KLYSTRON	DISTANCE
7	432	139.0
8	426	130.2
9	414	124.0
10	408	120.8
12	420	133.4
13	420	145.6
14	420	126.0
15	426	121.8

SECTOR BUS = 59.6

$W_T = 17,594$
 $I^2R = 411,097$

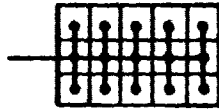
SECTOR DROPS = 140

$W_T = 1,225$
 $I^2R = 164,315$

ORIGINAL PAGE IS
 OF POOR QUALITY

Table S-6. Antenna Power Sector Conductor Summary (Continued)

POWER SECTOR TYPE IV



SECTOR NO.	KLYSTRONS	DISTANCE
11	450	124.6

SECTOR BUS = 39.7

$$W_T = 1,570$$

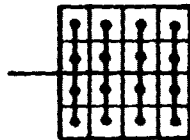
$$I^2R = 34,229$$

SECTOR DROPS = 207.5

$$W_T = 227$$

$$I^2R = 30,442$$

POWER SECTOR TYPE V



SECTOR NO.	KLYSTRONS	DISTANCE
18	408	124.1
22	396	139.1
23	432	126.1

SECTOR BUS = 29.8

$$W_T = 3,236$$

$$I^2R = 77,081$$

SECTOR DROPS = 251.8

$$W_T = 614$$

$$I^2R = 95,505$$

POWER SECTOR TYPE VI



SECTOR NO.	KLYSTRONS	DISTANCE
16	432	139.1
17	432	137.3
20	428	135.4
21	450	131.3

SECTOR BUS = 49.6

$$W_T = 7,591$$

$$I^2R = 171,060$$

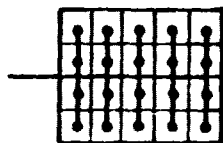
SECTOR DROPS = 248.8

$$W_T = 808$$

$$I^2R = 125,823$$

Table 5-6. Antenna Power Sector Conductor Summary (Continued)

POWER SECTOR TYPE VII



SECTOR NO.	KLYSTRONS	DISTANCE
19	432	138.7
24	432	123.2
25	424	135.4
26	406	127.3
31	432	149.0
32	448	134.1

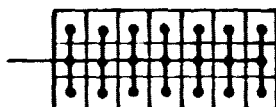
SECTOR BUS = 39.7

$W_T = 8,978$
 $i^2R = 205,376$

SECTOR DROPS = 314.6

$W_T = 697$
 $i^2R = 322,308$

POWER SECTOR TYPE VIII



SECTOR NO.	KLYSTRONS	DISTANCE
30	428	123.2

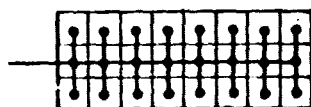
SECTOR BUS = 69.5

$W_T = 2,583$
 $i^2R = 59,922$

SECTOR DROPS = 290.2

$W_T = 107$
 $i^2R = 49,552$

POWER SECTOR TYPE IX



SECTOR NO.	KLYSTRONS	DISTANCE
33	404	129.9
29	456	122.0

SECTOR BUS = 69.5

$W_T = 5,251$
 $i^2R = 119,846$

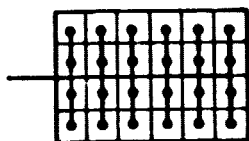
SECTOR DROPS = 331.7

$W_T = 245$
 $i^2R = 113,276$

ORIGINAL PAGE IS
 OF POOR QUALITY

Table 5-6. Antenna Power Sector Conductor Summary (Continued)

POWER SECTOR TYPE X



SECTOR NO.	KLYSTRONS	DISTANCE
27	416	124.1
28	440	140.0
39	412	138.6
40	424	122.5

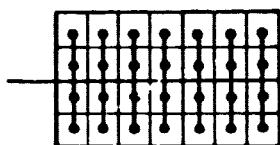
SECTOR BUS = 49.6

$W_T = 5,138$
 $I^2R = 257,857$

SECTOR DROPS = 377.6

$W_T = 414$
 $I^2R = 222,255$

POWER SECTOR TYPE XI



SECTOR NO.	KLYSTRONS	DISTANCE
34	444	128.8

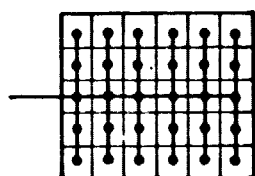
SECTOR BUS = 59.6

$W_T = 1,348$
 $I^2R = 77,461$

SECTOR DROPS = 440.5

$W_T = 121$
 $I^2R = 64,820$

POWER SECTOR TYPE XII



SECTOR NO.	KLYSTRONS	DISTANCE
36	416	142.0
38	444	144.2
41	408	136.8

SECTOR BUS = 49.6

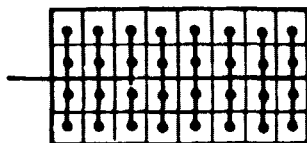
$W_T = 3,204$
 $I^2R = 193,392$

SECTOR DROPS = 575.1

$W_T = 473$
 $I^2R = 253,878$

Table 5-6. Antenna Power Sector Conductor Summary (Continued)

POWER SECTOR TYPE XIII



SECTOR NO.	KLYSTRONS	DISTANCE
37	440	146.0

SECTOR BUS = 69.5

$W_T = 1,558$

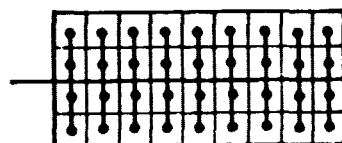
$I^2R = 90,328$

SECTOR DROPS = 503.4

$W_T = 94$

$I^2R = 61,148$

POWER SECTOR TYPE XIV



SECTOR NO.	KLYSTRONS	DISTANCE
35	430	134.3

SECTOR BUS = 79.4

$W_T = 1,733$

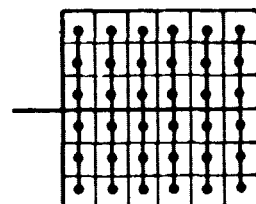
$I^2R = 103,194$

SECTOR DROPS = 566.4

$W_T = 106$

$I^2R = 68,801$

POWER SECTOR TYPE XV



SECTOR NO.	KLYSTRONS	DISTANCE
48	399	122.5
49	443	138.6

SECTOR BUS = 49.6

$W_T = 2,128$

$I^2R = 128,978$

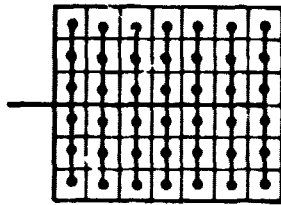
SECTOR DROPS = 772.7

$W_T = 289$

$I^2R = 187,720$

Table 5-6. Antenna Power Sector Conductor Summary (Continued)

POWER SECTOR TYPE XVI:



SECTOR NO.	KLYSTRONS	DISTANCE
46	438	120.6

SECTOR BUS = 59.6

$$W_T = 1,330$$

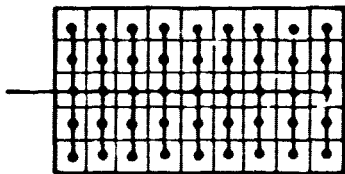
$$I^2R = 77,461$$

SECTOR DROPS = 831.5

$$W_T = 155$$

$$I^2R = 101,002$$

POWER SECTOR TYPE XVII



SECTOR NO.	KLYSTRONS	DISTANCE
42	413	124.0
43	432	138.0

SECTOR BUS = 79.4

$$W_T = 3,418$$

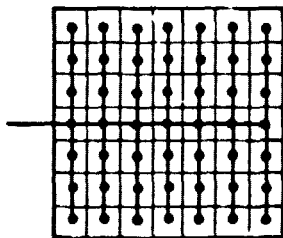
$$I^2R = 206,389$$

SECTOR DROPS = 862.7

$$W_T = 323$$

$$I^2R = 209,584$$

POWER SECTOR TYPE XVIII



SECTOR NO.	KLYSTRON	DISTANCE
45	444	131.3

SECTOR BUS = 59.6

$$W_T = 1,348$$

$$I^2R = 77,461$$

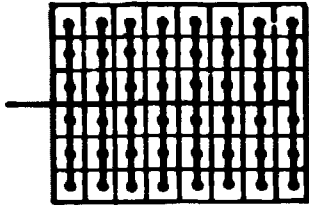
SECTOR DROPS = 1212.2

$$W_T = 154$$

$$I^2R = 121,547$$

Table 5-6. Antenna Power Sector Conductor Summary (Continued)

POWER SECTOR TYPE XIX



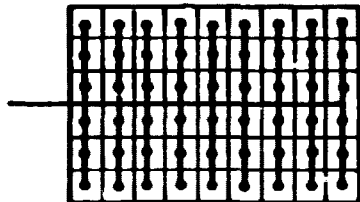
SECTOR BUS = 69.5

SECTOR DROPS = 1030.2

SECTOR NO.	KLYSTRONS	DISTANCE
47	442	133.7

$W_T = 1,565$
 $I^2R = 90,328$
 $W_T = 131$
 $I^2R = 103,298$

POWER SECTOR TYPE XX



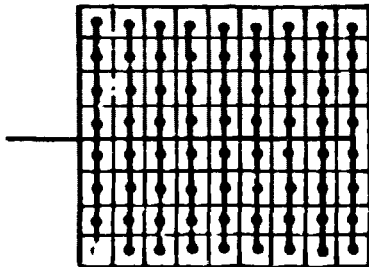
SECTOR BUS = 79.4

SECTOR DROPS = 1159.1

SECTOR NO.	KLYSTRONS	DISTANCE
44	404	137.0

$W_T = 1,675$
 $I^2R = 103,195$
 $W_T = 148$
 $I^2R = 116,223$

POWER SECTOR TYPE XXI



SECTOR BUS = 79.4

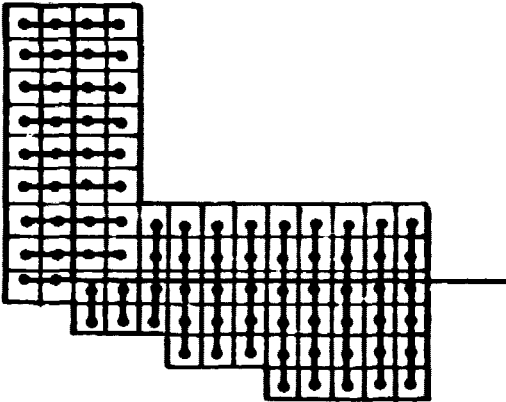
SECTOR DROPS = 2198.1

SECTOR NO.	KLYSTRONS	DISTANCE
50	380	132.9

$W_T = 1,537$
 $I^2R = 103,195$
 $W_T = 163$
 $I^2R = 168,199$

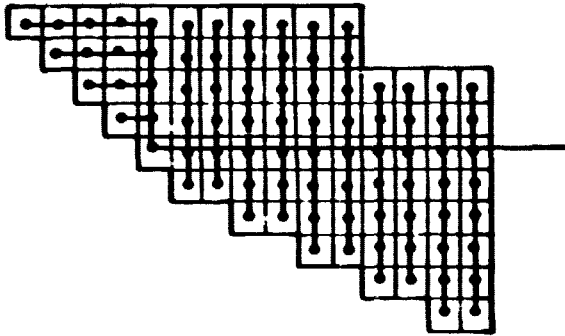
Table S-6. Antenna Power Sector Conductor Summary (Continued)

POWER SECTOR TYPE XXII



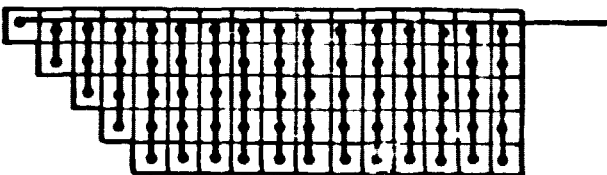
SECTOR NO.	KLYSTRON	DISTANCE
51	434	132.2
SECTOR BUS	= 200.9	$W_T = 4443$ $I^2R = 261,105$
SECTOR DROPS	= 1613.5	$W_T = 120$ $I^2R = 123,465$

POWER SECTOR TYPE XXIII



SECTOR NO.	KLYSTRONS	DISTANCE
52	412	144.6
SECTOR BUS	= 165.8	$W_T = 3,480$ $I^2R = 215,486$
SECTOR DROPS	= 2241.8	$W_T = 166$ $I^2R = 171,543$

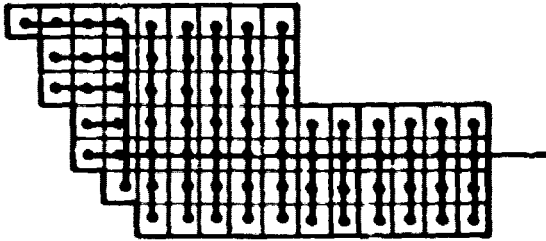
POWER SECTOR TYPE XXIV



SECTOR NO.	KLYSTRONS	DISTANCE
53	403	140.0
SECTOR BUS	= 158.8	$W_T = 3,260$ $I^2R = 206,389$
SECTOR DROPS	= 1307.6	$W_T = 97$ $I^2R = 100,057$

Table S-6. Antenna Power Sector Conductor Summary (Continued)

POWER SECTOR TYPE XXV



SECTOR NO.	KLYSTRONS	DISTANCE
54	407	122.0

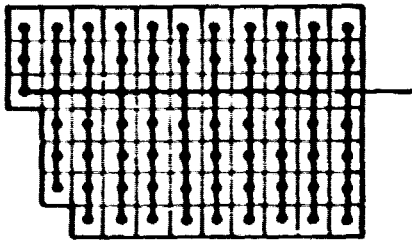
SECTOR BUS = 165.0

$W_T = 3.422$
 $I^2R = 214.447$

SECTOR DROPS = 1647.1

$W_T = 122$
 $I^2R = 126.036$

POWER SECTOR TYPE XXVI



SECTOR NO.	KLYSTRONS	DISTANCE
55	417	143.2

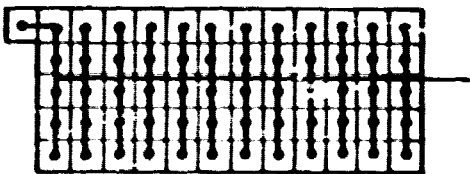
SECTOR BUS = 99.3

$W_T = 2.118$
 $I^2R = 129.058$

SECTOR DROPS = 1740.3

$W_T = 129$
 $I^2R = 133.168$

POWER SECTOR TYPE XXVII



SECTOR NO.	KLYSTRONS	DISTANCE
56	387	155.2

SECTOR BUS = 109.2

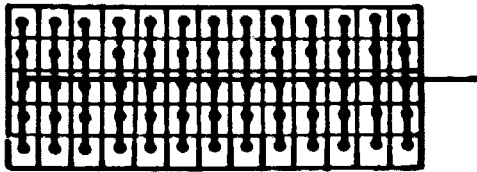
$W_T = 2.153$
 $I^2R = 141.925$

SECTOR DROPS = 1194.7

$W_T = 89$
 $I^2R = 91.418$

Table 5-6. Antenna Power Sector Conductor Summary (Continued)

POWER SECTOR TYPE XXVIII



SECTOR NO.	KLYSTRONS	DISTANCE
57	426	125.3

SECTOR BUS = 119.1

$W_T = 2,585$
 $I^2R = 154,792$

SECTOR DROP = 1246.1

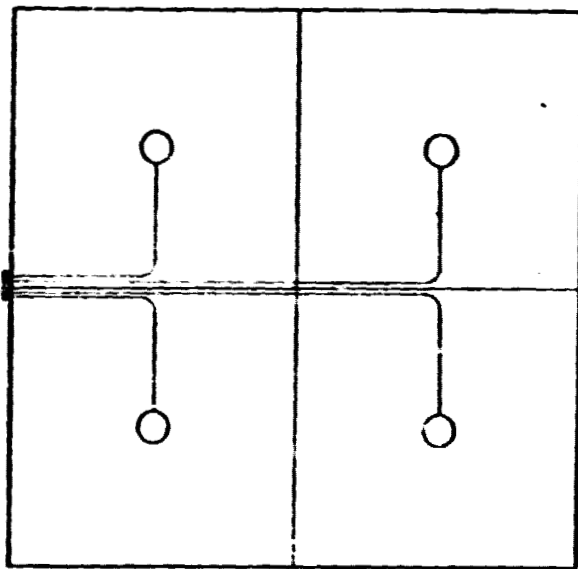
$W_T = 92$
 $I^2R = 95,352$

SECTOR BUS $M_T = 103,750$

SECTOR BUS $I^2R = 4,137,729$

SECTOR DROPS $M_T = 8,442$

SECTOR DROPS $I^2R = 3,453,459$



11.484

4 KLYSTRONS 2X2

VOLTAGE	CURRENT/TUBE	TOTAL CURRENT
21,050		
42,100	0.089	0.352
21,050	0.044	0.176
25,140	0.088	0.352
28,470	0.154	0.616
37,890	0.330	1.320
48,800	1.452	5.808
10 V	5.000	20.000
100V (2 EA)	10.000	40.000
COMMON	7.156	28.624

$L_T = 32.816 + \text{PIGTAIL}$

$W_W = 241.06$

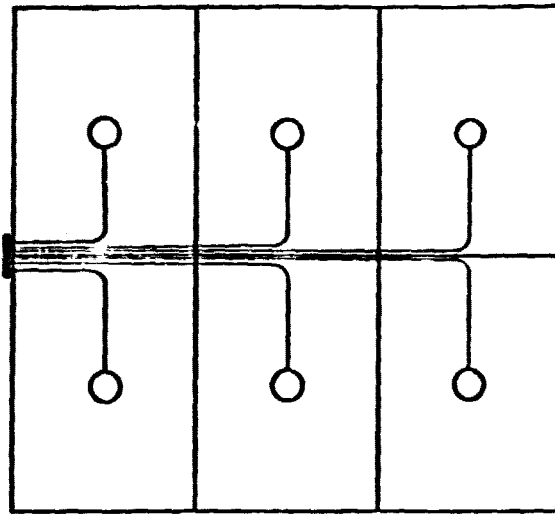
$I^2R = 241.06$

WIRE		NO. REQ'D	WIRE SIZE AWG.	INSUL THICK (MIL)	WT/M KG.	I ² R/M WATTS
VOLTAGE (REF TO BODY ANODE)	CURRENT					
21,050		1	30	3.6	.0009	
	0.088	1	30	8.6	.0009	0.004
21,050	0.044	1	30	8.6	.0009	0.001
16,940	0.088	1	30	6.8	.0007	0.004
12,630	0.154	1	28	5.2	.0007	0.008
4,210	0.330	1	27	2	.0004	0.030
2,100	1.452	1	22	1	.0010	0.184
42,100	5.000	1	18	16.8	.0068	0.861
42,100	7.156	1	16	16.9	.0090	1.107
42,100	10.000	2	15	15.4	.0103	1.709

$\Sigma = 0.0419 \quad 5.617$

Figure S-15. Four Klystron Subarray Conductor Summary

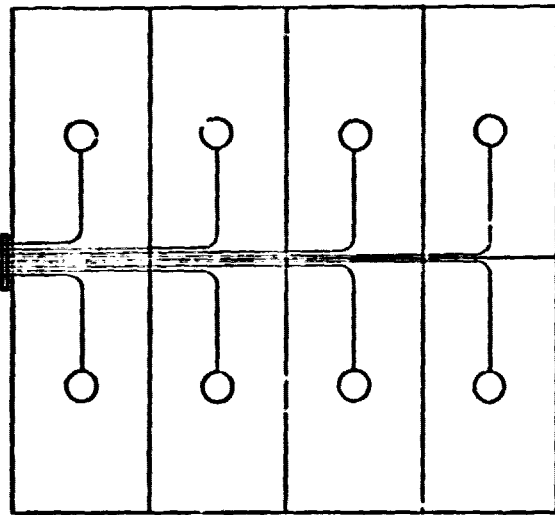
D180-22876-4



VOLTAGE	TOTAL CURRENT
21,050	—
42,100	0.528
21,050	0.264
25,180	0.528
29,470	0.924
37,890	1.980
40,000	8.712
10	30.000
100	60.000
COMMON	42.936

$L_T = 49.374 \text{ M}$
 $W_W = 2.49 \text{ Kg}$
 $I^2R = 333.50$

6 KLYSTRONS 2X3



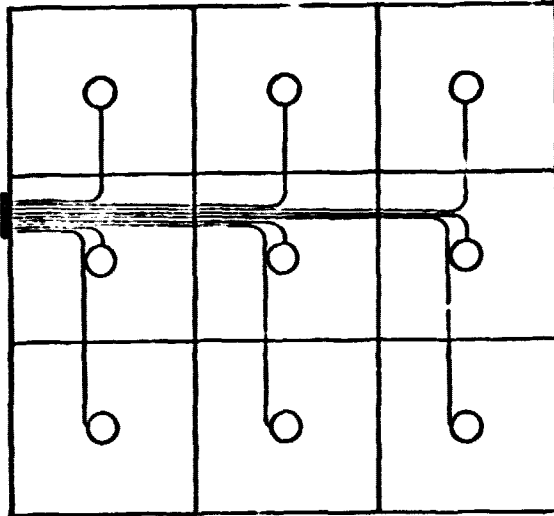
VOLTAGE	TOTAL CURRENT
21,050	—
42,100	0.724
21,050	0.352
25,180	0.724
29,470	1.232
37,890	2.640
40,000	11.616
10	40.000
100	80.000
COMMON	57.248

$L_T = 65.832$
 $W_W = 3.18 \text{ Kg}$
 $I^2R = 369.78$

8 KLYSTRONS 2X4

Figure 5-16. Six and Eight Klystron Subarray Conductor Summary

D18C-22876-4



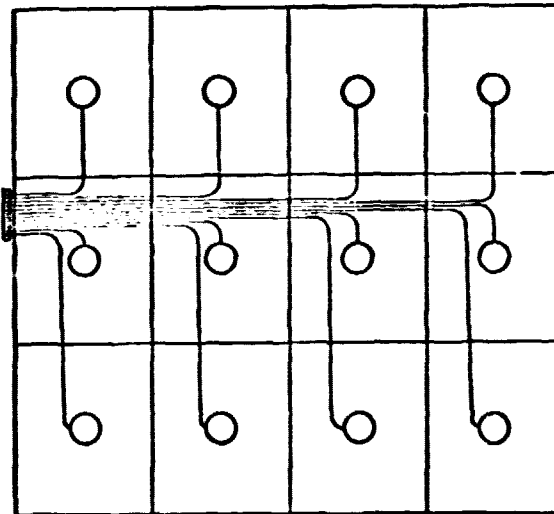
VOLTAGE	TOTAL CURRENT
21,050	—
42,100	0.792
21,050	0.396
25,160	0.792
29,470	1.386
37,890	2.970
40,000	13.068
10	45.000
100	90.000
COMMON	64.404

$L_T = 71.579$

$W_W = 3.42 \text{ Kg}$

$I^2R = 458.23$

9 KLYSTRONS 3X3



VOLTAGE	TOTAL CURRENT
21,050	—
42,100	1.056
21,050	0.528
25,160	1.056
29,470	1.848
37,890	3.960
40,000	17.424
10	60.000
100	120.000
COMMON	85.872

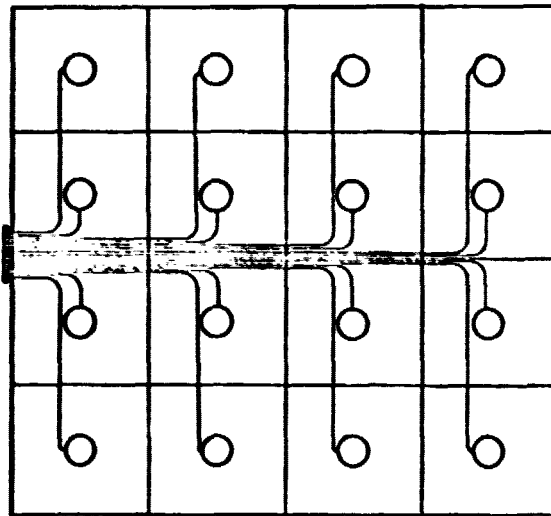
$L_T = 95.439 \text{ M}$

$W_W = 4.42 \text{ Kg}$

$I^2R = 582.25$

12 KLYSTRONS 3X4

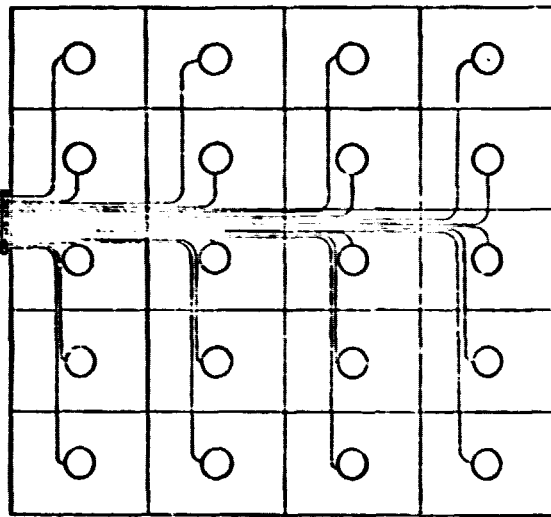
Figure 5-17. Nine and Twelve Klystron Subarray Conductor Summary



VOLTAGE	TOTAL CURRENT
21,050	—
42,100	1.408
21,050	0.704
25,160	1.408
29,470	2.464
37,890	5.280
40,000	23.232
10	80.000
100	160.000
COMMON	114.496

$L_T = 131.664$
 $W_W = 5.94 K_g$
 $I^2R = 795.73$

16 KLYSTRONS 4X4

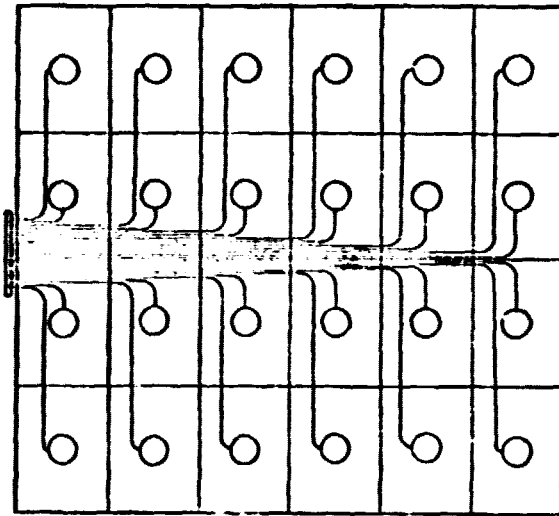


VOLTAGE	TOTAL CURRENT
21,050	—
42,100	1.760
21,050	0.880
25,160	1.760
29,470	3.080
37,890	6.600
40,000	29.040
10	100.000
100	200.000
COMMON	143.120

$L_T = 166.566 M$
 $W_W = 7.40 K_g$
 $I^2R = 991.77$

20 KLYSTRONS 5X4

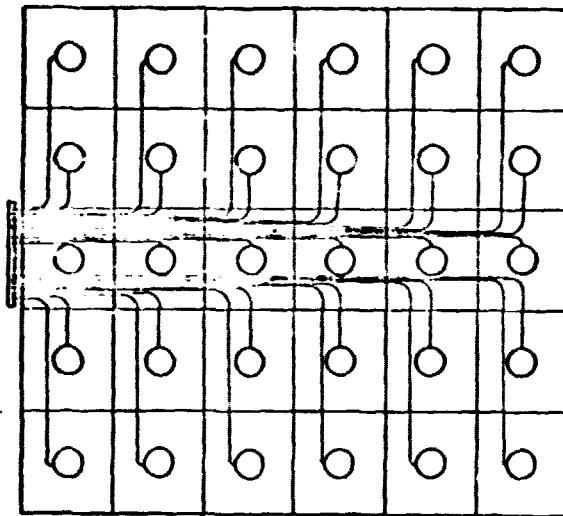
Figure 5-18. Sixteen and Twenty Klystron Subarray Conductor Summary



VOLTAGE	TOTAL CURRENT
21,050	—
42,100	2.112
21,050	1.056
25,160	2.112
29,470	3.696
37,890	7.920
40,000	34.848
10	120.000
100	240.000
COMMON	171.744

$L_T = 197.496$
 $W_W = 8.89 \text{ Kg}$
 $I^2R = 1,165.51$

24 KLYSTRONS 4X6

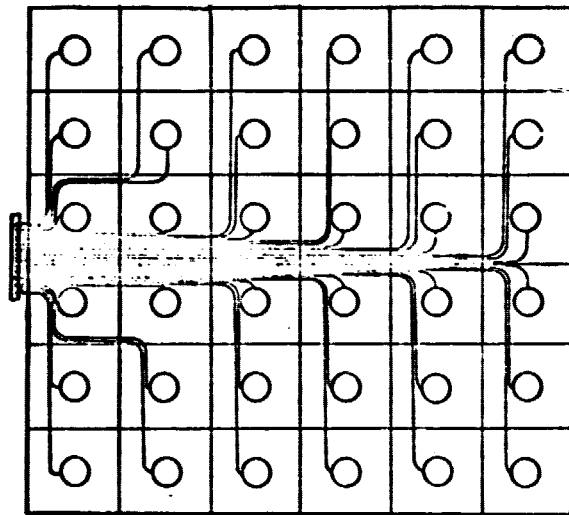


VOLTAGE	TOTAL CURRENT
21,050	—
42,100	2.640
41,050	1.320
25,160	2.640
29,470	4.620
37,890	9.900
40,000	43.560
10	150.000
100	300.000
COMMON	214.680

$L_T = 231.677 \text{ M}$
 $W_W = 10.13 \text{ Kg}$
 $I^2R = 1,357.50$

30 KLYSTRONS 5X6

Figure 5-19. Twenty-four and Thirty Klystron Subarray Conductor Summary



VOLTAGE	TOTAL CURRENT
21,060	—
42,100	3.168
21,060	1.584
25,180	3.168
29,470	5.844
37,890	11.688
40,000	52.272
10	180.000
100	360.000
COMMON	257.616

$L_T = 296.244 \text{ M}$
 $W_W = 12.83 \text{ Kg}$
 $I^2R = 1,720.17$

36 KLYSTRONS 6X6

Figure 5-20. Thirty-six Klystron Subarray Conductor Summary

SP2-4382

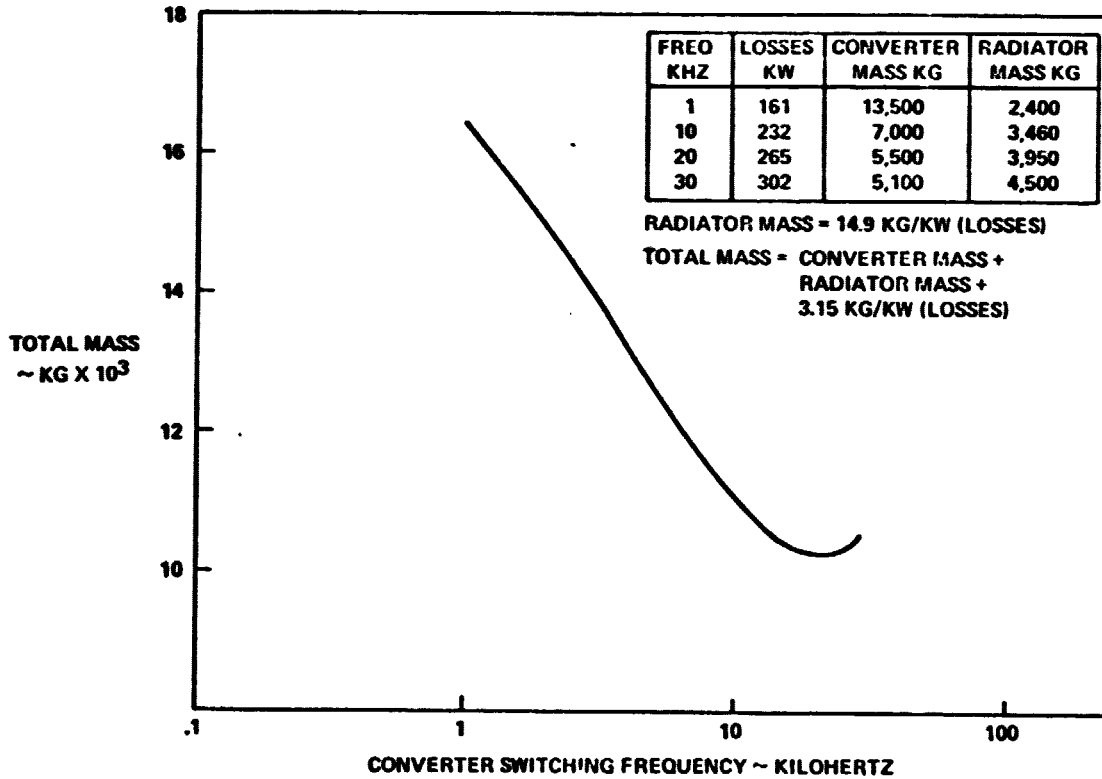


Figure 5-21. DC/DC Converter Optimization

Table 5-7. Antenna Power Distribution Fault Protection

FAULT AREA	PROTECTION SCHEME
MAIN BUS	REMOVE ALL SATELLITE POWER SOURCES
ANTENNA SUB DISTRIBUTION BUS	OPEN APPROPRIATE MAIN ANTENNA CIRCUIT BREAKER
ANTENNA DC/DC CONVERTER	OPEN CONVERTER CIRCUIT BREAKER
KLYSTRON INTERNAL ARCING	TAKE KLYSTRON MODULATING ANODE TO CATHODE POTENTIAL
OUTPUT WAVEGUIDE ARCING	REMOVE KLYSTRON INPUT RF DRIVE

General Electric performed SPS switchgear studies. The study results are included in Appendix B. Three likely candidate switchgear types were considered for use on the SPS. They are: 1) Vacuum DC circuit interrupter with commutation circuitry, 2) Solid State Circuit interrupter, and 3) a Liquid-Metal Plasma Valve Switch with a parallel mechanical contactor and commutation circuitry (Ref. 5-4).

There are three basic types of switchgear required in the MPTS power distribution systems. These are as follows:

1) Klystron Collector A Supply

Switchgear Rating: $V = 40,800$ volts
 $I = 620$ amps
Momentary Current = 6,200 amps
Load: Klystron Collector #5 (420 ea. approx.)

2) Klystron Collector B Supply

Switchgear Rating: $V = 38,700$ volts
 $I = 290$ amps
Momentary Current = 2,900 amps
Load: DC/DC Converters
Klystron Collector #4 (420 ea. approx.)

3) Klystron Clamp

Switchgear Rating: $V = 21,500$ volts
 $I = 0$ amperes
Momentary Current = 0 amperes
Load: None - Normally open - Takes modulating anode to cathode potential.

The purpose of the klystron clamp is to stop current flow in the klystron. The modulating anode is a non-intercepting anode and, hence, draws no current. A very large series resistance (20 megohms for instance) can be placed in series with the anode, limiting the current from the modulating anode supply to approximately 1 milliamperes when the clamp is on. The clamp must operate extremely rapidly in order that the waveguide and/or klystron not suffer damage due to sustained arcing. Other klystron internal arcing near the depressed collector will be extinguished using the power sector control circuit breakers. However, considerably more conductor mass is present in the collector plates than on the waveguide walls. In addition, some conductor resistance is present between the klystron and the power sector control substation to limit currents during arcing.

An alternate approach which was considered incorporated individual switchgear at each sub-array for each sub-array power input. These switchgear, nine per sub-array, would be smaller than the sector control switchgear and would provide protection from the energy stored in the output filters of the power sector DC/DC converter. The sub-array switchgear would be over and above the existing power sector control switchgear. A total of 62,388 additional breakers would be required for each antenna. This approach was not implemented since detailed converter filter design was not available and a detailed transient analysis was not performed. Fault transient analysis and the requirement of switchgear fault interruption times are discussed further in paragraph 5.3.

5.2.5 Energy Storage

It is anticipated that significant increase in the MTBF of klystrons can be achieved if thermal cycling of the klystron cathode heater can be minimized. There are 97,056 klystrons per antenna each requiring heater power of 50 watts at 30 VDC. Thus, a total of 4.853 megawatts of power is used for klystron heaters. If a distribution loss of 20% (because of the low voltage) and a period of 2 hours required for operation from stored energy are assumed, then 11.647 megawatt hours of stored energy are required for klystron heaters. If an additional load of 200 kilowatts are postulated for antenna pointing, phase control and other antenna avionics system, then approximately 12 megawatt hours of stored energy are required.

Gas electrode battery systems offer the promise of better rechargeable prospects and higher energy densities. A Nickel Hydrogen battery system should provide at least four times the service life of Nickel Cadmium batteries (Ref. 5-5). With an energy storage system of this size, an energy density of 57.3 watt-hours/kg (26 WHr/lb) including tankage was derived. With a depth of discharge of 0.7 during a normal 2 hour operation, a density of 40.1 WHrs/kg is used to determine the mass of the required energy storage system. The estimated mass for the energy storage system is 299.3×10^3 kilograms (299.3 metric tons).

5.2.6 Weight and Efficiency

The weight and power loss of the MPTS power distribution and control system is shown in Table 5-8. The total losses, including DC/DC converter losses, are approximately 250 megawatts per antenna. The antenna power distribution and control system efficiency is approximately 97%.

5.3 AREAS FOR FURTHER INVESTIGATION

During the course of the conceptual design and analysis of the power distribution system, issues developed which through time and/or manpower restrictions, were not thoroughly investigated. The issues of main concern are discussed in the following paragraphs.

Table 5-8. Antenna Power Distribution System

	MASS (KG)	i^2R LOSS (WATTS)
ROTARY JOINT TO POWER SECTOR CONTROL	270,577	145,453,890
SECTOR CONTROL TO SUBARRAYS	109,722	49,903,520
SECTOR CONTROL DC/DC CONVERTERS AND SWITCHGEAR	1,377,604	49,644,720
SUBARRAY WIRING (INSULATION INCL.)	35,871	4,774,760
TOTAL	1,793,974	249,776,890

% LOSS = 2.99%

DC/RF Converter Protection

Each MPTS antenna in the baseline design contains over 97,000 DC/RF converters and 228 power sector control substations. During the conceptual design of the klystron, an effort to minimize the mass of the individual tube elements resulted in an overall lightweight tube. However, removing mass from the tube imposes the requirement that the probability of internal arcing must be minimized and, in the event that arcing should occur, rapid removal of the power sources is required. Preliminary requirements placed on the MPTS switchgear were extremely stringent--10 microseconds current interruption time. The development of switchgear to perform this task will require an improvement of two orders of magnitude in current interruption time over present switchgear capabilities (milliseconds to hundredths of milliseconds). Analyses are required of possible klystron design changes and possible uses of current limiting reactors to increase this time.

Plasma Effects

Some effort was expended during this study on the effects the quiescent LEO plasma has on the SPS array for the self-powered transfer from LEO to GEO. However, due to study priorities, no effort was expended on the effects of the quiescent plasma on power distribution system conductors since the effects were assumed to be small due to the surface area of the sheet conductors being small with respect to the array area, and the relatively low quiescent plasma level at GEO. In addition, no effort was expended to analyze the effects of plasma at GEO during magnetic substorms.

There are significant interactions between the ambient plasma and the large SPS array that need to be investigated, particularly for the LEO case. The mechanisms include (but are not limited to) snow plowing of ions, large geomagnetically induced potentials, local electron acceleration and ionization of neutral gas, concentration of particle fluxes, charge buildup on dielectric surfaces, and possibly collective wave distribution. Such effects are due to well known principles of plasma physics and their magnitude is sharply enhanced by the size, shape and the field intensity of its unshielded electrical system. Since these interactions may deteriorate the performance of SPS, it would be prudent to analyze their magnitude with simple physical models. A thorough investigation may be warranted in some cases to identify design configurations that suppress power losses to the plasma.

Integrated Power Management

The trend in earth-based power generation stations is more and more toward automated control with minimum operator action except during startup. Should unattended SPS operation be selected, complete automated operation will be required for all phases including startup, operation, voltage regulation, fault detection and removal, load control, and shutdown. While the system designed will serve the functions of power distribution, fault detection and control, and isolation. A further step in system definition is required to perform the management of the integrated SPS power system.

D180-22876-4

6.0 ANTENNA INTEGRATION

6.1 INTRODUCTION

This section describes the antenna configuration selection of non-RF components and integration of the antenna subsystems into a workable microwave power transmission system (MPTS).

6.2 INTEGRATION CONCEPT

6.2.1 System Requirements

The SPS features which affect the MPTS configuration are:

Ground power output	5×10^9 watts
Nominal antenna diameter	1000 meters
Power density taper	Quantized 10 db gaussian

System design objectives include a high first-mode frequency, low thermal distortion, accurate pointing, and compatibility with operating environment.

The major hardware components for the MPTS reference design are:

Klystron	70 kw radiated output
Waveguide	Standing wave type
Thermal control	Passive, using heat pipes and/or radiators
Power distribution	Buses and distributed power converters

This section discusses these major components, associated design constraints and interfaces which were resolved to develop a compatible MPTS.

6.2.2 Design Constraints

The major RF elements have constraints and/or tolerances that affect the overall configuration and establish subsystem interfaces. The klystron module and subarray are a major component in this category.

A klystron module consists of the RF amplifier itself: solid state driver and control; power supplies; thermal control; feed and radiating waveguides, and structural support. A subarray is composed of an integer number of klystron modules attached to a common structure, and pointed as a unit.

The waveguide "stick" must be an integer number of guide wavelengths long so as to establish within it an optimum standing-wave pattern. The guide wavelength depends on the waveguide-stick cross-section dimensions. The klystron module must contain an even number of radiating waveguide sticks to balance the two output ports on each klystron.

All of the subarrays should have the same dimensions so that the pointing units can have a common design. To achieve power density tapering across the antenna, it is necessary to vary the numbers of klystron modules per subarray. These waveguide constraints for the klystron module and the dimensional tolerances in Figure 6-1 lead to a set of solutions for waveguide and subarray sizes which result in the desired reference power density taper (see Sec. 6.4).

6.2.3 System Compatibility

Antenna subsystems must not only interface compatibly with other subsystems and supporting structure, but also must be capable of being constructed and maintained in space. Placement and arrangement of subsystem elements become important, as is the level to which the line replaceable unit (LRU) is designated. The subarray has been selected as the LRU at present, but a klystron module may be considered as a candidate at a later time.

6.3 STRUCTURAL CONSIDERATIONS

The supporting structure for the MPTS components must have the lowest practical mass, must be easy to assemble and maintain, and must constitute a stable platform for the transmission of RF energy to the ground antenna. The adopted two-tier structure has a dense secondary structure to support the RF elements, and a deeper, low-density primary structure to provide stiffness and stability.

6.3.1 Design Drivers

The design drivers, as based on criteria established by system design constraints and tolerances, are summarized in Table 6.1.

Low density is an important design driver because it relates directly to low structure mass, leading to lower material and transportation costs. Also, it interferes less with efficient radiation of waste heat from thermal radiators.

High rigidity minimizes deformation due to attitude control, maneuvering, pointing and temperature changes. Thus, good RF beam integrity requires a rigid platform.

SPS-1170

D180-22876-4

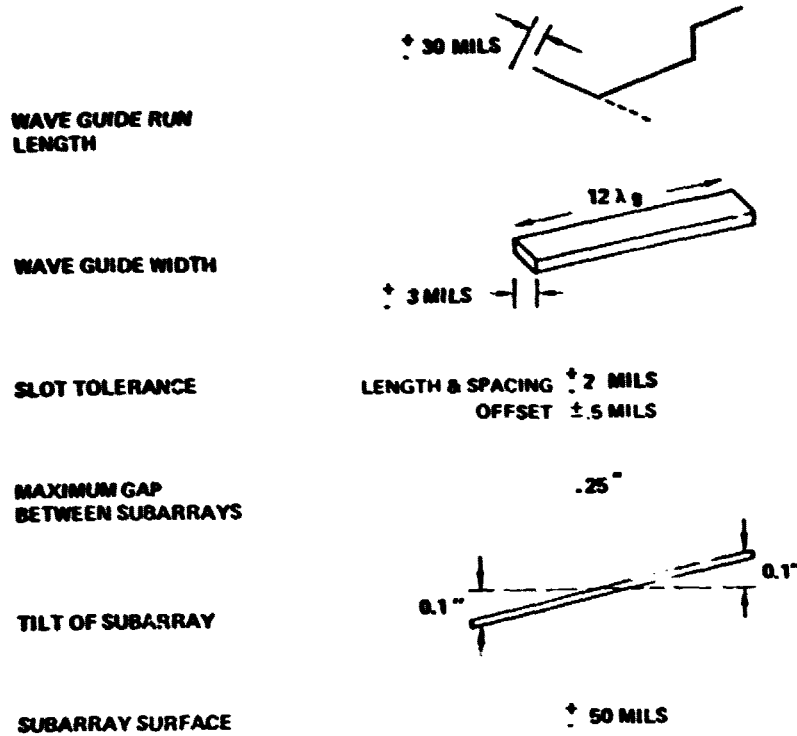


Figure 6-1. Dimensional Tolerances

SPS-1175

Table 6-1. Structural Design Factors

	<u>DESIGN DRIVERS</u>	<u>SELECTION REASON</u>
A. PRIMARY STRUCTURE	<ol style="list-style-type: none"> 1. LOW DENSITY 2. HIGH RIGIDITY 3. HIGH 1ST MODE FREQUENCY 4. COMPATIBLE WITH SECONDARY STRUCTURE 	TETRAHEDRAL PLANAR TRUSS/ LOWEST MASS AND HIGHEST 1ST MODE FREQUENCY FOR PLANAR AREA OBTAINED
B. SECONDARY STRUCTURE	<ol style="list-style-type: none"> 1. SAME AS A.1.2.3 2. COMPATIBLE WITH SUBARRAY STRUCTURE 	TETRAHEDRAL PLANAR TRUSS/ SAME REASONING AS A.
C. SUBARRAY STRUCTURE	<ol style="list-style-type: none"> 1. SAME AS A.1.2.3 2. COMPATIBLE WITH MODULE STRUCTURE 3. POINTING AT THIS LEVEL 	' BEAM "EGGCRATE" / COMPATIBLE WITH STRUCTURAL & INTEGRATION REQUIREMENTS
D. MODULE STRUCTURE	<ol style="list-style-type: none"> 1. COMPATIBLE WITH RF REQMT'S A. POWER TAPERING B. WAVEGUIDE SPECIFICATIONS 2. HIGH RIGIDITY AT SUBARRAY LEVEL 3. INTEGRAL WITHIN SUBARRAY STRUCTURE 4. PROVIDE MOUNTING AND INTERFACE REQMTS 	I-BEAM "EGGCRATE" / SAME REASONING AS C

D180-22876-4

High first oscillation mode frequency determines to what extent large oscillations will be excited by low frequency vibrations induced by docking, attitude control, pointing, yoke movement, or other operations. These low frequencies should not couple to the antenna in a manner that would disturb MPTS operation.

In addition, selected structure must be based on materials and processes that are compatible with a low absolute pressure, variable heat loads due to daily attitude changes and eclipses, and particulate and UV radiation.

6.3.2 Structure Selection

The selected structure incorporates tetrahedral planar trusses wherever possible, having the lowest mass and highest first mode frequency when compared with other generic trusses of equal depth and platform area (Ref. 6.1). A tetrahedral module consists of three repeating tetrahedrons joined at a common apex. The upper and lower surfaces are formed with the addition of three members of identical length. The upper module-surface plane is bordered by members which form a hexagon, and at the lower surface, the structural members form triangles. This basic module is repeated to develop required depth and platform area.

The best candidate materials appear to be composites, which are advantageous in strength-to-mass ratio, adaptable to space construction, and can be designed to give low thermal expansion, thus reducing deformations during thermal cycling.

The subarray structure, consisting of a face of rectangles, must mate with the tetrahedral truss in the secondary structure; the face of the secondary structure on the other hand, is composed of equilateral triangles. For the two structures to match, the subarray length-to-width ratio must equal the cosine of 30° . This constraint affects waveguide, module and subarray sizing, as will be shown later.

The module structure is an integral part of the subarray structure and as such must provide for MPTS subsystem interfaces at the module level.

6.4 THERMAL ANALYSIS

6.4.1 Thermal Analysis Approach

To provide a thermal control system for MPTS, an analysis of the operating thermal environment was developed. Thermal limitations of major system components were defined to provide adequate thermal controls.

D180-22876-4

The assumed temperature limits for materials and equipment operation are given in Table 6-2. A design approach was developed for the collector (500°C) and the dc-dc converter (70°).

6.4.2 Heat Sources

The heat sources at the modules and their dissipating temperatures, shown in Table 6-3, were used in the selection of thermal control equipment. The DC-DC converters, which release by far the most heat at low temperature, require large thermal radiators.

6.4.3 Thermal Control Devices

Heat can be carried to radiators passively by heat pipes or actively in forced flow fluid loops. References 6.2 and 6.3 provide design data. Reliability is an advantage of heat pipes, which normally fail only from physical damage which breaks the pressure containment or fractures the capillary wick. Appropriate redundancy will give a properly designed heat pipe assembly an almost indefinite life. A copper rod substituted for a heat pipe would weigh a hundred times as much.

Data used in sizing the heat pipes appears in Figures 6-2 and 6-3, along with a specific example of a heat pipe/radiator. A heat transport rate of 150 watts/cm² was used for water and 500 watts/cm² for liquid metal.

The heat pipe becomes inefficient for the long spacing between the 70°C dc-dc converters and their low-temperature radiators. A trade study showed that an active fluid-loop was better for this case in spite of its pumps and control valves which can fail, and fluid-containing pipe joints which must be opened when replacing components. Appropriate redundancy was incorporated into the configuration, and a heat flow of 1000 watts/cm² was used for sizing pipes, (Fig. 6-4).

Active cooling was also considered for klystrons (Fig. 6-5). It was rejected because klystron tubes will probably have to be replaced during the MTPS operating life, and having to break fluid connections would certainly complicate maintenance. Furthermore, the high heat-rejection temperature makes the klystron a natural application for heat-pipe-and-radiator cooling.

Thus passive thermal control chosen for the klystron modules, and active heat-transport was chosen for dc-dc converters.

6.5 REFERENCE DESIGN CONFIGURATION

Having an integration concept, a structural configuration, and a thermal control concept, we were able to develop a reference design configuration. The following paragraphs describe the reference configuration and the selection processes involved.

D180-22876-4

SPC-1462

Table 6-2 Thermal Limitation Assumptions

KLYSTRON:	COLLECTOR	500°C
	SOLENOID AND CAVITIES	300°C
	SOLID STATE CONTROL CIRCUITS	70°C
POWER DIST:	DC-DC CONVERTERS	70°C
	BUSSING	DESIGNED TO THERMAL ENVIRONMENT
STRUCTURES:	COMPOSITE MATERIALS	
	1. GRAPHITE-EPOXY	175°C
	2. GRAPHITE-POLYIMIDE	260°C

SPC-1463

Table 6-3. Waste Heat Sources

<u>SOURCE</u>	<u>LEVEL</u>	<u>QUALITY</u>
A. KLYSTRON:		
1) COLLECTOR	8.0 KW/UNIT	500°C
2) CAVITY LOSSES	3.8 KW/UNIT	300°C
3) SOLENOID	1.4 KW/UNIT	300°C
B. SOLID STATE CONTROL DEVICES	10 W/UNIT	0-70°C
C. RADIATING AND FEED WAVEGUIDE	1.0 TO 9.1 KW/SUBARRAY	0-125°C
D. POWER CONVERTERS	218 KW/UNIT	0-70°C

SP-1572

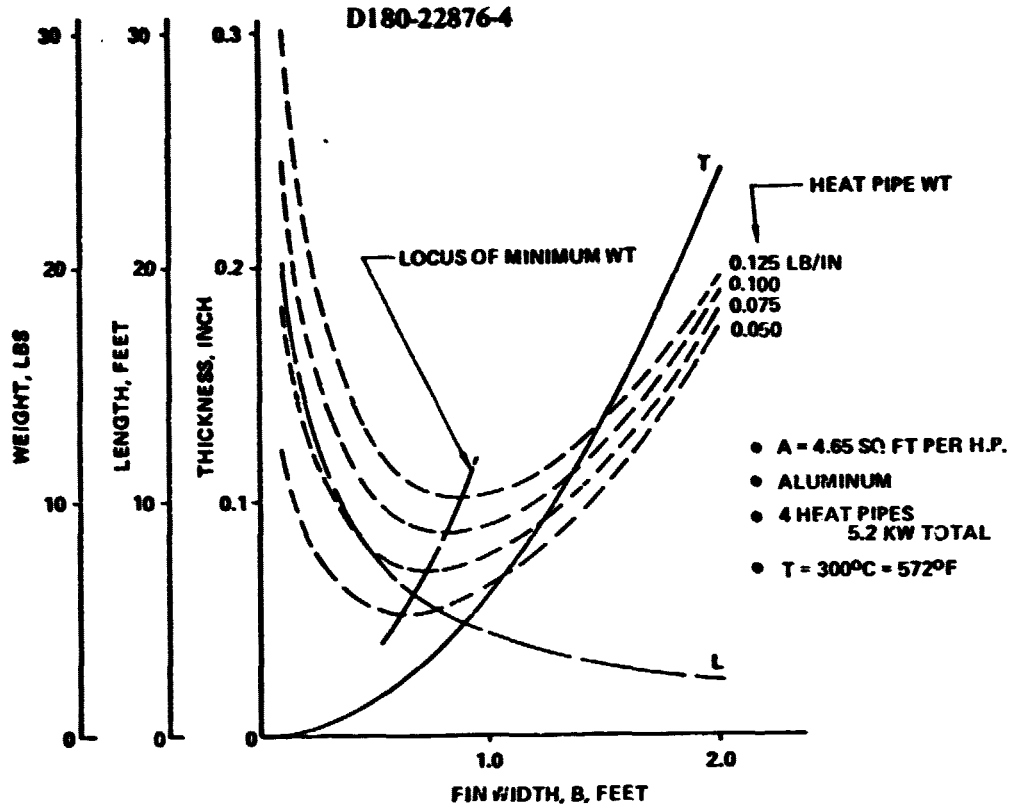


Figure 6-2. Klystron Cavity & Solenoid Heat Pipe/Radiator

SP-1573

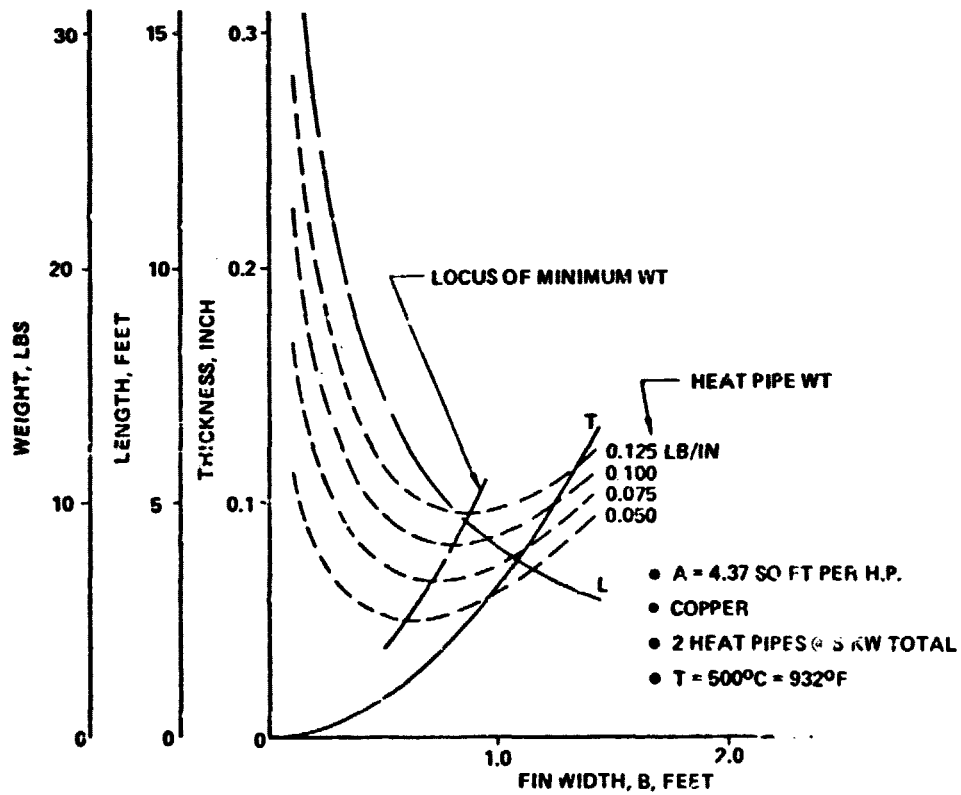


Figure 6-3. Klystron Collector Heat Pipe/Radiator

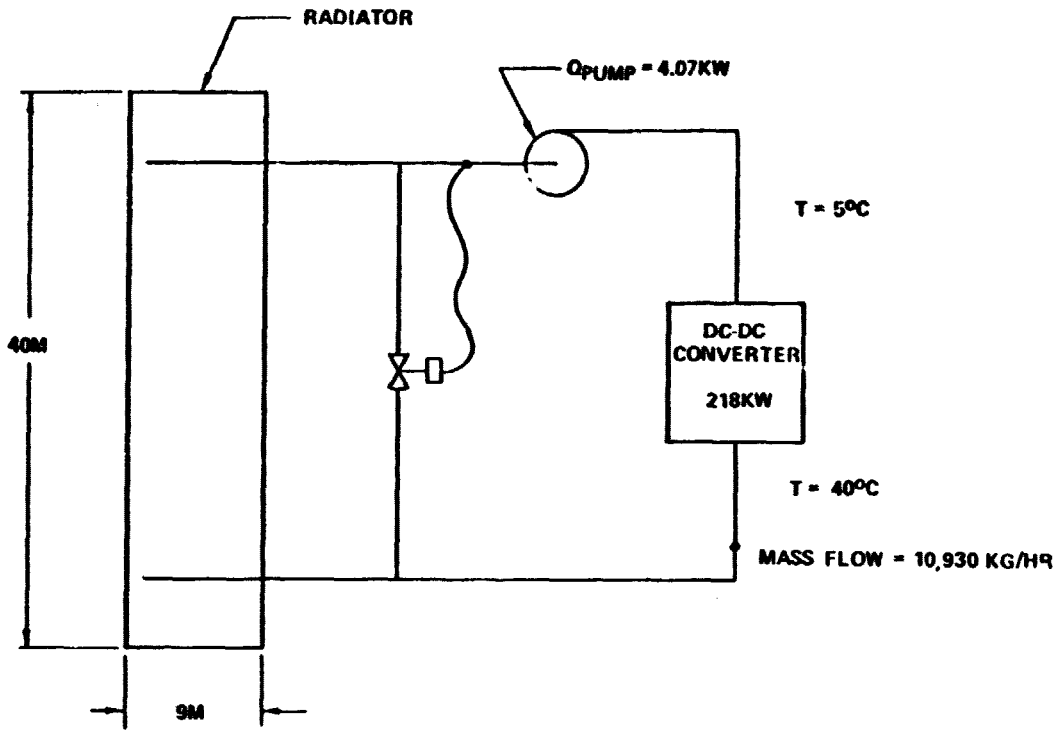


Figure 6-4. Active Thermal Control for DC-DC Converter

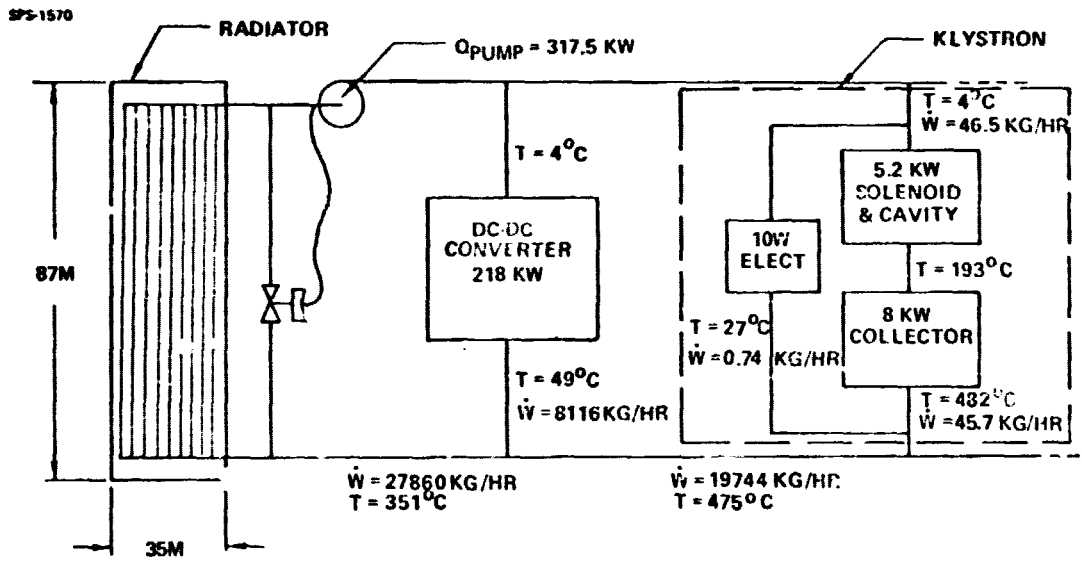


Figure 6-5. Active Thermal Control for Antenna Systems

6.5.1 Component Installation and Integration

6.5.1.1 Klystron Module

The lowest integral element in the MPTS is the klystron module, composed of a klystron, its feed and radiating waveguides, thermal control, solid state driver and RF control, power distribution, power return, and the support structure. Most of the module mass is in the klystron (Fig. 6-6). The mass estimate for the klystron appears in Table 6-4. The klystron input/output interfaces are summarized in Table 6-5.

The high power density at the center of the beam is generated by 36 klystrons, each rated 70 kW, radiating RF from an area slightly larger than 110m^2 . The 36 klystrons are organized into a 6 by 6 matrix. At the edge of the 10 dB tapered antenna a subarray should have 3.60 klystrons. Since 3.60 is not an integer number, each edge subarray would have either 4.0 or 3.0 klystrons, formed into a 2 by 2, 4 by 1, or 3 by 1 matrix. Matrix configurations were similarly established for each power density step in the taper.

The dimensions of the basic waveguide stick must not only meet the RF constraints, but also be suitable for the varying number of klystron modules within the subarrays. The following equations were developed and solved for the optimum waveguide dimensions:

$$L = 60 \lambda_g, \text{ where} \quad (1)$$

L = length of the subarray waveguide stick
 λ_g = guide wavelength
 60 is a number divisible by the integers 1,2,3,4,5 and 6 to give an integer quotient.

This expression provides a waveguide length that can be segmented as required for the variable number of modules per subarray. Each stick can be an integer number of λ_g long.

$$\frac{L}{W} = 60n \cos 30^\circ \quad (2)$$

$\frac{L}{W}$ – length to width ratio of the subarray
 30° – permits mounting the subarray on the equilateral triangular support provided by the secondary structure.
 60 – provides the integer division in the length as stated previously.
 n – An integer multiple of 60, such that the width of the subarray can also be divided into several segments. n must be so chosen that there will be an even number of waveguide sticks within the module. For example, if $n = 2.0$, then $60n = 120$, a number which is divisible by 1,2,3,4,5, and 6 with the quotient being an even integer.

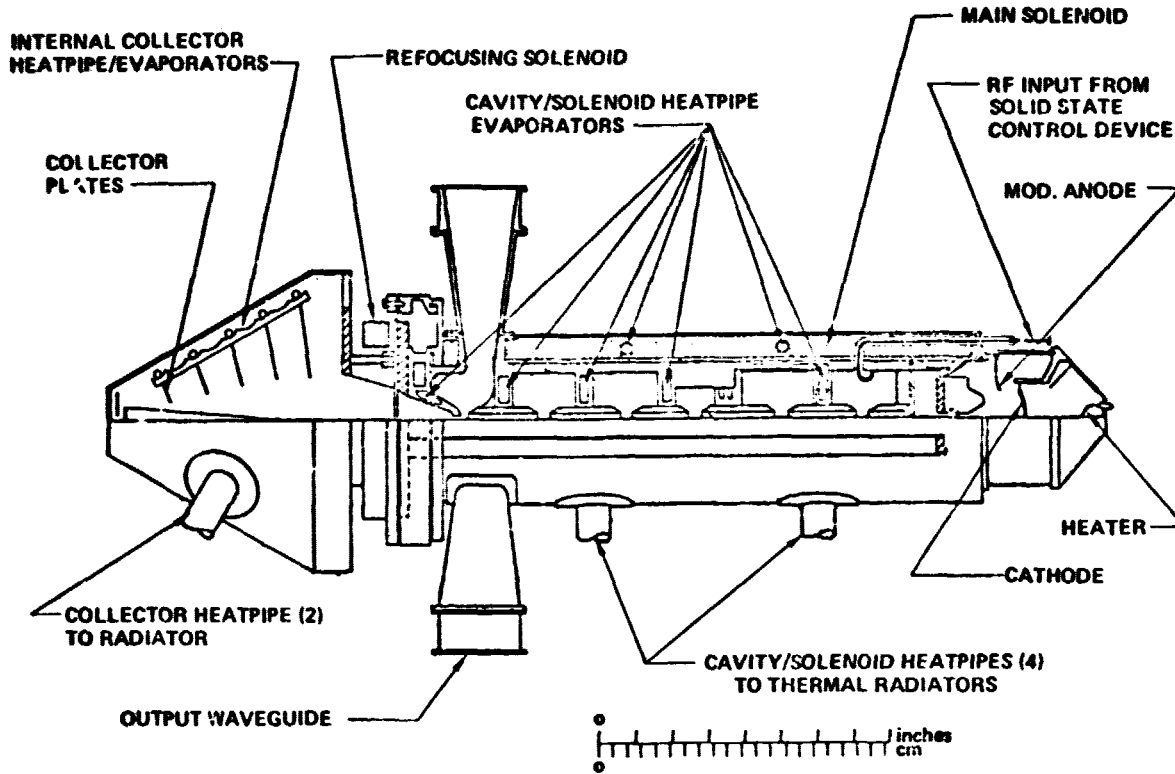


Figure 6-6. 70 Kw Klystron

Table 6-4. Klystron Mass Estimate

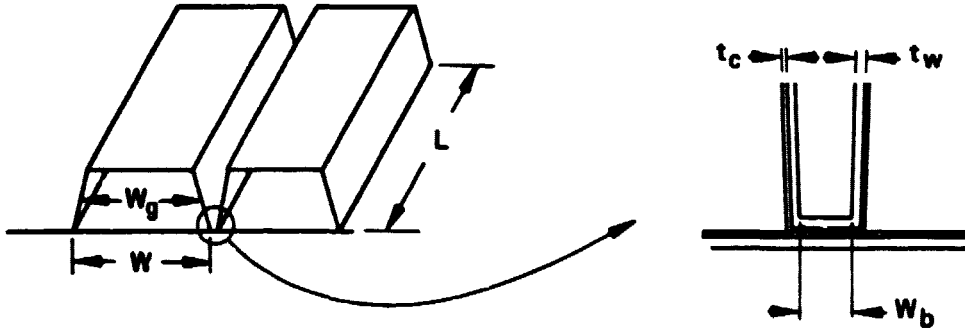
ITEM	MATERIAL	PRINCIPAL DIMENSIONS (CM)	MASS (kg)
SOLENOID WIRE INSULATION	COPPER	OD = 11.4, ID = 7.6, L = 41.9 (75% OF SOLENOID VOLUME)	16.4
	ALUMINA	(5% OF SOLENOID VOLUME)	16.0
			0.4
CAVITIES ASSEMBLY	COPPER	D = 7.6, L = 41.9, Z = 0.95	7.4
POLE PIECES (2)	IRON	D = 15.2, d = 2.5, Z = 1.02	2.8
SOLENOID HOUSING	STEEL	D = 12.7, L = 41.9, Z = 0.32	4.2
COLLECTOR PLATES			4.6
PLATE 1 (LWR)	TUNGSTEN	D = 15.2, d = 5.1, H = 0.8, t = 0.53	1.7
PLATE 2	TUNGSTEN	D = 15.2, d = 5.1, H = 1.0, t = 0.30	1.0
PLATE 3	TUNGSTEN	D = 15.2, d = 5.1, H = 1.3, t = 0.15	0.5
PLATE 4	TUNGSTEN	D = 15.2, d = 5.1, H = 1.5, t = 0.08	0.2
PLATE 5	TUNGSTEN	D = 15.2, d = 5.1, H = 1.3, t = 0.08	0.2
PLATE 6 (UPP)	TUNGSTEN	D = 15.2, d = 5.1, H = 2.0, t = 0.28	1.0
PROBE	TUNGSTEN	D = 2.5, d = 0, H = 3.8, t = 0.15	~
COLLECTOR PLATE ISOLATOR	ALUMINA	OD = 18.3, ID = 15.2, H = 15.5, t = 1.22	2.9
COLLECTOR SECTION COVER	STEEL	D = 20.3, H = 19.1, t = 0.13	2.0
OTHER COMPONENTS: REFOCUSING COIL, HEAT PIPES, HIGH-VOLTAGE CERAMIC SEALS, MODULATING ANODE CONNECTOR, CATHODE CONNECTOR, HEATER, OUTPUT WAVEGUIDES (2), VAC. ION CONNECTOR, CAVITY TUNING PROVISIONS, INTERNAL CABLING, ETC., AND ASSEMBLY AND INSTALLATION HARDWARE.			7.7
			(48 kg)

Table 6-5. Klystron Module Interfaces

<u>INPUTS</u>		
MODULATING ANODE		— MAIN POWER DISTRIBUTION
BODY ANODE		
CATHODE		
SOLENOID (MAIN)		
REFOCUSING COIL		
COMPRESSED COLLECTOR (5-STAGES)		
RF-INPUT WITH PHASE CONTROL	—	SOLID STATE CONTROL CIRCUITRY
 <u>OUTPUTS</u>		
RF-OUTPUT	—	TO RADIATING WAVEGUIDE
ARC SENSORS		— TO SOLID STATE CONTROL CIRCUITRY
DIPLEXERS		
PHASE SENSORS		
WASTE HEAT FLUX	—	TO MODULE THERMAL CONTROL SYS.

$$\lambda_g = \frac{12.24}{\sqrt{1 - \frac{37.45}{W_g^2}}} \quad (3)$$

This equation relates the guide wavelength to waveguide stick width (W_g).



$$W = W_g + 2 t_c + 2 t_w + W_b \quad (4)$$

W = External waveguide stick width
 W_g = Mean internal width of waveguide stick
 t_c = Conductive coating thickness
 t_w = Waveguide wall thickness
 W_b = Bond width

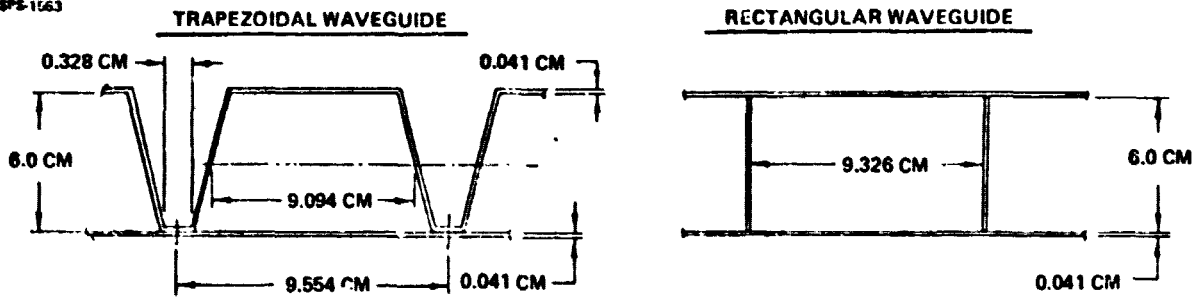
Choosing $n=2.0$ and reasonable dimensions for the wall and conductive coating thicknesses, a solution to the above equations yield:

$$\begin{aligned}
 W_g &= 9.0942 \text{ cm} \\
 \lambda_g &= 16.547 \text{ cm} \\
 W &= 9.554 \text{ cm} \\
 W_{\text{subarray}} &= 11.464 \text{ m} \\
 L_{\text{subarray}} &= 9.928 \text{ m}
 \end{aligned}$$

A subarray, 120 waveguide sticks in width and $60 \lambda_g$ long, can be powered by from 3 to 36 klystrons to approximate a Gaussian power density taper.

The choice of waveguide stick cross section was based on two major factors, total mass and constructability. The mass trade is in Figure 6-7. The lightest waveguide would be rectangular rather than trapezoidal, however constructability in space favors the trapezoid cross section. Because of the required close tolerances and the resulting construction difficulty, the trapezoidal configuration was chosen. Had the waveguides been shipped intact, the rectangular configuration would have been chosen and the subarray size would have been different.

SPS-1563



STRUCTURAL MAT'L: GR-EP -8PLY
 CONDUCTING MAT'L: ALUMINUM (T = 6.67 μM)

PER SUBARRAY	TRAPEZOID _{μL}	RECTANGULAR
MASS OF GR-EP :	234.5 KG	204.7 KG
MASS OF ALUM.:	9.3 KG	9.3 KG
MASS OF WAVEGUIDE	243.8 KG	214.0 KG
UNASSEMBLED PACKING MASS DENSITY:	1568.4 KG/M ³	1579.8 KG/M ³
VOLUME OF ASSEMBLED WAVEGUIDE:	6.97 M ³	6.92 M ³
ASSEMBLED PACKING MASS DENSITY:	35.0 KG/M ³	30.9 KG/M ³
MASS/ANTENNA:	1690.0 MT	1483.5 MT

Figure 6-7. Waveguide Configuration Comparison

Three waveguide conductive coatings were traded with respect to coating thickness, mass and system losses (Table 6-6). The over two to one mass advantage of aluminum made up for its higher loss, so aluminum was chosen.

6.5.1.1.2 Thermal Control

Using the rationale in Section 6.4, and design techniques in Reference 6.2, heat pipes and radiators were designed to dissipate klystron losses. The heat pipe evaporators, an integral part of the klystron, pick up the waste heat for transfer to the radiator (Fig. 6-8). Table 6-7 shows the heat pipe and radiator mass. The klystron thermal radiator has six sections, two small sections for the collector and the four larger ones for the cavities and solenoid. The collector section radiates at 500°C and the cavity/solenoid section at 300°C.

With permanent magnet focusing for the klystron instead of a solenoid, the 300°C section of the radiator would have one fewer section. Also, the collector section could run at 700°C, reducing the collector radiators to forty percent of their present size. However, the system shown uses the thermal limitation assumptions stated in Section 6.4 and is designed accordingly.

Even though the thermal control removes the heat released by module components, a high temperature still existed at module components such as solid state control, power distribution buses, and composite materials in the structure and waveguides. A lower temperature environment for these components was provided simply by isolating the high temperature sections of the klystron and the back side of its thermal radiator with thermal insulation (Table 6-8). This measure is discussed further in Section 6.4.

6.5.1.1.3 Solid State Control

The solid state control must be so located that its temperature will not exceed 70°C. Its power supplies and sensors must be isolated from other equipment to avoid EMI. The best location to mount this device appears to be on a klystron-module which is isolated from a view of the thermal radiator by the klystron, but which has a view of space for dissipating a small heat loss.

6.5.1.1.4 Power Distribution

The klystron and its driver require power at several voltages. Power converters must be easily installed and removed for maintenance. High-voltage electrical connections must be easily secured, and also shielded to prevent shorts by drifting objects. The main supports for the power distribution buses are provided in the subarray structure, with cables carrying power to the klystron modules.

Table 6-6. Waveguide Conductive Coating Comparison

	<u>ALUMINUM</u>	<u>COPPER</u>	<u>SILVER</u>
DENSITY:	2.70 G/CM ³	8.96 G/CM ³	10.49 G/CM ³
THICKNESS FOR 4 SKIN DEPTHS:	6.67 μ M	5.32 μ M	5.19 μ M
AREA PLATED/SUBARRAY:	3.00 X 10 ⁶ CM ²	SAME	SAME
VOLUME OF COATING/SUBARRAY:	2.46 X 10 ³ CM ³	1.96 X 10 ³ CM ³	1.92 X 10 ³ CM ³
MASS OF COATING/SUBARRAY:	6.64 KG	17.6 KG	20.1 KG
MASS OF COATING/ANTENNA:	46.3 MT	122.7 MT	140.2 MT
COMPARATIVE LOSSES (PER 10W STICK):	0.37%	0.30%	0.28%

2 - COLLECTOR RADIATORS - 0.246 M X 1.65 M (COPPER)
 4 - CAVITY AND SOLENOID RADIATORS - 0.253 M X 1.71 M (ALUMINUM)

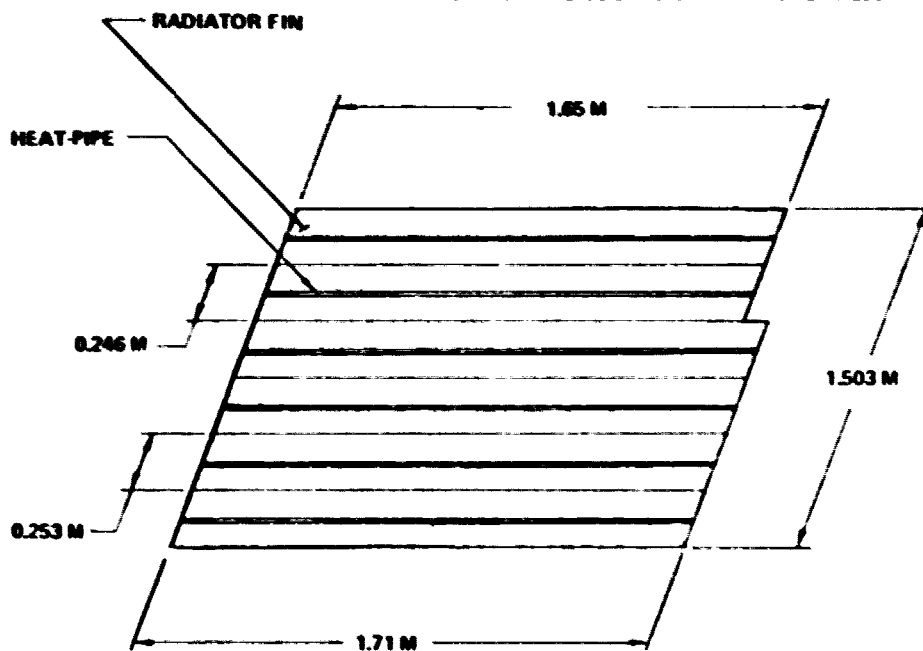


Figure 6-8. Typ. Module Thermal Radiator

D180-22876-4

SPS-1556

Table 6-7. Klystron Thermal Control

CAVITY AND SOLENOID SECT.ON:	300°C HEAT PIPE TYPE - 1.339 KG/M WORKING FLUID - H_2 4 HEAT PIPES - 1.30 KW EACH RADIATOR - ALUMINUM - THICKNESS - .051 CM - AREA - 0.432 m^2 EACH MASS (EACH) - 3.18 KG
COLLECTOR SECTION:	500°C HEAT PIPE TYPE - 1.339 KG/M WORKING FLUID - H_2 2 HEAT PIPES - 4.0 KW EACH RADIATOR - COPPER THICKNESS - 0.056 CM AREA - 0.406 m^2 EACH MASS (EACH) - 3.08 KG

MASS/KLYSTRON = 18.9 KG

SPS-1557

Table 6-8. Thermal Insulation

COMPONENTS:	TYPE:
500°C COLLECTOR SECTION (RADIATOR & KLYSTRON)	- 9 LAYER MULTIFOIL (ZrO SPACER) - 6 LAYER KAPTON (QUARTZ NET SPACER)
300°C CAVITY & SOLENOID (RADIATOR & KLYSTRON)	- 15 LAYER KAPTON (QUARTZ NET SPACER)
WAVEGUIDES	- 10 LAYER KAPTON (QUARTZ NET SPACER)

MASS/MODULE = 2.80 KG

6.5.1.1.5 Module Structure

The module structure is integral with the I-beam "egg-crate" subarray structure. This arrangement meets the major design drivers of Section 6.2 and is superior to alternates with respect to both space construction and transport.

6.5.1.1.6 Integration

Figure 6-9 shows an integrated klystron module sized for installation near the center of the antenna. The length of the waveguide supplied by one klystron depends on the number of modules per subarray. The quantization steps which define the number of modules per subarray for the reference configuration are described in Section 6.4.

6.5.1.2 Subarray

For this study, the subarray was chosen as the LRU. The structure supporting the klystron is designed to accept the variable number of modules per subarray necessary for output tapering. An integrated subarray for the lowest power density is illustrated in Figure 6-10. This structural configuration shows where the module components are located and how the integral structure was achieved. The same basic approach was used to layout a subarray structures and component locations for other power densities.

6.5.1.3 Secondary Structure

The spacetenna secondary structure supporting the subarrays is a tetrahedral planar truss, a module of which is shown in Figure 6-11 with subarrays installed. The modules may be built up in a planar fashion to form the planar radiating face of the antenna (Ref. 6.1).

Sixty-one of the hexagon structural cells shown in Figure 6-11 are arranged in five rings to form the complete secondary structure.

The subarray dimensions of 9.928m by 11.464m set the secondary structural member length of 11.464m. These members form equilateral triangles with a base of 11.464m and a height of 9.928m which will provide three support points for each subarray. The secondary module is supported at three points by the primary structure. The members of the secondary structure were sized and weighed on the basis of using graphite epoxy composite material and L_p of 200.

6.5.1.4 Primary Structure

The spacetenna primary structure is also a tetrahedral planar truss and gives depth to the antenna for stiffness and stability. It supports the secondary structure, power distribution buses, power conditioning equipment, thermal control components and antenna yoke attachment.

SPS-1576

D180-22876-4

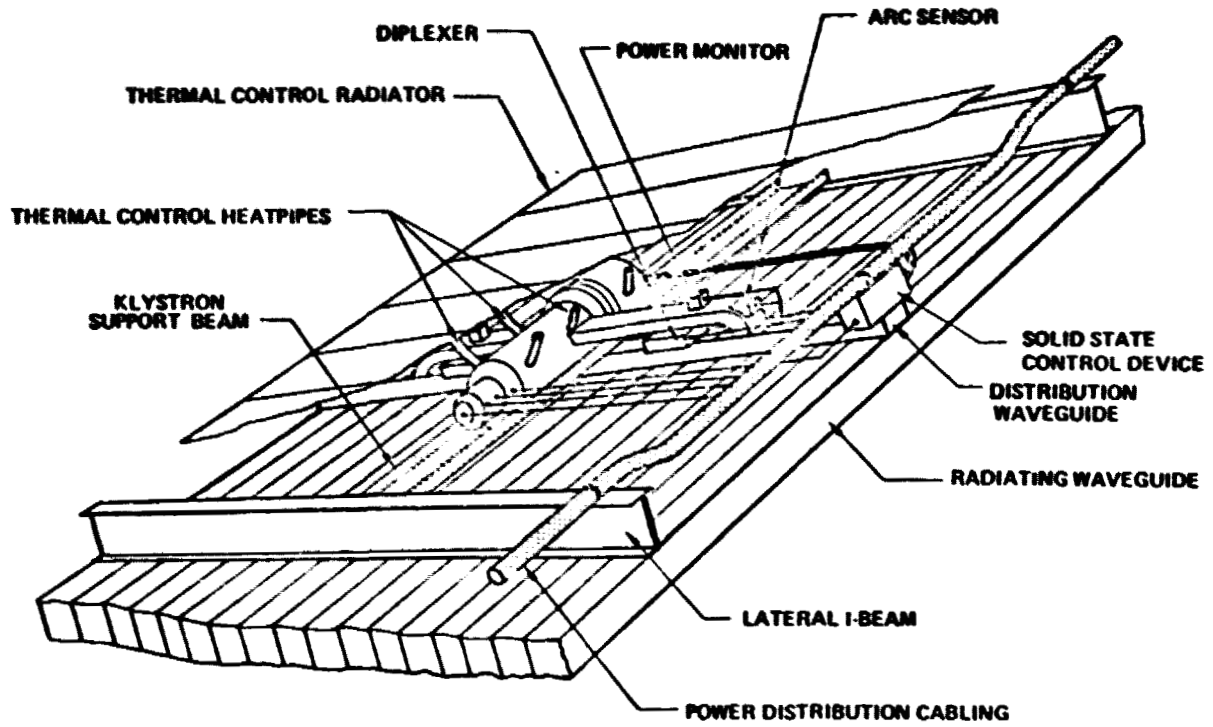
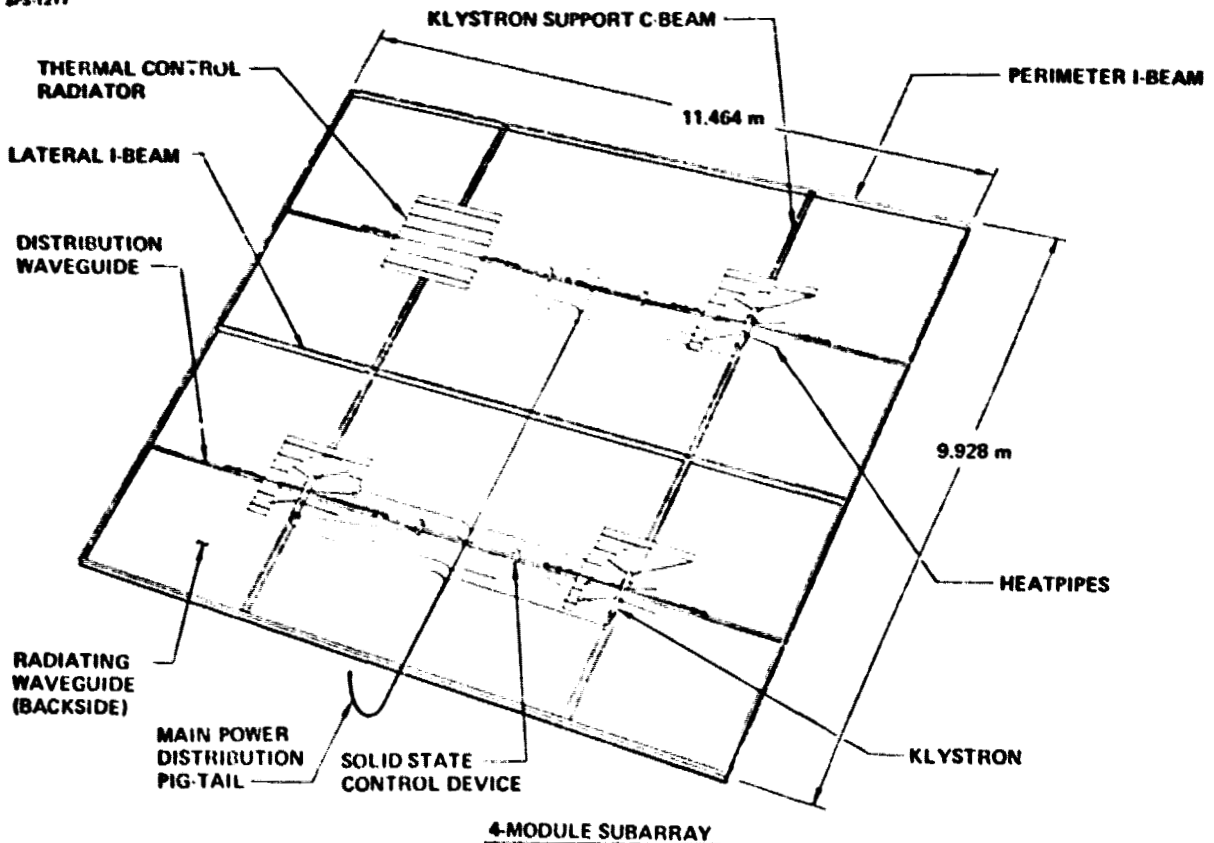


Figure 6-9. Integrated Klystron Module

SPS-1217



4-MODULE SUBARRAY

Figure 6-10. Integrated Subarray

D180-22876-4

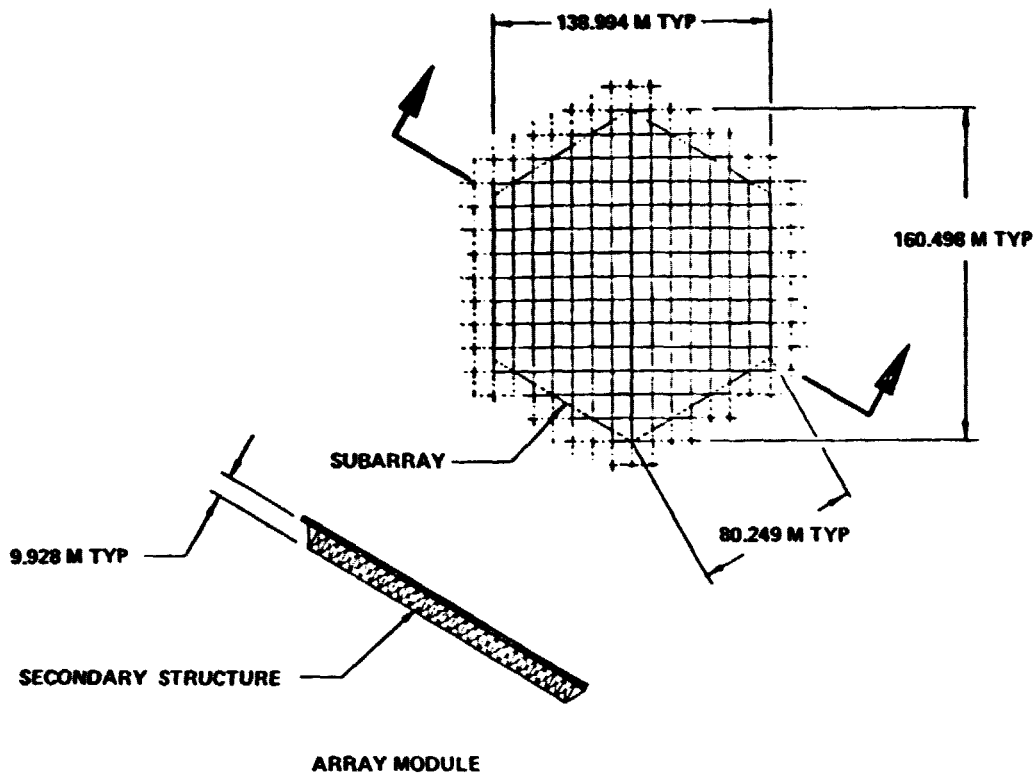


Figure 6-11. Secondary Truss-Module (Subarrays Shown)

D180-22876-4

The same structural design criteria used for the secondary structure led to the use of a five-meter beam in the primary structure. The length of the primary structure members was established by the requirement for supporting each hexagonal secondary structural module at three points. The primary structure is also made from graphite epoxy for reasons stated previously. The primary structure with secondary modules installed is shown in Figure 6-12.

The DC-DC converters and their thermal control are located on the back surface of the primary structure as shown in Figure 6-13. The required number and location of the power converters determine how many converters are located at each of the primary structural nodes (Sec. 5.0). A typical structural node with eight DC-DC converters is also shown. An active thermal control with built-in redundancy is required for the DC-DC converters. Such a system, sized in Section 6.4, is included in the mass statement of Section 6.5.4.

Distribution busses carry power from the rotary joint to the DC-DC converters and on to the subarrays and the klystron modules. The busses from the converters to the subarray run along primary and secondary structural members.

The calculated total mass of the MPTS structural components is less than five percent of the system mass. This structure, which meets all the design constraints, can be further optimized by removing the outer tetrahedral ring (Ref. 6.1) from the primary structure. This will reduce the mass of the primary structure and slightly increase the first mode frequency of the system.

6.5.1.5 Alternate Structures

A completely different structural approach, developed by J. C. Jones, NASA/JSC (Ref. 6.5), is shown in Figure 6-14. This type of structure is optimized for space fabrication by continuous-beam building machines. Since antenna loads are small there is little need to use optimum beam cross-sections. The structure is a small fraction of the MPTS mass, so even though this alternate structural arrangement may have to be slightly heavier to meet the stiffness and thermal-deformation requirements, its impact on overall MPTS mass will probably be insignificant.

The alternate structure interfaces better at the subarray. Waveguides would have to be resized and the power density steps for achieving power taper would have to be recomputed in evaluating fully this alternate structure.

6.5.2 Power Density Quantization

The actual integrated power density taper of the reference design was determined by evaluating all possible numbers of modules per subarray.

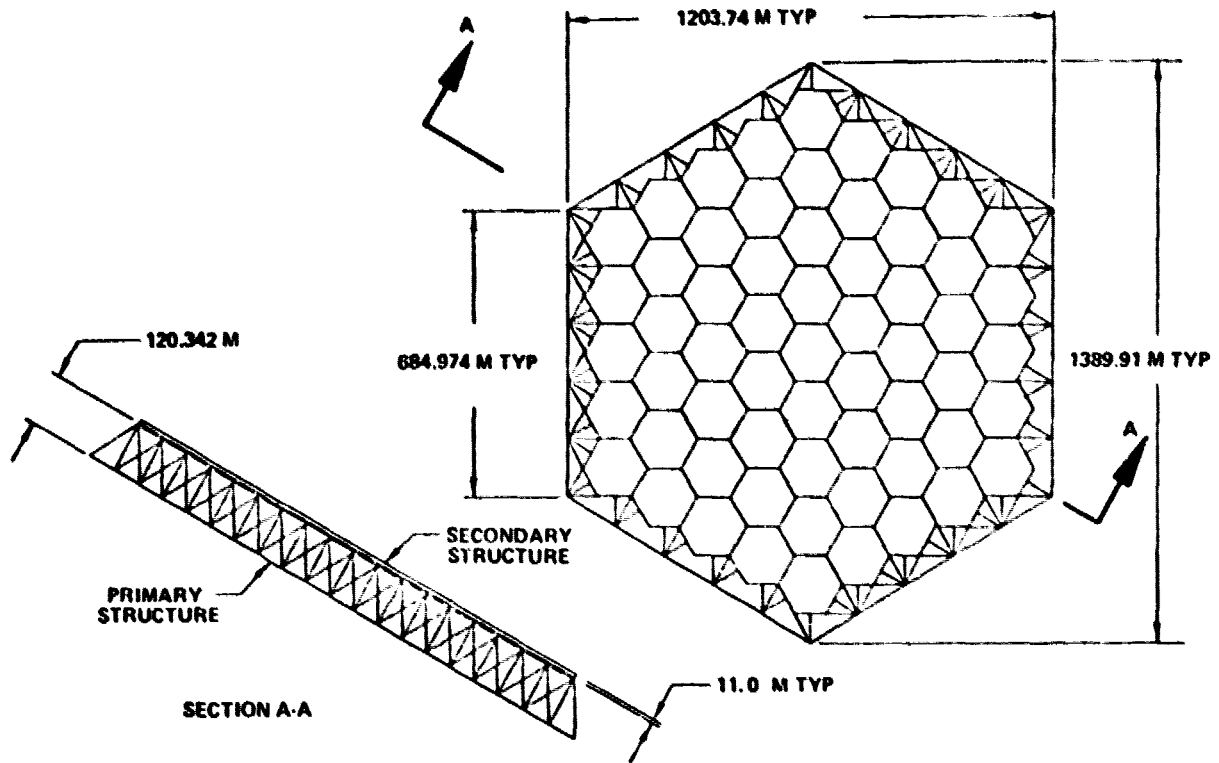


Figure 6-12. Primary Structure (Secondary Modules Shown)

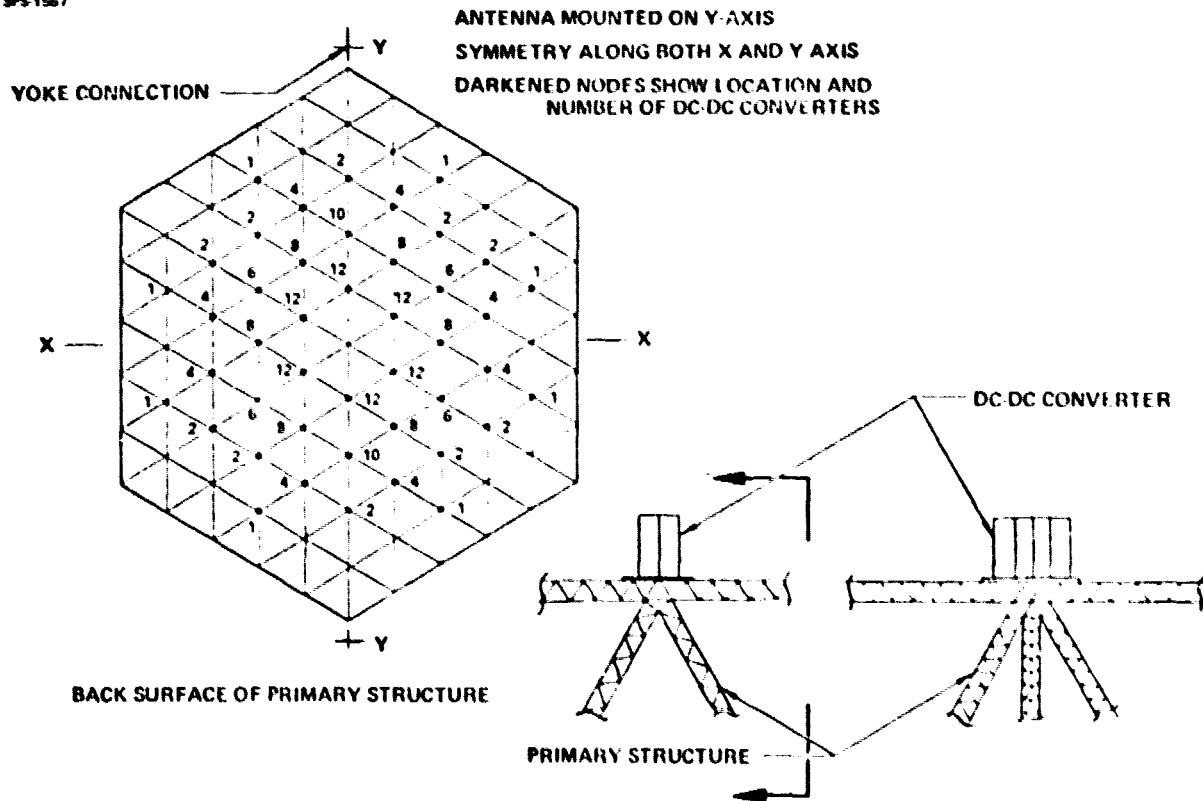


Figure 6-13. DC-DC Converter Placement Concept

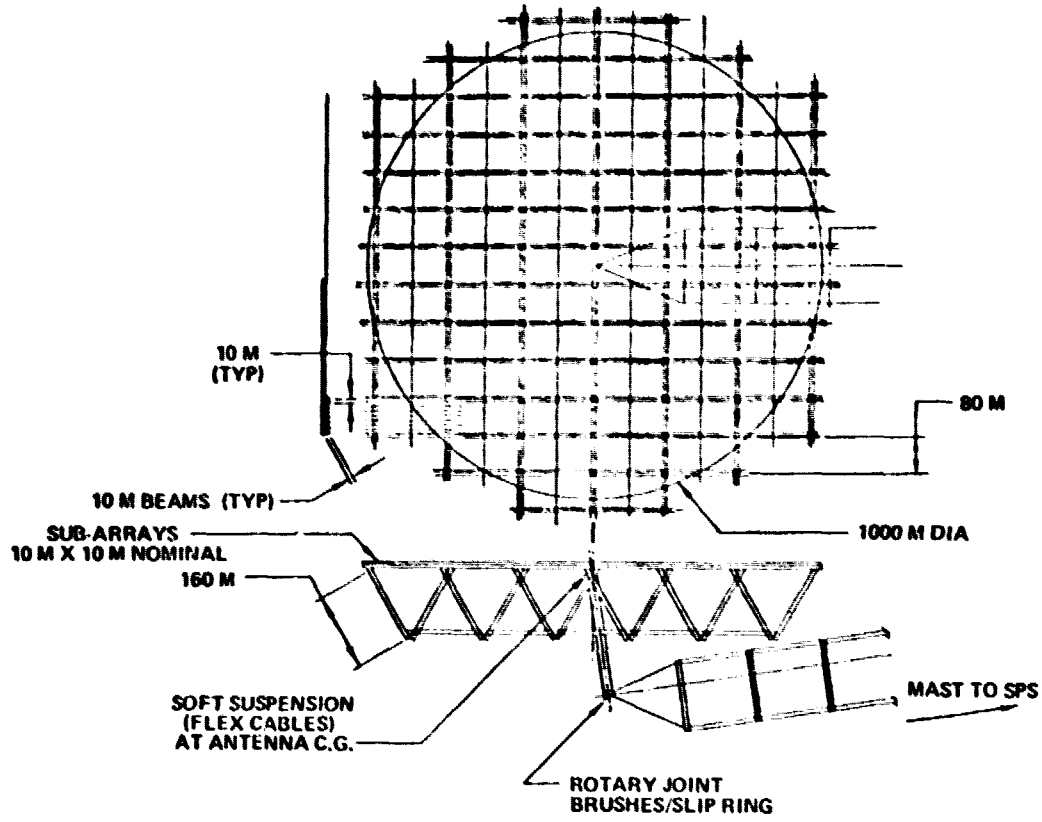


Figure 6-14. MPTS Alternate Configuration

D180-22876-4

To achieve an approximate 10 dB power density taper on the MPTS, the relation of power density levels as a function of antenna radius was:

$$\frac{P}{P_0} = e^{-2.302(\rho/a)^2}$$

P = Power density at the radius being investigated

P₀ = Power density at the center of the RF beam

ρ = Radius at which power density is being evaluated

a = Radius of antenna

Since there are only certain unique power densities available, due to the finite numbers of klystron modules per subarray, another set of relationships were used to better approximate a true Gaussian power taper:

$$\rho_H = \sqrt{\left(L_n \frac{P}{P_0} \right) a^2} \quad ; \quad \rho_V = \sqrt{L_n \left[\frac{P_n + \left(\frac{P_{n+1} - P_n}{2} \right)}{P_0} \right] a^2}$$

ρ_H -- radius at which the power density being investigated will horizontally intercept the gaussian curve.

ρ_V -- radius that the power density being investigated will vertically intercept the gaussian curve.

P_n -- power density being investigated at step n.

P_{n+1} -- power density at the previous step, n+1.

Computation of the possible number of modules per subarray, the respective power densities, horizontal and vertical intercepts was then accomplished and tabulated:

Step No.	Number of Klystron Modules/Subarray	RF Power Density (KW/M ²)	ρ _H (m)	ρ _V (m)
1	36	22.14	0	97.2
2	30	18.45	140.7	176.8
3	24	14.76	209.8	231.3
4	20	12.30	252.7	274.4
5	16	9.84	296.8	320.3
6	12	7.38	345.4	365.8
7	9	5.54	387.9	395.9
8	8	4.92	404.2	421.7
9	6	3.69	441.1	463.0
10	4	2.46	488.5	500.0

A complete integration of these parameters was accomplished on the MPTS array. Figure 6-15 shows a representative quarter of the array subdivided into steps that approximate a gaussian power taper with the power density levels available. This configuration delivers 5×10^9 watts to the power grid from the ground station, based on the beam and conversion efficiencies reported in Part I of this study.

6.5.3 Overall MPTS Characteristics

The MPTS can be characterized in terms of the microwave beam quality described in Section 2, thermal environment, thermally induced deformations, input power required, RF power output, size, and mass.

The thermal environment in the MPTS was analyzed using the heat coming from the klystrons, dc-to-dc converters and the variable heating sunlight. Figures 6-16 and 6-17 show the temperature of the antenna surface and other components, both with the sun on the RF radiating face and the sun on the back side of the antenna. The maximum temperatures are well within limitations assumed in Section 6.3.

Slope induced on the array face by the structure heating must be less than three arc minutes. Thermally induced deformations of the MPTS structure were predicted with a two module ring section, using Boeing IR&D data. The results of the calculation showed a maximum slope of six arc seconds. Extrapolating that data to estimate the total slope on the antenna face leads to a total slope of less than three arc minutes. Further work is needed before an overall antenna slope and deformation can be predicted accurately.

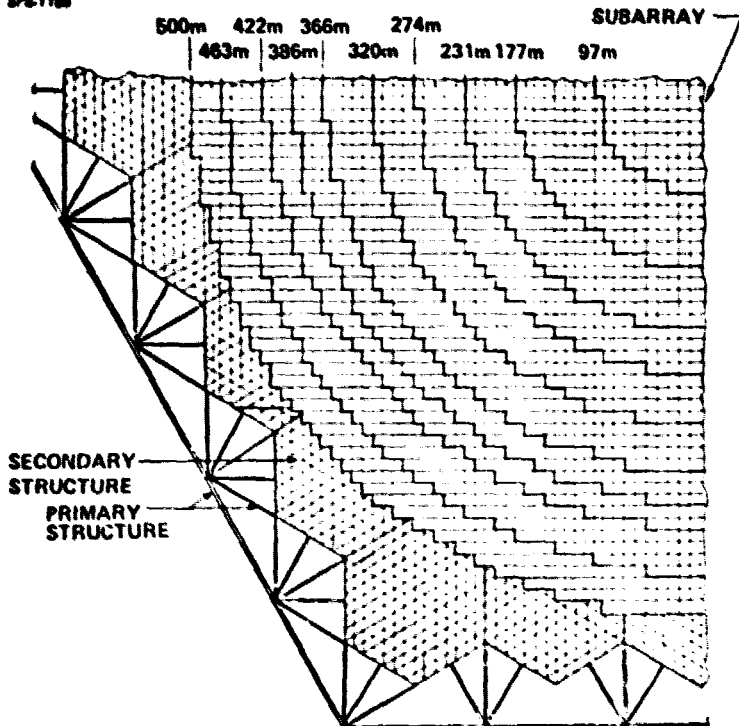
The rotary joint supplies to the MPTS 8.22×10^9 watts to generate 6.78×10^9 watts of RF radiated from the array. The earth receiving station delivers 5×10^9 watts to the power grid. Uncertainty analysis of system efficiencies and effect of tolerances will refine these values.

The physical size of MPTS is put in better perspective in Figure 6-18, along with the quantity and characteristics of its major components.

6.5.4 MPTS Mass Estimate

The mass of components was calculated and combined into major subsystems for the reference MPTS in Table 6-9. These are compared with NASA/JSC mass estimates in Table 6-10. The major mass drivers are the klystrons, thermal control systems, and power distribution. Mass and cost of the MPTS, by WBS elements, are summarized in Table 6-11.

SPS-1100



STEP	NO. SUBARRAYS	NO. KLYSTRONS
1 @ 36	272	9792
2 @ 30	580	17420
3 @ 24	612	14688
4 @ 20	612	12240
5 @ 16	756	12096
6 @ 12	864	10368
7 @ 8	628	5652
8 @ 8	576	4608
9 @ 6	1032	6192
10 @ 4	1000	4000
TOTALS	6,932	97,056

POWER OUTPUT: (ANTENNA) 6.78 GW
(GROUND) 5.01 GW

Figure 6-15. Power Taper Integration

SP-1876

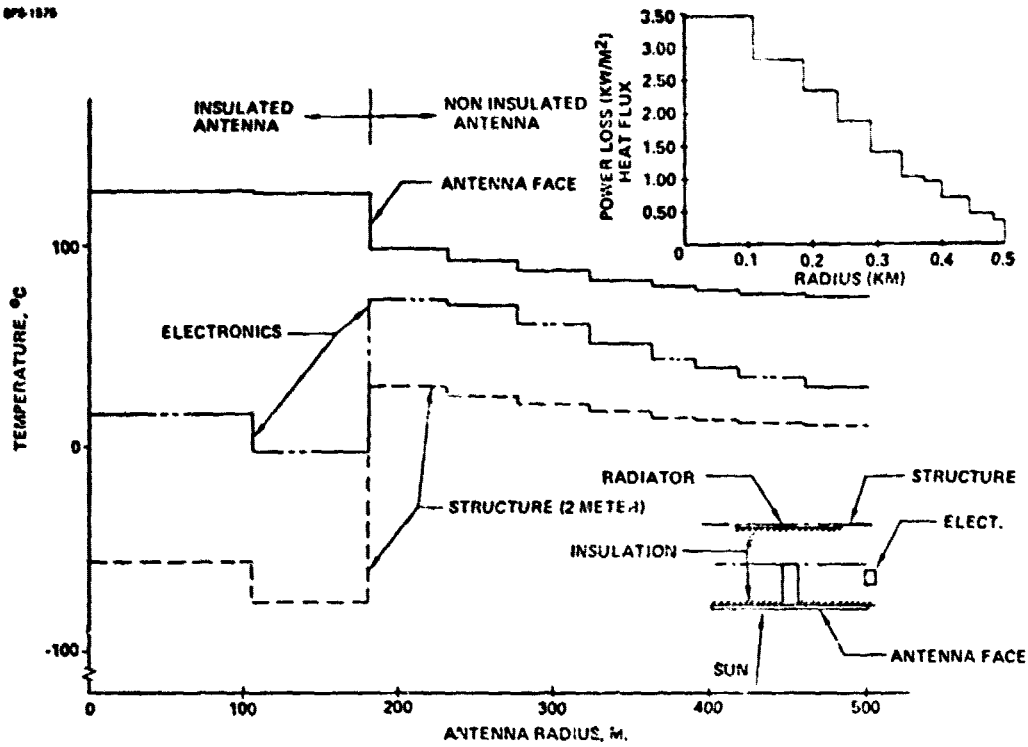


Figure 6-16. Antenna Temperature Profile (Sun On The Front)

SP-1874

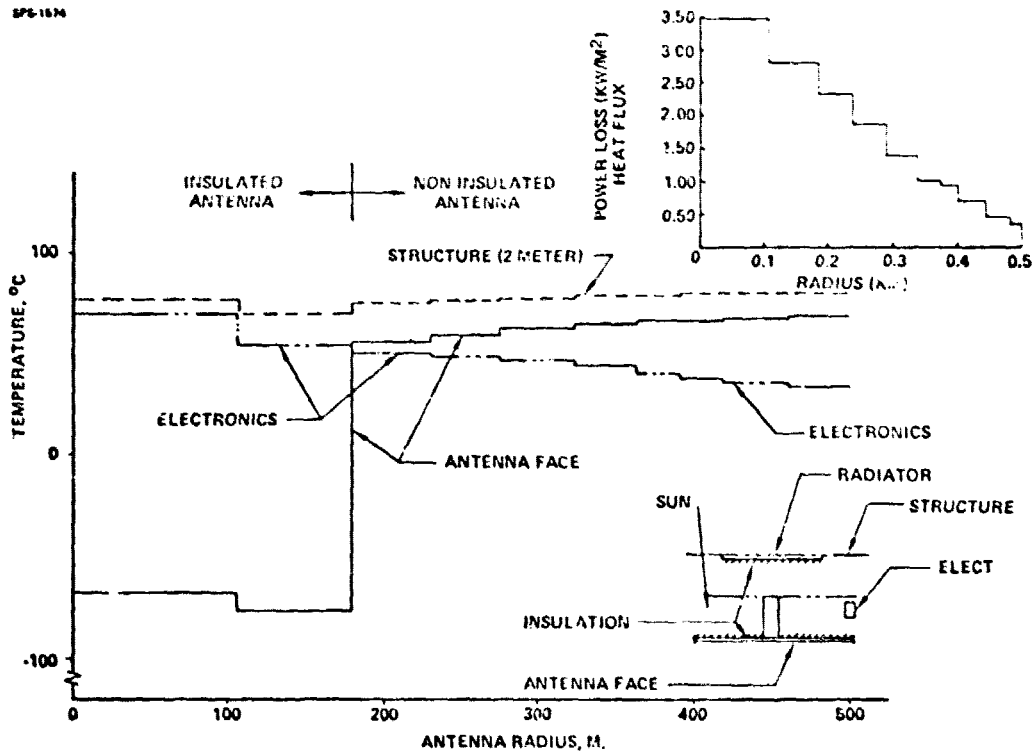
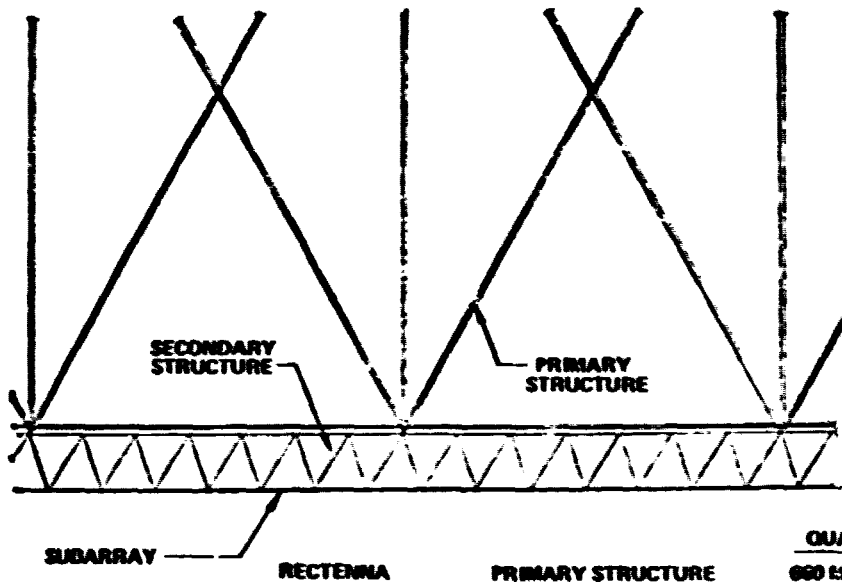


Figure 6-17. Antenna Temperature Profile (Sun On The Back)

SP-1000

D180-22876-4



	<u>QUANTITY</u>	<u>CHARACTERISTICS</u>
PRIMARY STRUCTURE	660 MEMBERS	138.84 M LENGTHS
SECONDARY STRUCTURE	79,422 MEMBERS	11.464 M LENGTHS
SUBARRAYS	6,932 10 TYPES	11.464 M X 9.928 M POWER TAPER
KLYSTRONS	97,056 TUBES	70 KW EACH

Figure 6-18. Reference Structural Characteristics

SP-1197

Table 6-9. Reference Antenna Mass Estimate

COMPONENT	MASS (MT)
PRIMARY STRUCTURE	- 52.5
SECONDARY STRUCTURE	- 197.5
POWER DISTRIBUTION	- 2494.1
RF GENERATION AND DISTRIBUTION	9430.0
KLYSTRONS	- 4659
THERMAL CONTROL	- 2093
WAVEGUIDES	- 1724
DISTRIBUTION AND CONTROL	- 521
SUBARRAY STRUCTURE	- 433
	12,174 MT/ANTENNA
	- 24,348 MT/SATELLITE

D180-22876-4

Table 6-10. MPTS Mass Comparison

SFS 1088

	JCS NOMINAL CASE	CURRENT REFERENCE
	MASS (MT)	
PRIMARY STRUCTURE	382	185
SECONDARY STRUCTURE	518	385
SUBARRAY STRUCTURE	300	886
THERMAL CONTROL (KLYSTRON)	23	4186
MECHANICAL SYSTEMS	30	(30)
ROTARY JOINT	635	94
POINTING CONTROL	100	(100)
POWER DIST. (W/THERMAL CONTROL)	167	5060
PHASE CONTROL	358	(358)
MICROWAVE GENERATORS (W/SOLID STATE CONTROL)	8846	10,288
WAVEGUIDES	4002	3447
TOTAL MASS (MT)	15,371	24,929

Table 6-11. MPTS Mass and Cost Estimate

SFS 1140

		MASS (MT)	COST (\$ x10 ⁶)
1.01.01.03	MPTS	12,749	1004.29
1.01.01.04.00	COMMON	3,326	358.99
1.01.01.04.00.00	STRUCTURE	250.0	13.7
1.01.01.04.00.01	CONTROLS	(358)	157.5
1.01.01.04.00.02	POWER DIST.	26.8(+TBD)	144.7
1.01.01.04.00.03	COMM/DATA	(100)	44.0
1.01.01.04.01	TYPE 1 SUBARRAY	833.1	59.1
1.01.01.04.02	TYPE 2 SUBARRAY	1,506.3	107.0
1.01.01.04.03	TYPE 3 SUBARRAY	1,305.0	91.6
1.01.01.04.04	TYPE 4 SUBARRAY	1,122.2	77.4
1.01.01.04.05	TYPE 5 SUBARRAY	1,151.1	29.1
1.01.01.04.06	TYPE 6 SUBARRAY	1,042.9	70.9
1.01.01.04.07	TYPE 7 SUBARRAY	613.6	40.8
1.01.01.04.08	TYPE 8 SUBARRAY	507.7	32.3
1.01.01.04.09	TYPE 9 SUBARRAY	759.9	49.6
1.01.01.04.10	TYPE 10 SUBARRAY	581.2	38.6
FOR 10.0 GW, 2 ANTENNAS,		25498 MT	\$ 2008.6 (10⁶)

6.6 DISCUSSION

The reference MPTS configuration that evolved from this study illustrates two important points: (1) The MPTS impacts significantly on the mass, cost, and complexity of the solar power satellite, and (2) an integrated MPTS can be designed without needing breakthroughs or new technology.

The reference MPTS in this section is not the only workable configuration but it represents integrated approach useable in trade studies leading to a final MPTS. Component and system selections were accomplished by minimizing system mass and complexity, but further optimization is possible and should be carried out.

The areas in the MPTS configuration that need to be addressed in greater detail to establish a more complete integrated system are: (1) a more complete thermal analysis considering thermal deformations, (2) vibrational mode analysis; (3) pointing and attitude control, and (4) the construction/maintenance scenarios which establish the most efficient LRU of the system.

The thermal analysis should be based on a system model that is sufficiently detailed to permit prediction of the thermal transients that occur during seasonal variations, and the computation of structural deformations caused by the thermal transients. This would aid in identifying elements that would require adjustments or design features that compensate for thermally induced deformations.

The dynamic analysis of the reference configuration will provide data for developing compatible attitude and pointing-controls, which can be evaluated for their impact on MPTS mass and performance.

The thermal analysis, dynamic analysis and more comprehensive construction/maintenance scenarios would lead to a more complete evaluation of the system LRU. For this part of the study, the subarray was chosen, somewhat arbitrarily, for the system LRU. A klystron module as the LRU, illustrated in Figure 6-19, is an alternate that needs to be evaluated.

Lastly, the MPTS structural configuration proposed by J. C. Jones of NASA JSC requires further analysis and elaboration to a depth compatible with that done in Part II of this study.

D180-22876-4

SP6-1871

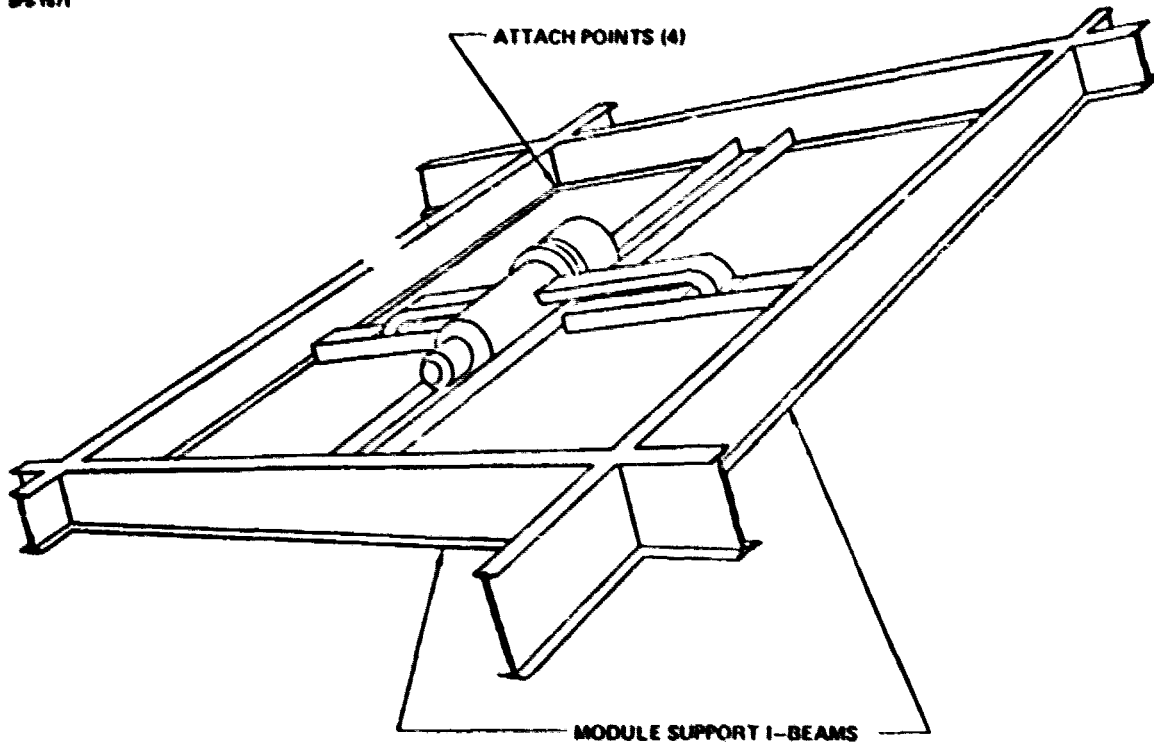


Figure 6-19. Klystron Module LRU

6.7 MPTS EFFICIENCY BUDGET

The MPTS end-to-end efficiency chain is a critical parameter in the overall practicality and cost-effectiveness of the SPS. The elements of this chain are listed in Table 6-12 along with estimates of their associated minimum and maximum boundary values. This section summarizes the rationale on which these values are based and derives a nominal value of the MPTS efficiency chain as 56.3% with a worst case value of 41.2% and a maximum value of 68.3%. These are derived on the basis of previous NASA-JSC work and estimates from sections referred to in this report. They are grouped into (6.7.1) Spaceborne power distribution losses, (6.7.2) RF conversion and distribution losses, (6.7.3) Antenna Array losses and transmission medium losses, and (6.6.4) ground based reception and distribution losses. Section 6.7.5 discusses the effect of component failures.

6.7.1 Space Power Distribution Losses

Essential to the SPS is transfer of power across the rotary joint that couples the sun-facing power source to the earth-oriented spacetenna. The candidates considered were the power clamp, rotary transformers, and slip rings. The slip ring is the simplest, lightest and has a nominal efficiency approaching 100%. This value has been selected with the understanding that as with many other components in the MPTS, the 30 year life and performance must yet be demonstrated.

The spacetenna power distribution and processing efficiency loss is shown in Table 6-13 as derived from Section 5.2.6. The power distribution data resulted from a mass and efficiency optimization of flat and circular aluminum conductors and power conditioning equipment and included consideration of an optimized distribution system to the various elements of the high efficiency klystron design, with about 85% of the power in an unprocessed form.

6.7.2 RF Conversion and Distribution Losses

Klystron conversion efficiency estimates discussed in Section 4.2 range from 80% to 87%. Optimization of electronic efficiency, circuit efficiency, and collector energy recovery. Although it is relatively easy to increase the overall efficiency from 50 to 65% using a 3-stage depressed collector energy recovery of about 70%, the task of obtaining an 85% efficient klystron will likely require the use of a 5-stage collector. With an undepressed efficiency of 74% and a collector recovery of 50%, a net efficiency of 85% would be realized. The design parameters for the 70 kW klystron support this estimate as shown in Table 4.4.

The Waveguide I²R loss was computed on the basis of an average waveguide length (2.76 meters) and a geometry utilizing a dual power output for the klystron. The calculated I²R loss of 1.5% refers to the dissipative power loss component associated with an aluminum plated composite waveguide having the selected internal dimensions of 9.09 cm x cm. Thermal distortions over the expected temperature ranges were found to be negligible. The plating thickness of less than 5 skin depths was used in the mass estimate, and the loss uniformity with this plate thickness need to be verified experimentally.

D180-22876-4

Table 6-12. MPTS Efficiency Chain

SECTION	EFFICIENCY ITEM	NOMINAL	MINIMUM	MAXIMUM
6.6.1	ROTARY JOINT	1.0	1.0	1.0
	POWER DISTRIBUTION AND PROCESSING	.97	.95	.98
6.6.2	DC-RT CONVERSION	.85	.80	.86
	WAVEGUIDE I ² R	.985	.985	.985
6.6.3	IDEAL BEAM	.965	.965	.99
	INTER-SUBARRAY	.956	.88	.97
	INTRA-SUBARRAY	.981	.97	.99
	ATMOSPHERIC ABSORPTION	.98	.98	.98
6.6.4	BEAM INTERCEPT	.95	.90	.98
	RECTENNA RF-DC	.848	.79	.92
	GRID INTERFACING	.97	.96	.98
	MPTS TOTAL	.563	.412	.683

Table 6-13. Spacetenna Power Distribution and Processing Loss

	I ² R LOSS (WATTS)	% LOSS
ROTARY JOINT TO POWER SECTOR CONTROL	145,453,890	1.74
SECTOR CONTROL TO SUBARRAYS	49,903,520	0.60
SECTOR CONTROL DC/DC CONVERTERS AND SWITCHGEAR	49,644,720	0.59
SUBARRAY WIRING (INSULATION INCL.)	4,774,760	.06
TOTAL	249,776,890	2.99

6.7.3 Antenna Array Losses

The ideal beam efficiency for the circular spacetenna geometry was calculated numerically on Boeing's computer system as described in Section 2.3.1. The ideal beam efficiency value of 96.5% is the percentage of energy contained in the main beam of the far-field energy distribution, relative to the total power radiated, for a continuous 10dB Gaussian taper.

Inter-subarray effects were evaluated using a modified version of the NASA JSC "Bigmain" computer program. This program numerically integrates contributions from all subarrays to obtain beam patterns, total power, and efficiencies. The 4.4% loss is based on a Gaussian phase error with a standard deviation of 10 degrees and Gaussian amplitude error with a standard deviation of ± 1 dB. No failures were included. The above loss is independent of subarray size.

Intra-Subarray losses were evaluated on the basis of assumed mechanical errors within the subarrays as described in Section 2.2.3.

Because of manufacturing tolerances and thermal distortions, waveguide size as well as slot shape and position will be displaced from nominal values. These dimensional changes will produce unwanted scattering and impedance mismatch resulting in a reduction in efficiency. Factors affecting the losses in the subarrays were studied for a set of given manufacturing and control tolerances and are summarized in table 2-1. These were found to produce non-dissipative power losses totaling 1.87%. A number of factors including tolerance in the feeder guide from the klystrons and beam squint due to stick errors were found to produce negligible power losses.

Atmospheric absorption at 2.45 GHz is listed in Table 6-7 at a value of 2% as previously derived from NASA-JSC estimates (JSC-11568). Polarization losses due to Faraday rotation have not been evaluated in this study and are judged to be low except perhaps during severe solar storm activity.

6.7.4 Ground Based Reception and Distribution Losses

The elements in this group include rectenna siting for cost effective collection, rectenna conversion efficiency and power grid interface losses. The efficiency chain up to this point includes all the radiated power in the main beam. The beam intercept efficiency is defined as that portion of the main beam energy captured by the rectenna due to its finite size. In our study, this was taken as 95%, since in our preliminary optimization it was found that the large rectenna size increment required to capture the remaining energy at a decreasing conversion efficiency is not cost effective. Further refinement in this figure may slightly change its exact value.

The RF-to-DC conversion efficiency of the dipole-fed GaAs rectifiers was derived by numerical integration of measured and projected efficiency values, with receiver element efficiency varying as a function of incident intensity. The current reference value is probably slightly pessimistic for two reasons: (1) the average was based on a receiver filling the entire main beam. The cost-optimized receiver does not intercept the low-intensity outer part of the beam and its average intensity should be slightly greater; (2) recent projections by Raytheon and JPL indicate slightly higher element efficiencies.

However, these projected values, particularly at low incident r.f. density assume r.f. combining techniques and GaAs improvements which need to be verified experimentally.

The grid interface efficiency of 97% is the combination of a 2% loss for the solid state power conditioning processors required to feed the d.c. power into the grid and a 1% loss for power distribution. These values are a topic of further verification in the current SPS Phase III study.

6.7.5 Effect of Failures

Clearly, component and subsystem failures will further reduce the end-to-end efficiency indicated in Table 6-12. The detailed nature of the effects of different types of MPTS failures is beyond the scope of the present study. However, some comments on r.f. transmitter failures can be made. For example, with the choice of dc-dc power converter size, supplying an average of 420 klystrons, the effect of one converter failure was evaluated in Section 2.4.1. The results in Figure 2-30 indicate that, on the average, the total collected power reduction is 0.91%, composed not only of the reduced transmitter power (0.43%) but also the reduced beam antenna efficiency (0.48%) as determined by the "Bigmain" computer comparison. This is also accompanied by a slight increase in sidelobe level of 0.4 to 0.5 db.

In some previous analyses, a criteria of allowable subarray failure was stated as 2%. If these are distributed randomly, resulting in a random thinning of the array, the reduction in end-to-end efficiency would approach 4%, composed of the reduction in antenna gain of 2% (proportional to the area loss, to first order) and a reduction in transmitted power of 2% on the average. If the lowest replaceable unit (LRU) is selected at the klystron level, and individual klystrons are identified as failures, somewhat different results can be expected. It is of interest to note that data in Figure 2-30 can be extrapolated to indicate that if 2% of subarrays all fail in the center, a beam efficiency reduction of roughly 6% can be expected whereas if 2% of subarrays fail at the periphery, only a 1% reduction in efficiency occurs. These values must again be augmented by the additional r.f. power loss. An indepth analysis of the various types of system failure will be a subject of continuing studies.

7.0 RECOMMENDATIONS

Although a workable integrated baseline configuration has been sized, costed, and optimized for a 5 GW output per antenna at the tentatively selected industrial band (2.45 GHz) frequency, there are a number of additional finite analytical and small-scale laboratory tasks which have been defined, whose output would further reduce uncertainty and provide answers to important current issues. These are categorized as follows:

- 7.1 Baseline Design Refinements**
- 7.2 Elaboration of Ground Based MPTS Element**
- 7.3 Alternate Design Factors**

The effort contains tasks for both near term and ongoing work.

7.1 BASELINE DESIGN REFINEMENTS

The suggested tasks are designed to further reduce risk and to supply information which would assist in go/no go decisions. The laboratory tasks include a measurement program on subarray elements to answer questions relating to interference, long life, and critical element design. These include:

- **Measurement of higher order modes of the slotted waveguide configuration to determine capability of the array to suppress radiation of harmonics or of noise at some distance away from the carrier.**
- **A laboratory program for the design of a cross guide feed configuration meeting klystron VSWR requirements and subarray waveguide stick matching requirements.**

To arrive at a workable analytical reliability model of the r.f. transmitter further work is required. As a start, an updating of current life experience on thermionic and cold cathode tube types as derived from industry and DoD sources should be undertaken. Various cathode type options which have potentially long life need to be further explored with industry. This will include identification of problem areas in ground testing, cathode interfaces with other materials in the tube envelope and life test results which will ultimately lead to a better reliability model of the transmitter. In conjunction with the thermal behavior of the spacetenna as a whole, an improved thermal model under eclipse conditions is needed to further refine predictable deformations and their effects on array efficiency and sidelobe distribution.

From the microwave environment point of view, further answers on the behavior of far out sidelobes is needed, particularly in a multi-SPS configuration. The antenna pattern analysis computer program adapted from NASA/JSC, with some modifications, is able to examine far out sidelobe

D180-22876-4

behavior as a function of phase control precision, transmitter failures, illumination taper and taper quantization. Means of minimizing far out sidelobe intensity should be determined and these means reflected as possible design requirements on the system.

To bring the phase control system up to the level of definition of the rest of the MPTS, the requirements on beam steering due to pilot frequency offset to eliminate squint, should be further examined. Alternatively, a trade study to determine the requirements on the antenna stabilization system in conjunction with feasible diplexer designs should be undertaken.

The RFI environment of the SPS has yet to be evaluated. The main contributors in this area are transmitter noise and harmonics. The status of transmitter assessment is far enough along to enable a detailed description of development specifications for a klystron manufacturer. Although some data on AM/PM noise near the carrier of klystrons and CFA's is available more relevant values are needed for the actual operating conditions and circuit configuration of the SPS transmitter. From this starting point, data could be evolved giving estimates of potential interference levels in the vicinity of the microwave beam.

7.2 ELABORATION OF GROUND BASED MPTS ELEMENTS

Certain tasks are recommended related to the optimization of rectenna characteristics which received little attention in the current SPS study. An investigation of baseline dipole spacing and some specific alternatives to the reference design are suggested in order to reduce overall number of rectifier elements, allowing higher efficiency and lower cost.

An analytical determination of rectenna efficiency as a function of element spacing should be undertaken leading to an overall optimal spacing based on total system cost. An analytic investigation of non-beam-normal rectenna configurations should be conducted together with a design approach that would lead to an efficient planar horizontal rectenna. A conceptual design for a cost-effective rectenna power collection, distribution, processing and grid-interfacing system would be desirable from this work as a separate task. The "BIGMAIN" JSC Program could be modified to analyze the case of the elliptical rectenna.

7.3 ALTERNATE DESIGN FACTORS

In view of possible proliferation of SPS's in various geographic locations, operation at other frequencies may be feasible and desirable. The next higher industrial band at 5.8 GHz is particularly suitable in areas of relatively low rainfall. An integrated design definition should be developed for a transmission system operating at 5.8 GHz. This development will include selection of power level, spacetenna and rectenna size, and development of comparative data for all elements of the transmission efficiency chain, with particular attention to:

D180-22876-4

- **Klystron efficiency and power rating**
- **Distribution and radiation waveguide contributions to phase error and other losses**
- **Phase control errors**
- **Atmospheric absorption including weather**
- **Rectenna efficiency, based on available or estimated as diode efficiency**

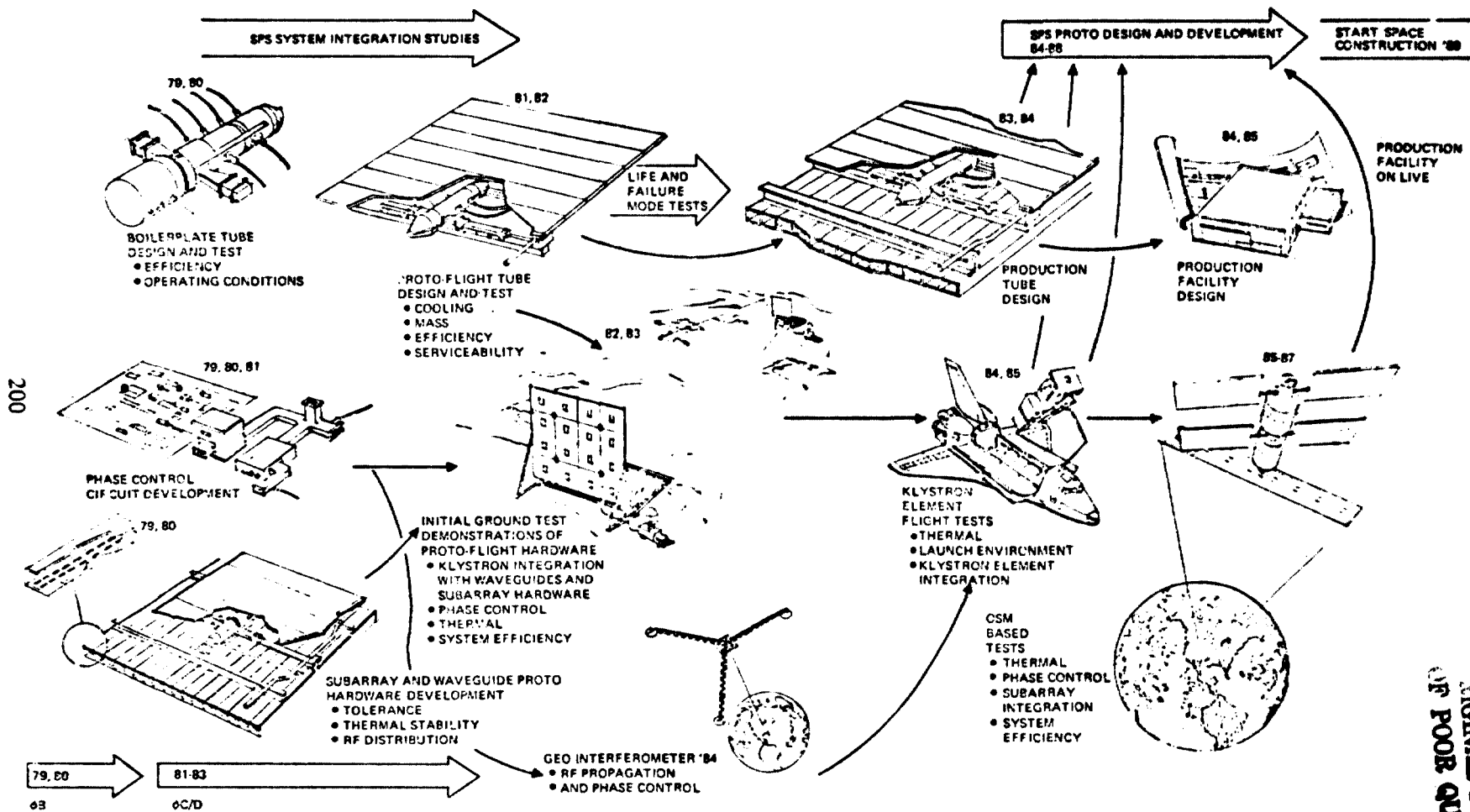
Cost comparison data should be developed which will include:

- **Efficiency and size effects on total cost**
- **Rectenna size and parts count**
- **Transmitter differences**

Current analyses of alternate candidates have identified some promising features of end fire arrays and of the "enhanced" slot as a means to control mutual coupling, i.e., lower sidelobe level and higher efficiency. Although the simple slotted waveguide still emerges as the most viable candidate, further analytical effort (prior to laboratory tests which require perhaps 30 elements or more) would provide a better data base on which to recommend further action. These include variation of element spacing, assessment of weight and ease of construction, and better estimates of radiation efficiency.

Evaluation of alternate radiating elements for both the rectenna and spaceborne antenna should be extended to include analysis of edge effect reduction through the use of enhanced slot elements, and element number reduction through the use of end fire radiators.

The above tasks will further the SPS indepth technology understanding to a point where some major steps for ground testing can be initiated, and from which planning for initial space evaluation may be pursued. The steps along which these could proceed are indicated in the flow chart of Figure 7-1, the elaboration of which is recommended for further study. Even prior to full scale testing, a number of aspects of beam shaping, open envelope testing of the transmitter, and ionospheric interactions monitored from a nearby spaceborne platform could be tested. Some parameters suitable for shuttle tests have been defined in Fig. 7-1.



D180-22876-4

SIGNAL PAGE 19
OF POOR QUALITY

Figure 7-1. SPS System Integration Flow Chart

D180-22876-4

Appendix A

**THE KLYSTRON AS A MICROWAVE POWER SOURCE
in the
SOLAR POWER SATELLITE APPLICATION**

November 1977

**Note: A consolidated version of this Appendix has been issued as a separate document.
Appendix A contains selected sections of this document.**

**Prepared for:
THE BOEING COMPANY**

by

**Varian Associates, Inc.
Palo Alto Microwave Tube Division
611 Hansen Way
Palo Alto, California 94303**

A.1 KLYSTRON FAILURE MODES AND OPEN CONSTRUCTION

Certain types of klystron failure modes would be affected by the use of open construction. In some cases the failure mode may be eliminated; in others, some of the adverse effects may be mitigated.

Possible failure modes that may be considered are:

- Loss of vacuum
- Internal outgassing
- Leaks
- Ceramic fractures
- Insulator leakage
- Cathode emission
- Miscellaneous

Loss of Vacuum

The known desirable range of vacuum in microwave klystrons is roughly 10^{-7} to 10^{-10} Torr. It seems likely that higher vacuum than 10^{-10} would be beneficial, but there is no actual experience to validate this idea. At 10^{-6} Torr, poisoning effects on oxide or matrix cathodes become noticeable. At 10^{-4} Torr, arcing between electrodes may occur, and at 10^{-3} , failure is generally imminent. These figures may vary at least an order of magnitude from one tube type to another; they are quoted only as a rough scale of orders.

Good industrial practice requires vacuum of the order of 10^{-8} Torr at bakeout temperatures of 400 to 650° C, falling to 10^{-9} Torr at room temperature. During processing and aging the pressure may rise temporarily to 10^{-6} Torr, but should settle down in the 10^{-7} to 10^{-8} Torr region for a good, fully-processed tube. This level should be maintained throughout the life of the tube, generally with the aid of an ion pump in larger tubes.

Even when the pressure is kept more or less constant, the vacuum is not a static affair but is highly dynamic. Molecules which constitute the gas at any instant are continually moving from one part of the tube to another; absorbed, retained, and re-evaporated under varying electrical conditions.

In terrestrial service, vacuum may be degraded or lost from several causes:

Internal Outgassing

Internal outgassing may occur because of parts reaching higher temperatures than in processing, or to material porosity allowing migration from deep reservoirs or from enclosed pockets, "virtual leaks." No tube part is ever fully degassed (Langmuir estimated that to remove the last monolayer of oxygen from tungsten would require 1 year at 1500° C). Because of the dynamic nature of the

D180-22876-4

vacuum, gas driven from areas under electron bombardment may accumulate in adjacent areas. Then a change of operating conditions may shift the area of bombardment to these areas and cause a rapid release of this gas, possibly to a level sufficient to cause arcing or other undesirable effects. Whenever a tube is shut down, similar redistributions of gas occur, manifesting themselves as temporary performance anomalies on startup. Thus, degassing effects can extend far into the life of the tube and cannot be thought of simply as a quasi-static gas content decreasing with time.

Opening the tube envelope at synchronous altitude will prevent gas pressures from building up to the harmful levels which would ultimately cause tube failure. Removal of larger areas of the envelope will smooth out the bursts of gas caused by changes in operating conditions. Thus the use of the vacuum properties of space will alleviate the effects of outgassing. They will not, however, eliminate them, even under the best conditions.

Leaks

In the leak category, we consider poor metal-metal or metal-ceramic brazes, intergranular leaks due to too thin sections of material susceptible to grain boundary growth (such as copper), porous envelope material, and direct penetration of ceramic parts by electron bombardment. Most bad brazes are discovered during assembly and processing, but naturally there is a class of leaks that are too small to be detected in this way, though still non-zero and capable of affecting the life of the tube in terrestrial service. Operation in space, of course, eliminates this cause of failure, even if the tube is not modified in any way, because the driving force for gas entry has been reduced far below the level at which it could compete with other causes of failure. A leak which would cause failure in an hour on the ground would require 100,000 years to become serious in low earth orbit.

Pinhole leaks in ceramics resulting from bombardment are similarly harmless in space, unless the bombardment reduces enough ceramic to metal for the electrical properties to be changed.

Fractures

Ceramic parts of tubes are known to fracture under a variety of conditions.

The rf field pattern in a waveguide window is nonuniform, so that dielectric heating is uneven. At sufficiently high average power, thermal expansion stresses may cause fracture. (In older glass windows, melting and suck-in may occur first. Few glass windows are now used on microwave tubes.) Local multipactor discharges may cause even more uneven heating and can cause either fracture or perforation.

Window failures in terrestrial tubes are nowadays not a serious problem except in two cases: extreme high power, and large bandwidth combined with moderately high power. What is high power depends on frequency. It ranges from tens of MW peak and up to 200 kW average at around 1 GHz, to tens of kW peak and 100 W average in the upper mm wave band. In these cases, failure may occur due to simple dielectric loss, as well as to more exotic causes. In medium power tubes

D180-22876-4

with large bandwidths (more than 1/2 octave), the problem is not simple dielectric loss, but the fact that ghost modes and trapped modes (resonances confined to the region of the window assembly) cannot be avoided over so large a frequency range. These resonances can cause failure at power levels much lower than those which the window can withstand away from the resonances.

For typical communications tubes the bandwidth is less than 10%, and there is no difficulty in designing structures with no spurious modes over this range. Further, the typical power levels used in space are not extreme by terrestrial standards. Consequently, present space tubes do not fall into either of the two classes for which window failures are serious causes of tube losses on the ground. Then elimination or removal of a window cannot have a major effect on reliability, though it can have incidental advantages.

Cathode ceramics also fracture although pinhole leaks are more common; in this case the high voltage across the ceramic is an added stress, and rf is not necessarily absent (electron gun oscillations are not uncommon and are generally considered to have been sufficiently controlled if they are banished to "rabbit ear" regions occurring only during the rise and fall of cathode voltage). Local bombardment due to undesired small beams of electrons escaping from the gun structure can occur. These may heat either the ceramic or adjacent metal parts so that seal failure occurs. Cathode ceramic fractures can also occur because of arcing either internally due to a gas burst, or externally.

In terrestrial service, any window or cathode ceramic fracture is immediately fatal. In space, it is less clear what will happen: the causes of fractures are mostly still present, and in some cases increased - the outside surface of a window is now subject to multipactor as well as the inner one, for example - but the differential pressure stress has been removed, and the leak resulting from a fracture has negligible gas flow. In the case of a window, a simple crack will relieve the thermal expansion stresses, but everything will remain in place, and the electrical properties of the window will not be changed. A window fracture could therefore have a harmless effect.

A cathode ceramic fracture is more likely to be serious, since this ceramic has a support function as well as an envelope function. If the ceramic fractures circumferentially, the cathode structure will not simply fall off, as it would on the ground. Certainly as long as high voltage is applied, the electrostatic attraction will be the dominant force (unless very stiff cathode and heater leads are used), and will hold everything together. Even when voltage is removed, this may still be true because of the substantial polarization that develops in high alumina ceramics. However, even a very slight movement to relieve stresses may upset critical gun alignment. Thus gun ceramic fracture should be considered as probably serious even in an excellent exterior vacuum, where window fracture may be tolerable.

For tubes to be processed completely in space, assuming that the space environment is good enough to allow this, the window is not a necessary component at all. The cathode ceramic is still necessary

because of its support function, but it could be reduced to a number of ceramic posts, in which the likelihood of fracture is very much reduced.

Insulator Leakage

A significant number of failures occur due to the development of leakage paths across insulators, usually the cathode ceramic. The most common cause seems to be evaporated or sputtered material from metal electrodes, but direct reduction of the oxide under electron bombardment is believed to occur, and gradual accumulation of contamination from the gas atmosphere in the tube is possible. Under the combination of heat and high voltage, changes in composition of the ceramic itself can occur by electrolysis. These effects are often difficult to observe and analyze on the ground; thin metal films may build up to the point where concentrations of heating or electric field cause the ceramic to crack, whereupon the tube goes to air and the metal film may immediately reoxidize, and become undetectable. In space there would be no reoxidation, but the accumulating leakage itself could cause failure simply by overloading the power supply.

Leakage failures due to evaporation from overheated parts may be reduced if the temperature can be lowered by allowing direct radiation, but sputtering will not be reduced unless the ion population is brought down also. Leakage is normally controlled by a combination of grooving and shielding of the ceramic, but even this may be ineffective if there are gas bursts which allow molecules to "get around the corners" while the mean free path is momentarily low. Opening to space would undoubtedly improve this situation.

Cathode Emission

Loss of cathode emission can occur either from loss of emissive material from the cathode surface, or from poisoning of the surface by foreign materials. The interactions are very complex, and cannot be summarized easily. If the vacuum is very poor, material will be lost from the surface by sputtering, which is basically independent of the cathode temperature. When the vacuum is good, material is lost by evaporation which is very temperature dependent. If the vacuum, though good, includes elements which are poisonous to cathodes, then either this poisoning will occur, or the cathode may be deliberately operated at a higher temperature to re-evaporate the poisons. Loss of material by evaporation will then be increased. For "reservoir" types of cathode (impregnated tungsten matrix usually), life is also governed by the reaction rate of processes occurring in the reservoir which release active material to migrate through the pores to the working surface. These reaction rates are also very temperature dependent, and may be in conflict with the evaporation rate. In this type of cathode there is always plenty of material available in the interior, even after tens of thousands of hours, but the conditions may be such that it cannot reach the surface in a suitable form, if the reaction rate goes as a higher power of the temperature than the evaporation rate, then there is a minimum cathode temperature below which the evaporation that still occurs will not be replenished, and lowering the temperature further will reduce life.

D180-22876-4

It is not sufficient for just the gross emission of the cathode to be maintained: in a finely-focused linear beam tube, a small patch of poisoning on the cathode surface can unbalance the space charge forces in the beam and deflect it enough to affect the performance of the tube, or possibly even cause serious damage.

Thus, thermionic cathode life is not an isolated problem, but interacts closely with tube vacuum, processing, possible presence of contaminants, and choice of operating temperature. It is not amenable to calculation except in the most idealized cases.

There is no doubt that improvement in the vacuum is always beneficial to cathode life over the range for which we have experience. But there is the possibility that some molecular "scrubbing" is beneficial, and that geosynchronous orbit vacuum levels ($\approx 10^{-18}$ Torr) could be "too good." One does not expect it, but he should allow for the possibility, since it is such a large extrapolation beyond our present experience.

At a given vacuum, reduction of cathode temperature will always reduce the evaporation rate, but it may not improve life if the cathode is reaction-rate-limited, or if slow poisoning is occurring.

It may be noted that some tube engineers have made a deliberate policy of starting bakeout at a relatively high pressure of a nonharmful gas, high enough to make the mean free path shorter than the anode-cathode spacing, so that the major initial contamination released by the anode is carried away to the pump instead of reaching the cathode. The amount of some contaminants needed to poison a cathode is exceedingly minute.

Young associates chlorine poisoning with partial pressures of 10^{-8} Torr or less; 10^{-8} Torr chlorine in a vessel of 1000 cm^2 internal surface area deposits less than 0.001% of a monolayer if completely adsorbed. Early quantitative work indicating the extremely small proportion of free (and thus poisonable) alkaline-earth metal atoms in an oxide cathode was reported to T. P. Berdennikowa. Berdennikowa measured the number of free metal atoms bound by water vapor in terms of the pressure of the hydrogen released by the reaction. She was able to measure quantities as small as 5×10^{-8} grams of barium.

Miscellaneous

Numerous other causes of tube failure such as heater burnout, are not discussed in any detail because they do not appear likely to be affected one way or the other by the space environment. Present experience indicates that heater life should be a minor failure mode problem, in any event.

One possible new cause of failure in space which we do not see on the ground is long-path discharge external to the envelope, which may occur if the exterior vacuum and electrode spacing combination gets near the Paschen curve minimum. This will certainly not occur at synchronous altitudes.

D180-22876-4

but may be a possibility in low earth orbit. Tests must be made in space chambers at NASA or elsewhere, once specific geometries have been decided on.

Current Klystron Experience on Life

The Varian VA-842 klystron is the best example of a high power tube with long life. This klystron is used in BMEW radar transmitters and currently has a MTBF of 4.5 years.

Figure 1 is a plot on Weibull hazard paper which shows life performance for:

- (1) the VA-842
- (2) a tube with a hypothetical 30 year MTBF
- (3) a tube with an objective failure rate of 1% per year

The probability scale at the top of the graph shows the probability of failure for a unit at a particular time. $F = 1 - \exp(-t/MTBF)$. These curves with a slope of $\beta = 1$ apply to the random failure period of life. The MTBF is determined at the 63.2% probability of failure point.

The VA-842 history represents current state of the art capabilities. The attainment of a MTBF of 30 years and the objective of a 1% per year failure rate (MTBF of 100 years) require an extension of 6.7 and 22 times the current demonstrated life performance. The effort to obtain this extension must address the problems discussed above under klystron failure modes.

Replacement Requirements

The Weibull hazard plot may also be used for estimating replacement rates by reading the probability of failure scale at the one year intercepts. The values may be interpreted as the replacement rates; the percentage replaced per year. The plots show values ranging from 1% to 22%. The ratios of replacement rates are the same as the MTBF ratios and indicate the need for maximum extension of life from the present state of the art to obtain the corresponding reduction in replacement rate.

Burn-in Effects

A burn-in program is designed to screen out the infant failures such that tubes are in the random failure stage when put into operation. Figure 2 is a Failure Symptom Tree. The stage of life at which the failures are most likely to occur is noted in parenthesis.

A.2 SERVICE AND MAINTENANCE

Service and maintenance will involve detecting faults, replacing component assemblies or modules, overhauling defective units, and installing klystrons. Presumably a large crew of trained resident space-electronic technicians will be on hand to perform these tasks. While it is not within the experience or purview of the klystron designer to explain how all the activities will be accomplished

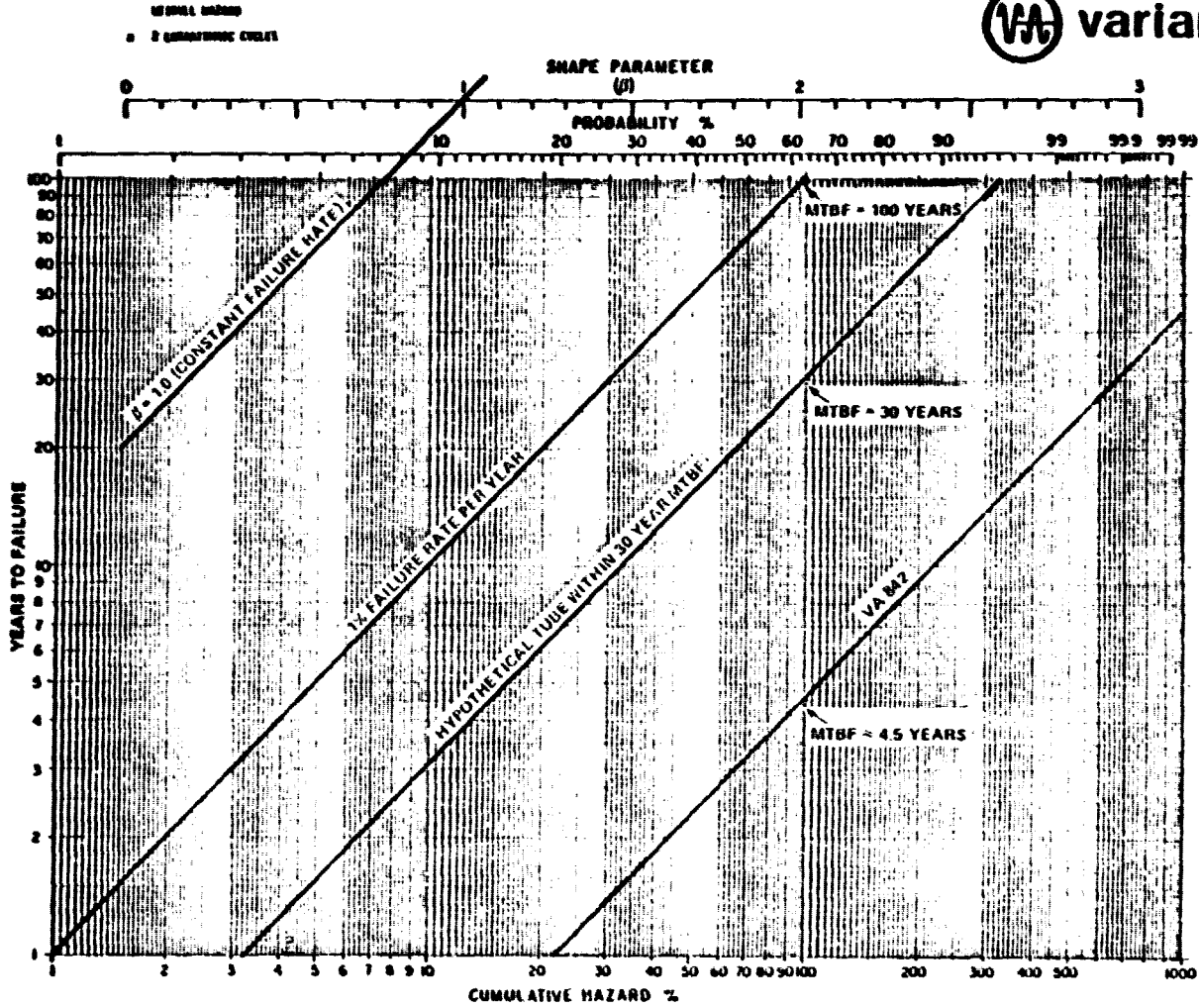
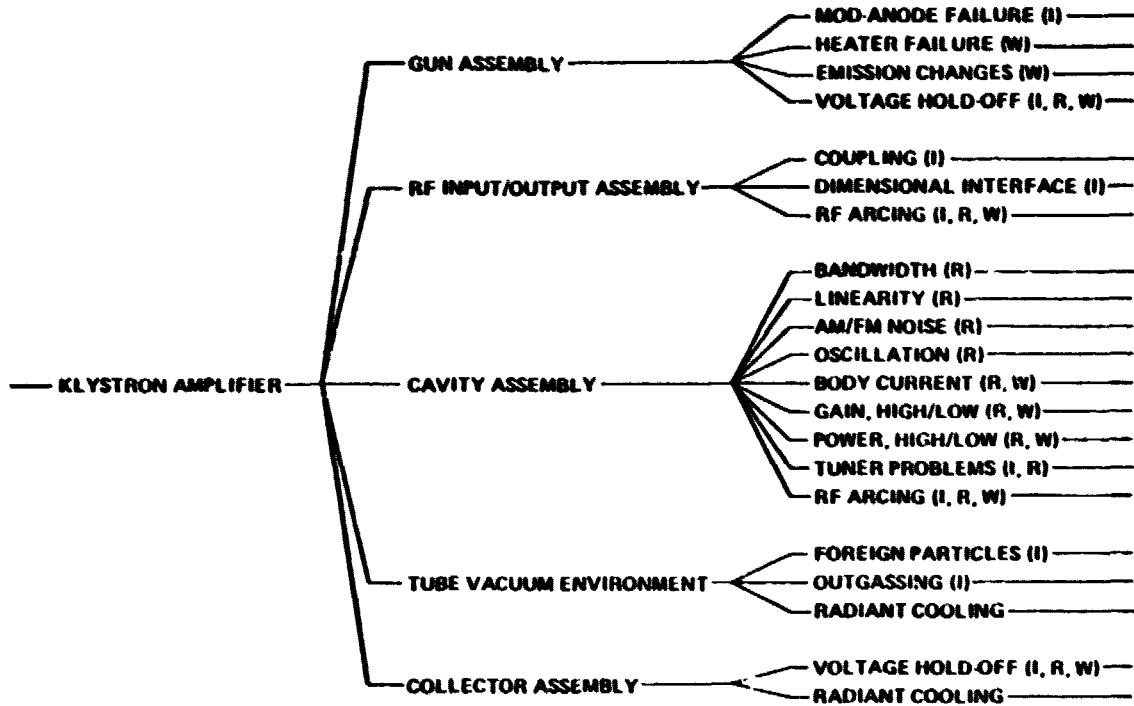


Figure A-1 Cumulative Hazard %

D180-22876-4



FAILURE STAGE:

I - INFANT

R - RANDOM

W - WEAR-OUT

Figure A-2 Failure Symptom Tree

in the sizable operating SPS installation, yet the characteristics and requirements of the individual tube may be considered as they might fit into the overall picture.

The operating high power SPS klystron will have three principal areas where faults may sometimes be encountered, though it is anticipated that klystron reliability will be high and these experiences rare. One of these areas is in the region of the electron gun, mod-anode, and body. Another includes the rf output cavity and waveguide structure. A third includes components of the depressed collector assembly. In the areas of electron gun and collector occasional dc arcing or "spitting" may be encountered in some tubes, particularly should foreign matter find its way into positions between high voltage electrodes. In the area of output cavity and waveguide rf breakdown may sometimes be experienced. The three areas will be considered in turn.

A.2.1 Electron Gun, Mod-Anode, and Body

Figure A-3a illustrates an SPS klystron in simplified form. The cathode provides current for the electron beam, which is focused and then accelerated through the mod-anode by the potential of the gun power supply. This voltage determines the electron gun uperveance and the beam current, although no beam current is supplied by the power supply. Uperveance is simply a factor expressing the relationship between electron beam current and voltage, in this case between cathode and mod-anode.

$$K_0 = I_0/V_0^{1.5}$$

Mod-anode power supply voltage is added to that of the gun supply to further accelerate the beam and to establish final beam uperveance and velocity. Various ratios of power supply voltage are possible for creation of the electron beam. A half and half division of the total required beam voltage results in a desirable gun uperveance and is the case considered here. The mod-anode power supply furnishes no beam current either. The two supplies control the beam and supply only the relatively small klystron body current.

The power supplies must be well regulated on a short-term basis to allow stable power output and phase characteristics. Any ripple or other rapid variation of voltage will be accompanied by simultaneous ripple or variation in rf power output and in phase shift across the klystron from rf input to rf output. Variations in these parameters are calculable. For moderate voltage changes, efficiency may be taken as constant and power output then varies as the five-halves power of the beam voltage. The 70 kW klystron, for example, would show a power output sensitivity to beam voltage change of about 5.4 kW per kV. Phase change is more complex but for a 50 dB gain tube will be about 25°/kV.

Slow changes in beam voltage, such as a gradual falling off with time, will have a similar effect. In this case, the klystron electron gun operating point could be shifted to higher microperveance and

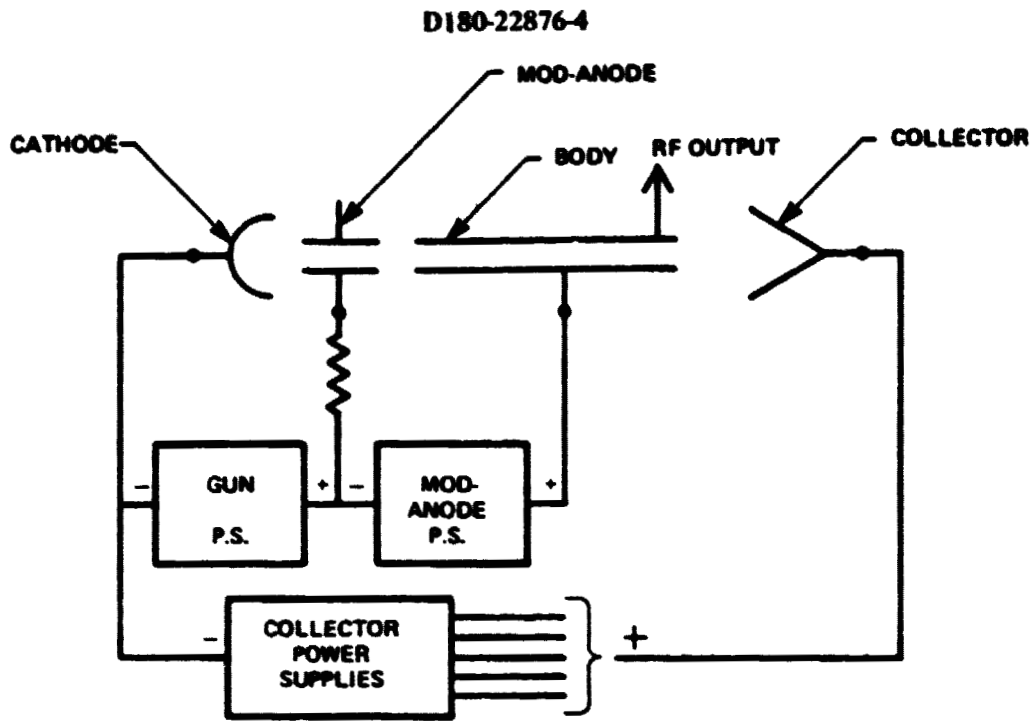


Figure A-3a Simplified Diagram Showing an SPS Klystron and Power Supplies

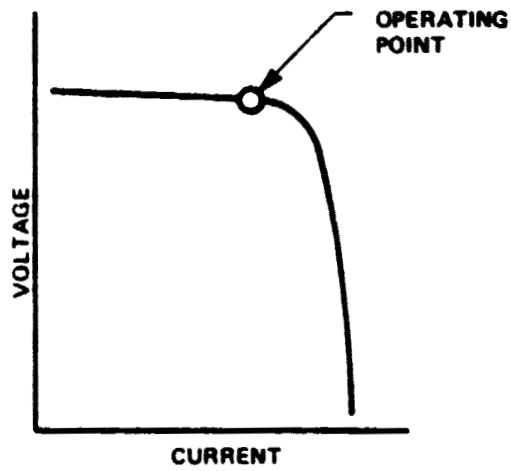


Figure A-3b Desirable Power Supply Volt-Ampere Characteristic

beam current by a compensating increase in gun voltage at the expense of mod-anode voltage. Thus beam current would be increased as beam voltage became less, holding power output constant. Phase correction could be made at the rf input. Experience and data are lacking to verify performance characteristics with gradually falling beam voltage, but it is believed that the calculations given and the expedients described are valid for beam voltage changes of at least 10 percent.

If high voltage arcing or "spitting" is to occur, the most likely region is between electron gun and mod-anode, where electron beam focusing requirements place some constraint on electrode spacings and shapes, and where the "hot" cathode acts as a source of vaporized materials as well as of electron current. Occasional arcing here is self-protective in the circuit shown. The instant an arc occurs, beam voltage and current drop to zero and operation is momentarily interrupted. The arc then clears and the klystron resumes normal operation. This sequence would occur in tens of microseconds. Since the mod-anode draws almost zero current, the designer may employ a relatively large series resistance which is across the gun power supply during the arc. Beyond this factor, if the power supply is designed to have the volt-ampere characteristic shown in Figure A-3b, the available power supply voltage would be very low during the arc. The graph of Figure A-3b is similar to the volt-ampere characteristic of the typical solar cell. It is also similar to the volt-ampere characteristic of the resonant power supply used in many applications where self protection is desired in the event of dc breakdown in the load circuit.

In very rare circumstances, a permanent fault could develop in the electron gun and mod-anode region, leading to a high rate of arcing, momentary shut down, return to normalcy and re-arcing. Such behavior must be detected and the klystron shut down, as by disabling the electron gun power supply. An indicating system must direct attention to the faulty klystron so that maintenance may be effected.

A.3 BAKEOUT AND PROCESSING

Bakeout and processing have one main goal, the removal of gas and contaminant vapors from the interior of a microwave tube to an extent sufficient to permit normal klystron operation without dc or rf breakdown. Bakeout consists of heating to drive gas and contaminants out of tube parts. An exhaust system pumps them away. In processing, dc and then rf voltages are applied, first at low level and then at progressively higher and higher levels. This allows gradual high voltage seasoning, ordinarily accompanied by gas evolution. The klystron processing operation is usually carried to a power level substantially above normal rating. Bakeout and processing are completed when "smooth" full power arc free operation is achieved while the vacuum level indicates about 10^{-7} Torr or better. Considerably better vacuum should be possible in deep space. "Smoothness" of operation is a somewhat relative expression and may vary to some degree from one tube type to the next.

With SPS klystrons of open construction, the ultimate situation may be one in which the manufacturer supplies component assemblies or modules rather than complete klystrons. These modules

could be individually baked out and processed on earth, but will probably require some additional seasoning when installed. The necessary seasoning may consist of a short operating period at reduced power level, with gradual increase to full power. It will be necessary to work out suitable processing schedules for the various modules and/or completely new tubes.

High temperature bakeout in deep space will probably not be necessary with these modules. They will have been baked out and processed on earth prior to shipment. An example of a similar procedure may be found in the bakeout and processing techniques employed with large, high power linear accelerators. The various components of these high energy machines are baked out and processed individually prior to final assembly at the site. Then high voltage dc and rf processing are undertaken, much in the manner proposed for modules of the SPS klystron of open construction. The high power accelerator, it may be mentioned, is typically equipped with roughing (rough vacuum) pumps and with Vacion pumps dispersed along the accelerator guide to achieve final high vacuum level.

SPS sealed-off klystrons will, of course, be baked out and processed like their earthbound counterparts. They will probably be provided with Vaclon appendage pumps for maintenance and monitoring of internal vacuum level. In deep space operation of such tubes, if and when possible contaminants are no longer a threat, valve-like openings would be desirable to allow use of the vacuum of deep space for pumping. These valves could be closed off if local contaminants became dangerous.

Tube Units, Modular Construction

Early klystron tube units will probably be quite similar in construction to klystrons built for use on earth, save for thermal arrangements necessary for radiant cooling. That is, they will be sealed off klystrons. As time passes, however, and at some appropriate period, it may be desirable to change over to klystrons of open construction. The benefits of this type of design in space use are many; some have been discussed.

In either case, modular construction arrangements would be advantageous. With sealed-off klystrons, the modules would be connected together with vacuum-tight seals. With open klystron construction, they would be connected together mechanically. The klystron divides naturally into a number of such modules. These are:

- Electron gun
- Circuit (body)
- Focusing magnet
- Collector

In sealed-off klystrons, one would also have an output window, a part not required with open construction. The open construction klystron might have two modules making up the collector. One

would constitute the beam refocusing section, the other the biased collector plate assembly.

With open klystrons in geosynchronous orbit, modular construction would permit replacement of damaged components without removal of the entire klystron. Alternately, it may sometimes be advantageous to make the klystron component exchange at a space shop set up for the purpose. In this case, a complete klystron replacement would be made, the damaged unit sent to the shop.

Large Volume Manufacture

Principal interest in large volume manufacture of SPS klystrons centers on costs. Manufacturing problems are discussed in a later section, III. Tube costs for the 70 kW klystron and a proposed 250 kW klystron have been estimated and are shown graphically in Figure A-4, which plots unit klystron cost versus manufacturing rate in large volume manufacture.

A.4 KLYSTRON DESIGN FOR SPS

Interest in a high power klystron CW amplifier for possible SPS use at first centered on a 2450 MHz, 50 kW, tube that would operate at under 40 kv and an efficiency of over .85. At Varian, the klystron coming closest to meeting these requirements was the VKS-7773. This tube met the power output and beam voltage requirements but operated at a tube base efficiency of but .744. Tube base efficiency, η_b , is simply electronic conversion efficiency, η_e , multiplied by output circuit efficiency, η_{ckt} .

$$\eta_b = \eta_e \times \eta_{ckt} \quad (1)$$

This simple relationship is fundamental to all klystrons. It states that the tube beam or base efficiency is the efficiency with which microwave rf energy is coupled from the electron beam to the output cavity multiplied by the efficiency with which the output circuit transfers this energy from the output cavity to the useful load. As it turns out, the principal factor which may tend to increase electronic efficiency, reduced electron beam microperveance, at the same time may tend to decrease circuit efficiency, and vice versa. Thus, there exists an optimum electron beam microperveance. This optimum falls between 0.25 and 0.35 for most CW designs.

The actual electronic convergence efficiency realized with a particular optimum microperveance design also depends critically on the electron beam bunching achieved at the output cavity interaction gap. A very important factor is electron beam current density. Reduced electron beam current density tends toward improved electron bunching at the output cavity interaction gap and toward higher electronic efficiency. Thus, a large drift tunnel diameter appears indicated. The coupling factor between the electron beam and the output cavity interaction gap, however, is largest for the smallest feasible drift tunnel size. Hence, for maximum electronic conversion efficiency

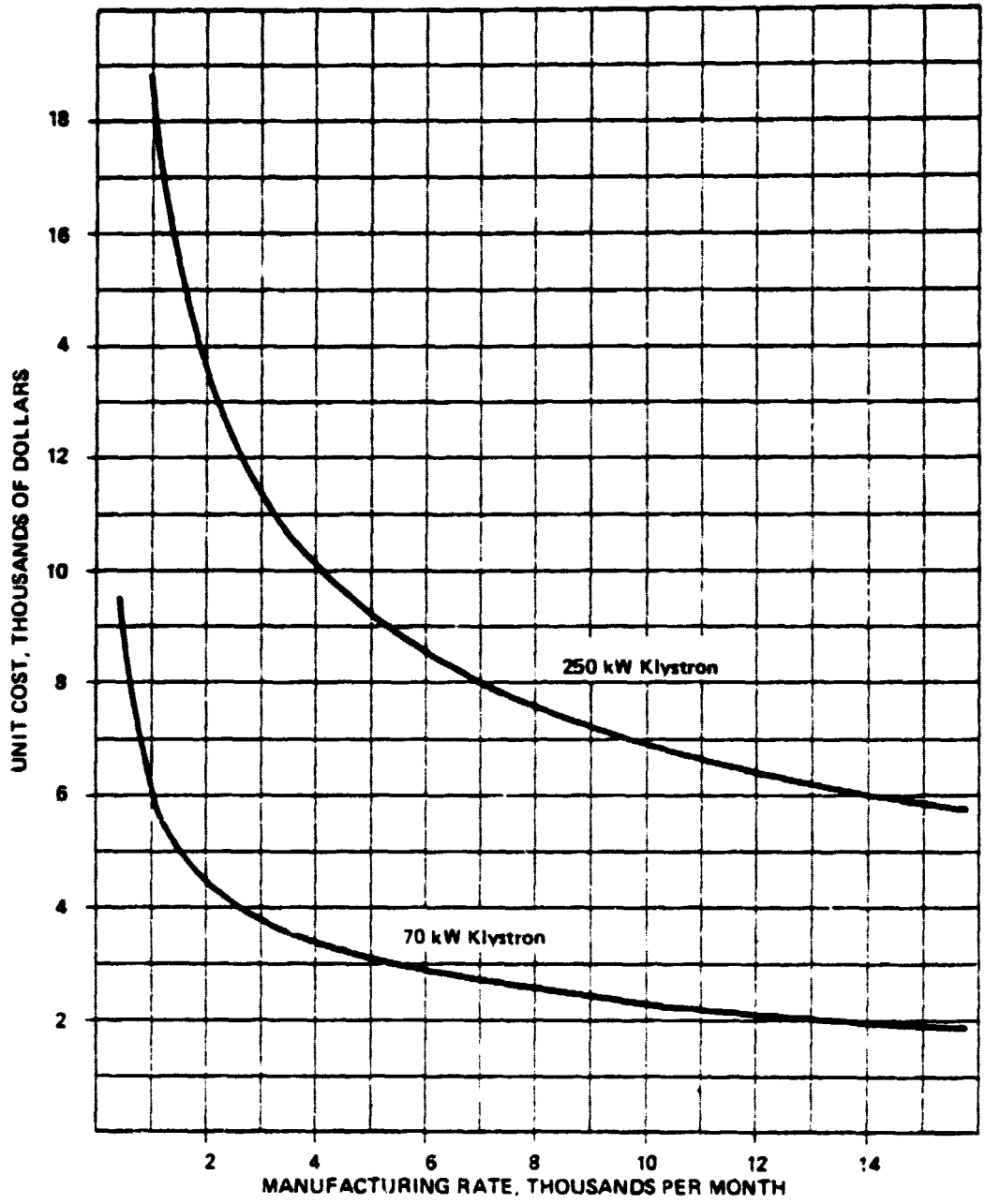


Figure A-4 Unit Klystron Cost vs Manufacturing Rate for Large Volume Manufacture

there exists an optimum drift tunnel diameter, for a given electron beam microperveance and a total beam current.

The VKS-7773 operates with a beam input of 28 kv at 2.4 amperes, or an electron beam microperveance of 0.5. The electronic conversion efficiency is close to .76. By reducing the microperveance to 0.25, increasing beam voltage to 36.5 kv to maintain power output at 50 kW and optimizing drift tunnel diameter for the reduced electron beam current, it was felt that an electronic conversion efficiency of .79 might be realized. This concept pivoted on the known behavior of the VKS-7773 klystron and was bolstered by independent calculations of Kosmahl and Albers, who determined that an electronic conversion efficiency as high as 0.83 might be expected in a similar case. The output circuit efficiency of the new klystron was expected to be close to .97 leading to a tube base efficiency close to .77. Collector depression at a recovery efficiency of .55 would be necessary to realize the required .85 total efficiency. The 50 kW klystron CW amplifier deriving from the VKS-7773 was the subject of a paper given at the 1976 International Electron Devices Meeting in Washington, D.C. A reprint is included as Appendix A.

Present interest in an SPS klystron centers on a 70 kW power output tube. Even higher power outputs have been discussed, the maximum being close to 300 kW. The 70 kW klystron, with its higher electron beam current, may exhibit efficiency characteristics differing to some extent from those of the VKS-7773. A 300 kW power output klystron may differ substantially. Short of going into a detailed computer analysis of each design, it is not possible to predict these differences with great accuracy. Such an effort is beyond present treatment of the SPS klystron problem. In order to have some facile estimate of the variables concomitant with various power output levels and electron beam microperveances, however, a computer calculating program was written around the characteristics of the VKS-7773 klystron, also making use of detailed computer analyses of several microperveance 2.0, 1.0 and 0.5 high efficiency klystrons. The program is labeled BOEKLY (Boeing Klystron). It is listed in Appendix B.

The BOEKLY computer program takes the electronic conversion efficiency as a linear approximation of computer data generated for several designs having values of electron beam microperveance between 2.0 and 0.5.

$$\eta_e = 0.79 - 0.06 K_o \quad (2)$$

The expression is somewhat less optimistic than that used for the klystron derived from the VKS-7773. This is because of the higher electron beam currents of the 70 kW and higher power output tubes.

Circuit efficiency is taken from an expression identical to that used in the case of the klystron derived from the VKS-7773.

$$\eta_{\text{ckt}} = \frac{1}{1 + \frac{1}{(G_L/G_0)(R/Q) Q_0 \sqrt{V_0} K_0 10^{-6}}} \quad (3)$$

where $G_L/G_0 = 1.2$
 $R/Q = 120$
 $Q_0 = 4000$ (as at 300°C)

Microperveance, K_0 , and beam voltage, V_0 , are variables generated in the BOEKLY computer program in connection with the power output level of interest in the particular calculations.

Klystron base efficiency is taken as the product of electronic and circuit efficiencies. Collector recovery efficiency is assumed by the program user and entered as an input along with the power level of interest.

The program may be somewhat pessimistic for low microperveance cases at 70 kW power output and somewhat optimistic for the higher microperveance cases at 150 kW, and more. The outputs include electron beam conditions, magnetic fields, efficiencies, waste powers and drift tunnel diameter. While beam current density is held constant for all cases computed, no attempt is made to introduce effects of varying γ_a , a factor of interest to klystron designers in connection with drift tunnel size and electron beam to output cavity coupling.

The BOEKLY computer program was used to calculate parameters for 70 kW, 150 kW and 300 kW power output klystrons. Selected data are shown in the form of graphs in Figures A-5 through A-8.

Figure A-5 compares indicated tube base efficiencies for the 70 kW and 300 kW power output cases. For the 300 kW power output case, beam input varied from 46 kv at 8.879 amperes at microperveance 0.9 to 63 kv at 6.325 amperes at microperveance 0.4.

Figure A-6 shows indicated klystron total efficiencies for the three-power output levels with collector recovery efficiency as a parameter. Data for all three power output cases were quite close and were averaged for each value of collector recovery efficiency.

Figure A-7 shows the estimated power loss at the output cavity for the three cases. This power loss is made up of two components: rf power loss in the output cavity related to circuit efficiency, and electron beam interception in the presence of rf saturation. The latter is taken essentially as only one percent of the beam power, thought to be possible but possibly somewhat optimistic. Removal of waste heat from the output cavity is one of the difficult problems in SPS klystron design. The data indicate one expedient for reducing this power, a change to a higher electron beam microperveance.

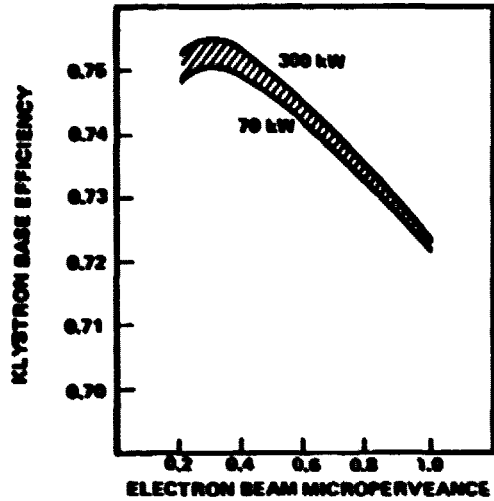


Figure A-5. Klystron Base Efficiency ($\eta_e \times \eta_{CKT}$) vs Electron Beam Microperveance. Data are from BOEKLY computer program.

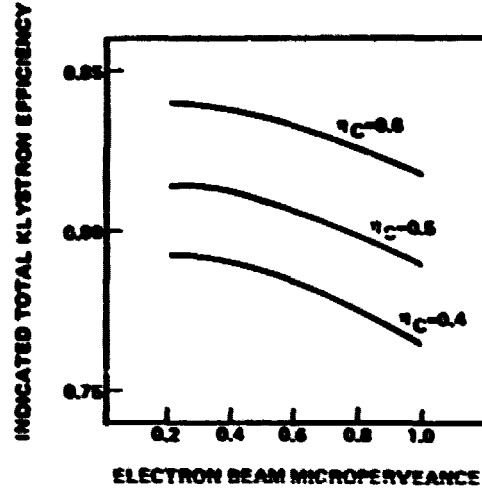


Figure A-6. Indicated Total Efficiency vs Electron Beam Microperveance with Collector Recovery Efficiency, η_c , as a Parameter. Data are from BOEKLY computer program, averaged for the 70, 150, and 300 kW klystrons.

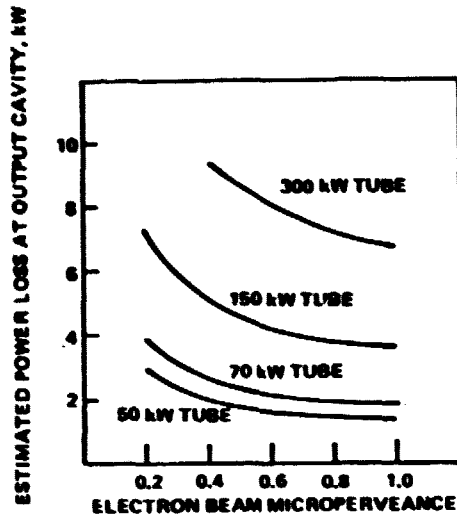


Figure A-7. Estimated Power Loss at Output Cavity vs Electron Beam Microperveance. Data are from BOEKLY computer program.

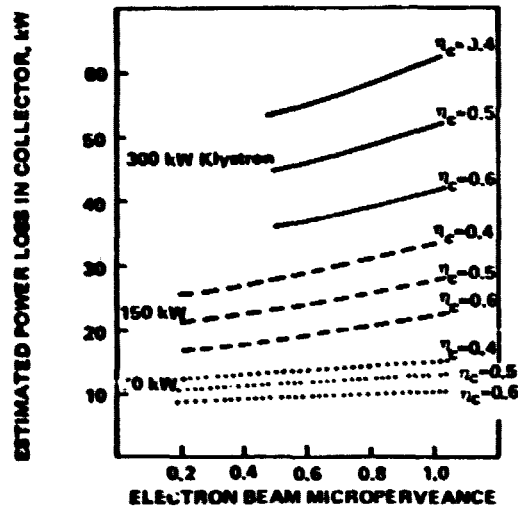


Figure A-8. Estimated Power Loss in Collector vs Electron Beam Microperveance with Collector Recovery Efficiency as a Parameter. Data are from BOEKLY computer program.

Figure A-8 shows the estimated power loss in the collector for the three power output cases with collector recovery efficiency as a parameter. The use of higher microperveance increases collector waste heat power loss, although it reduces output cavity waste heat.

70 kW Klystron

The preliminary design of a 70 kW klystron was carried out using the BOEKLY and KDC computer programs. BOEKLY has been discussed. KDC makes accurate computations of beam and propagation characteristics from inputs of beam voltage, beam microperveance, drift tunnel diameter and beam diameter. A beam voltage of 33 kv and a microperveance of 0.5 were chosen in this case. Drift tunnel and beam diameters were taken from results obtained from BOEKLY. Klystron length was estimated by scaling and estimating from the VKS-7773. In practice, design of a high efficiency klystron would proceed from this point to large signal computations and plots of electron trajectories to determine electrical details of the design. This is work considered beyond the scope of present efforts.

The important characteristics resulting from this exercise are listed in the table below:

70 kW Klystron

Beam Voltage, kv	33	Brillouin Field, G	445
Beam Current, A	2.997	Practical Field, G	1113
Microperveance, UP	0.5	Drift Tunnel iD, in	.279
Power Input, kW	98.914	γa , radians	.498
Power Output, kW	73.543	Be, radians/inch	3.803
Efficiencies:		Waste Powers, kW:	
Electronic	.760	Driver Cavities	.297
Circuit	.981	Output Cavity	2.441
Base	.746	Collector	11.316
Collector	.50		
Total	.808		

These parameters were calculated for a klystron body operating temperature of 300°C. Total efficiency does not take account of heater or electromagnet powers.

Klystron Length

The length of the VKS-7773 circuit, cathode magnetic pole to collector magnetic pole, is 15.5 inches. The axial electronic propagation constant $Be = 4.100$ radians/inch. For the 70 kW klystron, $Be = 3.803$ radians inch. The equivalent pole-to-pole length would be 16.7 inches. Allowing 6.0

inches for the electron gun and mod-anode, 6.0 inches for a beam refocusing section between output cavity and collector entrance, and 10.0 inches for depressed collector plates, total estimated length would be 38.7 inches.

Heat Radiation in Space

Klystron waste heat must be radiated from suitable panels in space. These heat radiators must handle not only waste heat from the klystrons, but also heat received from other sources. Solar radiation in space, for example, is equivalent to about 1.4 kW/meter². Factors of viewing and absorptivity are applied heat received from the sun. Heat to be radiated may be expressed as

$$Q_1 = P_k + K_a K_b A_r 1.4 + W_e A_r \tag{4}$$

where

- Q₁ = heat to be radiated, kW
- P_k = klystron waste heat, kW
- K_a = solar view factor
- K_b = solar absorptivity
- A_r = radiator area, meters²
- W_e = earth's albedo, kW/meter²

The heat that will be radiated may be expressed in terms of temperature, the Stefan-Boltzmann constant, radiator area, and radiator emissivity.

$$Q_2 = (T_r^4 - T_s^4) (5.67 \times 10^{-11}) A_r \epsilon \tag{5}$$

where

- Q₂ = heat radiated, kW
- T_r = radiator temperature, °K
- T_s = deep space temperature, 4°K
- A_r = radiator area, meters²
- ε = radiator emissivity

The Stefan-Boltzmann constant is expressed in kW/meter²-°K⁴.

Since Q₁ = Q₂, the two expressions may be equated, leading to an equation giving radiator area,

$$A_r = \frac{P_k}{(T_r^4 - 256) (5.67 \times 10^{-11}) \epsilon - K_a K_b 1.4 - W_e} \tag{6}$$

Body and Electromagnet Waste Heat

Choice of an electron beam microperveance of 0.5 for the 70 kW klystron limits the estimated waste power at the output cavity to about 3.5 kW, close to the value obtained from the BOEKLY program for the 50 kW klystron at microperveance 0.25. The concentration of waste power at the output cavity constitutes one of the difficult problems of klystron design where one contemplates use of a heat pipe assembly for moving heat outward to a radiator. Power loss at the output cavity is a function of temperature, 300°C has been tentatively selected as the maximum practicable. It constrains output cavity loss, allows heat transfer, and permits design of a body radiator of relatively moderate area.

Summing up the heat to be handled by the body radiator:

Output cavity	2.441 kW
Driver cavities	297 kW
Electromagnet	<u>~.750 kW</u>
Total	3.488 kW

Using Equation 6 and the assumptions discussed earlier, calculations involving the klystron body heat radiator give the following results for geosynchronous and for low earth orbits.

Klystron Body Temp ^{°C}	Radiator Temp ^{°C}	Geosyn Radiator Area M ²	LEO Radiator Area M ²
300	230	1.380	1.414

Thus, it appears from this exercise that conditions in low earth orbit are somewhat more demanding than those in geosynchronous orbit, though the difference is not large.

Design of a depressed collector for the 70 kW high efficiency klystron will be one of the very important tasks of tube development. Depressed collectors are relatively easy to design for linear beam tubes of low efficiency. Collector recovery efficiencies of 80 percent, or more, have been achieved with TWT's of modest tube base efficiency. With high efficiency tubes, on the other hand, there has been little incentive up to the present to add the complexity of collector depression, considering the relatively modest improvement in overall efficiency that may result. In the case of the SPS klystron, the relative importance of each point in efficiency leads to serious consideration of this means for recovering energy. Some work has been reported for an experimental 1 to 2 kW L-band klystron of 55 percent base efficiency, which achieved about 70 percent total efficiency with collector depression. The fundamental problem is that the electron beam emerging from the output cavity of a high efficiency tube has a wide distribution in axial and radial electron velocities. There must exist a large population of relatively "slow" electrons. The use of a beam refocusing section between output cavity and collector entrance allows electron beam sorting, which may lead

D180-22876-4

to improved depressed collector operation. The nature of the spent electron beam leaving the output cavity may be studied both theoretically and experimentally. Computer programs exist for design of both the electron beam refocusing section and the depressed collector. As in many aspects of klystron design, actual performance and optimization may be determined only through test, modification, refinement and retest.

Emissivity, ϵ , is taken as .87. In geosynchronous orbit the view factor, K_a , is taken as .5, in low earth orbit as .35. While certain special coatings may be employed to give low absorptivity while retaining high emissivity, in general it is assumed that these degrade over long time periods. Thus, absorptivity, K_b , is taken as .9. The earth's albedo varies inversely as the square of the distance and would be insignificant at geosynchronous orbit. It is taken as .25 kW/meter² for low earth orbit.

Collector Waste Heat, Open Klystron Construction

With open klystron construction, the depressed collector may radiate directly into space. Figure A-9 illustrates a hypothetical structure for the 70 kW tube. Assuming a collector recovery efficiency of 0.5, from the BOEKLY program, waste heat would be 11.316 kW. For the purposes of this exercise, it is assumed that the five depressed collector plate structures may be dimensioned, shaped, positioned and biased so that each one radiates one-fifth of the total waste heat into space. Bias voltages, incidentally, are closest to cathode potential near the top of the collector; they approach body potential toward the bottom. The central spike is at cathode potential. The radiation shields at the bottom are at body potential. Thus, there are actually seven different potentials present for influencing and collecting the electron beam. In addition, a shaped magnet field exists in the beam refocusing section, with a leakage field in the collector plate region.

Radial portions of the plates collect the electron beam and conduct heat outward toward the radiating sections. In this example these are assumed to operate at a temperature of 550°C throughout. The use of heat pipe assemblies for the individual plate structures would hold the radial temperature drop to a low value. The maximum diameter in this example would be about 30 inches. With a higher radiating temperature, and, of course, a correspondingly higher plate operating temperature, the maximum diameter would be smaller.

Calculations from Equation 6 for geosynchronous and for low earth orbits gave the following results.

Plate Radiating Temp ^{°C}	Geosyn Area M ²	LEO Area M ²
500	.666	.669
550	.514	.516
600	.404	.405
650	.322	.322
700	.260	.260

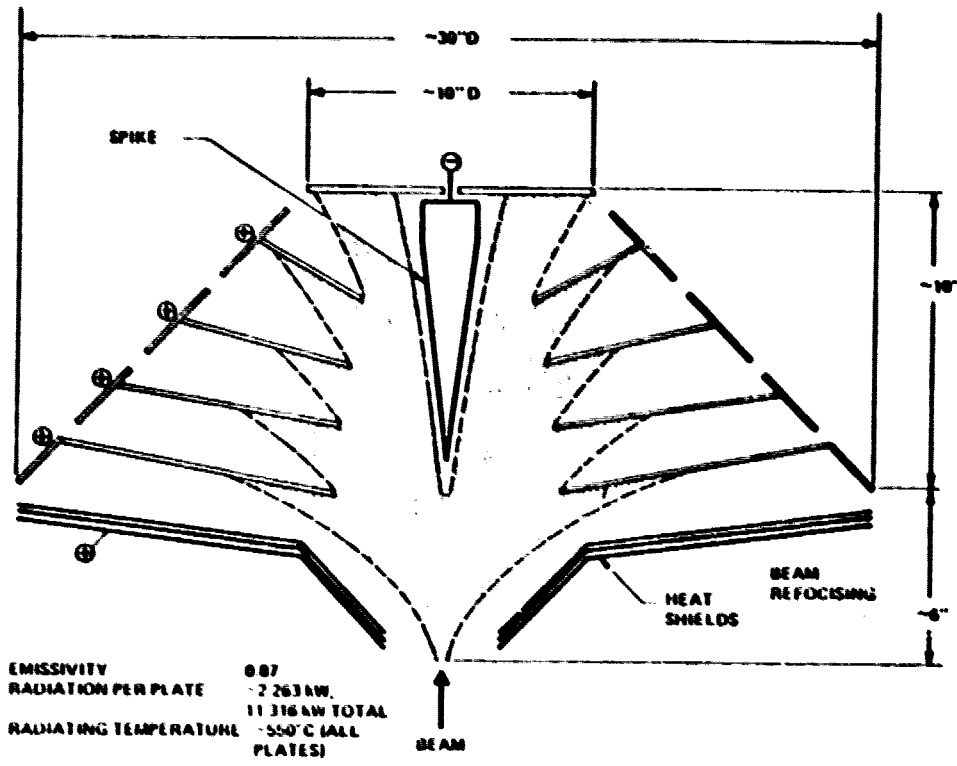


Figure A-9. Hypothetical Depressed Collector for 70 kW Klystron of Open Construction

Thus, at these somewhat elevated temperatures, changes in the heat environment from geosynchronous altitude to low earth orbit tend to be compensating.

Collector Waste Heat, Sealed Off Klystron

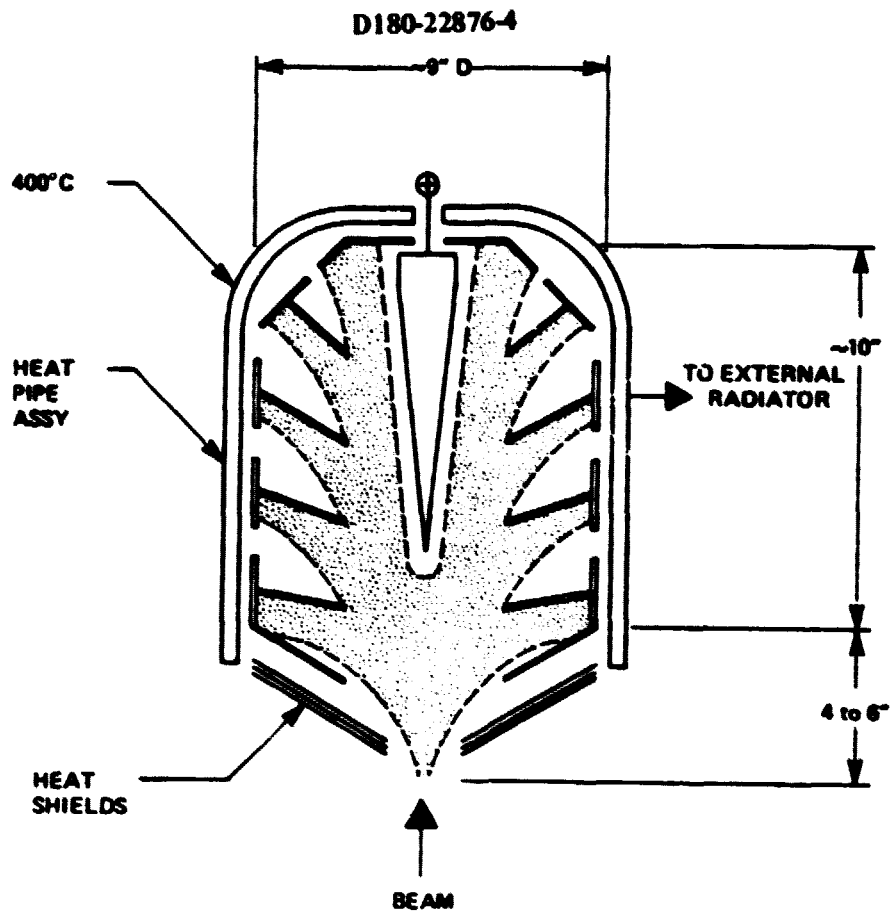
With sealed off klystron construction, the depressed collector plates might radiate to an intermediate surface forming a portion of the vacuum envelope. This surface might be cooled by heat pipes, which would transfer heat to an external collector radiator. This radiator would radiate directly into deep space. A wide variety of radiator surface temperatures and sizes, both within the tube and external to it, may be imagined, depending on various assumptions. From the point of view of the klystron designer, the intermediate surface should have as low a temperature as feasible to permit use of smaller and lower temperature depressed collector plates. From the point of view of the system designer, the intermediate surface should have as high a temperature as feasible to permit use of a smaller size external collector heat radiator.

One may take the klystron collector envelope temperature as 70°C above that of the external radiator, which is connected to the intermediate envelope by heat pipes. Then assuming a uniform temperature for the internal collector plates, thermal calculations may be made for various possible geometries. Figure A-10 illustrates one such geometry. The following table lists data calculated for the arrangement:

Collector Plate Temp ^o C	Klystron Coll Envelope Temp ^o C	Radiator Temp ^o C	Geosyn Radiator Area M ²	LEO Radiator Area M ²
980	500	430	.991	.996
969	450	380	1.357	1.367
960	400	330	1.921	1.941
953	350	280	2.841	2.885
947	300	230	4.477	4.588

The effective radiating area of the collector internal plates for this example would be about 0.1 meters². These plates would be constructed of refractory materials. Pyrolytic graphite is one possibility.

As with the collector of the klystron of open construction, plate bias voltages are closest to cathode potential near the top of the collector and nearest to body potential toward the bottom. The required potentials would be applied through insulating and support structures piercing the intermediate shell wall.



RADIATION PER PLATE 2.263 kW, 11.316 kW TOTAL
 RADIATING TEMPERATURE 980°C ALL PLATES
 EMISSIVITY 0.87
 RECOVERY EFFICIENCY 0.5

Figure A-10. Possible Collector Arrangement, Sealed Off Klystron

A.5 SPACE TUBE FACTORY AND FACILITIES

The manufacturing of klystrons for SPS should follow in large part the concepts of most high-production factories. A high degree of automation in addition to computerized controls and a minimum of human labor would be required. The work flow would entail a logical progression of materials from the receiving dock to the shipping dock with strategic arrangement of ancillary administration and services.

We see under these conditions unique devices and delivery systems that place parts in proper position and sequence of assembly. Joining also would be accomplished in a programmed manner by mechanical means, as applicable. For more critical and vacuum-tight requirements, techniques such as compression and electron beam welding could be used. It seems that an in-line progression of assembly would be the least complex, although rotary apparatus, or a combination of the two, may have advantages in some operations.

Yields of 90% and better will abide scant margin for error. To achieve such efficiencies, operations will be dependent to high degree on computerized controls. Parts will be precise both to produce operational modes and to function smoothly in assembly apparatus. Mechanical and electronic values, such as beam focusing, will be subject to computer controlled standards. Misfits will be ejected or adjusted rather than permit out-of-spec tubes to reach test stations and waste time, space and electrical energy.

The automotive industry employs an in-line concept of assembly but also uses a high labor content to place, fit and assemble components. The use of machinery to perform complex operations is not unique. Incandescent and fluorescent lamp production is highly automated. Receiving and television tubes are assembled and processed mechanically. If machines can pare, halve, can and cook a peach, pick tomatoes, sense a head of lettuce for moisture content and pluck it if it's right, certainly we can design and construct a machine that can put klystrons together and test them. The unique "feature" will be to perform operations in vacuum and provide for adjustments in an external manner. At the same time, we must deliver parts and remove the completed product without destroying the vacuum.

As awe-inspiring as the establishment of an automated factory for producing huge quantities of complex microwave tubes might appear from our present viewpoint, we would not be exactly pioneers venturing into a vast, uncharted land void of horizons. A glance at Assembly Engineering's Master Catalog will reveal a host of companies engaged in the design and construction of equipment for the automatic and programmed assembly of components and devices. A partial list of the classifications in this category provides some idea of the services at hand to assist in the design and to equip a factory for the automated assembly of SPS klystrons.

Assembly Machines, in-line, indexing

Assembly Machines, rotary, continuous motion

D180-22876-4

Assembly Machines, ultrasonic welding, sealing, etc.

Controls, automatic assembly

Conveyor Systems, dispatching, programmed

Feeders, custom designed

Hopper Feeds

Indexing Equipment

Inspection Equipment

Manipulators, automatic, hand

Parts Ejection Mechanisms

Parts Transfer Devices

Positioners, parts

Robots, industrial

Timers, programmed

Tooling, for assembly machines

Welders, electron beam

Welders, multi-station assembly

The magazine, *Tooling and Production*, August 1977, presents an interesting and timely article describing a new approach to automated engine assembly. The system was designed and built by Automatic Production Systems, a division of Ingersoll-Rand Co., for the Society of French and Italian Motor Companies. Although the assembly of automobile engines does not require many of the controls and considerations inherent with vacuum and thermionic emission, the mechanical aspects provide some interesting parallels. The engine design, for comparison, provides only .001 end-play clearance between block and crankshaft. The difficulty of lining up these elements manually makes the operation ideal for automation. Similarly, we would encounter a number of close tolerance and alignment requirements which could be made practically error-proof by the exactness of automatic assembly.

Design of equipment as well as design of the building will be related closely to the design of the klystron. Tube design would proceed first with the design of equipment following as fast as features of the klystron take on shape and size. In fact, the design of parts and subassemblies for adaptability to automatic assembly will require consideration almost parallel in importance to performance requirements of the klystron itself. Our design, moreover, would not be solely for labor savings; in addition to tailoring design to automation, the assembly of tubes within a vacuum must be accomplished almost entirely with people excluded at the same time from this environment.

Initially, it would seem that one-shift operation would be advantageous. Additional shifts could be added, if needed; however, adequate down-time would be essential for servicing equipment and stocking the line for the next shift's operation. Stand-by equipment and production capability would be provided to surmount breakdowns. It is expected that space freighters will depart on tight schedules and no allowance will be made for normal delays and late deliveries.

D180-22876-4

Such a factory ideally would be a one-floor arrangement. A basement would be advantageous to supply services, vacuum pumps, etc., and to provide access for their maintenance. Support and administrative services, of course, could be located on a second story or in an adjacent wing or structure. Consideration also should be given to multi-plant operations both from the standpoint of logistics and to offset any interruptions either from acts of nature or man.

Punch-press parts could be made on automatic progressive equipment. Fine-blanking techniques would be employed where the control of burrs was necessary. Impact forming and extruding would play important roles. Tape controlled, metal cutting, machine tools could be relied upon if required for the production of some parts, however, every attempt would be made to design parts to minimize the production of chips. Auxiliary, non-critical parts possibly would come from outside sources. Reliance would be heavy on mass production processes such as powder metallurgy, die casting, automatic screw machines and other high-speed, automated, cutting and shaping methods.

We will assume that most parts will be fabricated within the factory, particularly to control cleanliness and contamination. Conceivably this would include the reduction of materials received in the form of billets to usable shapes and sizes. Especially this would be advantageous for parts subject to contamination and oxidation. These considerations become apparent, for example, if we are to make the maximum use of aluminum because of weight and continuing availability. Moreover, the winding of anodized aluminum foil for solenoids appears advisable but would require more than commercial control of oxidation and abrasive particles. "Cleanroom" conditions would be maintained for processing and assembly areas. While particles within earth-bond tubes are a concern, they do tend to bottom out but their behavior under gravity-free conditions is unknown. Their presence in either case intuitively is *persona non grata*.

It would seem advisable, moreover, to assemble tubes in vacuum through pinch-off. To do so would eliminate the difficult mechanical arrangements of conveyoring pumps. As a bonus, it would produce tubes free from oxides and scale which, hopefully, would require no further cosmetic grooming before plugging them into their celestial sockets. Assembly in vacuum has the additional advantage of simulating space techniques, if ever it is decided to perform assembly operations in either LEO or GEO stations. Parts and subassemblies would be placed within the vacuum chamber during down-time, if possible, ready for automatic feeding and assembly during operation. Otherwise, a system of air-vacuum locks would be devised to keep hoppers loaded and the line running.

Varian has gained considerable experience with this type of apparatus which provides a good basis for future design and the estimation of costs. Presently under test is an in-line, conveyORIZED Vari-KromTM system for the vacuum sputtering of chrome on parts such as hub caps, grills and bumpers. This equipment was designed and built for a major manufacturer of automotive components. It is a relatively complex, computerized device costing approximately \$1,000,000. It consists of a series of stations and embodies the transfer of parts through progressive and declining levels of vacuum. This machinery, however, would be far less complex than the processing and assembly systems we

D180-22876-4

envison for our space tube facility. The Vari-Krom metallizing system is described in Attachment 1.

Testing conceivably could become a bottleneck in the progression of tubes and the overall consumption of electrical power would be proportional to the time required. One hour of test would require 18 MW to produce 4,000 tubes and, of course, more than three-fold this power when rates are increased to 12,500. Twenty-eight test positions would be required to process tubes at this level of production at better than 95% efficiency. It follows that testing must be completely computerized to speed up the process. As data are established, it might be possible to reduce testing to statistical sampling. Furthermore, to simulate the space environment, testing also should be conducted in vacuum.

Provisions for shipping will depend on shipping schedules. Seemingly, we should plan on daily shipments to the freight depot for space transportation and provide for several days of backlog to cover any slips on the production line. Staging areas at 12,500 tubes per month in stacks of 3 x 3 x 6 containers, four high, would require 12,000 spare feet to provide a three-day backlog. Use of automated stacking and loading, lifts and conveyors, packaging areas, storage of packaging materials, aisles, docks, etc., would require at least 75,000 square feet.

Allowing approximately four years for stabilization of tube and equipment design, we would hope to complete the construction and shakedown of equipment and the completion of buildings in another three years. It is envisioned that a factory to produce 12,500 tubes per month would occupy 1,000,000 square feet and would cost \$65,500,000 to construct. A cost of \$65 per square foot is estimated at current costs to build a factory suited for more normal types of manufacturing but with allowances made for the special requirements of sophisticated tube manufacturing. These construction costs were determined from a current study conducted by us to establish replacement costs for Varian facilities as requested by the Security and Exchange Commission. Additionally, we made use of "Building Construction and Cost Data" published by Robert Snow Means Co., Inc.

Based on Tooling and Production's account of the AFS system built for the consortium of French and Italian motor companies which is valued at \$4,000,000, we can project costs for an automated tube assembly line at \$6,850,000. This amount would provide for uninterrupted production in case of breakdowns. The supporting equipment for this line would total costs to \$1,149,500,000 and require 1,000,000 square feet overall. Additionally, a 40 MW power plant would be required consisting of 200,000 square feet at a cost of \$180,000,000.

Typically, the OEM price of color television picture tubes is just under one hundred dollars based on overall production of one million tubes per factory per year. Assuming a difficulty and complexity factor of 20, it would be reasonable to predict a price of not more than \$2,000 per klystron at full production and maximum efficiency. Through the learning cycle, we would expect a ratio of at least ten times the cost of tubes made at full production and efficiency, or approximately \$20,000 each. These costs are based on 70 kW tubes; 250 kW tubes might be expected to increase in cost by a factor of 3.

D180-22876-4

Attachment 1

Vari-Krome Metallizing System

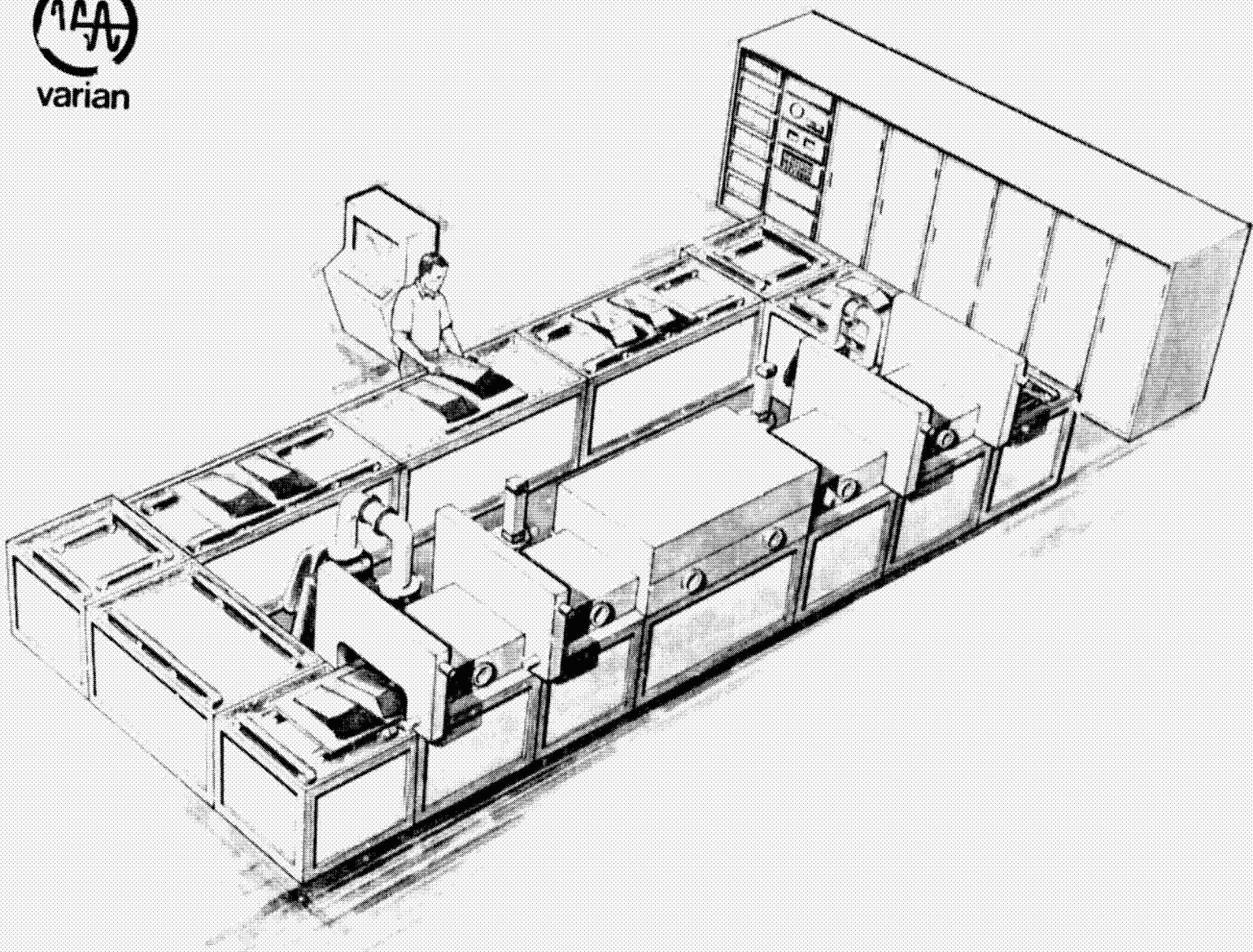


Figure A-11.

A-31

D180-22876-4

ORIGINAL PAGE IS
OF POOR QUALITY

VARIAN-PALO ALTO VACUUM DIVISION
SPECIFICATIONS
FOR
VARI-KROME™ METALLIZATION SYSTEM

1.0 GENERAL INTRODUCTION

The Vari-Krome™ metallization system is a fully automatic in-line system designed for high volume production of decorative metal coatings on plastic parts. The system is a complete metallization facility, including materials handling equipment to interface with normal parts flow within the factory. Base coated plastic parts are introduced into the system on specially designed platens which are routes through the Vari-Krome process. The parts are returned continuously to the load-unload area with a bright metal plating ready for application of top coat.

The Vari-Krome metallization system is capable of processing parts up to 34" x 42" in size. The coating zone is designed to deposit uniformly over irregular shapes such as automotive grilles with a maximum centerline height of 8". Production rates are dependent on part size and loading factors. Fifty-five (55) platens (34" x 42" coating area per platen) per hour may be processed in this system.

The system is designed for production operation in a rugged industrial environment with a major emphasis on reliability and maintainability. All phases of the system are designed for four shifts of continuous operation before planned maintenance shutdown for cleaning and material replenishment. Key operating parameters are continuously monitored for early warning of potential problem areas. The modular design of the system permits maximum flexibility in process set-up and maintainability of the system.

The heart of the Vari-Krome metallization process is the Varian S-Gun™ source, capable of high rate deposition without the substrate bombardment and heating effects normally associated with vacuum deposited coatings. The basic Vari-Krome process has a coating zone with six banks of four S-Gun sources each to permit uniform coating over a wide span. Twenty of these guns are active at one time with one bank of four guns held in reserve. Parts flow through the coating zone continuously for maximum utilization of source material.

Fully automatic control is basic to the Vari-Krome process system. Control of the system is electronic and critical maintenance functions are continuously monitored. The system is truly automatic. All set-up and operating parameters are under key control of the production or maintenance supervisor. Once production parameters are entered, the machine will automatically process parts until the coating zone material is depleted. If malfunctions occur which are detrimental to the process or the equipment, the system will go to a safe operating condition, display the malfunction and sound the alarm for supervisory attention. Routine shutdown for material replenishment and

cleaning is initiated by the production or maintenance supervisor with a keyed instruction. Once the maintenance function is complete, a keyed instruction will automatically take the system through the sequence of operations necessary to ready the system for production. Total control and monitoring of the system is accomplished at a control station which may be remotely located from the system. A CRT viewing screen and keyboard permit full control of the system from the control station, including production set-up, manual control for maintenance functions and fully automatic control.

2.0 PARTS ACCOMMODATION MATERIALS HANDLING

The parts accommodated in the Vari-Krome system can vary from small items (knobs, etc.), to large irregular shapes (automotive grilles, etc.). The transport platen may be fitted by the customer with an inexpensive sheet metal part holder which is designed for the production part being processed. Capacity of the holder is determined by part size and coating requirements. The basic platen has a coating area 34" wide x 42" long.

3.0 PRODUCTION THROUGHPUT

The basic Vari-Krome system is capable of depositing a uniform bright coating up to 1200 \AA thick across the 34" span at a production rate of 38 linear inches per minute. This corresponds to 1 platen every 60 seconds.

4.0 SYSTEM OPERATION

The Vari-Krome metallization process operates in a controlled vacuum environment. The metal coating is deposited on the plastic part (substrate) by high rate sputtering from Varian S-gun sources. Each source contains a target which is the source of material to be deposited. The basic system arrangement is shown on drawing D6519S2 - Revision A.

In operation, each platen is introduced into the process chamber via an air vacuum lock. The lock is isolated from the process section, cycled to atmospheric pressure and the external isolation valve is opened. A platen is rapidly transported into the lock, the external isolation valve is closed, and the lock is evacuated by the high speed vacuum system to a preset pressure. When space is available in the process section the transfer isolation valve opens and the platen is transported at high speed into the process section to a position just behind the preceding platen. The platen transfer speed is reduced to the coating speed to continue through the coating zone while the isolation valve closes. The air vacuum lock is vented to atmospheric pressure in readiness for the next platen. As platens are processed through the coating zone they exit the system via the exit air vacuum lock in a similar manner.

The finished platens are routed back to the system entrance via the load/unload area for removal of the finished part(s) and loading of new parts.

5.0 EQUIPMENT DESCRIPTION

5.1 ENTRANCE/EXIT SECTION

The entrance and exit sections of the system are designed for high speed evacuation to a level that permits entrance and removal of parts from the process section without detrimental effect on the parts in the coating zone. Each lock section is equipped with transport system and isolation valves for entrance to the system and the process section. Valves are sequenced and transport system is operated for high speed translation of parts from the external conveyor system into the process section.

Vacuum in each lock section is provided by a Roots Blower/Mechanical pump system with a vibration isolation roughing line.

5.2 PROCESS/COATING SECTION

The process/coating section consists of an entrance and exit transfer section plus the coating section. Each subsection has a self contained material transport system with interlocked feedback to the control system for positive indication of platen location within the system. Entrance and exit systems are capable of high speed translation of parts in and out of the section as well as matched speed to the coating zone for continuous flow.

The coating section contains a total of twenty-four (24) Varian S-Sun sources in zones of four each. Source location within each zone is designed for uniform coating across the part(s) on the transport system

A gas flow control system is included in the coating section providing the controlled atmosphere required for the Vari-Krome metallization process.

5.3 EXTERNAL MATERIALS HANDLING

An external material handling system is provided to route platens to a convenient load/unload area. This continuous return system for part holding platens permits operation adjacent to normal parts flow without the need for special equipment to return platens from an unload area to a load area.

The external system consists of four corner sections, two straight sections and a "power and free" load/unload section.

5.4 ELECTRICAL/CONTROL SYSTEM

The electrical control system includes conventional power distribution for the power supplies and vacuum pumps with automatic control for the overall Vari-Krome process. Power controls for the system are located in a power distribution center including all necessary motor starters and contactors. The material transport system features variable speed drive with feedback to maximize system efficiency.

The operator control console consists of a CRT viewing screen with terminal keyboard. The operation set-up parameters including S-Gun power level and transport operating speed are keyed in during set-up on the system. Once the instructions are keyed in they are placed under supervisory control, i.e., they cannot be changed by an operator unless the keyboard is "unlocked" by the supervisor. Operating parameters including maintenance interlock functions can be displayed on the viewing screen by keyed instructions. Shutdown for maintenance and subsequent start-up to production are automatically programmed into the operation from simple keyboard commands. Automatic protection features for parts and or equipment are incorporated into the control system to minimize down time.

6.0 UTILITY REQUIREMENTS

6.1 ELECTRICAL, 460 VOLT, 3 PHASE, 60 Hz PLUS EQUIPMENT GROUND

Basic System: 70 KVA

S-Gun Source Power Supply: 400 KVA

6.2 COOLING WATER

60-80°F, 75-100 psig; 30 gpm

6.3 COMPRESSED AIR

75-100 psig; 112 CFH

6.4 LIQUID NITROGEN

35 psig maximum, approximately 0.6 CFH

6.5 DRY NITROGEN LOAD LOCK (CHAMBER BACKFILL)

5 psig maximum, approximately 8000 CFH

6.6 ARGON, HIGH PURITY

30-60 psig, approximately 2 CFH

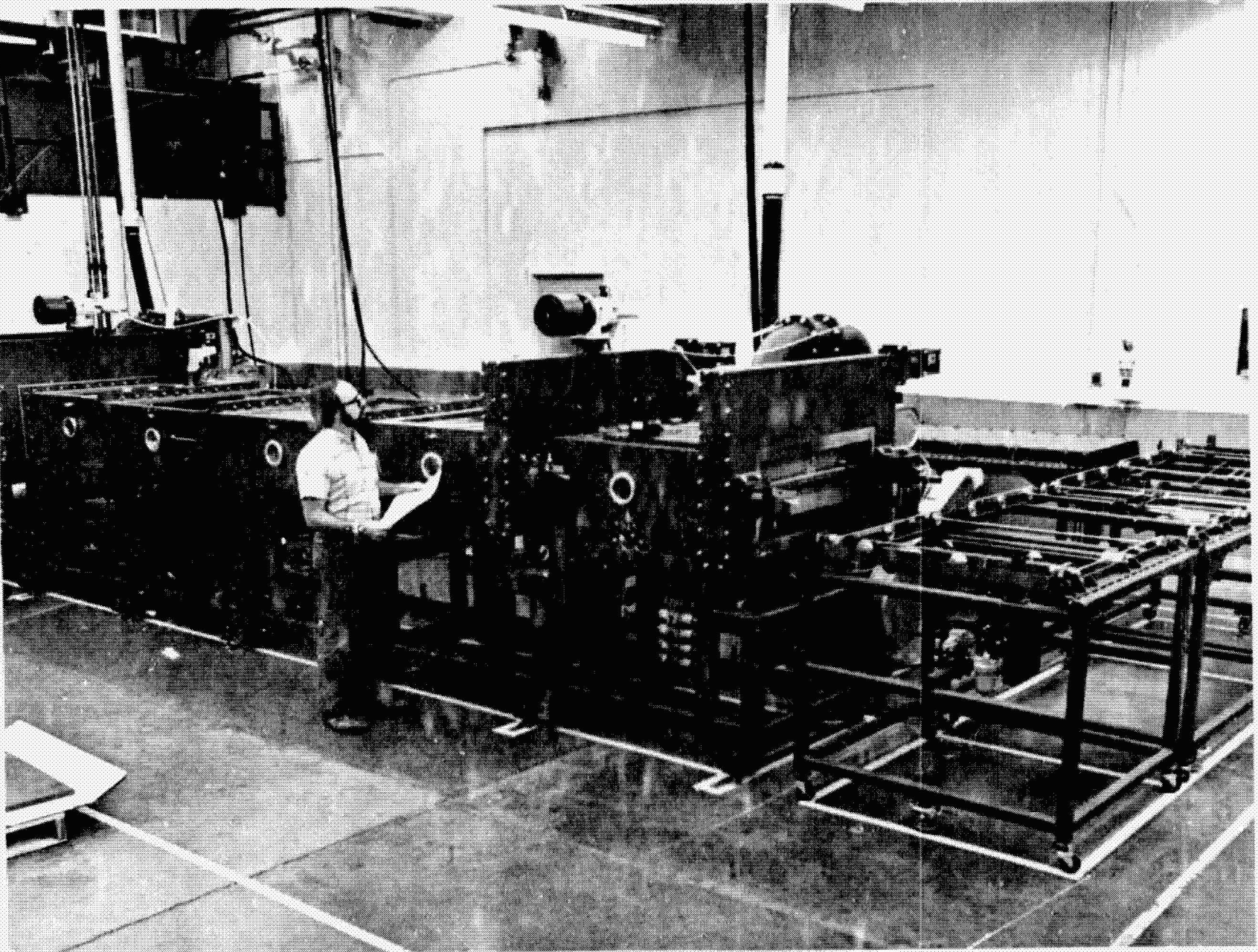


Figure A-12.

A-37

D180-22876-4

ORIGINAL PAGE IS
OF POOR QUALITY

**APPENDIX B
SOLAR POWER SATELLITE
POWER CONTROL & DISTRIBUTION
SUBSYSTEM**

- 1. POWER SEMICONDUCTOR TECHNOLOGY EVALUATION**
- 2. MPTS POWER CONDITIONING**

**This material was generated under a subcontract with the General Electric Co.,
Space Division, Valley Forge, Philadelphia, Pa.**

Roman W. Andryczyk

POWER SEMICONDUCTOR TECHNOLOGY EVALUATION

The commercial introduction of the silicon controlled rectifier (SCR) in 1957 initiated the diversified applications of solid-state power control devices. Since then, the power handling capability of silicon devices have improved so much that 8000 kVA phase controlled locomotives and high voltage DC transmission deploying 500 MW now use solid-state components.

Since the SCR's introduction, many other thyristor devices have been developed, including the gate turn-off switch, field controlled thyristors, power transistors, etc. Considerable R&D activity on power device applications is concentrated at higher frequencies above 10^4 Hz. Here, switching power supplies are projected to become a major market factor in the mid 1980's.

The current and voltage-handling capabilities of test-recovery power rectifiers are also improving rapidly. At present, fast-recovery rectifiers are also a limiting item in many applications because of available maximum voltage ratings, consistency of the turn-off mechanisms from device to device in a given production quantity, and cost. Schottky diodes now available have low forward drop, but are limited by operating temperature and peak reverse voltage, and often seem to have reliability problems.

Where the application of power switchings is concerned, the presently preference seems for power transistors over thyristors. As technology evolves over the next decade it is believed that power transistors will be successfully applied at 20 to 30 KHz (at 1000 V and 1000 Amps).

Transistors are quite suitable for many high-power applications beyond the capability of a single device by series and parallel connection.

In the last several years, introduction of the amplifying gate has increased the dynamic performance of thyristors considerably. Greater activity will take place in faster devices to meet the increasing commercial needs in the 20-30 KHz range.

The reverse-switching rectifier is another thyristor device being suggested for high-pulse power application. Its role on the market is also expected to grow. Such devices as 400 Amps and 1300 Volts are now available.

Another promising component is the power vertical field-effect transistor. These devices can handle several hundred watts of load power at several hundred volts. Because stored charge effects are absent, they provide much better frequency response than bipolar transistors.

Semiconductor-device power applications depend greatly on heat removal, thermal fatigue-free contacts to silicon, etc. The success of heat management and adequate maximum junction

D180-22876-4

temperature margins directly affects longevity and reliability. The judicious combination of heat pipe/heat sinking techniques can be of great benefit.

Using IC's for over voltage-under voltage detection, and other circuit abnormalities, can assure improved reliability and less strain on the power devices.

Power module designs (mounting multiple semiconductor chips in a single package) are beginning to address heat-removal problems at lower current and voltages. The power module concept can maximize heat dissipation while also optimizing device requirements for a given application. The resulting component provides not only improved reliability and performance, but eventually more favorable functional costs. A key feature of GE's power module line is direct copper bonding to the substrates. The advantages of direct bonding are multiple, some of them are:

- Improved thermal impedance
- Provision of thermatic seal
- Improved thermal fatigue
- Simpler fabrication process
- Lower total cost.

A whole new area of volume production involving power semiconductor devices involves the sale of unmounted chips. This has significant advantages in that the basic termination to the silicon pallet has been made and tested by the device manufactures, thus aiding the end user in final assembly. SCR's, transistors, and rectifiers are presently available in such a stage.

Prepackaged parallel transistor arrays are available up to 1200 amperes, with many products intended for electric vehicle control. Advances in processing quality, fine-line geometry, etc., all make power devices with greater dynamic properties possible in the future.

MPTS POWER CONDITIONING

The MPTS power control and distribution subsystem provides conditioned power for all MPTS elements. Each antenna is divided into 228 power control sectors, each sector providing power for 420 klystrons. The five depressed collector klystron requires conditioned power on all inputs except the two collectors which utilize power directly from the SPS Collector A supplies and Collector B supplies. The power conditioning subsystem block diagram is shown in Figure 1. The estimated input power to the DC/DC converter (Fig. 2) is about 5400 Kw.

The purpose of this exercise is to determine the size, weight and efficiency as a function of the projected solid-state power switching technology development in the mid 1980's.

Table 1 shows the projected switching speeds of power semiconductors (i.e., at 40 KV, 150 Amps).

Type of Switch	SCR	Transistor	FET	Thyristor	Rectifier
Switching Speed	30 KHz	50 KHz	50 KHz	30 KHz	40 KHz

Table 1. Projected Switching Speeds

Presently the switching speeds of the considered semiconductors range from 1 to 10 KHz. Due to this fact an analysis was conducted to determine the size, weight and losses as a function of frequency. Table 2 shows the results obtained.

Switching Freq.	Ploss KW	Size		Wt.		Per Unit Wt.	
		Ft ³	M ²	Lb.	Kg	Lb./KW	Kg/KW
1 KHz	161	520	14.7	30000	13500	6.0	2.7
10 KHz	232	260	7.36	15000	7000	3.0	1.4
20 KHz	267	208	5.9	12000	5500	2.4	1.1
30 KHz	302	195	5.4	11250	5100	2.25	1.02

Table 2. Size, Weight and Losses of DC/DC Converter

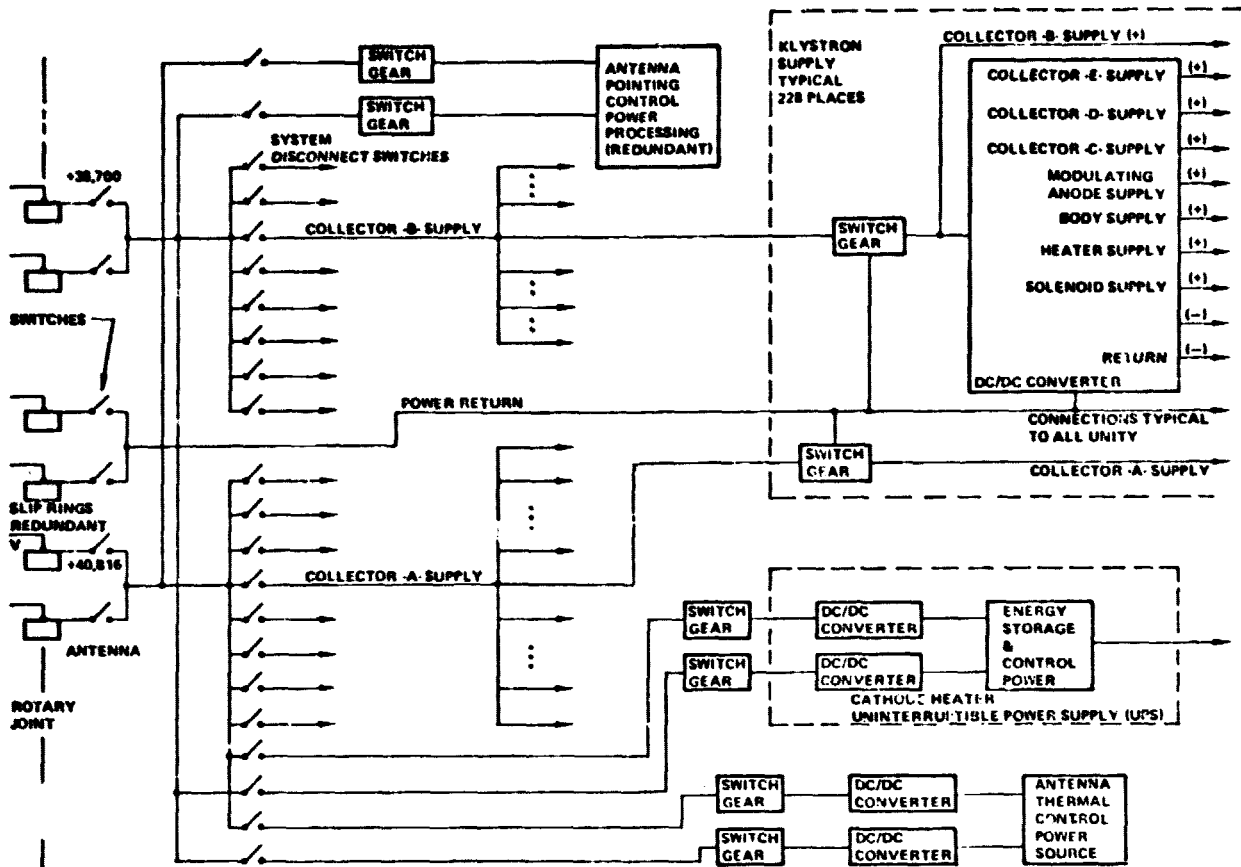
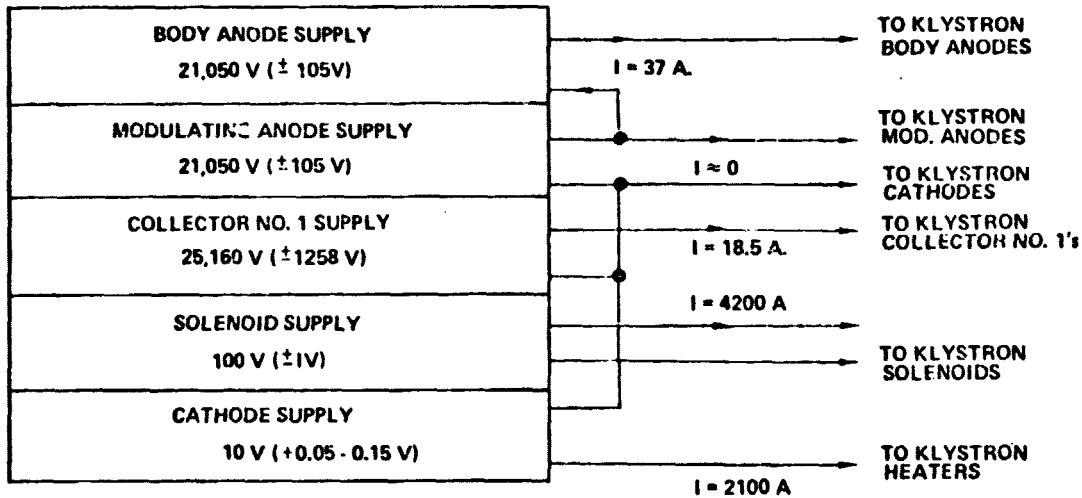


Figure 1 MPTS Power Conditioning Subsystem



$P_{out} = 2,464,160 \text{ W}$
 $\eta = 0.96$
 $P_{in} = 2,566,833 \text{ W}$

Figure 2 MPTS DC/DC Converter

Our conclusion is that a 20 KHz to 30 KHz switching speed is achievable in the next decade, but not much higher.

Figure 3 shows the block diagram used for analysis of the individual module losses shown in Table 3.

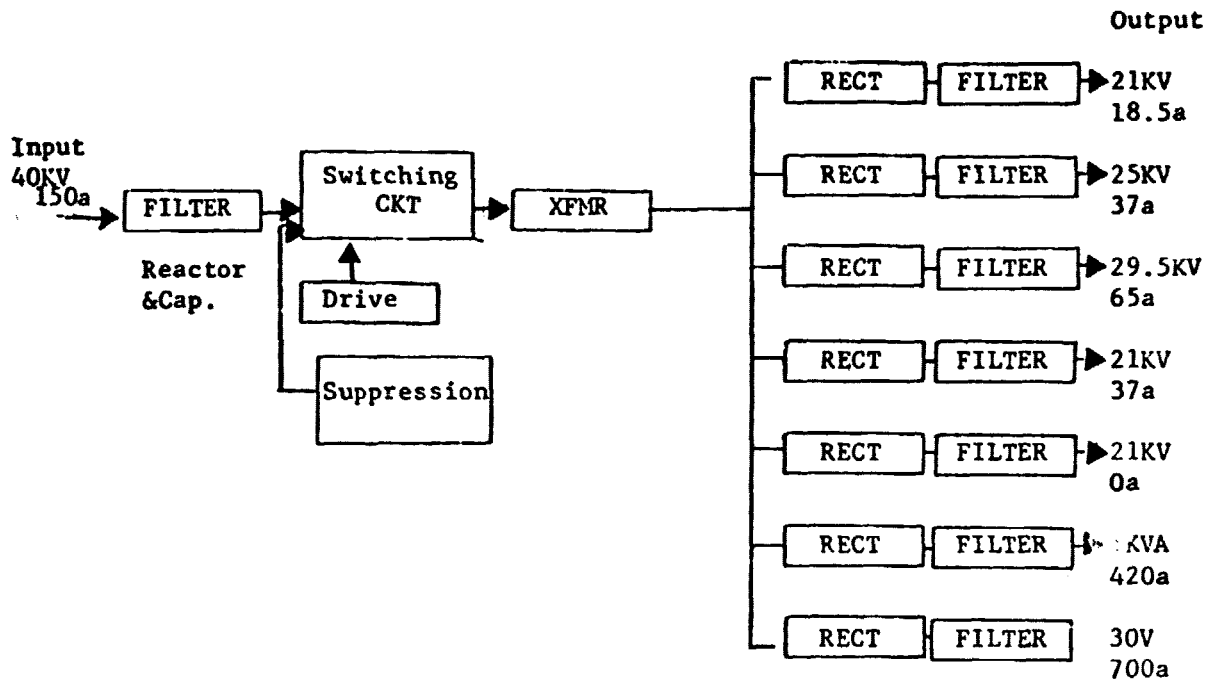


Figure 3. Simplified DC/DC Converter Block Diagram

Switching Freq.	1 KHz	10 KHz	20 KHz	30 KHz
Filter (Input)	25	35	40	45
Cond				
Switching SW	10 2	10 10	10 20	10 30
Drive & Suppression	2	5	10	15
98.6				
XFMR	70	70	70	70
RECT	2	2	2	2
Output Filter	50	100	115	130
Total Losses (KW)	161	232	267	302
% Eff.	96.9	95.6	94.9	94.3

Table 3. Itemized DC/DC Converter Module Losses

Basic Assumptions

(1) **Switching losses estimates:**

Use as a baseline 40 – GE C158/C159 SCR's with 10 in series and 2 in parallel, with each SCR forward voltage drop of 1.5 Volts.

(2) **Drive and suppression losses one 50 percent of switching losses.**

(3) **Rectifier losses:**

Using series connected 7.5 kV rectifiers per each output at an average forward voltage drop of 1.25 Volts.

(4) **Transformer:**

A transformer was designed with a 98.6 percent efficiency at 10 KHz. The design parameters are:

(a) 100 Volts/turn

(b) .007 inch grain oriented iron

(c) 10 watts/lb of iron loss

The total weight of the transformer is about 5000 lb, the size is 67 inches high and 30 inch diameter.

(5) **The estimated dimensions of the switching SCR Bridge Network are 7 x 9 x 3 ft and its weight is 500 lb.**

(6) **The total DC/DC converter weight is based on the assumption that the transformer is 1/3 of the total weight.**

Body Anode Cathode Heater and Solenoid Supply Regulator

Three types of regulators have been considered:

(1) **Series regulator – is the simplest, smallest and lightest, but the power losses are the highest.**

These losses occur due to the regulating element operating in the active region of the semiconductor in order to maintain regulation. The voltage (V) across this element would be from about 3 to 10 Volts depending on the load current (I). (The power loss is VXI .)

(2) **Pulsewidth regulator with integrating filter -- this method of regulation combines the inversion and regulation in the pulse width inverter stage.**

The switching reference frequency is generated by a separate oscillator circuit. The voltage regulation is maintained by an error simplifier that controls the duty cycle of the inverter switch. The power losses are minimal because the in-line switching semiconductor devices are always in saturation when conducting the load current at a voltage drop from 0.1 to 2 Volts depending on the switching current and the devices used.

The bulk of the weight is in the output filter, because this output inductor has to share the total energy during the off time of the inline switches. This is most likely to be the largest and heaviest method of regulation.

- (3) **Boost regulator** – this approach provides the same inline voltage drop of .1 to 2 Volts but only regulates the power above the minimum input voltage to the regulator, therefore it is the most efficient in terms of power losses. The power transformer only boosts the difference between the input and output voltage, therefore its size is moderate, and the output filter is also relatively small because the energy stored in the inductor only has to be the partial boosted energy, and compared to integrating filter of the second approach would be 5 to 10 times smaller and lighter.

Conclusions

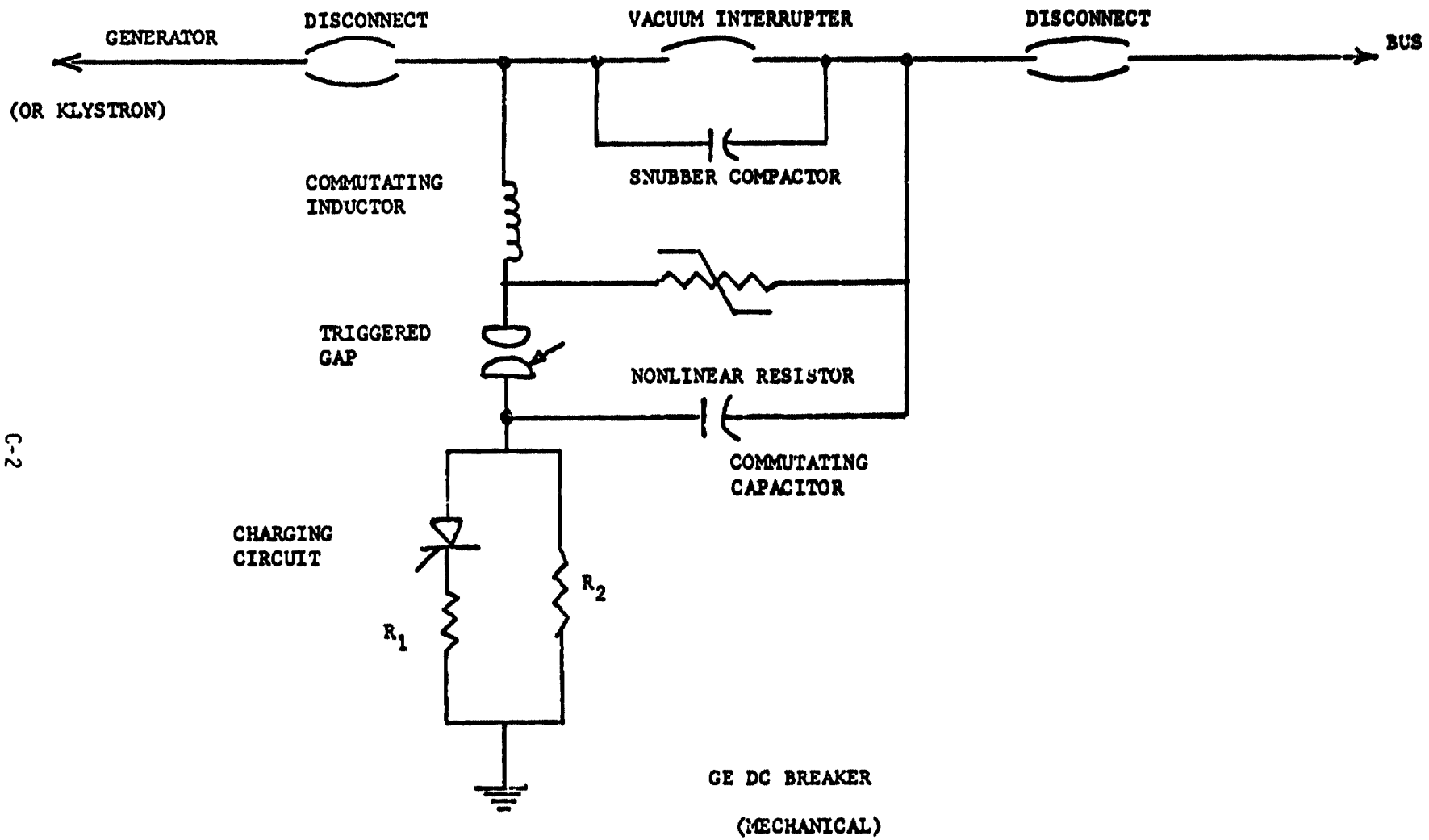
- (1) It can be assumed that 1 Kg/Kw and 1000 Kg/m² is achievable for power conversion within the next decade.
- (2) Solid-state switching devices (such as transistors, SCR's) will be available at high voltages and currents required for SPS with an efficient frequency up to 30 KHz.
- (3) The efficiency of the DC/DC power converter is 94 percent to 95 percent (at 20 KHz to 30 KHz).
- (4) Transformers with 98 to 99 percent efficiency are achievable for space application.
- (5) The Boost regulator seen to be the optimum method of regulations from the power loss and weight considerations.

**APPENDIX C
OPERATION OF GENERAL ELECTRIC DC BREAKER
(MECHANICAL)**

The basic principle of operation is a superposition of a high frequency alternating current on the load or fault current to be interrupted, producing instants of zero current in the main interrupter.

The commutating capacitor is kept charged from the DC bus through a large resistance to ground (R_2). During an interruption, the vacuum switch is opened, drawing an arc. At the proper instant the triggered gap is fired, discharging the commutating capacitor through the vacuum switch, achieving interruption. Any stored inductive energy is diverted to the nonlinear resistor. The snubber capacitor serves to limit the rate of rise of the voltage across the interruptor.

After an operation the SCR in the charging circuit is fired, rapidly recharging the commutating capacitor through a small resistance to ground. As the capacitor becomes charged, the current through the SCR falls to zero, enabling it to turn off. The breaker is then ready for another operation.

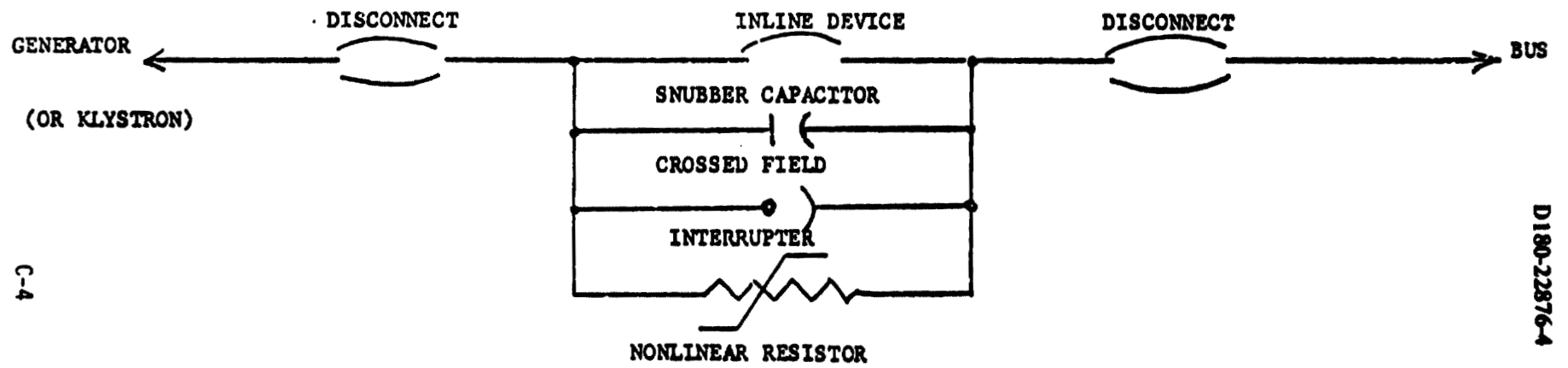


C-2

D190-22876-4

**HUGHES DC BREAKER
(MECHANICAL)**

Based on published data we estimated the Hughes breaker would utilize the crossed field interrupter. A mechanical inline device would carry the steady state current. During a fault or load current interruption, the inline device would be opened and the current transferred to the crossed field interrupter. After a time sufficient to insure deionization in the inline device, the crossed field interrupter reverts to a nonconducting state, transferring the current to the snubber capacitor. When the snubber becomes fully charged, current is transferred to the nonlinear resistor, and any remaining inductive energy is dissipated.



HUGHES DC BREAKER *
(MECHANICAL)

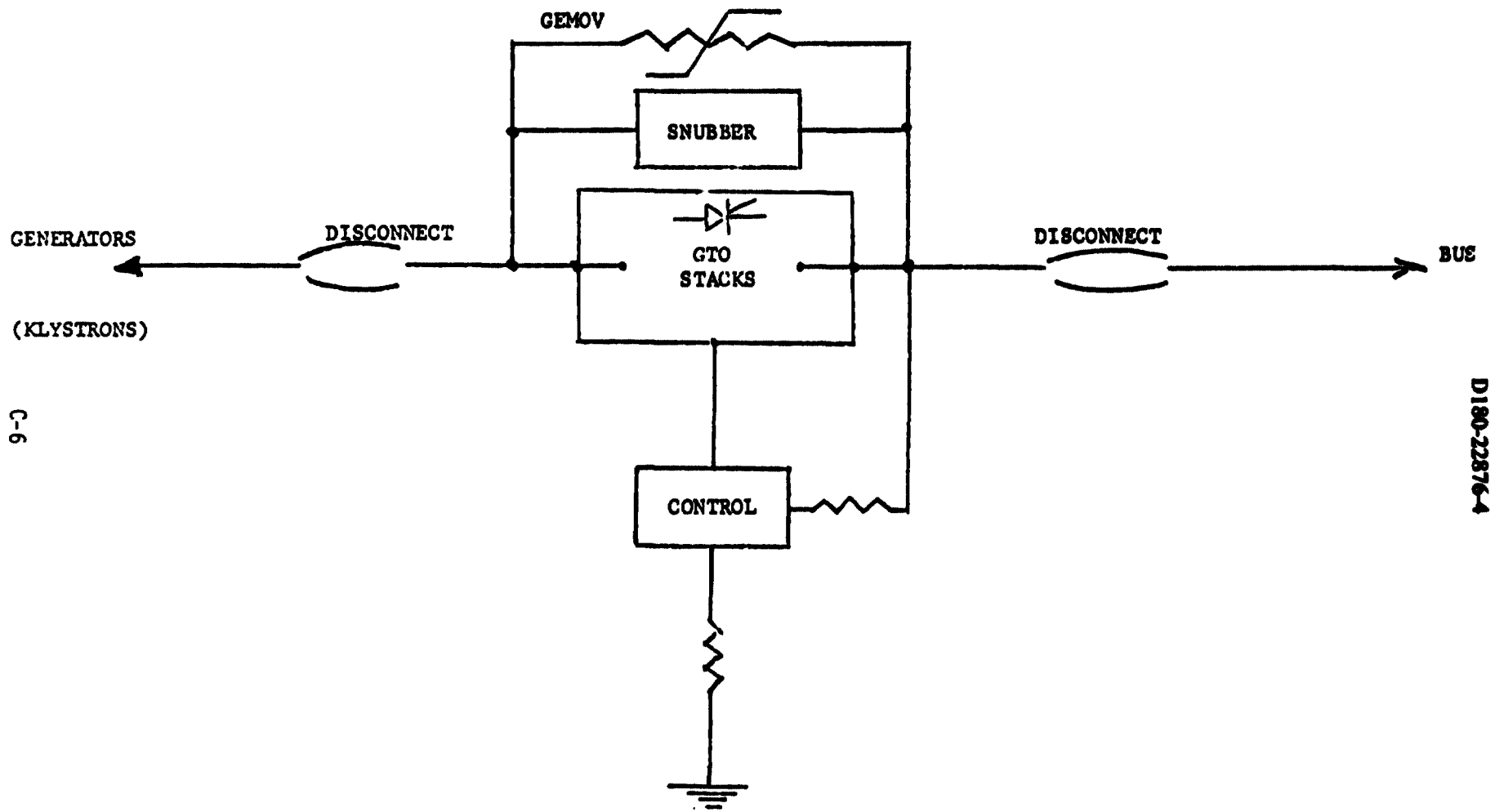
* ESTIMATED BASED ON PUBLISHED DATA

D180-22876-4

**GATE TURN OFF
DC BREAKER**

For a fast turn on and turn off (10 u sec) time, a solid state breaker must be utilized. A breaker employing gate turn off devices is recommended. The devices are connected in series/parallel to achieve the desired rating. A slaving technique is used for the series elements so that as each element in the stack turns on or off, it operates the gate of the next element in line.

To turn the breaker on, the GTO's are simply pulsed on. After the breaker is turned on, load current is carried through the GTO's. In the event of a fault, the control circuit pulses the GTO's off. Current is diverted into the snubber circuit, limiting the rate of rise of voltage across the GTO's. Finally, any stored inductive energy is dissipated by the GEMOV.



GENERATORS
(KLYSTRONS)

DISCONNECT

GTO
STACKS

CONTROL

DISCONNECT

BUS

GATE TURN OFF
DC BREAKER

C-6

D180-22876-4



SWITCHGEAR REQUIREMENTS



Voltage Capability KV	Steady State Continuous Current Amp.	Momentary Current Amp.	Opening Time	Quantity - Thermal System	Possible Switches
38.7	290	2900	10 u sec.	456	SOLID STATE ONLY
40.8	620	62000	10 u sec.	456	SOLID STATE ONLY
21	0	0	10 u sec.	97000	SOLID STATE ONLY
44	2500	12000	5 msec.	196	SOLID STATE OR MECHANICAL SWITCHING

C-7

D180-22876-4

SWITCHGEAR WEIGHT COMPARISON

Two mechanical switches under development by GE and Hughes were investigated and compared to a GTO solid state switch. The 44 kv switch used for turbogenerator power switching (requiring 5 milliseconds response time) should be a mechanical switch (substantial weight saving). The 21 kv switch used to clamp the klystron's anode and cathode (1 to 5 microseconds response time) must be a solid state switch. The 38.7 kv and 40.8 kv switches at the klystron should be traded off against the microwave tube. A considerable weight and cost savings in switchgear can be achieved if the tube can withstand excessive fault current for milliseconds instead of microseconds.



SWITCHGEAR WEIGHT COMPARISON



Switch Description	Total Number of Switch	GE DC Breaker		HUGHES DC Breaker		Solid State DC Breaker (GTO)	
		Weight/Unit LBS	Total Weight LBS	Weight/Unit LBS	Total Weight LBS	Weight/Unit LBS	Total Weight LBS
38.7 KV 290 AM(CONT.)	454	235	.107 x 10 ⁶	950	.43 x 10 ⁶	577	.26 x 10 ⁶
40.8 KV 620 AM(CONT.)	456	235	.107 x 10 ⁶	950	.43 x 10 ⁶	874	.40 x 10 ⁶
21 KV 0 AM	97000	-	-	-	-	40	3.88 x 10 ⁶
44 KV + 2500 A.M.(CONT.)	196	235	.046 x 10 ⁶	950	.18 x 10 ⁶	3296	.65 x 10 ⁶
TOTAL WEIGHT (LBS)			.26 x 10 ⁶		1.04 x 10 ⁶		1.31 x 10 ^{6*}

*Does Not Include the Weight of the 21 KV Switch

C-9

D180-22876-4

D180-22876-4

HUGHES/GE DC BREAKER WEIGHT COMPARISON

The Hughes mechanical interrupter is four times as heavy as the GE interrupter with the largest weight contributors being the snubber capacitor, the crossfield interrupters and the SF 6 switching device. In addition a tight control of the pressure must be maintained at the SF 6 switching device. The GE vacuum switching device is now used commercially.

The total weight of the Hughes switchgear is a GE estimate based on published information to date. This was done by scaling down the weight from a 100 kv to 40 kv (2.5 ka continuous).



HUGHES/GE DC BREAKER WEIGHT COMPARISON



<u>COMPONENT</u>	<u>HUGHES WEIGHT/BREAKER</u> <u>LBS</u>	<u>GE WEIGHT/BREAKER</u> <u>LBS</u>
CHARGING CKT FOR COMMUTATION CAPACITOR	-	5
COMPLETE OPERATING MECHANISMS	80	80
INLINE SWITCHING DEVICE	120 (SF6)	20 (Vacuum)
SNUBBER CAPACITOR	440	20
CROSSFIELD INTERRUPTER	150	20
ENERGY ABSORBING RESISTOR	10	15
SUPPORT AND CONTROL CONNECTIONS	150	75
TOTAL	950 lbs per breaker	235 lbs per breaker

C-11

D180-22876-4

D180-22876-4

**TOTAL COST OF SWITCHGEAR IN SOLAR THERMAL SPS
(1977 DOLLARS)**

The total cost of switchgear for SPS depends on the type of switchgear used. The total mechanical switchgear cost is about \$15M as compared to the solid state \$154M (excluding the cost of the 21 kv switch which is assumed to be solid state). This differential in cost as well as additional development cost and considerable weight penalty for the solid state switchgear should be considered when trading off the klystron vs. switchgear requirements.



**TOTAL COST OF SWITCHGEAR IN SOLAR THERMAL SPS
(1977 DOLLARS)**



Switch Description	Total No. of Switches	GE Vacuum Switch \$ Millions	Solid State Switch \$ Million
38.7 KV 290 AM(CONT.)	456	5.93 (\$13K Each)	30 (\$60 K Each)
40.8 KV 620 AM(CONT.)	456	5.93 (\$13K Each)	46 (\$101K Each)
21 KV 60 AM	7000	NOT AVAILABLE	388 (\$4K Each)
44 KV 2500 AM(CONT.)	196	2.74 (\$14 K Each)	78 (\$396K Each)

C-13

D180-22876-4

D180-22376-4

TECHNOLOGY ADVANCEMENT

GE DC Breaker—Key components of the prototype switch such as the:

- (A) high speed mechanism
- (B) compensation circuit with the GE vacuum interrupter
- (C) non-linear resistor (energy absorber)

have been tested at a rating of 400 kv, 2 ka continuous and 10 ka fault current.

Hughes DC Breaker—Switch has been field tested at 100 kv, \cong 500 amps continuous and 4 ka fault current. The Hughes interrupter uses SF₆ (sulfur hexoflouride) as the medium with a 2 millisecond response time compared to the GE vacuum interrupter with a 3 millisecond response time.

Gated Turn Off Solid State Breakers—The way to go if microsecond response time is required. It is behind in technology, heavier and more expensive.



TECHNOLOGY ADVANCEMENT



C-15

	GE DC Breaker	Hughes DC Breaker	GTO Solid State Breaker
State of Technology 1977	Prototype Development. Components of the prototype successfully tested.	Prototype has been field tested.	Some laboratory model testing. Improvement in current carrying capability and heat transfer is needed for the particular use in space.
State of Technology 1987	Commercially available.	Commercially available.	It is expected that by 1987, some of these devices would be commercially available with improved current carrying and heat transfer capability.
General Remarks	<ul style="list-style-type: none"> ● GE switch commercially available. Light weight and compact. ● Uses vacuum as interrupting medium. ● Compatible with vacuum environment. 	<ul style="list-style-type: none"> ● Relatively heavier than GE switch. ● Uses SF6 switch. ● Slightly faster response than GE switch. 	<ul style="list-style-type: none"> ● GTO of 1 KV & 200 AM continuous rating not commercially available. Development stages. ● Very Expensive. ● Relatively heavy ● Extremely fast response time.

**APPENDIX D
ESTIMATE OF RF FIELD AT SPS ARRAY SURFACE**

Summary

Initial assessment indicates that the RF electric field at each waveguide slot is of the order of 3-4 kV/cm. Currently, spaceborne antenna systems @ GEO typically have RF fields one order of magnitude lower.

Procedure

- 1) Energy density @ SPS center for 5 GW system is $22 \text{ kW/m}^2 = 2.2 \text{ W/cm}^2$.
- 2) Slot spacing is $\lambda_g/2 \cong 8.2 \text{ cm}$ and lateral slot separation is $.78\lambda \cong 9.5 \text{ cm}$, i.e., each slot occupies 79 cm^2 , giving $2.2 \times 79 = 174 \text{ watts CW per slot}$. ($\lambda = 12.1 \text{ cm}$ for 2.45 GHz.)
- 3) Resonant slot impedance for slot $.475\lambda \times .01\lambda = 2(530 + j0)$

(Ref. Kraus, "Antennas," page 370), i.e., voltage $V = \sqrt{PR}$

$$V = \sqrt{PR} = \sqrt{(174)(2)530} = 429 \text{ Volts}$$

$$\text{and } E = V/d = 429/0.122 = 3.5 \text{ kV/cm SPS}$$

For current S/A system, the Canadian Satellite, a comparable value is calculated as follows:

$$P = 200 \text{ Watts CW}$$

$$\text{Width of 14 GHz waveguide feeding 30 ft antenna} = .475 \text{ in}$$

$$\text{Waveguide impedance is } \sim 500\Omega, \text{ i.e.} \quad = 1.2 \text{ cm}$$

$$V = \sqrt{(200)500} = 316 \text{ Volts, i.e.,}$$

$$E = 316/1.2 = 262 = .26 \text{ kV/cm}$$

APPENDIX E
HIGH POWER CAPABILITY OF COMPOSITE WAVEGUIDES FOR SPS

Summary

Preliminary calculations, verified by extrapolated Hughes experimental results at 10 GHz in ambient air indicate that in the vacuum environment for the SPS array geometry, CW powers of about 16 kW are sustainable at 100°C and about 101 kW at 300°C for a graphite epoxy 2.5 GHz waveguide 16 mils thick, with internal silver plating of the order of 1 mil.

Thermal Analysis

The analysis, conducted by Mr. Geo. Roe encompasses the following steps:

- 1) The capability of convective cooling in an X-band waveguide (1 in x 1 1/2 in x .050 in) operating at 235°F in a 70°F room was estimated for each of 4 walls of a graphite epoxy waveguide 50 mil thick, with 2 mils of silver plating, totaling 69.4 W/meter. To this was added the radiative cooling component, 51.8 W/meter, totaling 121.2 W/meter of length. This compares roughly with an experimentally derived number (Ref. 1) from test results of 2 kW of transmitted power at 235°F, which corresponds to 92 W/meter for an assumed attenuation of 6 dB/100 ft, the calculated attenuation at midband for a metal-alloy waveguide.
- 2) The capability of radiative cooling only in a space vacuum environment was calculated for an S-band waveguide geometry (1.8 in x 3.5 in x .016 in) considering the waveguides butted together on the narrow wall, with a viewing factor of 1 in the front of the array facing the earth (17° subtended angle), and rest as space at 97°K; and 50% of the back of the array as space and 50% as Aluminum at 300°C. This calculation yielded a heat rejection capability of 112.8 W/meter for an equilibrium temperature of 100°C and 688.9 W/meter for 300°C. With an assumed waveguide loss of 1 dB per 100 ft (metal alloy at midband), a value of transmitted power of 16.6 kW at 100°C and 101 kW at 300°C was arrived at. The appropriate minimum thickness plating is yet to be determined and an experiment to verify the above numbers is recommended.

Reference

1. Manufacturing Methods for Dimensionally Stable Composite Microwave Components, AFML-TR 74-70, May 1974, Hughes Aircraft Company, Culver City.

APPENDIX F
INTERACTION OF MICROWAVES WITH THE IONOSPHERE

An analysis has been made of the stimulated Rayleigh scattering by the entropy mode of a Gaussian microwave beam traversing the ionosphere. The model used is: 1) An electron density wave (either a plasma electron wave or a plasma wave) acts as a diffraction grating and scatters the main microwave beam. 2) A scattered electromagnetic wave beats with the main microwave beam and causes an ohmic heating wave. 3) The heating wave causes an electron temperature wave which is large only in directions perpendicular to the magnetic field direction because of the extremely anisotropic electron thermal conductivity. 4) The temperature wave causes the assumed electron density wave.

Plasma ion waves give larger growth rates than plasma electron waves. Above a rather small intensity threshold there are convective instabilities. The directions of the large growth rate scattered electromagnetic waves lie on a conical surface whose axis is the magnetic field direction and whose half angle is the angle between the main microwave beam direction and the magnetic field direction.

The spatial growth rate is inversely proportional to the plasma ion wavelength (a result which differs from some other published results) but the scattering angle is also inversely proportional to the plasma ion wavelength so that the scattered waves with larger growth rates do not stay as long (and grow) in the finite width main microwave beam. The total spatial growth is thus approximately constant for all the scattered electromagnetic waves on the conical surface. The noise level in the ionosphere under the main microwave beam can be hundreds of decibels above the noise level at a larger altitude in the ionosphere for some power satellite cases. The spatial growth is proportional to the percentage ionization and thus is approximately constant over an altitude range of thousands of kilometers in and above the F region of the ionosphere. Further work to verify the above analysis is in progress by Dr. D. Nelson.

This work was conducted on a Boeing IR&D program and is included due to its relevance to this contract.